Semiconductors, Vol. 34, No. 9, 2000, pp. 1004–1010. Translated from Fizika i Tekhnika Poluprovodnikov, Vol. 34, No. 9, 2000, pp. 1046–1052.

ATOMIC STRUCTURE AND NONELECTRONIC PROPERTIES OF SEMICONDUCTORS

Generation of Bulk Defects in Some Semiconductors by Laser Radiation in the Transparency Region of the Crystal

S. V. Plyatsko

Institute of Semiconductor Physics, National Academy of Sciences of Ukraine, Kiev, 252028 Ukraine

Submitted February 21, 2000; accepted for publication March 21, 2000

Abstract—Laser-stimulated dissociation of regions enriched with metal and redistribution of point defects in the bulk of a semiconductor crystal under the effect of infrared laser radiation (for photon energies lower than the band gap) were studied. It is shown that the defect-generation rate depends on the power density and wavelength of the laser radiation and on the impurity concentration. Two mechanisms of migration for the laser-induced defects were ascertained, and the activation energies for migration during laser irradiation and after irradiation was terminated were estimated. *© 2000 MAIK "Nauka/Interperiodica".*

Interest in the interaction between laser radiation and semiconductor crystals has been aroused in relation to the possibility of modifying and ultimately controlling the properties of both monatomic and more complex semiconductor compounds. Depending on the relation between the band gap E_g and the energy of the laser-radiation quantum $\hbar\omega$, either the properties of near-surface layers (if $\hbar\omega \geq E_g$) or the bulk properties (if $\hbar\omega < E_g$) can be modified in the zone exposed to laser radiation.

In both cases, the interaction of the laser radiation with the material not only gives rise to new defects but also stimulates the migration and redistribution of point native defects, impurities, and their complexes that are already present in the crystal.

The mechanism of laser-stimulated formation of defects in the case where radiation corresponding to the fundamental absorption in a semiconductor is used is reduced to pulsed heating and a high ionization level, which enhances impurity diffusion and structural changes even in the solid phase. In addition, an optical pulse generates a pressure pulse that may amount to several kbar and may generate the point defects even outside the zone exposed to radiation. Large values of electric-field strength in a laser pulse (~10^5 V/cm) bring about the ionization of impurities and also affect the migration of both the host and impurity atoms [1].

As for the mechanism of defect generation in the case where laser radiation corresponding to the transparency region of the crystal is used, this mechanism remains unclarified in spite of the large number of publications devoted to this subject.

This paper is a continuation of investigations into the laser "annealing" (under the conditions of $\hbar\omega < E_g$) of bulk defects in single crystals of binary and ternary IV–VI semiconductor compounds, silicon doped with phosphorus, and also III–V compounds. The concentration of charge carriers was in the range of n = 10^{15}–10^{20} cm^{-3}. The samples were initially kept at room temperature; according to measurements, the temperature during irradiation was no higher than 473 K. Thermal annealing at such temperatures under absolutely identical conditions did not bring about changes in the bulk properties of the studied materials. The values of the radiation power densities (W) were in the range below the damage threshold for the sample. Either a CO laser (λ = 5–6 μm) or a CO_2 laser (λ = 10.6 μm) was used for irradiation.

IV–VI crystals were grown by the Czochralski and Bridgman–Stockbarger methods and by planar crystallization from the melt and vapor phase. Silicon and III–V compounds were grown by the Czochralski method. The samples were doped directly during growth. Impurities were introduced mainly to change the concentration of charge carriers, but such impurities as manganese, europium, and phosphorus also acted as indicators of the localization of impurity centers in the lattice.

In order to clarify the laws governing laser-stimulated processes, which occur in the crystal lattice, we studied optical reflection and transmission; electron spin resonance (ESR); and also the electrical, photoelectric, and structural properties of the crystals.

In order to reduce the contribution of the irradiated near-surface layer, this layer was removed by treatment in a polishing etchant to a depth of 30–100 μm.

The condition $\hbar\omega < E_g$ is necessary for changing the bulk properties, because no changes of such properties occur in the crystals of PbSnTe and PbSnSe compounds with the composition for which the above condition is not satisfied.

It is well known that almost all semiconductor compounds feature a certain degree of deviation from stoichiometry and also incorporate inclusions in the form of microdefects, complexes, and clusters in the matrix; these inclusions involve intrinsic components (and also impurity components in the case of doping) and exhibit

1063-7826/00/3409-1004$20.00

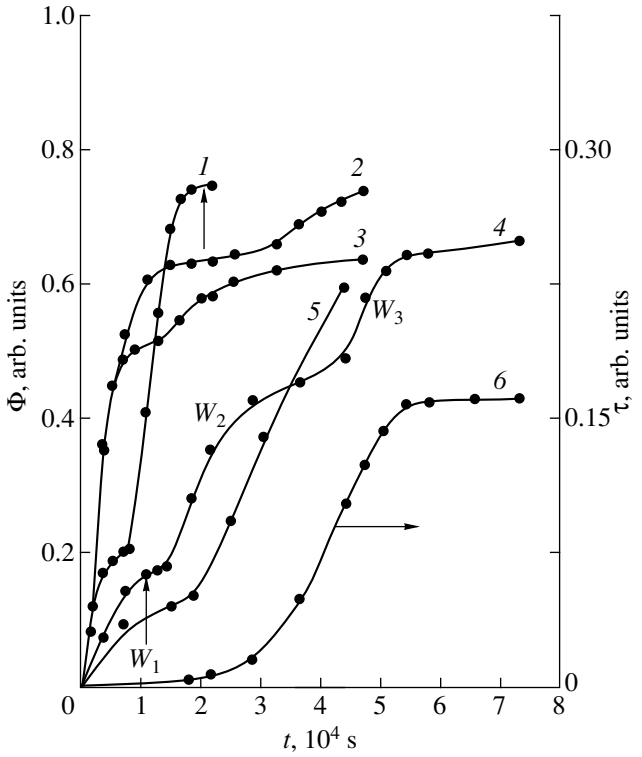

Fig. 1. Dependences of the annealed-defect fraction Φ on the laser-irradiation duration t for crystals of (*1*) Si:P, (*2*) PbTe:Tl, (*3*) PbTe:Na, (*4*) PbTe, and (*5*) GaAs:Te. By way of an example, vertical arrows indicate the regions that correspond to the irradiation duration t_s. The radiation-power densities in different portions of the curves are $W_1 < W_2 < W_3$. Curve *6* represents the optical transmission τ of a PbTe single crystal (W = 35 W/cm^2).

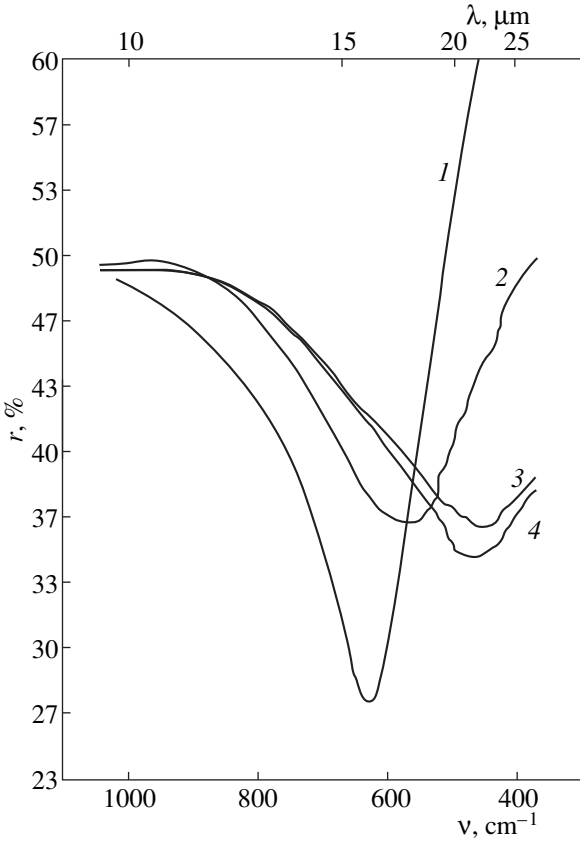

Fig. 2. Spectral dependences of the reflection coefficient $r(\lambda)$ in p-$Pb_{1-x}Sn_xTe$ (x = 0.2) crystals (x = 0.2): (*1*) before irradiation, (*2*) for the surface irradiated for t = 30 min, (*3*) for the surface irradiated for t = 130 min, and (*4*) for the unirradiated (rear) surface (the irradiation duration is t = 130 min).

a large spread in sizes [2]. The composition of microdefects in doped crystals may vary from single-component to more complex, depending on the matrix and the type of impurity [3]. The stability of these defects is governed by the relation between the bond strengths (the atomization energies) in the complex itself and in the matrix. Thus, for example, for almost all impurities of Groups II, III, and IV in the IV–VI compounds, the atomization energy for impurity complexes exceeds that for the matrix [4, 5].

A high proportion of such defects are not electrically active in the sense that they do not supply free charge carriers to the allowed bands. However, potential barriers formed at the defect–matrix boundaries effectively scatter the charge carriers and serve as additional recombination centers or traps [6, 7].

The conventional line of attack on the problem of homogenization of semiconducting crystals consists in long-term (up to several months) isothermal annealing; using such annealing, it is possible to change the concentration of free charge carriers in the bulk of semiconductor wafers, but it is virtually impossible to get rid of structural imperfections.

Figure 1 shows the fraction of defects "annealed" as a function of the duration of laser irradiation: $\Phi(t) = [N_0 - N(t)]/N_0$, where N_0 and $N(t)$ are the initial and final (at the point in time t) defect concentrations. It can be seen that two portions are typical of the curve $\Phi(t)$ for each value of the radiation-power density W: initially, the dependence $\Phi(t)$ is described by an exponentially ascending curve, whereas, at a later stage, variations occur more slowly.

A characteristic feature of the dependence $\Phi(t)$ is the fact that it is qualitatively the same for all studied crystals, i.e., Si, GaAs, PbSn(Ge)Te(Se), and PbS. In crystals with the same history, $\Phi(t)$ varies more steeply with increasing W and tends to unity, which should correspond to the complete elimination of lattice defects.

In order to clarify the causes of such behavior of $\Phi(t)$, we studied the spectral dependence of optical reflection r in $Pb_{1-x}Sn_xTe$ (x = 0.20) crystals 1 mm thick. The reflection spectra $r(\lambda)$ are shown in Fig. 2. The minimum in the spectral dependence of the reflection coefficient $r(\lambda)$ corresponds to the plasma frequency for a given concentration of charge carriers with effective mass m_c: $\omega_p = (4\pi e^2 n/m_c\varepsilon_\infty)^{1/2}$. The hole con-

centration determined from ω_p was in satisfactory agreement with that obtained from the Hall-effect measurements.

The spectral dependence $r(\lambda)$ was studied for both surfaces of the sample. Before irradiation, the plasma frequencies in both cases were virtually identical ($\omega_{p1} \approx \omega_{p2}$).

After the dependence $r(\lambda)$ and the Hall coefficient R_H had been measured preliminarily, one of the sample surfaces was exposed to laser radiation ($\lambda = 10.6$ μm) with a given power density W = const for a certain time t, after which the dependence $r(\lambda)$ and the Hall effect were studied again. Then, the sample was again irradiated for a certain time, and the measurements of $r(\lambda)$ for irradiated and unirradiated surfaces and also R_H were repeated. This procedure was repeated again and again.

In the early stages of irradiation, the plasma minimum in $r(\lambda)$ measured on the irradiated surface (ω_{p1}) shifts to longer wavelengths (Fig. 2, curve *2*), whereas the position of the minimum for the unirradiated surface (ω_{p2}) remains unchanged. On further irradiation, a shift in the plasma minimum is observed for both surfaces; however, variations in ω_{p2} occur with an insignificant delay. This delay starts to decrease after the attainment of an exposure range where ω_{p1} varies only slightly; ultimately, ω_{p2} becomes equal to ω_{p1}. On further irradiation, the spectral positions of the plasma minimums remain virtually unchanged (Fig. 2, curves *3*, *4*). In this case, the irradiation-time dependence of the charge-carrier concentration determined from the Hall effect also becomes weak. As the radiation-power density W increases, the spectral position of the plasma minimum for the irradiated surface shifts again to longer wavelengths, and the concentration of free holes decreases.

The above results indicate that the generation of defects (these are donors in the case under consideration) occurs at the irradiated surface; the generation front moves to the bulk of the sample with irradiation time and reaches the unirradiated surface. On further irradiation with the given W, the quantities $\Phi(t)$ and $\omega_p(t)$ vary slowly. It is a mechanism of formation and motion of defects during irradiation of the crystal such as this that is responsible for relatively long "annealing" times. The propagation velocity for the front of the laser-induced defects can be determined from experimental dependences $r(\lambda, t)$ and $R_H(t)$. For the case under consideration, the velocity of the transverse mass transport is $V_{cr} \approx 10^{-6}$ cm/s. It is apparent that V_{cr} depends on the power density W and may significantly exceed the above value for $W = 25$ W/cm^2.

The spatial distribution of generated defects can be inferred from the measurements of optical transmission τ in PbSnTe(Se) crystals that are 0.8–1.0 mm thick and have an initial concentration of free holes equal to $n = (2.5–3.5) \times 10^{18}$ cm^{-3}. The dependence $\tau(t)$ is shown in Fig. 1 (curve *6*). It can be seen that transmittance of the sample increases significantly in the course of irradiation, which is caused by a decrease in the free-hole concentration.

It is known that native defects capable of reducing the hole concentration in IV–VI compounds primarily include the interstitial Pb and the chalcogen vacancies [8, 9]. It is not conclusively established at present which of these defects is mainly responsible for electron conduction. However, the results of studies of metal-atom diffusion in *n*-type crystals suggest that electron conduction can be caused to a large extent by interstitial atoms of metals [10–12]. This is also confirmed by ESR studies of PbTe(Se):Mn crystals exposed to laser radiation [13, 14]. At the initial stage of irradiation, the concentration of interstitial manganese increases by more than an order of magnitude, and the transition to electron conductivity is observed. The line corresponding to the substitutional-Mn hyperfine structure just becomes distinct. However, the conductivity-type inversion is not governed by the manganese concentration ($N_{Mn} \leq 1 \times 10^{18}$ cm^{-3}), because the latter is much lower than the concentration of metal vacancies ($N_{V(M)} \sim 1 \times 10^{19}$ cm^{-3}) and, thus, cannot bring about a full compensation of electrically active Pb vacancies and the conductivity-type inversion. In this case, the manganese impurity is an indicator of the localization of a metal component in the lattice and testifies that, as a result of laser-induced transformation, the concentration of metal ions (including those of Pb) in the crystal increases substantially; the metal ions compensate for the acceptor effect of vacancies in the metal sublattice irrespective of whether the atoms of the metal component reside at the lattice sites or interstices, because in both cases these atoms act as donors. At later stages of irradiation, when there is already electron conduction, an increase in the concentration of manganese ions at the lattice sites and a decrease in this concentration at the interstices become prevalent. This result is indicative of a decrease in the contribution of interstitial defects to the electron concentration; it also indicates that, in the case of laser annealing, the chalcogen vacancies may be considered as making the major contribution to electrical conduction only if the charge-carrier concentration is $n \geq 5 \times 10^{18}$ cm^{-3}, which corresponds to the disappearance of a hyperfine structure of interstitial manganese.

It is also noteworthy that the defect-introduction rate $V_d = dN/dt$ decreases with decreasing irradiation temperature and depends on the type and concentration of impurity in the neutral regions (Fig. 3).

A convenient object for verification of the dependence of the defect-generation rate on the concentration of the impurity that resides within the microdefects are PbTe single crystals doped with a donor impurity, for example, indium. A characteristic feature of In-doped PbTe is the fact that the concentration of free holes in the crystal remains unchanged virtually up to $N_{In} = (1–3) \times 10^{19}$ cm^{-3} [15], because a high proportion of In

impurity is in an electrically inactive state within the precipitates. The hole concentration was virtually constant and amounted to (2.5–3.0) × 10^{18} cm^{-3} in the entire range of In concentrations.

It can be seen from Fig. 3 that two linear portions are characteristic of the generation-rate dependence, which indicates that defects of different types are generated by laser irradiation. For a low impurity concentration, the rate of variation in the defect concentration is close to that in undoped crystals, in which case the laser radiation interacts predominantly with the intrinsic component, whereas, for indium concentrations of $N_{In} \gtrsim 5 \times 10^{18}$ cm^{-3}, the mechanism of laser-stimulated doping with indium becomes prevalent. The electron concentration in PbTe:In crystals exposed to laser radiation had a characteristic temperature dependence and corresponded to the introduced impurity.

The defect-introduction rates in PbSnTe(Se) doped with various impurities (although at a fixed concentration of charge carriers and impurity) are different, which may be caused by the dependence of the laser-stimulated redistribution of the components on their diffusion coefficients D, and the relative contribution of each of these components to physical properties may depend on the ratio of the corresponding values of D for equal concentrations of the components.

Dissociation of inclusions or a decrease in the concentration of atoms in the enriched regions of the crystal are conducive to homogenization owing to the filling of vacancies and a diminishing of the influence of structural lattice imperfections on the electrical properties of the samples. In the crystals of IV–VI compounds, a power-law temperature dependence of mobility $\mu(T) \propto T^{-\beta}$ is typically observed in wide ranges of temperatures and charge-carrier concentrations. The value of β is defined by the prevalent mechanism of carrier scattering, because this mechanism is almost invariably mixed. Depending on the degree of structural perfection of the crystals, the doping level, and the type of impurities, the experimental value of β may even be negative at low temperatures. Figure 4 shows the dependence of β on the duration of irradiation for PbSe:Mn(Eu) crystals in which no anomalies in the behavior of $\mu(T)$ were observed. It can be seen from Fig. 4 that, as a result of irradiation, the mechanisms of scattering of charge carriers vary from mixed scattering ($\beta = 1.71$) in crystals with hole conduction to polar scattering by longitudinal optical phonons ($\beta = 2.5$) in crystals with electron conduction in the same temperature range ($77 \le T \le 300$ K). A similar behavior and dependence of β on the duration of irradiation are also observed for the PbSnTe samples.

The properties of the crystals remain time-independent (Fig. 5, curve *3*) if laser irradiation is terminated in the time region of $t > t_s$ where the dependence $\Phi(t)$ levels off. However, if the irradiation is terminated in the portion of $\Phi(t)$ that corresponds to the time range of $0 \le t \le t_s/2$ (see Fig. 1), a partial relaxation of generated defects is observed (Fig. 5, curve *1*). The relaxation times may be as long as several days; then the properties of the crystal become time-independent. The higher the radiation-power density (for t = const), the more profound the relaxation effect. Such behavior of the

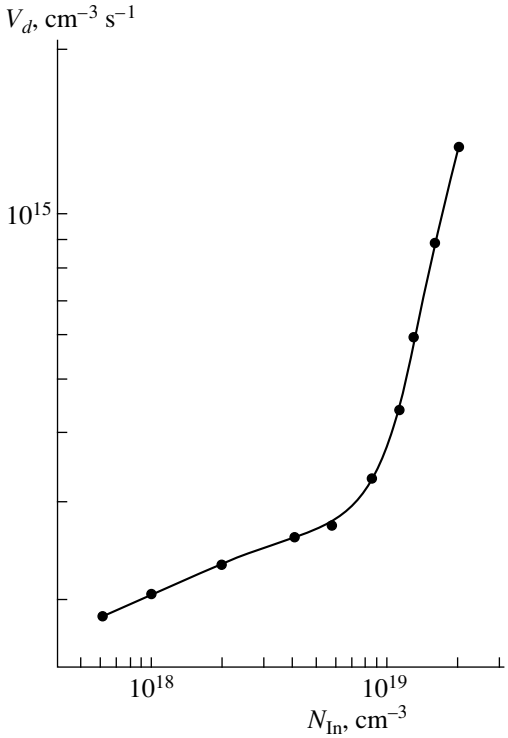

Fig. 3. The defect-generation rate V_d as a function of In concentration in PbTe:In single crystals. W = 20 W/cm^2.

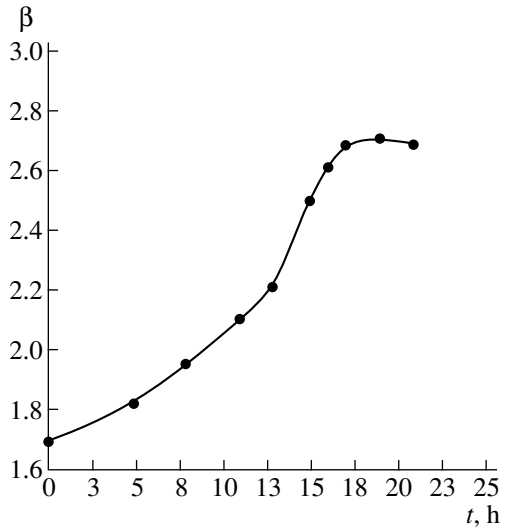

Fig. 4. Changes in the mechanism of charge-carrier scattering in relation to the duration of laser irradiation of PbSe:Mn(Eu) single crystals.

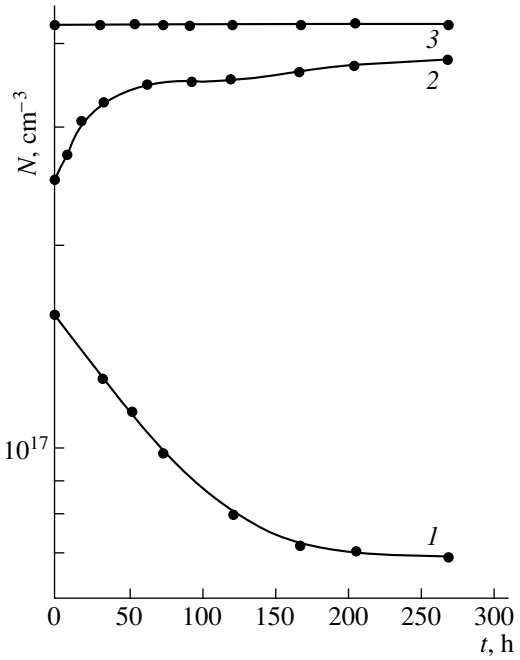

Fig. 5. Variations in the concentration of laser-induced defects in n-$Pb_{1-x}Sn_xTe$ ($x = 0.2$) single crystals after laser irradiation ($W = 40$ W/cm^2) for $t = (1)$ 4 h ($t < t_s/2$), (2) 8 h ($t > t_s/2$), and (3) 10 h ($t = t_s$).

relaxation processes is due to the return of ionized interstitial atoms to the region of inclusions.

If the laser-stimulated process of defect generation is terminated in the time range of $t_s/2 \le t \le t_s$, an aftereffect is observed over a certain time period (≤10 h); i.e., the defect concentration continues to increase but never attains the level corresponding to t_s (Fig. 5, curve *2*). The value Φ_s can be attained solely as a result of additional irradiation with the same power density W.

In the first case, the concentration of emerging individual atoms exceeds that of trapping centers (vacancies and interstitials in the vicinity of a macrodefect), which is observed at the initial stage of irradiation; therefore, the unannihilated atoms return to the inclusion when irradiation is terminated. The relaxation time is controlled by the radiation-power density W and the irradiation time t. The higher the power density W and the shorter the time t, the higher the concentration of activated (electrically active) atoms in the immediate vicinity of the source and the shorter the relaxation time. Accordingly, the relaxation effect is most profound in the IV–VI crystals that were preliminarily annealed thermally and have a charge-carrier concentration of $\lesssim 1 \times 10^{17}$ cm^{-3}, in which case a major portion of Pb vacancies are filled.

In the second case, for a given power density during "annealing," the inclusion becomes "exhausted," and individual atoms are no longer admitted to the lattice; this occurs prior to the completion of migration of activated nonequilibrium atoms. Changes in the system of point defects will then occur with the passage of time even after laser irradiation is terminated and continue until all activated atoms occupy the stable lattice sites.

In epitaxial, structurally perfect films of IV–VI compounds, noticeable laser-stimulated transformations can be observed for high W and charge-carrier concentrations of $n \ge 10^{18}$ cm^{-3}.

It is well known that the mechanisms of thermal annealing can be effected by virtue of the fact that the processes of generation of new point defects (and redistribution of those already present in the crystal), their migration, recombination, and complex formation and dissociation occur in the crystal. The same processes are also responsible for laser-stimulated transformations in a crystal, but the driving forces, in contrast with the case of thermal annealing, are not only thermodynamic. However, it is still possible to estimate certain parameters of the processes occurring in the crystal.

Thus, for example, the diffusion coefficient of defects in IV–VI compounds can be estimated from the experiment with the combined action of the electric fields E_L and E_{ex} [14]. Knowing the longitudinal-migration length l (for example, for an ESR-active impurity), the electric-field strength E and the interaction time t, we can determine the longitudinal-drift velocity V_l, which exceeds V_{cr} by more than an order of magnitude, and the ion mobility from the formula $u = l/Et$. Then, using Einstein's relation, we obtain the diffusion coefficient $D \sim 1 \times 10^{-8}$ cm^2/s, which exceeds by 7–8 orders of magnitude the known values for electrically active intrinsic components at temperatures corresponding to laser annealing.

In addition, using the results of experiments with the combined action of E_L and E_{ex} and with the relaxation and aftereffect in n-PbSnTe single crystals, and also the published data [10], we can estimate the activation energy for the migration of defects in these cases. The obtained values are ~0.38, ~0.69, and ~0.71 eV, respectively, which indicates that the mechanisms of migration of electrically active defects in a crystal during laser irradiation and after it are different. The activation energy for the relaxation and aftereffect is somewhat lower than that for the interstitial doubly charged Pb ion [10], in which case diffusion via interstices is prevalent.

A possible mechanism of the defect migration in the course of laser irradiation may also be inferred from the dependence $\Phi(t)$ represented as an $\Phi - t^{-1/2}$ plot, which is linear for each value of W and for $t \le t_s$; this indicates that correlated vacancy–interstitial pairs can exist in crystals before annealing and can be generated and annihilated during laser annealing [16]. These inferences are consistent with ESR studies of IV–VI compounds, in which case an interstice–site redistribution of paramagnetic Mn ions is observed as the duration of irradiation increases. In Si:P, an identical process manifests itself in an enhancement of the interchange inter-

action of substitutional phosphorus whose concentration increases substantially with the time of irradiation [17]. At the same time, if the phosphorus concentration in silicon is increased up to $N_P \gtrsim 10^{17}$ cm^{-3} by direct doping during growth, the intensities of hyperfine-structure lines (related mainly to individual impurity atoms and their small groups) decrease to the point of complete disappearance, whereas the intensity of the line related to the interchange interaction increases [18].

It is worth noting that the dependences of Φ and V_d on the laser-radiation wavelength are observed experimentally as well (IV–VI compounds were studied alone); this, in turn, is additional confirmation of the nonthermal mechanism of laser-stimulated transformations. Thus, for example, the value of Φ in PbTe:Tl(Na) single crystals with a hole concentration of $\sim(5 \times 10^{19}$–$10^{20})$ cm^{-3} virtually cannot be changed using a CO_2 laser even in the case of combined effects of both E_L and E_{ex}. However, if these crystals are irradiated by a CO laser, the dependence $\Phi(t)$ reproduces qualitatively that for crystals with lower charge-carrier concentrations in the case of CO_2-laser irradiation. In undoped crystals, the times corresponding to the conductivity-type inversion (from the hole to electron type) become significantly shorter for initially equal charge-carrier concentrations. In the range of electron conduction, annealing with a CO laser makes it possible to attain an electron concentration of $\sim(4$–$5) \times 10^{19}$ cm^{-3} in undoped $Pb_{1-x}Sn_xTe$ crystals ($0 \le x \le 0.24$). Apparently, this concentration is limiting and is controlled by the concentrations of both the chalcogen vacancies and interstitial Pb.

Thus, summing up the above, we may state that the main special features of laser annealing ($\hbar\omega < E_g$) may be explained in terms of a model that involves, first, the generation of individual intrinsic (impurity) atoms as a result of the dissociation of inclusions and, second, the subsequent migration of these atoms in the bulk of the crystal (via the formation of activated states) until they become localized at lattice sites.

Among the most likely mechanisms of emergence of individual atoms in the case of steady-state laser annealing is the effect of the temperature gradient between the inclusion and the matrix due to the direct absorption of radiation by the inclusion and to the emergence of the thermal-diffusion flux, which would dominate over the diffusion flux for certain values of the power density W [19, 20]. The characteristic times of the thermal-diffusion export of material from the inclusion are 1.5–2 orders of magnitude shorter than those in the case of pure diffusion and decrease as the irradiation intensity increases. In addition, it follows from this model that the temperature of the inclusion depends on its size and shape; this imposes certain restrictions on the applicability of this model for inclusion sizes comparable to the laser-radiation wavelength, because, in this case, the necessary overheating of inclusions compared to the matrix is not ensured. On the other hand, this model makes it possible to explain the dependence of the processes under consideration on the laser-radiation wavelength and the duration of irradiation. However, taking into consideration that the temperature gradient decreases rapidly in the region of the matrix, this mechanism cannot account for the migration of individual centers over the lattice; rather, it can act as a source of atoms in the vicinity of the inclusion.

Submicrometer-sized inclusions whose concentration is also high in the crystal may decompose as a result of a local increase in compressive stress [15] induced by the filling of vacancies and interstices with atoms dissociated from large inclusions.

Apparently, the migration mechanism should be considered in a system of interaction of the laser-wave electric field with free charge carriers and activated atoms. It is also not improbable that activated atoms can tunnel in the laser-wave electric field as a result of multiphonon processes [21]. The fields of elastic stresses and macroscopic strains [22] may also play an important role in the formation and migration of mobile defects; these fields inevitably arise when the point defects emerge in a practically "cold" matrix.

REFERENCES

1. A. V. Dvurechenskiĭ, G. A. Kachurin, E. V. Nidaev, and L. S. Smirnov, *Pulsed Annealing of Semiconducting Materials* (Nauka, Moscow, 1974).
2. R. Breshi, A. Camanzi, and V. J. Fano, J. Cryst. Growth **58**, 399 (1982).
3. Sh. M. Duguzhev and V. A. Moshnikov, in *Proceedings of the All-Union Conference on Physicochemical Foundations of Doping of Semiconducting Materials, Moscow, 1988.*
4. L. V. Gurevich, G. V. Karachevtsev, V. N. Kondrat'ev, Yu. A. Lebedev, V. A. Medvedev, V. K. Potapov, and Yu. S. Khodeev, *Bond-Breaking Energies. Ionization Potentials and Electron Affinity* (Nauka, Moscow, 1974).
5. T. A. Smorodina, N. N. Sheftal', and A. P. Tsuranov, *Accomodation of Impurity Centers in a Crystalline Semiconductor Layer* (Nauka, Leningrad, 1986).
6. S. D. Darchuk, G. N. Panin, S. V. Plyatsko, *et al.*, J. Phys. Chem. Solids **51**, 1333 (1990).
7. S. D. Darchuk, T. Dietl, L. A. Korovina, *et al.*, Fiz. Tekh. Poluprovodn. (St. Petersburg) **32**, 786 (1998) [Semiconductors **32**, 700 (1998)].
8. M. Fujimoto and J. Sato, Jpn. J. Appl. Phys. **5**, 128 (1966).
9. A. V. Novoselova, V. P. Zlomanov, A. M. Gas'kov, and O. I. Tananaeva, Vestn. Mosk. Univ., Ser. 2: Khim. **21**, 107 (1980).
10. G. W. Pratt, J. Nonmet. **1**, 103 (1973).
11. T. V. Saunina, D. B. Chesnokova, and D. A. Yas'kov, Fiz. Tekh. Poluprovodn. (Leningrad) **17**, 985 (1983) [Sov. Phys. Semicond. **17**, 620 (1983)].

12. H. Heinrich, Lect. Notes Phys. **133**, 407 (1979).
13. S. V. Plyatsko, Yu. S. Gromovoĭ, S. K. Kadyshev, and A. A. Klimov, Fiz. Tekh. Poluprovodn. (St. Petersburg) **28**, 138 (1994) [Semiconductors **28**, 83 (1994)].
14. Yu. S. Gromovoj, S. V. Plyatsko, F. F. Sizov, and L. A. Korovina, J. Phys: Condens. Matter **2**, 10 391 (1990).
15. V. I. Fistul', in *Proceedings of the I All-Union School on Thermodynamics and Technology of Semiconductor Crystals and Films, Ivano-Frankovsk, 1986*, Part 1, p. 3.
16. T. R. Warte, J. Chem. Phys. **28**, 103 (1958).
17. Yu. S. Gromovoj and S. V. Plyatsko, in *Abstracts of the 1st International Conference on Materials Science of Chalcogenide and Diamond-Structure Semiconductors, Shernivtsi, 1994*, Vol. 2, p. 143.
18. E. M. Gershenzon, N. M. Pevin, and M. S. Fogel'son, Fiz. Tverd. Tela (Leningrad) **11**, 1986 (1969) [Sov. Phys. Solid State **11**, 1599 (1969)].
19. N. N. Grigor'ev, T. A. Kudykina, S. V. Plyatsko, and F. F. Sizov, Semicond. Sci. Technol. **3**, 951 (1988).
20. N. N. Grigor'ev, T. A. Kudykina, S. V. Plyatsko, and F. F. Sizov, Infrared Phys. **28**, 307 (1988).
21. S. D. Ganichev, I. N. Yassievich, and W. Prettl, Fiz. Tverd. Tela (St. Petersburg) **39**, 1905 (1997) [Phys. Solid State **39**, 1703 (1997)].
22. *Atomic Diffusion in Semiconductors*, Ed. by D. Shaw (Plenum, London, 1973; Mir, Moscow, 1975).

Translated by A. Spitsyn

Semiconductors, Vol. 34, No. 9, 2000, pp. 1011–1015. Translated from Fizika i Tekhnika Poluprovodnikov, Vol. 34, No. 9, 2000, pp. 1053–1057.

ATOMIC STRUCTURE AND NONELECTRONIC PROPERTIES OF SEMICONDUCTORS

Electron Mobility and Electron Scattering by Polar Optical Phonons in Heterostructure Quantum Wells

J. Požela, K. Požela, and V. Jucienė

Semiconductor Physics Institute, Vilnius, 2600 Lithuania

Submitted March 14, 2000;
accepted for publication March 21, 2000

Abstract—Basic features of confined electron scattering in quantum wells (QWs) by confined polar optical (PO) phonons are analyzed. The dependence of electron mobility in $Al_{0.25}Ga_{0.75}As/GaAs/Al_{0.25}Ga_{0.75}As$ QWs on the well width is calculated. It is demonstrated that increases and decreases in electron mobility (relative to the bulk value) as a function of the QW width occur due to resonance intersubband scattering. The dependence of electron mobility limited by PO phonon scattering on the electron density n_s in the QW is calculated. It is shown that anomalous behavior of electrical conductivity, which in certain cases decreases with increasing electron density, can take place in $Al_{0.25}Ga_{0.75}As/GaAs/Al_{0.25}Ga_{0.75}As$ QWs for $n_s > 10^{16}$ m^{-2}. © *2000 MAIK "Nauka/Interperiodica".*

INTRODUCTION

Scattering of electrons confined in AlGaAs/GaAs/AlGaAs or AlGaAs/InGaAs/GaAs heterostructure quantum wells (QWs) is affected by the concurrent confinement of polar optical (PO) phonons. This leads to certain peculiarities in the electron transport in such two-dimensional (2D) heterostructures, which open the way to electron-scattering engineering in QWs. At temperatures above 80 K, scattering by confined PO phonons is the dominant scattering mechanism in the 2D channels of heterostructure modulation-doped transistors (MODFETs), which governs the electron mobility in the channel.

Further enhancement of the high-speed performance of MODFETs is related to the reduction of electron scattering by PO phonons and an increase in the level of modulation doping.

In this paper, we consider possible ways to decrease the rate of confined-electron scattering by confined PO phonons in heterostructure QWs and evaluate the effect of increasing the MODFET channel electron density on this scattering process.

1. A SIMPLIFIED MODEL OF ELECTRON SCATTERING BY POLAR OPTICAL PHONONS IN QUANTUM WELLS

We have already suggested that one can make use of the independent confinement of electrons and PO phonons in heterostructures to reduce electron–phonon scattering and, thus, to increase electron mobility [1]. Independent confinement can take place, since the effects of electron and phonon quantization are caused by different physical factors: electrons are confined in potential QWs, and PO phonons are confined in layers between the heterojunctions. We employed a simplified model, where the coordinate dependence of electron and phonon wave functions in the direction normal to the heterostructure planes is described by sinusoidal functions: for electrons in a QW of width L

$$\varphi_e \sim \sin k_z z, \tag{1}$$

where $k_z = n\dfrac{\pi}{L}$ (n = 1, 2, 3, …); and for the phonon potential in a QW of width d

$$\varphi_q \sim \sin q_z z, \tag{2}$$

where $q_z = n\dfrac{\pi}{d}$ (n = 1, 2, 3, …). The results obtained with this model demonstrated that the displacement of electron QW with respect to the phonon QW does not result in the reduction of intrasubband scattering. Quite the reverse, the intrasubband scattering was found to increase on decreasing the electron QW width. On the other hand, a sharp reduction (by 5–6 times) of the scattering rate occurs if the phonon spectrum in the electron QW is split by the insertion of a thin barrier (AlAs in GaAs) [2]. This indicated that a significant mobility enhancement in the MODFET channel is possible and stimulated the development of a more accurate model describing electron–PO phonon scattering to account for the influence of all modes that exist due to phonon confinement in QWs.

1063-7826/00/3409-1011$20.00

2. CONFINEMENT OF POLAR OPTICAL PHONONS IN A LAYERED HETEROSTRUCTURE AND ELECTRON–PHONON SCATTERING RATE

Quantization of PO phonons and features of the phonon potential at the interfaces in layered structures have been considered in a large number of publications [3–16]. Several models describing the PO phonon modes in semiconductor heterostructures have been proposed. Among these, the dielectric continuum model proved to be the most acceptable and is commonly used to describe electron–PO phonon scattering and electron transport [3–13]. The hybrid model appeared to be less adequate in describing transport phenomena, but it is more accurate in describing Raman spectra [14–16]. It is conventional to classify the PO phonon modes into two types, the confined and the interface ones. The potential of phonons confined in a QW has nodes at heterostructure interfaces. Elastic vibrations of the polar-crystal lattice ions at the interfaces result in a potential that decays exponentially away from the interfaces.

In the context of the dielectric continuum model, electron–PO phonon scattering is described in the following terms. The rate of QW-confined electron transitions from the initial state of momentum $\mathbf{k}_i$ in the subband E_{si} into any final state of momentum $\mathbf{k}_f$ in the subband E_{sf} resulting from interaction with a PO phonon mode ν is given by

$$W^{\pm}_{if\nu}(k_i, E_{si}) = \sum_{\mathbf{k}_f} \frac{4\pi m e^2}{\hbar^3} |G_\nu(z)|^2 F^2_{q\nu}\left(N_{q\nu} + \frac{1}{2} \pm \frac{1}{2}\right)\delta(k_f^2 - k_i^2 + \beta_\pm), \quad (3)$$

$$G_\nu(z) = \int_{L_e} \varphi_{e1}(z)\varphi_{e2}(z)\varphi_{q\nu}(z)dz. \quad (4)$$

Here, z is the direction normal to the QW plane; L_e is the QW width; $\varphi_{ei}(z)$ and $\varphi_{q\nu}(z)$ are the z-components of electron and phonon wave functions, respectively; $N_{q\nu}$ is the number of phonons in the νth mode; and

$$\beta_\pm = \frac{2m}{\hbar^2}(E_{sf} - E_{si} \pm \hbar\omega_\nu). \quad (5)$$

The positive sign corresponds to phonon emission; and the negative sign, to phonon absorption. $F_{q\nu}$ is the normalized electron–phonon coupling coefficient [8]:

$$F_{q\nu} = \frac{\hbar}{S}\left[\left(\frac{d\varepsilon_1}{d\omega}\right)_\nu \int_1 f_\nu dz + \left(\frac{d\varepsilon_2}{d\omega}\right)_\nu \int_2 f_\nu dz\right]^{-1}, \quad (6)$$

where S is the normalization area in the QW plane, ε_1 and ε_2 are the permittivities of the materials composing the heterostructure, and

$$f_\nu = q_{0\nu}^2 |\varphi_{q\nu}|^2 + \left|\frac{d\varphi_{q\nu}}{dz}\right|^2, \quad (7)$$

where $q_{0\nu}$ is the wave vector of emitted or absorbed phonons (belonging to the νth mode) in the QW plane:

$$q_{0\nu}^2 = k_i^2 + k_f^2 - 2k_i k_f \cos\theta, \quad (8)$$

$$k_f^2 = k_i^2 + \beta_\pm. \quad (9)$$

Confinement of electrons and phonons affects their wave functions. The overlap integral $G_\nu(z)$ of electron and phonon wave functions determines the so-called electron–phonon scattering form factor.

In the following treatment, the electron mobility limited by inelastic electron–PO phonon scattering is calculated as

$$\mu = \frac{e}{m}\left\langle \frac{1}{\tau}\right\rangle^{-1}, \quad (10)$$

where

$$\frac{1}{\tau} = \sum_\nu W_{if\nu}.$$

The pointed brackets $\langle\ \rangle$ denote averaging over electron energies.

3. SCATTERING RATE AND MOBILITY OF ELECTRONS IN HETEROSTRUCTURE QUANTUM WELLS

The rate of confined electron scattering by PO phonons in single QWs has been calculated by many authors [6–21]. A number of important features of this process have been revealed. Here are the most significant of them.

(i) It is established that the so-called rule of sum is fulfilled [6, 11, 22, 23]: the sum of form factors corresponding to electron scattering by each of the confined and interface phonon modes is equal to the form factor corresponding to scattering by bulk (unconfined) phonons. This means that if the electron–phonon coupling strength is equal for all phonon modes, phonon confinement does not alter the electron-scattering rate with respect to the case of their scattering by bulk phonons. The strength of electron–phonon coupling is determined by the phonon mode frequency. Thus, phonon confinement in heterostructures affects the electron-scattering rate only due to a shift of the phonon mode frequencies with respect to the frequency of the bulk mode. In heterostructures based on GaAs, InGaAs, and AlGaAs, the frequencies of confined and interface phonon modes are close to each other; consequently, when calculating the intrasubband scattering rates, one can neglect phonon confinement

and take into account only the electron–bulk phonon interaction.

(ii) When calculating the potential and the frequency spectrum of the interface phonon modes, one should treat the modes related to each interface independently [13, 18, 24]. Interaction between interface phonon modes occurs only in the case where their oscillation frequencies are equal. This situation, in particular, takes place in symmetric heterostructures [10].

(iii) It is shown that intrasubband electron–phonon scattering in a given QW subband decreases with an increase in the well width: $W_{11} \sim 1/L$. Seemingly, this implies a paradoxical result: as the QW width increases, the electron mobility can rise to values exceeding the mobility in the bulk material. This paradox is resolved if the intersubband scattering is taken into account. Intersubband scattering with optical phonon absorption limits the mobility increase. With increasing QW width, the number of upper subbands separated from the lower subband by an energy smaller than the optical phonon energy grows. Consequently, variations in the width of the QW layer result in periodic increases and decreases in mobility, which take place each time one of the upper subbands approaches the lower subband by an energy smaller than the optical phonon energy [13, 17, 25, 26]. In Fig. 1, we plot the dependences of electron mobility in an AlGaAs/GaAs/AlGaAs QW on the well width, which are calculated by expression (10).

(iv) Intersubband optical-phonon scattering exhibits resonance features. Scattering resonance occurs if the energy gap between the subbands is equal to, or higher than, the optical phonon energy. In this case, electrons from the upper subband can make transitions into the lower one by phonon emission, which leads to a strong increase in the electron–phonon intersubband scattering rate [27]. Especially sharp variations in the intersubband scattering rate are related to resonance scattering by interface phonons [28, 29]. Conversely, the intersubband scattering rate drops sharply when the energy gap between the subbands becomes smaller than the optical phonon energy, which hinders the nonequilibrium (e.g., photoexcited) electron transfer from the upper to the lower subband. This results in nonequilibrium carrier population inversion between the first (lower) and the second (upper) electron levels in the QW, which manifests itself in an anomalous photoluminescence spectrum [30]. Resonance intersubband electron transitions due to PO phonon emission represent a basic mechanism that controls the population inversion between the QW sublevels in solid-state heterostructure lasers [25, 31–33]. We note that an especially effective mechanism for introducing the intersubband population inversion is provided by sharp resonances in intersubband transitions caused by interface phonons.

(v) Insertion of a thin (5–10 Å wide) AlAs barrier in AlGaAs/GaAs/AlGaAs QW of a certain width does result in electron mobility enhancement. However, similar to the result obtained with the simplified model, the reduction of electron scattering by confined phonons (separated by the wall) appears to be partially compensated by increased scattering by interface phonons. Full compensation does not occur: the frequency of the interface phonon mode differs considerably from that of the confined phonon mode, which is equal to the frequency of the optical phonon in a bulk semiconductor [13, 24, 28]; consequently, the electron–phonon coupling strengths differ as well. An increase in the electron mobility in a QW with an inserted thin barrier has been observed experimentally [34]. Thus, effects of independent electron and phonon confinement can be used to achieve higher electron mobility in heterostructures and, consequently, better high-speed performance of heterostructure transistors, as well as to create conditions for population inversion between the quantized levels in solid-state laser structures.

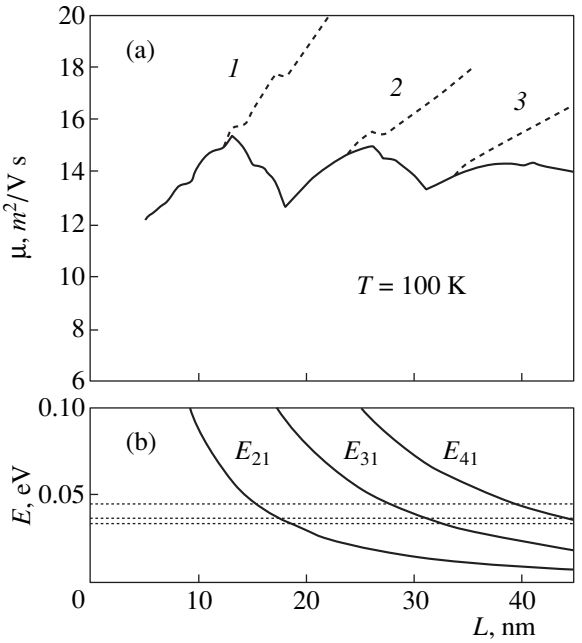

Fig. 1. Variation of (a) electron mobility μ and (b) subband energy level positions with respect to the lower subband energy with the width L of an $Al_{0.25}Ga_{0.75}As/GaAs/Al_{0.25}Ga_{0.75}As$ QW. Energies of the confined phonons (36.2 meV) and interface phonons (45.9 and 33.1 meV) are shown by horizontal lines. Abrupt changes in the electron mobility occur when the subband energy becomes close to the optical phonon energy. Dotted lines represent the results of the mobility μ calculation as a function of the well width with only a restricted number of subbands accounted for. Numerals above each curve indicate the number of subbands taken into account, starting from the ground (first) subband.

4. SCATTERING BY OPTICAL PHONONS IN THE CASE OF DEGENERATE ELECTRON GAS IN A QUANTUM WELL

The enhancement of heterotransistor speed is achieved by increasing the level of modulation doping, which results in a higher 2D density n_s of the charge carriers in

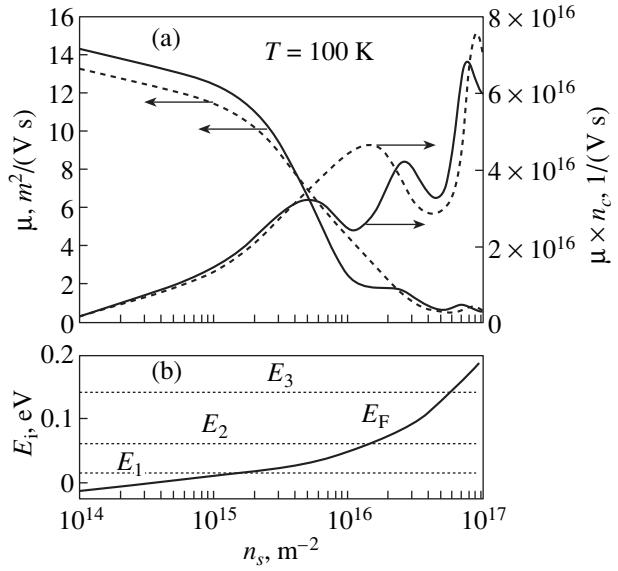

Fig. 2. Variation of (a) electron mobility μ and conductivity μn_s and (b) the Fermi level position with respect to the subband energies as a function of electron density n_s in an $Al_{0.25}Ga_{0.75}As/GaAs/Al_{0.25}Ga_{0.75}As$ QW of width L = 15 nm. Dotted lines represent the dependences calculated for μ and μn_s in the QW with a thin (d = 1 nm) AlAs barrier inserted at the center. One can see that in some regions conductivity decreases with increasing density.

the channel. At high doping levels, the electron gas in the channel becomes degenerate. Thus, when calculating optical-phonon inelastic scattering rates, one should account for the occupation of initial and final states involved in electronic transition. Then, the following expression is obtained for the reciprocal electron lifetime in the initial state with the energy E_i with respect to the transition to the final state with the energy $E_f = E_i \pm \hbar\omega_\nu$ due to scattering by an optical phonon of type $\hbar\omega_\nu$ [13, 26, 35]:

$$\frac{1}{\tau} = W^+_{if}(E_i) = \sum_\nu W^e_{if\nu}\frac{1-f(E-\hbar\omega_\nu)}{1-f(E)} + W^a_{if\nu}\frac{1-f(E+\hbar\omega_\nu)}{1-f(E)}, \quad (11)$$

where $f(E)$ is the Fermi–Dirac distribution function and superscripts e and a stand for phonon emission and absorption, respectively. The sum is taken over all ν phonon modes.

Calculations demonstrate that under degeneracy conditions the electron mobility limited by PO phonon scattering decreases rapidly with increasing 2D electron density [26]. The plot of electron mobility as a function of electron density n_s in an AlGaAs/GaAs/AlGaAs channel, calculated using expressions (10) and (11), is given in Fig. 2. An unexpected effect occurs for $n_s > 6 \times 10^{15}$ m^{-2}: the channel conductivity (calculated in Fig. 2 as the product of mobility by electron density, μn_s) decreases with increasing electron density. An increase in the channel electron density leads to a sharp drop in electron mobility due to the increase in the electron–PO phonon scattering rate. A considerable reduction of electron mobility in AlGaAs/GaAs/AlGaAs and AlGaAs/InGaAs/GaAs QWs in comparison to its bulk value has been observed experimentally for $n_s = 2 \times 10^{16}$ m^{-2} [36]. This effect limits the possibility of achieving higher heterotransistor speeds by increasing the donor doping levels.

An increase in the PO phonon scattering rate results from the growth of the fraction of subband electrons whose kinetic energy is higher than the optical phonon energy. The rate of electron scattering due to PO phonon emission exceeds that due to PO phonon absorption by orders of magnitude. It is this type of scattering that is responsible for the large reduction in mobility.

Under the conditions of electron gas degeneracy in the first (lowest) subband, the Fermi level is located above the bottom of the subband and the fraction of electrons with kinetic energy exceeding the PO phonon energy is large; consequently, the mobility limited by PO phonon scattering is low. With the further growth of the carrier density, the Fermi level shifts to higher energies and the electron density in the next (second) subband increases. Electrons in the second subband have high mobility as long as their kinetic energy does not exceed the optical phonon energy. This is responsible for the increase in electron mobility in AlGaAs/GaAs/AlGaAs QW for densities above 1.1×10^{16} m^{-2} (see Fig. 2). The conductivity rises up to $n_s = 2.6 \times 10^{16}$ m^{-2} and then decreases again: the Fermi level becomes higher than the bottom of the second subband, and the fraction of electrons in this subband with kinetic energy exceeding the optical phonon energy grows.

The cycles of conductivity decreases and increases repeat each time the Fermi level crosses the bottom of the corresponding subband (see Fig. 2).

Insertion of a thin AlAs barrier at the center of AlGaAs/GaAs/AlGaAs QW results in increased electron mobility in the subbands and larger energy separation between the subbands. Consequently, the decline in conductivity occurs at higher electron densities ($n_s \approx 1.5 \times 10^{16}$ m^{-2}), and the cycles of conductivity variation shift correspondingly.

Thus, due to an increased maximum doping level, the insertion of such a barrier enables one to achieve a higher channel conductivity and, correspondingly, a higher speed of modulation-doped heterotransistors.

CONCLUSION

Thus, electron mobility in AlGaAs/GaAs/AlGaAs heterostructures limited by inelastic scattering by confined and interface PO phonons depends on the QW parameters and electron density in the following way.

(i) When the QW width is varied in the range below 40 nm, the electron mobility cyclically increases and

decreases, remaining close to its value in the bulk material. Each cycle of the mobility variation corresponds to a change in the number of subbands involved in electron scattering.

(ii) Resonance drops in mobility as a function of the QW width occur when energy gaps between the subbands become equal to the interface phonon energy.

(iii) Intercalation of a thin (1–2 monolayers) AlAs barrier in a GaAs QW leads, at certain well widths and electron densities, to an increase in mobility. This is related to the splitting of PO phonons between the two QWs and detuning of the intersubband electron–phonon resonances.

(iv) At high levels of modulation doping of a heterostructure QW, when the electron density there exceeds 10^{15} m^{-2}, a sharp rise in electron–PO phonon scattering occurs, which leads to a decrease in electron mobility.

For electron densities exceeding the critical value of $n_s = 5 \times 10^{15}$ m^{-2}, the rate of mobility decrease is higher than the rate of density increase. Thus, the conductivity drops with increasing densities.

This effect constrains the possibilities of increasing the speed of modulation-doped heterotransistors. Insertion of a thin barrier results in a shift of the critical density to $n_s = 10^{16}$ m^{-2}, which can be utilized to enhance the heterotransistor high-speed performance.

REFERENCES

1. J. Požela, G. Butkus, and V. Jucienė, Semicond. Sci. Technol. **9**, 1480 (1994).
2. J. Požela and V. Jucienė, Lithuan. J. Phys. **35**, 53 (1995).
3. R. Fuchs and K. L. Kliever, Phys. Rev. A **140**, 2076 (1965).
4. K. Huang and B. Zhu, Phys. Rev. B **38**, 13377 (1988).
5. J. Menendez, J. Lumin. **44**, 285 (1989).
6. N. Mori and T. Ando, Phys. Rev. B **40**, 6175 (1989).
7. H. Rücker, E. Molinary, and P. Lugli, Phys. Rev. B **45**, 6747 (1992).
8. I. Lee, S. M. Goodnick, M. Gulia, *et al.*, Phys. Rev. B **51**, 7046 (1995).
9. B. K. Ridley, Phys. Rev. B **39**, 5282 (1989).
10. K. W. Kim, A. R. Bhatt, M. A. Stroscio, *et al.*, J. Appl. Phys. **72**, 2282 (1992).
11. H. B. Teng, J. P. Sun, G. I. Haddad, *et al.*, J. Appl. Phys. **84**, 2155 (1998).
12. J. Požela, V. Jucienė, and K. Požela, Semicond. Sci. Technol. **10**, 1555 (1995); **10**, 1076 (1995).
13. J. Požela, V. Jucienė, A. Namajūnas, and K. Požela, Physica E (Amsterdam) **5**, 108 (1999).
14. X. F. Wang, I. C. da Cunha Lima, A. Troper, and X. L. Lei, J. Appl. Phys. **85**, 6598 (1999).
15. C. R. Bennet, M. A. Amato, N. A. Zakhleniuk, *et al.*, J. Appl. Phys. **83**, 1499 (1998).
16. B. K. Ridley, *Electrons and Phonons in Semiconductor Multilayers* (Cambridge Univ. Press, Cambridge, 1997).
17. T. Tsuchiya and T. Ando, Phys. Rev. B **47**, 7240 (1993); **48**, 4599 (1993).
18. J. Požela, V. Jucienė, A. Namajūnas, and K. Požela, Fiz. Tekh. Poluprovodn. (St. Petersburg) **31**, 85 (1997) [Semiconductors **31**, 69 (1997)].
19. X. Zianni, C. D. Simserides, and G. P. Triberis, Phys. Rev. B **55**, 16324 (1997).
20. C. R. McIntyre and T. L. Reinecke, Phys. Rev. B **56**, 13428 (1997).
21. J. Požela, V. Jucienė, A. Namajūnas, and K. Požela, Phys. Status Solidi B **204**, 238 (1997).
22. L. F. Register, Phys. Rev. B **45**, 8756 (1992).
23. J. Požela, V. Jucienė, and K. Požela, Lithuan. J. Phys. **35**, 359 (1995); **36**, 149 (1996).
24. J. Wang, J.-P. Leburton, and J. Požela, J. Appl. Phys. **81**, 3468 (1997).
25. J. Požela, A. Namajūnas, K. Požela, and V. Jucienė, Fiz. Tekh. Poluprovodn. (St. Petersburg) **33**, 1049 (1999) [Semiconductors **33**, 956 (1999)].
26. J. Požela, K. Požela, A. Namajūnas, and V. Jucienė, Lithuan. J. Phys. **39**, 55 (1999).
27. W. Xu, F. M. Peeters, and J. T. Devreese, Phys. Rev. B **48**, 1562 (1993).
28. J. Požela, V. Jucienė, A. Namajūnas, and K. Požela, J. Appl. Phys. **81**, 1775 (1997).
29. J. Požela, V. Jucienė, A. Namajūnas, and K. Požela, in *Proceedings of the 23rd International Conference on Physics of Semiconductors, Berlin, July 21–26, 1996*, Ed. by M. Sheffer and R. Zimmermann (World Scientific, Singapore, 1996), Vol. 3, p. 2391.
30. J. Požela, V. Jucienė, A. Namajūnas, *et al.*, J. Appl. Phys. **82**, 5564 (1997).
31. F. H. Julien, A. Sa'ar, J. Wang, and J.-P. Leburton, Electron. Lett. **31**, 838 (1995).
32. P. Boucaud, F. H. Julien, D. D. Yang, *et al.*, Appl. Phys. Lett. **57**, 215 (1990).
33. J. Faist, F. Capasso, D. Sivco, *et al.*, Science (Washington, D.C.) **264**, 553 (1994).
34. X. T. Zhu, H. Goronkin, G. N. Maracas, *et al.*, Appl. Phys. Lett. **60**, 2141 (1992).
35. V. Gantmacher and I. B. Levinson, *Scattering of Charge Carriers in Metals and Semiconductors* (Nauka, Moscow, 1984).
36. K. Inoue and T. Matsuno, Phys. Rev. B **47**, 3771 (1993).

Translated by M. Skorikov

Semiconductors, Vol. 34, No. 9, 2000, pp. 1016–1020. Translated from Fizika i Tekhnika Poluprovodnikov, Vol. 34, No. 9, 2000, pp. 1058–1062.

ELECTRONIC AND OPTICAL PROPERTIES OF SEMICONDUCTORS

Radiation Defects in *n*-4*H*-SiC Irradiated with 8-MeV Protons

A. A. Lebedev*, A. I. Veĭnger*, D. V. Davydov*, V. V. Kozlovskiĭ, N. S. Savkina*, and A. M. Strel'chuk***

**Ioffe Physicotechnical Institute, Russian Academy of Sciences, ul. Politekhnicheskaya 26, St. Petersburg, 194021 Russia*

***St. Petersburg State Technical University, ul. Politekhnicheskaya 29, St. Petersburg, 195251 Russia*

Submitted February 22, 2000; accepted for publication February 24, 2000

Abstract—Capacitance-related methods and electron spin resonance were used to study the deep-level centers formed in *n*-4*H*-SiC as a result of irradiation with 8-MeV protons. For the samples, Schottky diodes and *p–n* structures formed on the layers either obtained by sublimational epitaxy or produced commercially by CREE Inc. (United States) were used. It was found that the type of centers introduced by irradiation is independent of the technology of the material growth and the type of charged particles. On the basis of the results of annealing the defects and the data of electron spin resonance, the possible structure of the centers is suggested. © *2000 MAIK "Nauka/Interperiodica".*

1. INTRODUCTION

It is known that proton irradiation is used in semiconductor technology for the formation of local semi-insulating regions [1]. In a previous paper [2], we reported that we had managed to obtain semi-insulating (at room temperature) layers in the most commonly encountered 6*H*-SiC polytype of SiC [2–4] and had studied the parameters of the radiation defects formed in this material under proton irradiation. However, the 4*H*-SiC polytype of silicon carbide is more promising for the development of semiconductor devices, because this polytype has a wider band gap and lower ionization energy for the main donor levels. Therefore, in this study, we repeated with 4*H*-SiC the experiments reported previously [2] for 6*H*-SiC.

Thus, the objective of this study was to obtain semi-insulating 4*H*-SiC layers by proton irradiation and to determine the parameters of radiation defects that control the properties of these layers.

2. SAMPLES

For the samples, we used epitaxial SiC layers produced commercially by the CREE Company (United States) [3] and also the layers obtained by us using sublimational epitaxy [4]. In the latter case, the thickness of the *n*-layer was about 5 μm and the substrate was about 400 μm thick. The Schottky barriers were 300–1200 μm in diameter. The concentration of uncompensated donors ($N_d - N_a$) was (1–4) × 10^{16} cm^{-3} in the *n*-layer and (3–5) × 10^{18} cm^{-3} in the substrate. Thus, the doping level of the substrate exceeded that of the base *n*-layer by no less than two orders of magnitude. Since the generation rate of radiation defects in the semiconductor is virtually independent of its doping level [5], we assume that the resistance *R* of the structures in the forward direction is governed by the concentration of charge carriers in the *n*-layer. When studying the radiation defects by electron spin resonance (ESR), we used CREE-produced substrates with a thickness of about 0.5 mm and an initial nitrogen concentration of ~2 × 10^{18} cm^{-3}.

The samples were irradiated with 8-MeV protons using an MGTs-20 cyclotron. The doses were in the range of $D = 10^{14}$–10^{16} cm^{-2}.

3. EXPERIMENTAL RESULTS

3.1. Capacitance–Voltage (C–V) Characteristics

The *C–V* characteristics were measured using a conventional setup with a parallel equivalent circuit and a sinusoidal-wave frequency of 10 kHz. Studies of irradiated samples showed that the quantity $N_d - N_a$ measured at room temperature decreased with increasing proton dose, whereas the value of $N_d - N_a$ increased significantly if the structure was heated to 650 K (Fig. 1). As the proton dose increased, the difference between the high- and low-temperature values of $N_d - N_a$ increased.

Irradiation also resulted in an increase in *R* (the resistance of the Schottky barrier in the forward direction). As the proton dose increased, an increase in *R* rendered the capacitance measurements impossible, because the measured value of the capacitance ceased to depend on the applied voltage [6]. As the temperature increased, the value of *R* decreased by an exponential law with the activation energy ε_A (Fig. 2). As the

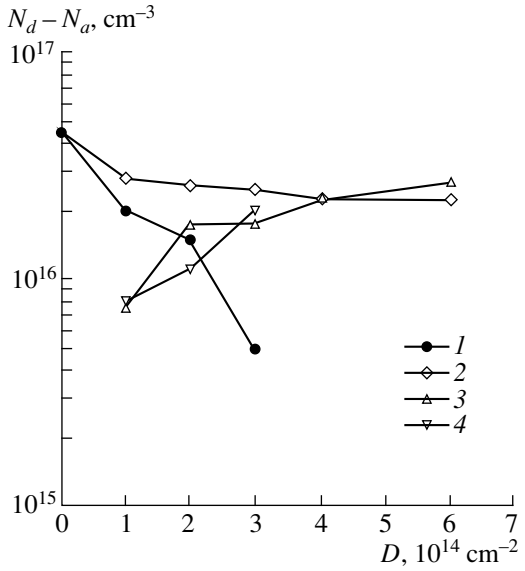

Fig. 1. Dependences of the values of $N_d - N_a$ at T = (*1*) 300 and (*2*) 650 K, (*3*) their difference, and (*4*) total concentration of radiation defects ($RD_{1/2}$ + RD_3 + RD_4) on the proton dose D.

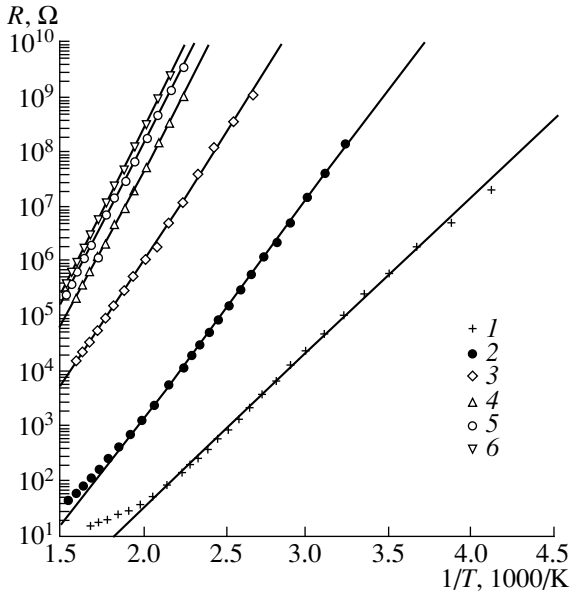

Fig. 2. Temperature dependences of the forward resistance R of the Schottky diode for a proton dose D of (*1*) 6×10^{14}, (*2*) 1×10^{15}, (*3*) 2×10^{15}, (*4*) 5×10^{15}, (*5*) 1×10^{16}, and (*6*) 2×10^{16} cm^{-2}.

proton dose D increased, the magnitude of $-\varepsilon_A$ increased, attaining the value of ~1.25 eV for $D = 2 \times 10^{16}$ cm^{-2} (Fig. 3). Such a variation in the resistance under the effect of irradiation (the pinning of the Fermi level) is also characteristic of other semiconductors (for example, GaAs [7] or 6*H*-SiC [2]).

3.2. The DLTS Measurements

When studying the deep-level centers in the upper half of the band gap, we detected five types of deep-level centers, most of which either were observed in *n*-4*H*-SiC implanted with He^+ ions [8] or were close in parameters to structural defects. The table lists the ionization energies $E_c - E_0$ for the observed defects, the capture cross sections for electrons σ_n, and the concentrations of these centers after irradiation with a dose of 2×10^{14} cm^{-2}. One type of center with a level at E_c = 0.18 eV was completely annealed out at temperatures of 500–650 K. We did not detect any difference between the spectrum of deep-level centers formed in the CREE epilayers and that in the layers grown by sublimational epitaxy. Figure 4 shows the Arrhenius plots for the detected radiation defects.

The observed radiation defects were completely annealed out at temperatures of ~1500 K.

3.3. Electron Spin Resonance of Radiation Defects Produced by Proton Irradiation

The bulk samples (part of the CREE substrate) were irradiated under the same experimental conditions as above (the proton dose was 2×10^{16} cm^{-2}). The ESR signals were measured at 77 K using an E-112 Varian spectrometer. Before irradiation, we observed the ESR of nitrogen-impurity atoms whose concentration was so high that the signal was represented by a single broadened line without any evidence of a hyperfine structure. In addition, significant electrical conductivity of the samples was observed at 77 K, which resulted in a decrease in the Q factor and a distortion of the line

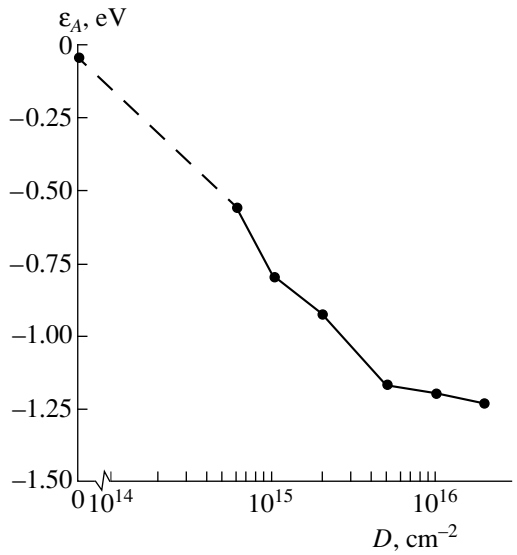

Fig. 3. The activation energy ε_A as a function of the proton dose for the Schottky diode (Fig. 2) based on the layer produced by sublimational epitaxy.

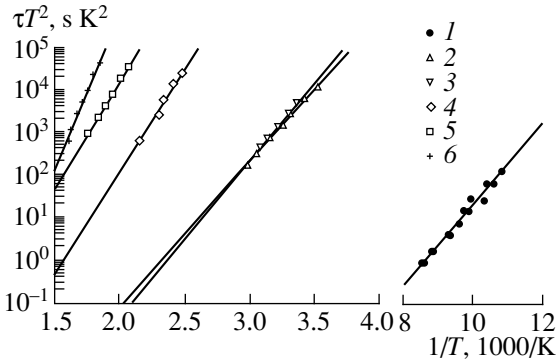

Fig. 4. The Arrhenius plots for the detected (*1*) radiation defects P_1/P_2, centers Z_1 (*2*) after and (*3*) before irradiation, and the radiation defects (*4*) $RD_{1/2}$, (*5*) RD_3, and (*6*) RD_4.

shape. The line acquired a Dysonian shape with a ratio of derivative wings equal to about three, which indicates that the skin-layer thickness is large compared to the mean free path for the spin relaxation [11]. As a result of irradiation, the electron concentration decreased by about a factor of 2.6 and the line narrowed and became more symmetric (the ratio of the derivative wings decreased to 1.3). Poorly pronounced additional peaks appeared against the background of this line; a fraction of these peaks may be assigned to the emergence of the spectrum corresponding to individual nitrogen atoms, and another fraction may be attributed to the emergence of new spectra related to radiation defects. In addition, as in the case of irradiated 6*H*-SiC, radiation-defect spectra with large fine splitting were observed [2]; the most pronounced of these spectra consisted of 12 lines for an arbitrary orientation of the sample. Other lines that did not belong to this spectrum had a much lower intensity.

4. DISCUSSION OF THE RESULTS

4.1. Compensation

The above results indicate that several types of centers with deep levels in the range of $E_c - E_0 = 0.96$–1.5 eV are formed in *n*-4*H*-SiC as a result of proton irradiation. As follows from the parameters of the $RD_{1/2}$ center, the time constant τ for recharging this center is 5×10^3 s at $T = 300$ K. Thus, the charge of this center (and of those with deeper levels) does not change in the course of *C*–*V* measurements at room temperature. At the same time, the value of τ for the Z_1 center whose level is closest to that of the $RD_{1/2}$ center is 36×10^{-3} s at 300 K. Consequently, the Z_1 center (and other centers with shallower levels) may be regarded as being completely depopulated in the course of *C*–*V* measurements at room temperature. For larger doses of irradiation, electrical conductivity of the samples begins to be controlled by thermal excitation of electrons from these centers, and the activation energy for resistance approaches the ionization energy of the center with the deepest level. The available experimental data do not allow us to decide unambiguously whether these centers are donors or acceptors (for more details, see [12]). However, irrespective of the nature of the radiation defects, as the dose *D* increases, the maximum activation energy of the base resistance would tend to that of the center with the deepest level, i.e., to ~1.5 eV. Thus, the difference between the values of $N_d - N_a$ measured at 300 and 650 K should be equal to the concentration of the centers $RD_{1/2} + RD_3 + RD_4$ determined from the DLTS spectra. As can be seen from Fig. 1, this equality is in good agreement with experimental data for doses of $\leq 3 \times 10^{14}$ cm^{-2}. For larger proton doses, the *C*–*V* measurements were impossible owing to the large value of *R*. The resistance of irradiated structures decreases exponentially with increasing temperature, which was previously observed experimentally [12].

4.2. Identification and Plausible Structure of the Centers

As can be seen from the table, there is good agreement between the spectra of radiation defects in 4*H*-SiC that are observed after proton irradiation and implantation of He^+ ions. There is also a correlation between the annealing temperatures T_{ann} for the introduced centers. Thus, it may be concluded that, in SiC, as in other semiconductors [7], different types of irradiation give rise to identical radiation defects; however,

Table

Parameters of detected deep-level centers				Correlation with published data		Possible structure of the defects
$E_c - E_0$, eV	σ_n, cm^2	N_g, cm^{-3}	T_{ann}, K	Implantation of He^+ [8]	Structural defects	
0.18	6×10^{-15}	2×10^{14}	500–650	P_1/P_2		Primary defects
0.63–0.70	5×10^{-15}	5×10^{15}	$800 < T_{ann} < 1500$	Z_1	Z_1 [8, 9],	V_C
0.96	5×10^{-15}	6.3×10^{15}	"	$RD_{1/2}$		
1.0	1×10^{-16}	6.3×10^{15}	"	RD_3	$E_c - 1.1$ eV [10]	$V_C + V_{Si}$
1.5	2×10^{-13}	5×10^{15}	"	RD_4		

the ratio of concentrations of these defects varies from one type of irradiation to another.

Notwithstanding the fact that the parameters of radiation defects coincide with those of certain native defects (Z_1, E_c = 1.1 eV), we believe that it is still too early to unambiguously identify the radiation defects under consideration with native defects. We are reminded that the radiation defects are annealed out completely at a temperature of ~1500 K, whereas the native defects (close in parameters to radiation defects) exist in *n*-4*H*-SiC epilayers grown by sublimation at 2100 K.

Positron-lifetime studies [13] of the formation and annealing of radiation defects in SiC showed that proton irradiation gives rise to carbon and silicon vacancies and also to other primary defects, which recombine on annealing at 400–600 K to form thermally stable complexes. Thus, on the basis of our studies of the DLTS spectra before and after annealing, we may assume that the center with the level at E_c = 0.18 eV is related to primary radiation defects.

The radiation-defect structure is readily determined from the ESR data. However, in order to relate the structure to the electrical properties, additional conditions are required; in particular, this is possible if the defects are photosensitive.

In the general case, attempts to unambiguously relate the structure of radiation defects in SiC to their electrical characteristics have not met with success. It has been possible to ascertain this relation for certain structural defects that emerge in SiC as a result of quenching and that have photosensitive ESR spectra [14]. We studied the influence of illumination on the amplitude of ESR signals in the SiC samples and showed that they were insensitive to illumination. In connection with this, in order to relate the structure of radiation defects to their electrical properties (as in the 6*H*-SiC polytype [2]), we compared the parameters of ESR spectra obtained by us with the parameters determined by studying the defects in quenched 6*H*-SiC samples [14] and radiation defects in 4*H*-SiC samples irradiated with neutrons and alpha-particles [15]. As was shown [14, 15], defects in SiC give rise to two types of ESR spectra: with a spin of S = 1/2 and with a spin of S = 1. In the latter case, a fine structure is observed. The ESR-spectrum parameters in both polytypes are almost the same, which suggests that there is similar correspondence between the ESR parameters and electrical characteristics in 4*H*-SiC as in the 6*H* polytype.

ESR spectra of two types were also observed in 6*H*-SiC. An anisotropic single line with a *g*-factor that is nearly the same as for nitrogen impurity corresponds to the center with spin S = 1/2. Since the spectrum of nitrogen atoms did not disappear and remained fairly intense in the studied samples, possible low-intensity hyperfine-structure lines originating from the interaction of electron spin with nuclear spins of ^{29}Si and ^{31}C isotopes were imperceptible against the background of the nitrogen spectrum. In connection with this, we failed to unambiguously determine the structure of the above center. However, a comparison with the spectrum of quenched-in defects suggests that the ESR-spectrum line with the spin S = 1/2 is related to an individual vacancy in the carbon sublattice with a thermal activation energy of 0.63–0.7 eV (the optical activation energy was measured previously [14] and was found to be 0.65 eV).

We were able to identify the center with a spin of S = 1 much more positively. In an arbitrary orientation, the corresponding spectrum includes 12 lines (as is the case of the 6*H* polytype); this means that the center responsible for such a spectrum has twofold symmetry and that the symmetry axis lies in the plane defined by the *c*-axis and one of the twofold axes. The largest observed value of fine splitting amounts to D = 567 Oe (508×10^{-4} cm^{-1}) and is found at an angle of 30° with respect to the *c*-axis. Such a spectrum is characteristic of the *G*2 center observed previously [15] in the 4*H* polytype; this center was identified with a pair of neighboring vacancies in the carbon and silicon sublattices. A photosensitive quenched-in defect *P*7 with an optical-activation energy of 1.17 eV was observed [14] in the 6*H* polytype and featured a similar spectrum as well. It is also worth noting that variously oriented divacancies feature almost identical activation energies. This suggests that the spectrum of a center with S = 1 may be assigned with high probability to one of the radiation defects with an activation energy of 0.96–1 eV (see table).

Thus, we managed to correlate the structure and electrical properties of two types of radiation defects in proton-irradiated *n*-4*H*-SiC: a carbon vacancy with an activation energy of 0.63–0.7 eV and a pair of vacancies in the carbon and silicon sublattices with an activation energy of 0.96–1 eV.

5. CONCLUSION

On the basis of the above results, we may draw the following two conclusions.

(i) Identity of properties and parameters of radiation defects produced by irradiating *n*-4*H*-SiC with various charged particles is observed.

(ii) In contrast with 6*H*-SiC, a decrease (rather than an increase) in total concentration of uncompensated donors in proton-irradiated 4*H*-SiC samples is observed. This indicates that irradiation either introduces acceptor centers in the lower half of the band gap or stimulates disintegration of donor centers in the upper half of the band gap. In addition, irradiation produces deep-level acceptor centers, with electrons being transferred to these centers from the donor levels with shallower levels. This causes the Fermi level to lower and results in the formation of *n*-4*H*-SiC layers that are semi-insulating at room temperature. Such layers may

be used in the technology of devices that are not designed to operate at elevated temperatures, for example, photodetectors or various radiation detectors.

REFERENCES

1. V. V. Kozlovskiĭ, V. A. Kozlov, and V. N. Lomasov, Fiz. Tekh. Poluprovodn. (St. Petersburg) **34**, 129 (2000) [Semiconductors **34**, 123 (2000)].
2. A. A. Lebedev, V. I. Veĭnger, D. V. Davydov, *et al.*, Fiz. Tekh. Poluprovodn. (St. Petersburg) (in press) [Semiconductors (in press)].
3. J. W. Palmor, J. A. Edmond, H. S. Kong, and C. H. Carter, Jr., Physica B (Amsterdam) **185**, 461 (1993).
4. N. S. Savkina, A. A. Lebedev, D. V. Davydov, *et al.*, Mater. Sci. Eng. B **61/62**, 165 (1999).
5. *Radiation Processing in the Technology of Electronic Materials and Devices*, Ed. by V. S. Ivanov and V. V. Kozlovskiĭ (Énergoatomizdat, Moscow, 1997).
6. A. A. Lebedev and N. A. Sobolev, Fiz. Tekh. Poluprovodn. (Leningrad) **16**, 1874 (1982) [Sov. Phys. Semicond. **16**, 1207 (1982)].
7. D. C. Look and J. P. Sizelove, J. Appl. Phys. **62**, 3660 (1987).
8. T. Dalibor, G. Pensl, H. Matsunami, *et al.*, Phys. Status Solidi A **162**, 199 (1997).
9. J. P. Doyle, M. O. Aboelfotoh, B. G. Svensson, *et al.*, Diamond Relat. Mater. **6**, 1388 (1997).
10. W. C. Michel, A. Saxler, R. Perrin, *et al.*, in *Abstracts of International Conference on SiC and Related Materials, Raleigh, NC, Oct. 10–15, 1999*, Abstract No. 281.
11. C. Pool, *Electron Spin Resonance* (Wiley, New York, 1967; Mir, Moscow, 1970).
12. R. K. Nadella and M. A. Capano, Appl. Phys. Lett. **70**, 886 (1997).
13. W. Puff, P. Mascher, A. G. Balogh, and H. Baumann, Mater. Sci. Forum **258–263**, 733 (1997).
14. A. I. Veĭnger, V. A. Il'in, Yu. M. Tairov, and V. F. Tsvetkov, Fiz. Tekh. Poluprovodn. (Leningrad) **15**, 1557 (1981) [Sov. Phys. Semicond. **15**, 902 (1981)].
15. N. M. Pavlov, M. I. Iglitsyn, M. G. Kosaganova, and V. N. Solomatin, Fiz. Tekh. Poluprovodn. (Leningrad) **9**, 1279 (1975) [Sov. Phys. Semicond. **9**, 845 (1975)].

Translated by A. Spitsyn

Semiconductors, Vol. 34, No. 9, 2000, pp. 1021–1023. Translated from Fizika i Tekhnika Poluprovodnikov, Vol. 34, No. 9, 2000, pp. 1063–1065.

ELECTRONIC AND OPTICAL PROPERTIES OF SEMICONDUCTORS

Breakdown of Shallow-Level Donors in Si and Ge on the Insulating Side of a Strain-Induced Metal–Insulator Transition

S. I. Budzulyak*, E. F. Venger, Yu. P. Dotsenko, V. N. Ermakov, V. V. Kolomoets, V. F. Machulin, and L. I. Panasyuk

Institute of Semiconductor Physics, National Academy of Sciences of Ukraine, Kiev, 252650 Ukraine
** e-mail: korbutyak@div47.semicond.kiev.ua*

Submitted August 16, 1999;
accepted for publication December 21, 1999

Abstract—Impact ionization of electron localized states on the insulating side of a strain-induced metal–insulator transition in Si:P and Ge:Sb crystals was investigated for donor concentrations appreciably exceeding the critical concentration for a transition caused by variations in the impurity concentration. Dependences of the activation energy and impact-ionization field on uniaxial stress were derived. Transitions from metallic-type conductivity to ε_2-conductivity in the region of high uniaxial pressures are analyzed on the basis of the transformation of the conduction band energy spectrum along a certain direction of the deformation axis in silicon and germanium crystals. *© 2000 MAIK "Nauka/Interperiodica".*

1. INTRODUCTION

A strain-induced transition from the electrical conductivity of the activation-type to the metallic conductivity for an arbitrary direction of the axis of strain was observed in slightly insulating *n*-Si:P samples in the temperature range $T = 3$–35 mK and uniaxial pressures as high as 0.8 GPa [1]. This transition is caused primarily by variation under the deformation of valley–orbit splitting. The conduction-band parameters do not change in this process.

A metal–insulator transition in degenerate *n*-Si and *n*-Ge crystals [2] was accomplished due to essential variations in the conduction-band parameters caused by transformation of the energy spectrum along certain directions of the axis of strain (pressure axis **X**) [3].

Both in silicon (at **X** || [111]) and in germanium (at **X** || [001]), transformation of the conduction-band energy spectrum under deformation results in an essential increase in the electron effective mass, a decrease in the Bohr radius, and the localization of an electron at the impurity atom. In silicon, for **X** || [111], the transverse component of the electron effective mass increases appreciably under high uniaxial pressures due to the nonparabolicity of Δ-valleys caused by deformation [4]. In germanium, for **X** || [001] and a pressure of $X > 2.1$ GPa, inversion of the absolute minimum (L–Δ inversion) occurs. Due to this fact, the electron effective mass increases and, as a result, the ionization energy of the shallow-level impurities (Sb, P, and As) increases in lightly doped crystals by approximately a factor of 4 [3]. In heavily doped crystals, this brings about a significant decrease in the Bohr radius and localization of an electron on the impurity center.

Thus, despite the different character of a strain-induced metal–insulator (MI) transition defined by the basically dissimilar character of the electron spectrum transformation in *n*-Si and *n*-Ge for the directions of the strain axis mentioned above, in both cases a transition from metallic conductivity to activation-type conductivity occurs in the region of high uniaxial pressures. Evidently, a strain-induced MI transition should basically differ for single-crystal heavily doped *n*-Si and *n*-Ge semiconductors. On the other hand, since the strain-induced MI transition is related in both cases to an increase in the electron effective mass m_e^* and to the localization of an electron at the impurity center, there should be common features of the transition from metallic conduction to activation-type conduction as uniaxial pressure X increases. These features include the appearance of and increase in the activation energy ε_a, which is identified in our conditions with ε_2-conductivity [2]; transformation of the linear current–voltage (I–V) characteristics into *S*-shaped characteristics; the transition from weak localization of the electron at the impurity center to strong localization; and others.

In this paper, we consider the above features of the strain-induced MI transition in heavily doped *n*-Si:P and *n*-Ge:Sb crystals caused by transformation of the conduction band energy spectrum in the region of high uniaxial pressures X.

1063-7826/00/3409-1021$20.00

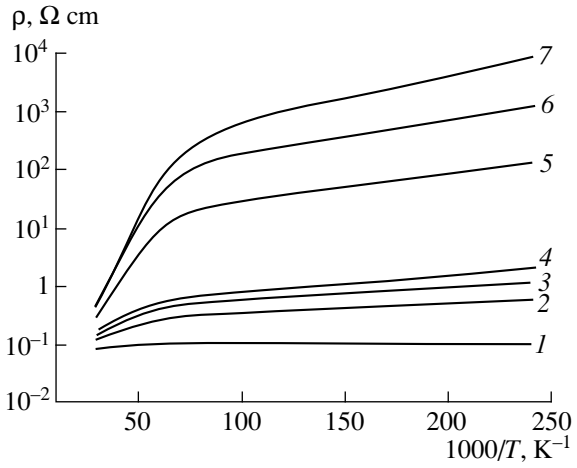

Fig. 1. Resistivity of *n*-Ge:Sb crystals versus reciprocal temperature for uniaxial pressure X = (*1*) 0, (*2*) 10, (*3*) 17, (*4*) 18, (*5*) 19, (*6*) 20, and (*7*) 21 GPa. Concentration $N_{Sb} = 1.8 \times 10^{17}$ cm^{-3}.

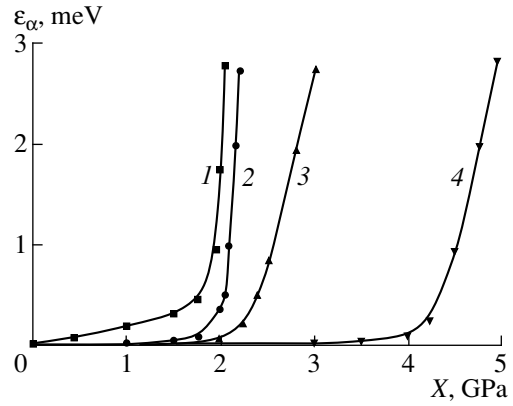

Fig. 2. Dependence of the activation energy on the uniaxial pressure X in the region of strain-induced MI transition for (*1* and *2*) *n*-Ge and (*3* and *4*) *n*-Si crystals. Impurity concentrations N_{Sb} in *n*-Ge: (*1*) 1.8×10^{17} and (*2*) 3.26×10^{17} cm^{-3}. Impurity concentrations N_P in *n*-Si: (*3*) 4.7×10^{18} and (*4*) 6.3×10^{18} cm^{-3}.

2. EXPERIMENT AND DISCUSSION

We studied a strain-induced MI transition using phosphorus-doped silicon samples with concentration $N_P = (4.2–6.2) \times 10^{18}$ cm^{-3} and two antimony-doped germanium crystals with concentrations $N_{Sb} = 1.8 \times 10^{17}$ and 3.26×10^{17} cm^{-3}. We measured dependences of the resistivity ratio of the crystals $\rho(X)/\rho(0)$ on the uniaxial pressure X at $T = 4.2$ K, I–V characteristics in the region of the MI transition in pulsed mode, and temperature dependences of the resistivity in the temperature range $T = 4.2$–50 K for various values of the uniaxial pressure X. Dependences of activation energy ε_a and the impact ionization field on pressure X were derived.

An appreciable increase in the resistivity of the *n*-Ge:Sb crystals under uniaxial pressure X at $T = 4.2$ K, which causes, as X increases, MI transition, and, at the same time, an increase in the slope of the resistivity ρ temperature dependences (Fig. 1) indicates that the activation energy of conductivity (ε_2-conductivity) increases due to inversion at **X** || [001] of the absolute minimum of the germanium conduction band (L–Δ inversion). As a result, the electron effective mass increases substantially [5]. In the case of electron localization at the hydrogen-like impurity, the Bohr radius of the electron ($a_B = h^2\chi/m_e^* e^2$) should decrease appreciably. For a fixed doping, this has to lead to transition from metallic conductivity which is typical of degenerate (at $X = 0$) crystals to activation-type conductivity for $X > 2$ GPa.

The emergence of and increase in the activation energy as uniaxial pressure X increases (**X** || [111] in *n*-Si and **X** || [001] in *n*-Ge) (Fig. 2) are related to the localization of the electron on the insulating side of the strain-induced MI transition. It can be seen that the shape of the curves $\varepsilon_a = f(X)$ differs significantly for *n*-Si and *n*-Ge, which is explained by a different mechanism of the conduction band transformation in silicon (strain-induced nonparabolicity of Δ-valleys) and in germanium (L–Δ absolute-minimum inversion). However, both in *n*-Si and in *n*-Ge, as the dopant concentration increases, the region of strong electron localization is shifted to larger values of X.

A series of I–V characteristics for various values of X, which demonstrates the strain-induced MI transition, is shown in Fig. 3 for *n*-Si crystals with a concentration of phosphorus $N_P = 4.7 \times 10^{18}$ cm^{-3}. Linear I–V characteristics in the region of small X are transformed

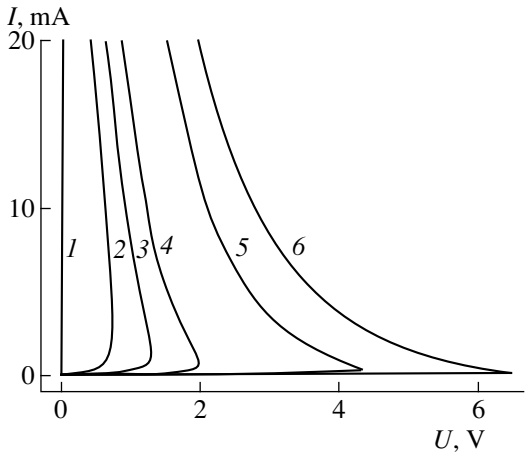

Fig. 3. Current-voltage (I–V) characteristics in pulsed mode of *n*-Si:P crystals at $T = 4.2$ K for uniaxial pressures X = (*1*) 0, (*2*) 2.7, (*3*) 2.8, (*4*) 2.9, (*5*) 3.0, and (*6*) 3.1 GPa. Concentration $N_P = 4.7 \times 10^{18}$ cm^{-3}.

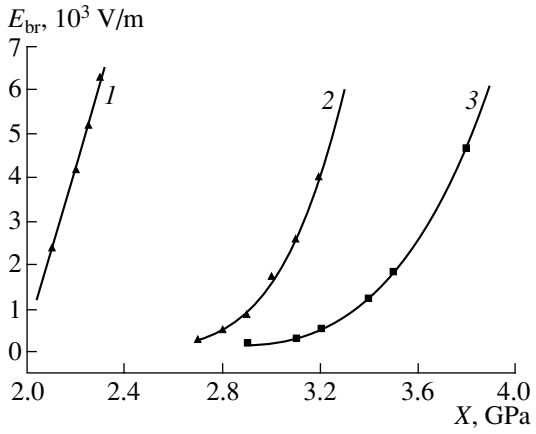

Fig. 4. Impact ionization field of localized states of shallow-level donors E_{br} versus uniaxial pressure X in Ge:Sb with a concentration of N_{Sb} (*1*) 1.8×10^{17} cm^{-3} and in Si:P with concentrations of N_P (*2*) 4.2×10^{18} and (*3*) 6.2×10^{18} cm^{-3}.

into nonlinear *S*-shaped *I–V* characteristics in the region of high uniaxial pressures ($X > 2.7$ GPa).

Impact ionization of the electron states localized at the impurity atom is characterized, as can be seen from the *I–V* curves, both by linear (Fig. 4, curve *1*) and by nonlinear (Fig. 4, curves *2*, *3*) dependences of the impact-ionization field E_{br} on the uniaxial pressure X.

The magnitudes obtained for the activation energy ε_a, which increases with X up to $\varepsilon_a \geq 3$ meV (Fig. 2); *S*-shaped *I–V* characteristics in the region of high uniaxial pressures X (Fig. 3); and temperature dependences of resistivity for varied X values (Fig. 1) are indicative of the strain-induced transition from metallic conductivity to ε_2-conductivity in crystals with concentrations of shallow-level impurities much higher than the critical concentration at which the MI transition related to variations in concentration occurs [6–9].

CONCLUSION

We studied the mechanisms of a strain-induced transition from metallic conductivity to activation-type conductivity for a concentration of shallow-level donors significantly exceeding critical concentrations at which the MI transition in *n*-Si:P and *n*-Ge:Sb crystals occurred. A series of experimental data (resistivity dependence on the uniaxial pressure X, *S*-shaped *I–V* characteristics, temperature dependences of resistivity for different X, dependences of the activation energy on X, and dependences of the impact ionization field on X) indicate that, in degenerate *n*-Si:P and *n*-Ge:Sb crystals, the transition to ε_2-conductivity occurs in the range of high uniaxial pressures X.

REFERENCES

1. M. A. Paalanen, T. F. Rosenbaum, G. A. Thomas, and R. N. Bhatt, Phys. Rev. Lett. **48**, 1284 (1982).
2. V. V. Baidakov, V. N. Ermakov, A. E. Gorin, *et al.*, Phys. Status Solidi B **198**, 149 (1996).
3. V. N. Ermakov, V. V. Kolomoets, L. T. Panasjuk, and V. E. Rodionov, in *Proceedings of the 20th International Conference on Physics of Semiconductors, Thessaloniki, 1990*, Vol. 3, p. 1803.
4. P. I. Baranskii, V. V. Kolomoets, and S. S. Korolyuk, Phys. Status Solidi B **116**, K109 (1983).
5. V. V. Baĭdakov, N. N. Grigor'ev, V. N. Ermakov, *et al.*, Fiz. Tekh. Poluprovodn. (Leningrad) **17**, 370 (1983) [Sov. Phys. Semicond. **17**, 234 (1983)].
6. T. F. Rosenbaum, K. Andres, G. A. Thomas, and R. N. Bhatt, Phys. Rev. Lett. **45**, 1723 (1980).
7. G. L. Bir and G. E. Pikus, *Symmetry and Strain-Induced Effects in Semiconductors* (Nauka, Moscow, 1972; Wiley, New York, 1975).
8. C. Yamanouchi, K. Mizuguchi, and W. Sasaki, J. Phys. Soc. Jpn. **22**, 859 (1967).
9. P. Dai, Y. Zhang, and M. P. Sarachik, Phys. Rev. B **45**, 3984 (1992).

Translated by I. Kucherenko

Semiconductors, Vol. 34, No. 9, 2000, pp. 1024–1026. Translated from Fizika i Tekhnika Poluprovodnikov, Vol. 34, No. 9, 2000, pp. 1066–1068.

ELECTRONIC AND OPTICAL PROPERTIES OF SEMICONDUCTORS

Mechanism of High Radiation Stability of Electrical Parameters of SmS Thin Films

L. N. Vasil'ev, V. V. Kaminskiĭ*, S. M. Solov'ev, and N. V. Sharenkova

Ioffe Physicotechnical Institute, Russian Academy of Sciences, ul. Politekhnicheskaya 26, St. Petersburg, 194021 Russia

**e-mail: Vladimir. Kaminski@shuvpop.ioffe.rssi.ru*

Submitted February 25, 2000; accepted for publication February 28, 2000

Abstract—The influence of gamma-ray irradiation on the electrical properties of thin polycrystalline films of samarium monosulfide with various crystal-lattice parameters was studied. The stability of the resistivity of films under an exposure dose in the range of $D = 10^8$–10^9 R is explained on the basis of the existence of a channel for the relaxation of radiation-induced excitations; this channel is related to the presence of different-valence samarium ions (Sm^{2+} and Sm^{3+}). © *2000 MAIK "Nauka/Interperiodica".*

Previously [1], we studied the influence of γ-ray irradiation on the electrical properties of thin polycrystalline semiconducting films of samarium monosulfide and revealed the high radiation stability of their resistivity (ρ) and temperature ($\alpha = \partial \ln\rho/\partial T$) and baric ($\beta = \partial \ln\rho/\partial P$) coefficients of resistivity. It was observed [1] that the crystal-lattice parameter a of polycrystalline SmS films affects the stability of β against gamma radiation. In connection with this, it is of interest to investigate the dependence of the stability of the films' parameters (in particular, the resistivity) on the crystal-lattice parameter a in order to clarify the mechanism of radiation stability of the electrical parameters of SmS films. This was exactly the objective of the study whose results we report in this paper.

Polycrystalline SmS films ~0.15 μm thick were deposited onto glass substrates (see [2] for details) and had a Hall electron concentration of $\sim 10^{21}$ cm^{-3} and sheet resistivity of $\rho_0 \approx 10^3$ Ω/sq. Samples having various crystal-lattice parameters were irradiated with ^{60}Co-source γ quanta with an energy of 1.25 MeV and an exposure rate of 7×10^5 R/h in the range of doses of $D = 10^6$–2.5×10^9 R. The resistivity ρ was measured at $T \approx 300$ K before and after irradiation. The samples to be irradiated were mounted in a sealed glass ampule evacuated to a residual pressure of $\sim 10^{-4}$ Torr. The ampule was placed in the operating zone of an Issledovatel' installation for gamma-ray irradiation. After attaining the specified exposure doses, the ampule was removed from the installation and was opened, after which the parameters were measured again.

Figure 1 illustrates the influence of gamma-ray irradiation on the resistivity of SmS films with various values of crystal-lattice parameters. It follows from Fig. 1 that the resistivity of samples with larger values of the lattice constant is less sensitive to gamma-ray irradiation. Furthermore, a relative stabilization of ρ is observed in the case of irradiation with doses of $\sim 10^8$ R if the dose is increased further. As is known [3], thin polycrystalline SmS films with various values of a have different concentrations of Sm^{3+} ions in the bulk of the film, whereas most samarium ions are in the state of Sm^{2+}. Thus, the radiation stability of electrical parameters of the SmS films may be related to the presence of samarium ions with different valence.

The known method for enhancing the radiation stability of optical properties of glasses is based on doping these glasses with rare-earth cerium ions, which may be found in the valence states of Ce^{3+} and Ce^{4+} [4]. The mechanism underlying this method is based on the fact that, on absorbing a gamma quantum, a Ce^{3+} ion is transformed into a Ce^{4+} ion, and an electron released in this case is absorbed by the nearest Ce^{4+} ion that is transformed into the trivalent state. Accordingly, the number of color centers emerging as a result of irradiating a glass decreases. In this case, a change in the valence of cerium ions plays the role of a channel for relaxing the energy of radiation-induced excitations. The high radiation stability of the electrical parameters of thin polycrystalline SmS films, where transitions between different-valence samarium ions play the role of the relaxation channel, may be explained in a similar way.

According to the concept of origination, migration, and disintegration of electronic excitations on the irradiation of thin SmS films with gamma quanta with energies of $E \gg E_g$ (E_g is the band gap), the generation of additional free carriers in the form of electron–hole pairs (an electron in the conduction band and a hole in the valence band, similar to the case of intrinsic conduction) occurs. In this case, the Sm^{2+} and Sm^{3+} ions that are present simultaneously may act as trapping centers for holes and electrons, respectively. As a result

of trapping, the roles of these centers are interchanged, and the process is repeated. The high concentration of different-valence ions compared to the case of a glass doped with rare-earth ions (~10^{22} cm^{-3} for SmS and ~10^{20} cm^{-3} for glasses, according to [4]) ensures a capture cross section that is sufficient for the resistivity to be independent of the exposure dose. Apparently, other radiation defects affecting electrical characteristics are not produced in this case.

The dynamics of the changes in the concentrations of different-valence ions under the effect of irradiation may be described in terms of a simple phenomenological model. If, for a given radiation intensity, the concentration of arising electron–hole pairs is kept constant, we may introduce the probability of converting the ions Sm^{3+} ions to the Sm^{2+} ions by trapping the charge carriers of corresponding signs ($p^{\pm}$) and the probability of inverse processes under the effects of irradiation ($q^{\pm}$) and temperature ($q_T^{\pm}$). We may then write the following equations for variations in the concentrations of bivalent and trivalent samarium ions (n^{2+} and n^{3+}, respectively):

$$dn^{2+} = [(N - n^{2+})p^{+} - n^{2+}(q^{+} + q_T^{+})]dD, \quad (1)$$

$$dn^{3+} = [(N - n^{3+})p^{-} - n^{3+}(q^{-} + q_T^{-})]dD. \quad (2)$$

Here, $N = n^{2+} + n^{3+}$ is the total concentration of samarium ions and D is the exposure dose proportional to time. Assuming that the initial distribution of divalent and trivalent samarium ions is uniform over the film thickness and the probabilities $p^{\pm}$, $q^{\pm}$, and $q_T^{\pm}$ are constant over the film volume, we can write the solutions to Eqs. (1) and (2) as

$$n^{2+} = n_0^{2+} + \left(\frac{Np^{+}}{p^{+} + q^{+} + q_T^{+}} - n_0^{2+}\right) \times \{1 - \exp[-(p^{+} + q^{+} + q_T^{+})D]\}, \quad (3)$$

$$n^{3+} = n_0^{3+} + \left(\frac{Np^{-}}{p^{-} + q^{-} + q_T^{-}} - n_0^{3+}\right) \times \{1 - \exp[-(p^{-} + q^{-} + q_T^{-})D]\}, \quad (4)$$

where n_0^{2+} and n_0^{3+} are the concentrations of Sm^{2+} and Sm^{3+} ions before irradiation. Figure 2 shows the resulting curves describing the dose-dependent concentrations of different-valence ions and tending to a certain level-off value. In the case under consideration, the value of n_0^{2+} is almost an order of magnitude larger than n_0^{3+} (see the insert in Fig. 1).

We now consider the behavior of the Sm^{2+}-ion concentration under the effect of irradiation. It can be seen from Fig. 2 that the quantity n^{2+} tends to a constant value with an increase in the dose of irradiation. We can use expression (3) to derive the following formula for the relative rate v of approach of n^{2+} to the limiting value:

$$v = \frac{n^{2+} - n_0^{2+}}{(Np^{+}/\tilde{p}) - n_0^{2+}} = 1 - \exp(-\tilde{p}D). \quad (5)$$

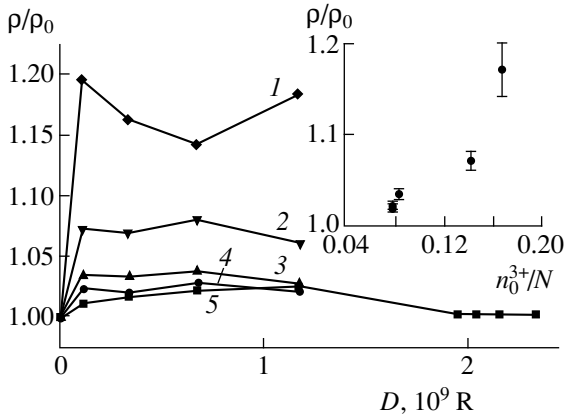

Fig. 1. Resistivity of SmS films with various crystal-lattice parameters a as a function of the exposure dose of gamma-ray irradiation (1.25 MeV and 7×10^5 R/h). a = (*1*) 5.855, (*2*) 5.883, (*3*) 5.941, and (*4*, *5*) 5.944 Å. Variations in the resistivity of the films irradiated with an exposure dose of $D \sim 10^8$ R as a function of the initial Sm^{3+}-ion concentration determined from the value of a according to [3] are shown in the insert.

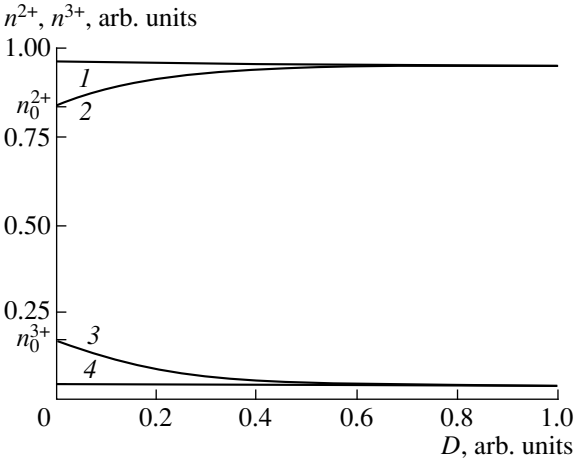

Fig. 2. Dependences of the concentrations n^{2+} and n^{3+} of Sm^{2+} and Sm^{3+} ions on the exposure dose D of gamma-ray irradiation; the dependences were calculated with formulas (3) and (4). Curves *2* and *3* represent the dependences of n^{2+} and n^{3+} on D and lines *1* and *4* correspond to the limiting concentrations of Sm^{2+} and Sm^{3+} ions for the given conditions of irradiation $n^{2+} = Np^{+}/(p^{+} + q^{+} + q_T^{+})$ and $n^{3+} = Np^{-}/(p^{-} + q^{-} + q_T^{-})$, respectively.

Here, $\tilde{p} = p^+ + q^+ + q_T^+$. It can be seen from formula (5) that the quantity ν is independent of n_0^{2+} and, consequently, is also independent of the lattice constant a of the sample. This means that, in films with different values of a, limiting values $n^{2+} \sim Np^+/\tilde{p}$ should be attained for the same values of D. Similar reasoning is also valid for Sm^{3+} ions. As a result, we have the stabilization of the ratio between the concentrations of bivalent and trivalent samarium ions. As shown elsewhere [2, 3], it is the value of this ratio that mainly controls the electrical properties of thin polycrystalline SmS films. In the experiment reported here, the stabilization of n^{2+} and n^{3+} manifests itself in the stabilization of the value of ρ for $D > 10^8$ R.

It is noteworthy that the quantities $p^\pm$, $q^\pm$, and $q_T^\pm$ are bound to depend on the exposure rate (in the case of $q_T^\pm$, this is due to variations in the heating of the sample). Therefore, for different exposure rates, the limiting values of n^{2+}, n^{3+}, and ρ would be dissimilar and would be attained for different values of D.

Thus, on irradiation of SmS films with different initial ratios of the concentrations of Sm^{2+} and Sm^{3+} ions, a process that optimizes this ratio occurs. As a result, dynamic equilibrium is established in the course of generation–trapping of nonequilibrium charge carriers. In this case, the optimal values of this ratio would be dissimilar for different exposure rates but identical for films with a different initial ratio of concentrations of bivalent and trivalent ions. In SmS films, there is a channel for the relaxation of radiation-induced excitations; this channel is related to the presence of different-valence samarium ions and is responsible for the fact that, under exposure to gamma rays, other radiation defects are not formed and electrical parameters of the films are stabilized.

ACKNOWLEDGMENTS

We thank E.D. Gornushkina for her assistance in performing the experiments. This work was supported by the Russian Foundation for Basic Research, project no. 00-02-16947.

REFERENCES

1. V. V. Kaminskiĭ, L. N. Vasil'ev, E. D. Gornushkina, *et al.*, Fiz. Tekh. Poluprovodn. (St. Petersburg) **29** (2), 306 (1995) [Semiconductors **29**, 152 (1995)].
2. V. V. Kaminskiĭ, N. M. Volodin, T. B. Zhukova, *et al.*, Fiz. Tverd. Tela (Leningrad) **33** (1), 187 (1991) [Sov. Phys. Solid State **33**, 108 (1991)].
3. S. V. Pogarev, I. N. Kulikova, E. V. Goncharova, *et al.*, Fiz. Tverd. Tela (Leningrad) **23** (2), 434 (1981) [Sov. Phys. Solid State **23**, 245 (1981)].
4. S. M. Brekhovskikh, Yu. N. Viktorova, and L. M. Landa, *Radiation Effects in Glasses* (Énergoizdat, Moscow, 1982).

Translated by A. Spitsyn

Semiconductors, Vol. 34, No. 9, 2000, pp. 1027–1030. Translated from Fizika i Tekhnika Poluprovodnikov, Vol. 34, No. 9, 2000, pp. 1069–1072.

ELECTRONIC AND OPTICAL PROPERTIES OF SEMICONDUCTORS

Influence of Erbium Ion Implantation Dose on Characteristics of (111) Si:(Er, O) Light-Emitting Diodes Operating in *p–n*-Junction Breakdown Mode

N. A. Sobolev*, A. M. Emel'yanov, and Yu. A. Nikolaev

Ioffe Physicotechnical Institute, Russian Academy of Sciences, Politekhnicheskaya ul. 26, St. Petersburg, 194021 Russia
**e-mail: nick@sobolev.ioffe.rssi.ru*

Submitted February 29, 2000;
accepted for publication March 1, 2000

Abstract—Characteristics of Si:(Er, O) light-emitting diodes (LEDs) fabricated by ion implantation on single-crystal (111) Si substrates and operating under the conditions of avalanche or tunneling breakdown of the *p–n* junction were studied. The Er^{3+} electroluminescence (EL) intensity depends nonmonotonically on the concentration of implanted rare-earth ions. An increase in the Er^{3+} ion EL intensity with temperature is observed in some tunneling diodes. © *2000 MAIK "Nauka/Interperiodica".*

1. INTRODUCTION

Interest in single-crystal silicon doped with rare-earth element erbium is due to its possible application in light-emitting structures for optoelectronics. Electroluminescence (EL) at the wavelength $\lambda \sim 1.54$ μm results from electron transitions from the first excited state $^4I_{13/2}$ to the ground state $^4I_{15/2}$ of Er^{3+} ions. The maximum EL intensity at room temperature is achieved in single-crystal silicon doped with erbium and oxygen under the conditions of *p–n*-junction breakdown. Extensive studies of LED properties have been performed using Si:(Er, O) samples with (100)-oriented substrate [1, 2]. Recently, we showed that high-intensity room-temperature EL from Er^{3+} ions can be obtained from (111)-oriented samples under avalanche-breakdown conditions [3–5]. The goal of this work was to investigate the influence of the erbium-ion implantation dose on the characteristics of LED structures on (111) Si substrates.

2. EXPERIMENTAL PROCEDURE

Polished *n*-type (111) Czochralski-grown Si wafers with 5 Ω cm resistivity were used as substrates. An optically active layer was formed by the coimplantation of erbium and oxygen ions, which was accompanied by amorphization of the near-surface silicon layer. The ion energies were 2.0 and 1.6 MeV for erbium, with doses of 1×10^{14} cm^{-2} (sample 3.1), 3×10^{14} cm^{-2} (sample 3.2), 9×10^{14} cm^{-2} (sample 3.3). For oxygen, the energies were 0.28 and 0.22 MeV and the doses were 1×10^{15} cm^{-2} (3.1), 3×10^{15} cm^{-2} (3.2), 9×10^{15} cm^{-2} (3.3). The energies used ensured the coincidence of the projected ranges of Er and O ions. To form heavily doped p^+- and n^+-layers, boron (40 keV, 5×10^{15} cm^{-2}) and phosphorus ions (80 keV, 1×10^{15} cm^{-2}) were implanted into the front and rear sides of the wafers, respectively. All the implantations were performed at room temperature. The samples were annealed in a chlorine-containing atmosphere under the most widely used conditions: first for 1 h at 620°C and then for 0.5 h at 900°C [1–5]. In the first (low-temperature) annealing stage, the amorphous layer recrystallized by the solid-phase epitaxy mechanism. In the second stage, optically and electrically active erbium-related centers were formed. LEDs with a mesalike periphery and operating area of $S = 2.3$ mm^2 were fabricated using vacuum evaporation of titanium and gold, photolithography, and chemical etching [5]. Current–voltage (*I–V*) characteristics of diodes were recorded at 32 Hz and a 0.5-ms pulse duration. The EL was excited with 1- to 5-ms rectangular pulses with a repetition frequency of 30 Hz. A system of lenses focused the light emitted by a diode structure onto the entrance slit of an MDR-23 monochromator, with the EL spectrum detected at the output with an uncooled InGaAs diode (7-nm resolution in the range $\lambda = 1.0–1.65$ μm).

3. EXPERIMENTAL RESULTS

Figure 1 shows the concentration profiles of Er and B impurities obtained by secondary ion mass-spectrometry (SIMS). The implantation and annealing formed *n*-type layers with a nearly constant concentration of Er atoms at a distance of 0.5–0.8 μm from the sample surface; this concentration increases with Er implantation dose: ~4×10^{18}, 1×10^{19}, and 4×10^{19} cm^{-3}. At 0.8–1.1 μm from the surface, dips in the Er concentration profiles are observed. Their formation is due to the variation of the segregation coefficient at the (amorphous layer)–(single crystal) interface moving in the course of solid-state epitaxial recrystallization [6].

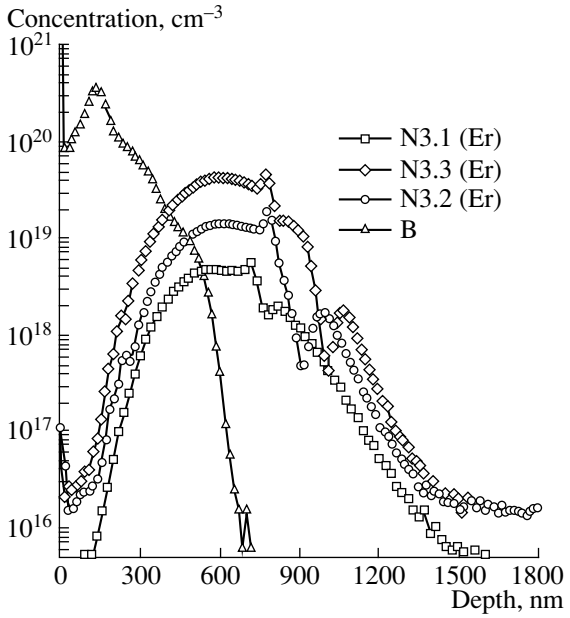

Fig.1. SIMS data. B and Er are the distributions of boron and erbium.

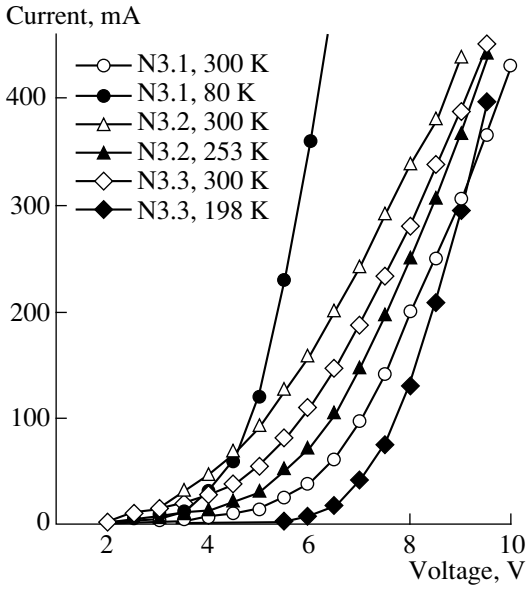

Fig. 2. Reverse portions of *I–V* characteristics of diodes at different temperatures.

Figure 2 shows the reverse-bias *I–V* characteristics for diode structures with different implantation doses, measured at different temperatures. For the sample with the lowest implantation dose, the extrapolated breakdown voltage at 300 K (~6.2 V) and its decrease with decreasing temperature point to the occurrence of avalanche breakdown. By contrast, for both high-dose implanted samples, the extrapolated breakdown voltage increases with decreasing temperature, which is typical of tunnel diodes [7]. It is interesting to note that the increase in the implanted Er and O ion concentrations in sample 3.3, compared with sample 3.2, is accompanied by an increase in the extrapolated breakdown voltage from ~4.2 V to ~5.2 V at room temperature.

Figure 3 shows EL spectra of the diodes at 300 K for a 300-mA reverse current. Along with the peak at λ = 1.538 μm associated with radiative transitions between the Er^{3+} $^4I_{13/2}$ and $^4I_{15/2}$ levels split by the crystal field, a relatively weak and nearly λ-independent emission is observed in the transparency region of silicon. It arises from "hot" electron transitions within the silicon conduction band (so-called "hot" EL) [8]. For avalanche diodes 3.1, the Er^{3+} EL and the hot EL start to grow steeply for a reverse current of ≤10 mA. For tunnel diodes 3.2 and 3.3, the threshold currents at which the Er-ion EL starts to grow substantially (~25 mA in sample 3.2 and ~200 mA in 3.3) are lower than the threshold currents for the hot EL (~75 mA and ~500 mA, respectively).

Figure 4 shows the intensity of EL from Er ions at λ = 1.538 μm as a function of the reverse-current density j for the diodes studied. The maximum EL intensity is observed in tunnel diodes of the 3.2 type, both at 300 K and at 80 K. However, the current density corresponding to the leveling-off of the dependence of EL intensity on current density is nearly an order of magnitude higher than that in the avalanche diodes, similarly to the case of the previously studied tunnel diodes on (100) Si [1]. The EL intensity for type 3.3 tunnel diodes is lower than that for type 3.2 diodes, despite the higher concentration of implanted erbium in the former. In addition,

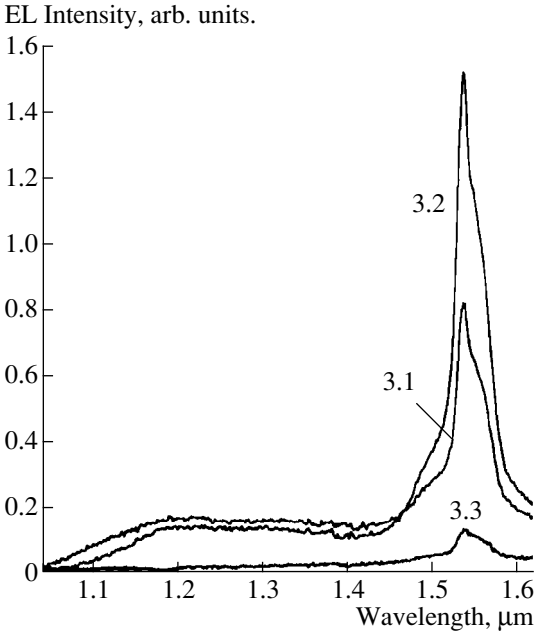

Fig. 3. EL spectra of the samples for j = 13 A/cm^2 at T = 300 K.

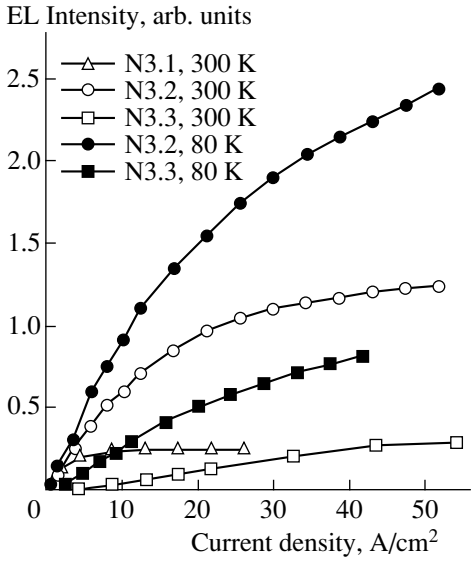

Fig. 4. Intensity of erbium ion EL vs. the reverse current density at 300 and 80 K.

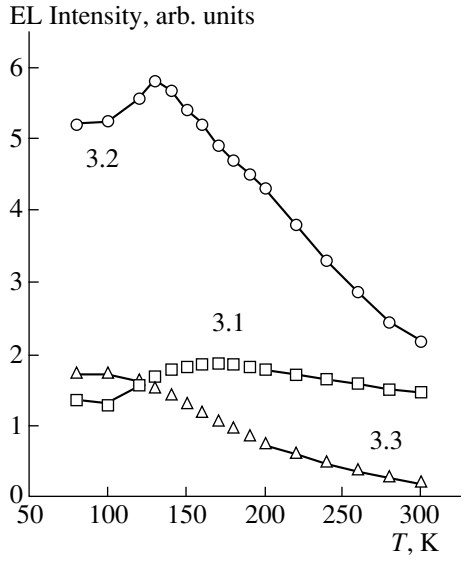

Fig. 5. Temperature dependences of the EL intensity at λ = 1.538 μm for structures studied at a current of 0.3 A (the measurements were made during sample heating).

in these diodes, the threshold currents of the onset of Er-ion EL and hot EL are significantly higher than those in the 3.2 type. Hot carriers with an energy of no less than ~0.8 eV are required for impact excitation of the erbium-ion EL [1]. Further, according to modern concepts [8], high-intensity hot EL in the wavelength range we studied is due to radiative electron transitions between the second Δ_2 and first Δ_1 subbands of the conduction band. Therefore, the high threshold current in the 3.3 diodes may result from insufficient carrier heating by the electric field of the *p–n* junction. One of the possible reasons for the lower EL intensity of the 3.3 sample compared to that of 3.2 may be the high defect density in the Er-doped silicon layer, leading, for example, to an inhomogeneous current flow through the *p–n* junction or formation of additional channels of nonradiative recombination.

For the (111) Si:(Er, O) tunnel LEDs studied in this work, the λ = 1.538 μm EL intensity at 80 K is substantially higher than that at 300 K (see Fig. 4). Figure 5 shows the temperature dependences of the erbium EL for these diodes. For type 3.3 diodes, the EL intensity decreases steadily with increasing temperature. This (conventional) character of the temperature dependences has been observed previously for (100) Si:(Er, O) tunnel [9] and (100) Si:(Er, O) avalanche [10] LEDs. For samples 3.1 and 3.2, regions of nonmonotonic variation (enhancement) of the EL intensity with increasing temperature are observed. We detected this effect previously in (111) Si:(Er, O) avalanche diodes [3] and attributed it to low-temperature filling of hole traps in the active region of the *p–n* junction, which changes the breakdown characteristics. Presumably, the same effect can account for the EL enhancement observed in the (111) Si:(Er, O) tunnel diode 3.2 in this study.

The variety of specific features of the (111) Si:(Er, O) LED characteristics observed in this study on increasing the dose of implanted ions is presumably due to the formation of structural defects during postimplantation annealing. Preliminary studies by transmission electron microscopy of (111) Si:(Er, O) LEDs [11] revealed two types of structural defects in the active region—microtwins and bent dislocations with a density higher than 10^{10} cm^{-2}. It might be expected that an increase in the implantation dose not only results in an increase in the concentration of these extended defects but also transforms them significantly, leading to a nonmonotonic variation of the electrical and optical properties of light-emitting structures.

4. CONCLUSION

A nonmonotonic dependence of the intensity of erbium EL on the concentration of implanted rare-earth ions was found for Si:(Er, O) LED structures that were fabricated on (111) Si substrates and operated under the conditions of *p–n*-junction breakdown. For some of the tunnel diodes, the temperature enhancement of the Er EL intensity is observed, similar to that in the previously studied avalanche diodes. The obtained experimental data indicate that structural defects formed in the course of solid-state epitaxial recrystallization of silicon layers amorphized during erbium implantation exert a strong influence on the electrical and optical properties of Si:(Er, O) LEDs.

ACKNOWLEDGMENTS

The authors are grateful to T.M. Mel'nikova, E.O. Parshin, and A.V. Shestakov for their assistance in sample fabrication.

This work was supported in part by the Russian Foundation for Basic Research, project no. 99-02-17750.

REFERENCES

1. S. Coffa, G. Franzo, and F. Priolo, Appl. Phys. Lett. **69**, 2077 (1996).
2. S. Coffa, G. Franzo, F. Priolo, *et al.*, Appl. Phys. Lett. **73**, 93 (1998).
3. A. M. Emel'yanov, N. A. Sobolev, and A. N. Yakimenko, Appl. Phys. Lett. **72**, 1223 (1998).
4. N. A. Sobolev, A. M. Emel'yanov, S. V. Gastev, *et al.*, Mater. Res. Soc. Symp. Proc. **486**, 139 (1998).
5. N. A. Sobolev, Yu. A. Nikolaev, A. M. Emel'yanov, *et al.*, J. Lumin. **80**, 315 (1999).
6. O. V. Aleksandrov, Yu. A. Nikolaev, and N. A. Sobolev, Fiz. Tekh. Poluprovodn. (St. Petersburg) **34**, 3 (2000) [Semiconductors **34**, 1 (2000)].
7. S. Sze, *Physics of Semiconductor Devices* (Wiley, New York, 1981; Mir, Moscow, 1984).
8. J. Bude, N. Sano, and A. Yoshii, Phys. Rev. B **45**, 5848 (1992).
9. G. Franzo, F. Priolo, S. Coffa, *et al.*, Appl. Phys. Lett. **64**, 2235 (1994).
10. N. A. Sobolev, A. M. Emel'yanov, and K. F. Shtel'makh, Appl. Phys. Lett. **71**, 1930 (1997).
11. N. A. Sobolev, A. M. Emel'yanov, Yu. A. Nikolaev, and V. I. Vdovin, Fiz. Tekh. Poluprovodn. (St. Petersburg) **33**, 660 (1999) [Semiconductors **33**, 613 (1999)].

Translated by D. Mashovets

Semiconductors, Vol. 34, No. 9, 2000, pp. 1031–1044. Translated from Fizika i Tekhnika Poluprovodnikov, Vol. 34, No. 9, 2000, pp. 1073–1085.

ELECTRONIC AND OPTICAL PROPERTIES OF SEMICONDUCTORS

Optical Bistability and Instability in a Semiconductor in the Case Where the Relaxation Time of Free Charge Carriers and Their Equilibrium Concentration are Temperature-Dependent

O. S. Bondarenko, T. M. Lysak, and V. A. Trofimov

Moscow State University, Vorob'evy gory, Moscow, 119899 Russia

Submitted October 19, 1999; accepted for publication March 15, 2000

Abstract—The influence of temperature dependences of the relaxation time of free carriers and their equilibrium concentration on the feasibility of the bistability and instability of steady states is considered. A model describing the process of interaction of optical radiation with a semiconductor was used in the consideration, with various assumptions concerning the conditions of this interaction made. *© 2000 MAIK "Nauka/Interperiodica".*

INTRODUCTION

The phenomenon of optical bistability has attracted the attention of researchers for many years [1–3] in connection with optical methods for data processing and the prospective development of optical computers. In addition, a search for new materials and mechanisms of nonlinearity for the implementation of optical bistability in order to minimize the energy expenditures and time that are required for switching from one state to the other still remains a topical problem.

For practical applications, it is very important to determine the stability of bistable states, because this stability governs the reliability of information storage. It is worth noting that the existence of various spatially inhomogeneous nonsteady structures in reactive gaseous media has been studied previously [4]. By the example of noncavity optical bistability in semiconductors, it is shown [5–7] that, if the temperature dependence of the relaxation time for free charge carriers is taken into account, an instability can develop, as a rule, at the upper branch of the bistable dependence of temperature on the intensity of the incident radiation beam. This results in self-switching of an optical-bistability system from the upper state to the lower state, with the ensuing loss of the stored information. In a spatially inhomogeneous system, the existence of instability brings about the development of complex periodic structures that oscillate simultaneously with several different periods; it is this effect that is responsible for the formation of a sequence of high-absorptivity domains.

The temperature dependence of the relaxation time also manifests itself in the fact that a new type of optical bistability can be achieved; this is the so-called relaxational bistability [7] (the term is due to the nonlinearity mechanism underlying this bistability). However, as the temperature increases, the equilibrium concentration of free electrons changes as well [8, 9]. Its influence on the occurrence of optical bistability and on the instability of one of the bistable states, which may basically change the dynamics of the switching-wave formation, is the object of this study. It is also worth noting that the trends and laws of the phenomena considered below can be generalized to the case of the effect of laser radiation on gaseous mixtures (including reactive media) if the optical energy is absorbed by vibrational levels of molecules.

1. MAIN EQUATIONS

In order to reveal the influence of the temperature dependence of the equilibrium concentration of free charge carriers on the emergence of an optical bistability and the stability of the corresponding steady states, we consider the interaction of laser radiation with a semiconductor in the context of an optically thin layer, assuming that the interaction occurs similarly in all longitudinal sections. Furthermore, we consider the near-axis region of the beam alone and approximate the transverse diffusion and thermal conductivity by the outflow-related components. We note that such an approximation is widely used [1–3], because it makes it possible to analyze qualitatively the processes occurring in such a system. We also take into account the photogeneration of free electrons (for example, from an impurity level) assuming that, in the situation analyzed, the population depletion of the impurity level is insignificant and the transition saturation can occur only owing to the Burstein–Moss dynamic effect [8, 9]. The generation of free charge carriers occurs under the effect of laser radiation with the wavelength either in

1063-7826/00/3409-1031$20.00

the vicinity of the fundamental-absorption edge (in this case, the temperature shift of the edge is taken into account) or away from this edge (the absorption coefficient is then assumed to be temperature-independent).

In the analysis that follows, the recombination of electrons from the conduction band is either described by a model term that is linear in concentration and corresponds to indirect transitions from the conduction band to a donor level or the mechanism of the Auger recombination is considered.

Summing up the above assumptions, we derive the following system of dimensionless equations that describe the interaction of optical radiation with a semiconductor in the context of a pointwise model:

$$\frac{dn}{dt} = \delta(n, T)I - R(n, T) - \frac{n}{\tau_D}, \qquad \frac{dT}{dt} = qR(n, T) - T. \tag{1}$$

Here, allowance is made for two types of free-carrier recombination whose rates are given by

$$R(n, T) = \frac{1}{\tau_r(T)}\begin{cases} n - n_0(T), & (2.1) \\ n[n^2 - n_0^2(T)]. & (2.2) \end{cases}$$

In Eqs. (1) and expressions (2.1) and (2.2), I is the intensity of incident radiation, $n_0(T)$ is the equilibrium concentration of free charge carriers and is attained for a given lattice temperature, $\tau_r(T)$ is the charger-carrier relaxation time, and T is a variation in the temperature of the semiconductor with respect to its unperturbed value T_0. The temperature is normalized to the transition energy. The outflow-related term in the equation for the temperature in system (1) describes the heat removal from the laser-beam axis. The time t is normalized to the characteristic time of heat removal. The concentration of free charge carriers is measured in units of the highest possible concentration attainable under given conditions (at $t = 0$), and the quantity q specifies the fraction of the absorbed laser energy spent on heating the sample in the course of electron recombination. The parameter τ_D in Eq. (1) accounts for the outflow of free charge carriers from the vicinity of the laser-beam axis. By definition of τ_D, this quantity cannot be either negative or zero.

Depending on the conditions of the impact of laser radiation on the semiconductor, the absorption coefficient is chosen in either of the three forms [8, 9]

$$\delta(n, T) = \begin{cases} 1, & (3.1) \\ \exp\left(-\dfrac{1}{T + T_0}\right), & (3.2) \\ (1 - n)\exp\left(-\dfrac{1}{T + T_0}\right). & (3.3) \end{cases}$$

In the first case, the energy of the radiation quantum exceeds the energy of electron transition to the conduction band. The second scenario takes place, as is known, if the frequency of the optical wave is close to that corresponding to the absorption-edge frequency for the given transition. In the third case, the leveling-off of the absorption coefficient is also taken into account.

The temperature dependence of the relaxation time is approximated by

$$\tau_r(T) = \tau_{rm}\begin{cases} 1, & (4.1) \\ \exp\left(-\dfrac{T}{\beta}\right), & (4.2) \end{cases}$$

where τ_{rm} is the maximal value of the relaxation time and β accounts for the rate of a decrease in the relaxation time with increasing temperature. Assuming that the absorptivity is linear (3.1), we can renormalize the temperature to β; in other cases, we will assume that $\beta = 1$.

The equilibrium concentration in the conduction band is approximated with the function [8, 9]

$$n_0(T) = a\left(\frac{T}{T_b}\right)^{3/2}\exp\left(-\frac{1}{T + T_0}\right). \tag{5}$$

The parameters a and T_b are positive constants. In view of the introduced dimensionless variables, the initial conditions for the system of Eqs. (1) have the form

$$T|_{t=0} = 0, \quad n|_{t=0} = n_0 = n(T_0). \tag{6}$$

In order to clarify the conditions for the existence of bistability and for the presence of instability for at least one of the bistable states, we studied the steady-state dependence of temperature T on the incident-beam intensity I. This study was based on the linear analysis of the stability of steady states for system (1).

2. RESULTS

Before proceeding to a discussion of the results of the performed analysis, it should be emphasized that the temperature dependence of the relaxation time forms a positive feedback. Thus, an increase in the temperature brings about a decrease in the relaxation time. This, in turn, causes the heat release to increase and the recombination process to be promoted. In the case of nonlinear temperature dependence of the absorption coefficient, an increase in the temperature brings about a further increase in the contribution of optical energy to the energy of the medium as well.

If, in the situation under consideration, the equilibrium concentration of free electrons is temperature-dependent, this dependence introduces a negative feedback: an increase in the temperature of the medium brings about an increase in the equilibrium electron concentration. As a consequence, the recombination

rate decreases, with an ensuing decrease in the heat-release, which results in a decrease in the contribution of optical energy to the energy of the medium.

A simultaneous consideration of temperature dependences of the above characteristics may drastically transform the manifestation of the absorption-related optical bistability based on the nonlinear temperature dependence of the absorption coefficient. As a result of the analysis, it was ascertained that, for both recombination mechanisms, the instability of bistable states (the upper or lower, or both of them simultaneously) is possible only in the case of nonlinear temperature dependence $\tau_r(T)$ of the free-electron relaxation time. In this situation, the instability regions are predominantly localized at the upper branch of the bistable dependence $T(I)$ even for the case of multistability described previously [10].

In order to reveal the influence of various physical factors on the emergence of unstable states (in the case of the impact of laser radiation on the semiconductor under consideration), we consider separately the case of linear recombination, which corresponds, for example, to the slight excitation of donor levels, and the case of Auger recombination. A comparison of the results obtained for these two cases makes it possible to clarify the role of concentration dependence of the recombination rate in the formation of bistable and multistable states and in their stability.

2.1. The Recombination with Linear Dependence on Concentration

In the case of the linear concentration dependence of the recombination rate, there are two mechanisms for the origination of optical bistability: the absorption-related optical bistability [1, 3] and relaxation-related optical bistability [7]. The simultaneous presence of the above mechanisms results in the expansion of the parameter-value ranges where bistability occurs and also in the situation where multistability may occur [10]. In this case, the temperature dependence of the free-electron equilibrium concentration $n_0(T)$ may narrow the bistability range and may bring together the temperatures of switching.

The emergence of instability portions (unstable nodes and focuses) in the dependence of T on I is possible only owing to the nonlinearity of the relaxation time $\tau_r(T)$ irrespective of the existence of optical bistability or multistability. In this case, the temperature dependence $n_0(T)$ and nonlinear absorptivity narrow the parameter range where instability occurs. It is noteworthy that the stabilizing role of nonlinear absorption manifests itself for relatively small values of the parameter τ_D that specifies the free-electron diffusion (for the considered value of the parameter β equal to unity, the stabilizing role of nonlinear absorption manifests itself for values of τ_D ranging approximately from 1.62 to 3.08). For larger τ_D, the boundary of the instability domain is independent of the specific form of the absorption coefficient [(3.1), (3.2), or (3.3)]. It is noteworthy that a variation in the parameter τ_D corresponds (all other factors being equal) to a change in the characteristic radius of the incident optical beam: a decrease in τ_D implies a transition to narrower optical beams.

2.1.1. Linear absorptivity [$\delta(n, T) \equiv 1$].

We consider the development of instability of bistable states under the impact of laser radiation with a wavelength away from the fundamental-absorption edge; in this case, we assume that the transition is not saturated [the absorption coefficient is given by (3.1)] and take into account the temperature dependence of the relaxation time (4.2). Consequently, in this case, the emergence of optical bistability has a relaxation-related origin. The results of calculations illustrating various modes of interaction are shown in Fig. 1. The boundary of the instability region (the solid line) and the boundary of the bistability region (the dashed line) partition the plane of the τ_{rm} and τ_D parameters into four domains (Fig. 1a). The presence of optical instability is characteristic of regions *1* and *3*, whereas the presence of instability of the type of unstable nodes (an exponential increase in perturbations that are as small as desired) or unstable focuses (oscillations develop as a result of perturbations that are as small as desired) is characteristic of regions *1* and *2*. Relations describing the boundaries of the bistability and instability regions are derived in the Appendix (see expressions A1.1–A2).

We note that, when studying the processes of spontaneous switching of the system from one bistable state to the other (the loss of stored information), the values of the parameters τ_{rm} and τ_D from region *1* in Fig. 1a are of particular interest. Optical bistability exists in this region if the characteristic times τ_{rm} and τ_D satisfy the inequality

$$\tau_{rm} > e^2\tau_D \tag{7}$$

and if the optical-bistability states at the lower branch are stable for $T < \beta$. However, a region of instability may exist predominantly at the upper branch. These values of the temperature T that correspond to unstable steady states are located in the vicinity of the state $T = (2 + 1/\tau_D)\beta$. It is important to emphasize that the development of oscillatory processes starting from arbitrarily small perturbations (as well as an exponential growth of perturbations that are as small as desired) is impossible for the values of the parameters τ_{rm} and τ_D satisfying the inequalities

$$\tau_{rm} < \exp\left(2 + \frac{1}{\tau_D}\right) \quad \text{or} \quad \tau_D < 1. \tag{8}$$

It follows from the above analysis that, for a fixed value of outflow of free electrons from the region of the beam (the parameter τ_D), an increase in the maximal value of the relaxation time τ_{rm} brings about a widening of the temperature range where the unstable states

Table 1. Dependences of temperatures (radiation intensities) for switching to the upper $T_\uparrow(I_\uparrow)$ and lower $T_\downarrow(I_\downarrow)$ states of the system and temperature interval ($T_{\omega1}$, $T_{\omega2}$) and the corresponding intensity interval ($I_{\omega1}$, $I_{\omega2}$) on the maximal value of the recombination time τ_{rm} in the case of linear dependence of the recombination rate on concentration and nonlinear temperature dependence of relaxation time $\tau_r(T)$ for $a = 0$, $q = 13$, $T_0 = 0.16$, $\beta = 1$, and $\tau_D = 2 \times 10^6$

	Bistability				Instability			
$\delta(n, T) = 1$								
τ_{rm}	$T_\uparrow$	$T_\downarrow$	$I_\uparrow$	$I_\downarrow$	$T_{\omega1}$	$T_{\omega2}$	$I_{\omega1}$	$I_{\omega2}$
7.3	–	–	–	–	–	–	–	–
7.4	–	–	–	–	1.95	2.05	0.15	0.16
8.0	–	–	–	–	1.65	2.45	0.13	0.19
10.0	–	–	–	–	1.41	2.99	0.11	0.23
$\delta(n, T) = \delta(T) = \exp\left(-\frac{1}{T + T_0}\right)$								
τ_{rm}	$T_\uparrow$	$T_\downarrow$	$I_\uparrow$	$I_\downarrow$	$T_{\omega1}$	$T_{\omega2}$	$I_{\omega1}$	$I_{\omega2}$
7.3	0.04	0.64	0.46	0.17	–	–	–	–
7.4	0.04	0.64	0.46	0.17	1.95	2.05	0.24	0.25
8.0	0.04	0.64	0.46	0.17	1.65	2.45	0.22	0.28
10.0	0.04	0.64	0.46	0.17	1.41	2.99	0.21	0.32
$\delta(n, T) = (1 - n)\exp\left(-\frac{1}{T + T_0}\right)$								
τ_{rm}	$T_\uparrow$	$T_\downarrow$	$I_\uparrow$	$I_\downarrow$	$T_{\omega1}$	$T_{\omega2}$	$I_{\omega1}$	$I_{\omega2}$
7.3	0.04	0.54	0.47	0.21	–	–	–	–
7.4	0.04	0.54	0.47	0.21	–	–	–	–
8.0	0.04	0.53	0.47	0.22	–	–	–	–
10.0	0.04	0.50	0.47	0.23	1.75	2.64	0.30	0.34

exist. For the purpose of illustration, Table 1 lists the dependences of characteristic values of the temperatures T and radiation intensities I on the maximal value of recombination time τ_{rm} in the vicinity of the boundaries of regions *2* and *4* in Fig. 1a for a large value of the parameter τ_D and the absence of bistable dependence of T on I. The first value of τ_{rm} in Table 1 corresponds approximately to its asymptotic value for $\tau_D \longrightarrow \infty$ (the horizontal dashed straight line in Fig. 1a). For this value of τ_{rm}, there is no instability region (there are no unstable focuses). An increase in τ_{rm} and transition to region *2* give rise to an instability domain (the second row in Table 1), which expands with an increase in τ_{rm}; this expansion concerns both the values of temperature and intensity (the third and fourth rows in Table 1). It is worth noting that, in the absence of the temperature dependence of the equilibrium concentration $n_0(T)$ ($a = 0$), the range of instability temperatures remains unchanged if the fraction of absorbed energy q spent on heating the semiconductor remains unchanged (Table 2). In this case, the corresponding values of irradiation intensities shift to smaller values with increasing q and the difference between the intensities corresponding to switching to the upper and lower states decreases.

If the equilibrium electron concentration varies with increasing temperature ($a \neq 0$), then, as the parameter

$$\chi = q\frac{a}{T_b^{3/2}} \tag{9}$$

increases, the temperature interval of the instability existence decreases, as well as the corresponding intensity range. If the quantity χ exceeds the critical value that depends on the parameters τ_{rm}, τ_D, and T_0, the instability ceases to exist. These trends are illustrated by the data in Table 3.

The temperature dependence of the equilibrium concentration of free electrons significantly affects the existence of the bistable dependence of T on I as well. It follows from the calculations we performed that, as a increases (as the role of the temperature dependence of the free-electron equilibrium concentration increases), the temperatures corresponding to switching become closer to each other until the condition $a = a_{cr}$ is met, where a_{cr} is the critical value for optical-bistability existence. For values of a exceeding a_{cr}, the depen-

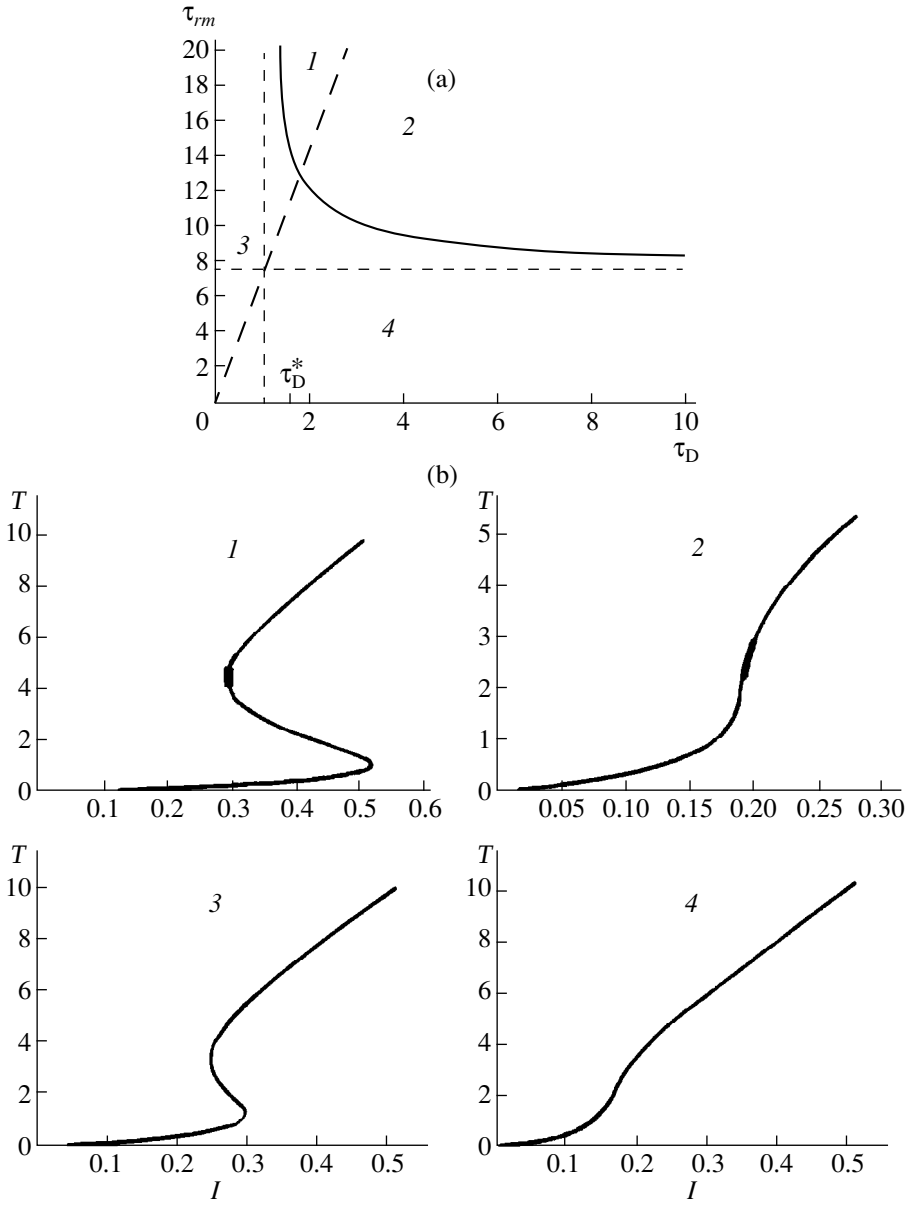

Fig. 1. (a) Domains of existence of instability and bistability in the plane of the parameters τ_{rm} and τ_D for the case of the linear dependence of the recombination rate on concentration, linear absorption coefficient, and the time-independent equilibrium electron concentration. The solid line separates the domain of existence of stable steady states from that of unstable steady states. The dashed thick straight line separates the domain of existence of relaxation-related optical bistability. The thin dashed straight lines are the asymptotes of the solid line. The characteristic point τ_D^* is shown [see Appendix, formulas (A1.1) and (A1.2)]. (b) The characteristic dependences of temperature T on the radiation intensity I for each of domains *1–4* (Fig. 1a) for (*1*) $\tau_{rm} = 50$ and $\tau_D = 2$; (*2*) $\tau_{rm} = 13$ and $\tau_D = 2$; (*3*) $\tau_{rm} = 13$ and $\tau_D = 1$; and (*4*) $\tau_{rm} = 10$ and $\tau_D = 2$. The values of other parameters are $q = 20$ and $\beta = 1$. The solid lines correspond to steady states. The regions of instability corresponding to the oscillatory growth of small perturbations and a region of instability (the thickest line) corresponding to the exponential rise of perturbations are indicated.

dence of T on I is monotone. In the more general case, the emergence of optical bistability is controlled by the value of χ [see (9)]. By way of illustration, Table 4 gives the dependences of the temperatures of switching and the corresponding radiation intensities on the parameter a for the case of the existence of optical bistability and the absence of instability (region *3* in Fig. 1a). The dependence of T on I for zero value of the parameter a is shown in Fig. 1b (curve *3*).

2.1.2. Nonlinear absorptivity.

A. The constant relaxation time $\tau_r(T) = \tau_{rm} = \text{const}$ and the concentration-independent absorption coefficient $\delta(n, T) = \delta(T)$.

Table 2. Dependences of temperatures (radiation intensities) for switching to the upper $T_\uparrow(I_\uparrow)$ and lower $T_\downarrow(I_\downarrow)$ states of the system and temperature interval ($T_{\omega1}$, $T_{\omega2}$) and the corresponding intensity interval ($I_{\omega1}$, $I_{\omega2}$) on parameter q that specifies the heating of the semiconductor in the course of recombination of free electrons in the cases of linear dependence of the recombination rate on concentration and the nonlinear temperature dependence of relaxation time $\tau_r(T)$ for $a = 0$, $\tau_{rm} = 10$, $T_0 = 0.16$, $\beta = 1$, and $\tau_D = 2 \times 10^6$

	Bistability				Instability			
$\delta(n, T) = 1$								
q	$T_\uparrow$	$T_\downarrow$	$I_\uparrow$	$I_\downarrow$	$T_{\omega1}$	$T_{\omega2}$	$I_{\omega1}$	$I_{\omega2}$
8	–	–	–	–	1.41	2.99	0.18	0.37
10	–	–	–	–	1.41	2.99	0.14	0.30
13	–	–	–	–	1.41	2.99	0.11	0.23
20	–	–	–	–	1.41	2.99	0.07	0.15
$\delta(n, T) = \delta(T) = \exp\left(-\frac{1}{T + T_0}\right)$								
q	$T_\uparrow$	$T_\downarrow$	$I_\uparrow$	$I_\downarrow$	$T_{\omega1}$	$T_{\omega2}$	$I_{\omega1}$	$I_{\omega2}$
8	0.04	0.64	0.74	0.28	1.41	2.99	0.33	0.51
10	0.04	0.64	0.59	0.22	1.41	2.99	0.27	0.41
13	0.04	0.64	0.46	0.17	1.41	2.99	0.21	0.32
20	0.04	0.64	0.30	0.11	1.41	2.99	0.13	0.21
$\delta(n, T) = (1 - n)\exp\left(-\frac{1}{T + T_0}\right)$								
q	$T_\uparrow$	$T_\downarrow$	$I_\uparrow$	$I_\downarrow$	$T_{\omega1}$	$T_{\omega2}$	$I_{\omega1}$	$I_{\omega2}$
8	0.04	0.38	0.78	0.45	–	–	–	–
10	0.04	0.44	0.62	0.33	2.09	2.34	0.44	0.45
13	0.04	0.50	0.47	0.23	1.75	2.64	0.30	0.34
20	0.04	0.55	0.30	0.13	1.58	2.80	0.17	0.21

Table 3. Dependences of temperatures (radiation intensities) for switching to the upper $T_\uparrow(I_\uparrow)$ and lower $T_\downarrow(I_\downarrow)$ states of the system and temperature interval ($T_{\omega1}$, $T_{\omega2}$) and the corresponding intensity interval ($I_{\omega1}$, $I_{\omega2}$) on parameter a that specifies the temperature dependence of the equilibrium free-electron concentration in the cases of the linear dependence of the recombination rate on concentration and the nonlinear temperature dependence of the relaxation time τ_r for $T_b = 2$, $q = 13$, $\tau_{rm} = 10$, $T_0 = 0.16$, $\beta = 1$, and $\tau_D = 2 \times 10^6$

	Bistability				Instability			
$\delta(n, T) = 1$								
a	$T_\uparrow$	$T_\downarrow$	$I_\uparrow$	$I_\downarrow$	$T_{\omega1}$	$T_{\omega2}$	$I_{\omega1}$	$I_{\omega2}$
0	–	–	–	–	1.41	2.99	0.11	0.23
0.05	–	–	–	–	1.66	2.25	0.13	0.17
0.1	–	–	–	–	–	–	–	–
$\delta(n, T) = \delta(T) = \exp\left(-\frac{1}{T + T_0}\right)$								
a	$T_\uparrow$	$T_\downarrow$	$I_\uparrow$	$I_\downarrow$	$T_{\omega1}$	$T_{\omega2}$	$I_{\omega1}$	$I_{\omega2}$
0	0.04	0.64	0.46	0.17	1.41	2.99	0.21	0.32
0.05	0.04	0.64	0.46	0.17	1.66	2.25	0.22	0.26
0.1	0.04	0.64	0.46	0.17	–	–	–	–
$\delta(n, T) = (1 - n)\exp\left(-\frac{1}{T + T_0}\right)$								
a	$T_\uparrow$	$T_\downarrow$	$I_\uparrow$	$I_\downarrow$	$T_{\omega1}$	$T_{\omega2}$	$I_{\omega1}$	$I_{\omega2}$
0	0.04	0.50	0.47	0.23	1.75	2.64	0.30	0.34
0.05	0.04	0.49	0.47	0.23	–	–	–	–
0.1	0.04	0.49	0.47	0.23	–	–	–	–

In this case, if the equilibrium concentration of free electrons is temperature-independent, the following inequality [3] should be complied with for bistability in a system to occur:

$$T_0 < 0.25. \quad (10)$$

The temperature dependence of the equilibrium free-electron concentration $n_0(T)$ ($a \neq 0$) manifests itself similarly to the case of linear absorptivity; however, the values of the parameter a are now much larger. Thus, as a increases, the switching temperatures approach each other (Table 5). In addition, there is a critical value of the parameter χ [see(9)] for which the bistability ceases to exist owing to the effect of negative feedback. In this case, an important role is played by the fraction of energy spent on heating the semiconductor in the course of free-electron relaxation (the parameter q). As q increases, the effect of the temperature dependence $n_0(T)$ becomes more pronounced. This effect manifests itself in an appreciable decrease in both the temperature corresponding to switching the system from the upper state to the lower state and the difference between the radiation intensities corresponding to switching. This, in particular, makes it possible to reduce the heating of the medium and solve to a degree the problem of heat removal.

B. Temperature dependences of the relaxation time and the absorption coefficient $\delta(n, T) = \delta(T)$.

The results of the analysis of stability for the system under consideration are shown in Fig. 2 for the values of $T_0 = 0.16$ and $\beta = 1$. Such a temperature of the surrounding medium is chosen because of the fact that, for $T_0 = 0.16$, the difference between the switching temperatures attains a maximum. Experimentally, it is simplest to vary the parameters τ_D (by choosing the beam radius) and τ_{rm} (by selecting the equilibrium temperature of the semiconductor). It is because of this that the plane of the parameters shown in Fig. 2a is considered.

It is noteworthy that, for any ratios between τ_{rm} and τ_D, the dependence of T on I is nonmonotonic owing, in particular, to the absorption-related mechanism of initiation of bistability (Figs. 2b, 2c). However, multistable states can also arise as a result of the temperature dependence of the relaxation time [10].

The plane of the parameters τ_{rm} and τ_D in Fig. 2a is divided into two parts: the part where the areas of instability of bistable states exist (part *1*) and the rest of the plane, for which all physically feasible states are stable. For the parameters under consideration, the instability areas belong to the upper branches of the bistable dependence $T(I)$. Expressions defining the instability boundary on the plane of the parameters τ_{rm} and τ_D (Fig. 2a) are given in the Appendix [see formulas (A3.1) and (A3.2)]. We note that instabilities (nodes or focuses) cannot exist if the values of τ_{rm} and τ_D are linked by relationship (8). As follows from Fig. 2a, the instability area in the plane of the parameters τ_{rm} and τ_D is smaller in the case of nonlinear absorptivity than that in the case of linear absorptivity.

Table 4. Dependences of temperatures (radiation intensities) for switching to the upper $T_\uparrow(I_\uparrow)$ and lower $T_\downarrow(I_\downarrow)$ states of the system on parameter a that specifies the temperature dependence of the free-electron equilibrium concentration in the cases of linear absorptivity $\delta(n, T) = 1$, the linear dependence of the recombination rate on concentration, and the nonlinear temperature dependence of the relaxation time $\tau_r(T)$ for $T_b = 2$, $q = 20$, $\tau_{rm} = 13$, $\beta = 1$, and $\tau_D = 1$

a	$T_\uparrow$	$T_\downarrow$	$I_\uparrow$	$I_\downarrow$
0	1.28	3.46	0.30	0.24
0.01	1.30	3.26	0.30	0.26
0.05	1.44	2.61	0.31	0.307
0.1	–	–	–	–

Table 5. Dependences of temperatures (radiation intensities) for switching to the upper $T_\uparrow(I_\uparrow)$ and lower $T_\downarrow(I_\downarrow)$ states of the system on parameter a that specifies the temperature dependence of the free-electron equilibrium concentration in the cases of constant relaxation time $\tau_r(T) = \tau_{rm}$, the transition unsaturable with respect to concentration $\delta(n, T) \equiv \delta(T)$, and a linear dependence of the recombination rate on concentration for $T_b = 2$, $q = 20$, $\tau_{rm} = 13$, $T_0 = 0.16$, $\beta = 1$, and $\tau_D = 2$

a	$T_\uparrow$	$T_\downarrow$	$I_\uparrow$	$I_\downarrow$
0	0.043	0.64	2.52	0.95
100	0.045	0.14	2.68	2.59
300	–	–	–	–

For fairly large parameter τ_D (for the values of T_0 and $\beta > 4$ under consideration) and in the absence of dynamic saturation of the absorptivity, the temperature range corresponding to the instability region is independent of whether the absorptivity is linear or nonlinear (Tables 1–3). In this case, for nonlinear absorption, the values of the intensity of incident optical radiation that correspond to the initiation of instability are somewhat larger. As an illustration, Fig. 2b shows the characteristic dependence $T(I)$ that includes a portion of unstable steady states of the type of unstable focuses (oscillatory growth of perturbations).

We emphasize that the effect of the fraction of energy converted to heat in the course of relaxation of free electrons on the stability of the states manifests itself only if there is a temperature dependence of the equilibrium concentration of free electrons; this dependence enhances the stabilizing role of the above effect. It is also of interest that the presence of instability of physically feasible states may lead to the situation where a multistable system would behave as a bistable one. This may happen if the instability portion of the last branch in Fig. 2d spans the values of intensity that correspond to the mean stable state present.

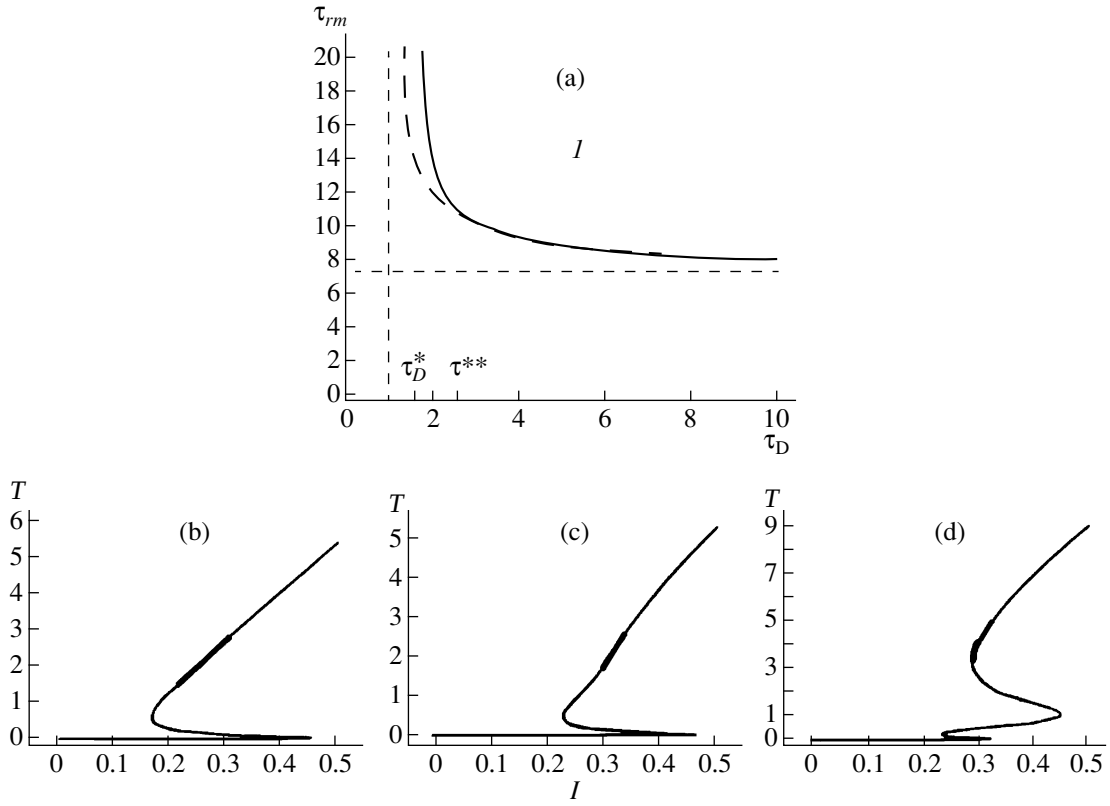

Fig. 2. (a) The domain of existence of instability in the plane of the parameters τ_{rm} and τ_D (for $T_0 = 0.16$ and $\beta = 1$) in the case of linear dependence of the recombination rate on concentration, nonlinear temperature dependence of the relaxation time, nonlinear absorptivity, and the transition unsaturable with respect to concentration. The solid-line curve separates instability domain *1*. The thick dashed-line curve corresponds to the boundary of the instability domain in the case of linear absorptivity. The thin dashed straight lines are the asymptotes to both of the above curves. The characteristic points τ_D^* and τ_D^{**} are indicated [see Appendix, formulas (A3.1), (A3.2)]. (b)–(d) The characteristic dependences of temperature T on radiation intensity I (for the values of the parameters τ_{rm} and τ_D from instability domain *1* in Fig. 2a) for (b) $q = 13$, $\tau_{rm} = 10$, and the transition unsaturable with respect to concentration; (c) $q = 13$, $\tau_{rm} = 10$, and the transition saturable in concentration; and (d) $q = 20$, $\tau_{rm} = 40$, and the transition saturable with respect to concentration. The values of the other parameters are $a = 0$, $T_0 = 0.16$, $\beta = 1$, and $\tau_D = 2 \times 10^6$. The solid lines with portions of thick lines denote the same as in Fig. 1b.

C. Temperature dependences of the relaxation time and absorption coefficient with dynamic saturation of the latter taken into account [$\delta(n, T)$].

Dynamic saturation of the transition brings about a situation in which the initiation of instability requires that a fairly large fraction of energy released in the relaxation of free electrons be spent on heating the semiconductor (Table 2).

In particular, if the equilibrium concentration of free electrons is temperature-independent, the existence of an instability portion in the bistable dependence $T(I)$ is controlled by the coefficient q for fixed values of τ_{rm} and τ_D: the instability cannot exist if the fraction of optical energy converted to heat is smaller than a critical value of the coefficient q. As q increases, the temperature range of instability expands and, for $q \longrightarrow \infty$, tends to the corresponding range in the case where there is no saturation of the transition (Table 2).

The nonzero equilibrium concentration of free electrons [$n_0(T) \neq 0$] brings about a further reduction in the temperature range of instability. For the same values of parameters, the temperature range of instability is wider in the absence of dynamic saturation of transition. Thus, for a fixed value of the coefficient q, the critical value of χ for which the instability of physically feasible states is still possible is smaller than the corresponding value of this quantity in the absence of the transition saturation (Table 3). By way of illustration, Fig. 2c shows the characteristic dependences $T(I)$ that correspond to the existence of concentration-saturated transition and include a portion with unstable focuses.

The consideration of absorption-coefficient saturation with respect to concentration also gives rise to multistability caused by splitting of the bistability region as a result of the effect of two different mechanisms for its initiation: relaxation- and absorption-related ones (Fig. 2d). It is worth noting that, for the same values of

parameters as in Fig. 2d, a system without a dynamic saturation of absorption does not exhibit multistability. Consequently, a dynamic saturation of transition with respect to concentration expands the existence domain of multistability.

2.2. The Mechanism Based on the Auger Recombination

Before proceeding to the detailed analysis of the above results, we formulate briefly the main revealed trends and laws. The presence of temperature dependence of the relaxation time $\tau_r(T)$ is necessary for the existence of unstable, physically feasible states of the type of unstable nodes and focuses. In this case, an important role in the initiation of instability is played by the coefficient q that specifies the fraction of energy spent on heating the semiconductor: as q increases, the instability domain expands and, for large values of q, instability occurs for almost any values of the parameters τ_{rm} and $\tau_D > 1$. The existence of the temperature dependence $n_0(T)$ results in narrowing of the range of parameters for which the instability is feasible.

As in the previous case, there are two mechanisms of initiation of optical bistability for the considered interaction of laser radiation with a semiconductor: the absorption- and relaxation-related mechanisms; here, the temperature range of instability (with respect to the parameter T_0) is wider than in the case of recombination that is linear in concentration. An increase in the fraction of energy spent on heating the semiconductor results in widening of the bistability range for both mechanisms of initiation of optical bistability. A temperature dependence of the equilibrium concentration of free electrons $n_0(T)$ causes the switching temperatures to become closer to each other.

2.2.1. Linear absorptivity [$\delta(n, T) \equiv$ const].

We now consider the conditions for the initiation of bistability and the development of instability of steady states in the case of laser radiation with a wavelength away from the fundamental-absorption edge under the assumption that the relaxation time depends nonlinearly on temperature. First of all, we note that the initiation of a relaxation-related optical bistability is possible for any values of τ_{rm} and τ_D in the case of a specific choice of other parameters, in particular, the coefficient q. The instability development is also basically possible for any values of τ_{rm} with $\tau_D > 1$. However, in the latter case, the fraction of energy spent on heating the semiconductor should increase as the parameter τ_{rm} decreases.

Various modes of interaction of optical radiation with a semiconductor are illustrated in Fig. 3 for the parameters $\beta = 1$ and $q = 10$. The boundary of the instability region (the solid line in Fig. 3a) and the boundary of the bistability region (the dashed line) separate the plane of the parameters τ_{rm} and τ_D into four areas. For areas *1* and *3*, the presence of bistability is characteristic; areas *1* and *2* include the regions of instability of the type of unstable nodes (exponential growth of perturbations that are as small as desired) and unstable focuses (spontaneous development of oscillations). In area *4*, there is neither instability nor bistability.

Relationships defining the boundaries of the regions of bistability and instability are given in the Appendix [see (A5.1)–(A6)]. It is important to note that, for a fixed fraction of energy spent on heating the semiconductor, the spontaneous development of oscillatory processes in the system is impossible for the values of the parameters τ_{rm} and τ_D that satisfy the inequalities

$$\tau_{rm} < \left(\frac{\beta}{q}\right)^2 (\sqrt{3})^3 (1+\sqrt{3})^2 \exp(1+\sqrt{3}) \quad \text{or} \quad 0 < \tau_D < 1. \tag{11}$$

The limiting values in inequalities (11) correspond to the asymptotes of the curve defining the boundary of the instability region (the dotted straight lines in Fig. 3a). If conditions (11) are violated, instability arises only for the values of the parameters τ_{rm} and τ_D that belong to regions *1* and *2*. In this case, as follows from expressions (A5.1) and (A5.2) that define the instability boundary, violation of the first of conditions (11) ensures the existence of instability in the limit of $\tau_D \longrightarrow \infty$.

It follows from inequalities (11) that, as the fraction of the energy spent on heating the semiconductor decreases, the condition for the development of instability with respect to the relaxation time becomes less stringent. Comparison of expressions (A1) and (A5) (see Appendix) describing the conditions for the initiation of instability shows that a nonlinear dependence of the recombination rate on the concentration of free charge carriers gives rise to radically different relationships for characteristic times of the process of interaction. Namely, the dependence of τ_{rm} on the quantities that specify the rate of heating the semiconductor (the parameters q and β) comes into existence; as a result, the initiation of instability becomes possible for any values of the parameter τ_{rm}.

In contrast with (7), the initiation of relaxation-related optical bistability also depends on the relation between the parameters that specify the input of optical energy converted to heat in the system. In this case, the relation between the characteristic initiation times for optical bistability also changes; i.e., we have

$$\tau_{rm} > \left(\frac{\beta}{q}\right)^2 (\sqrt{3})^3 (1+\sqrt{3})^2 \tau_D^3 \exp(1+\sqrt{3}), \quad \tau_D > 0. \tag{12}$$

The presence of nonlinear dependence of the equilibrium concentration of free electrons $n_0(T)$ ($a \neq 0$) causes the range of unstable steady states to narrow and the switching temperatures to become closer to each other, with the subsequent disappearance of instability

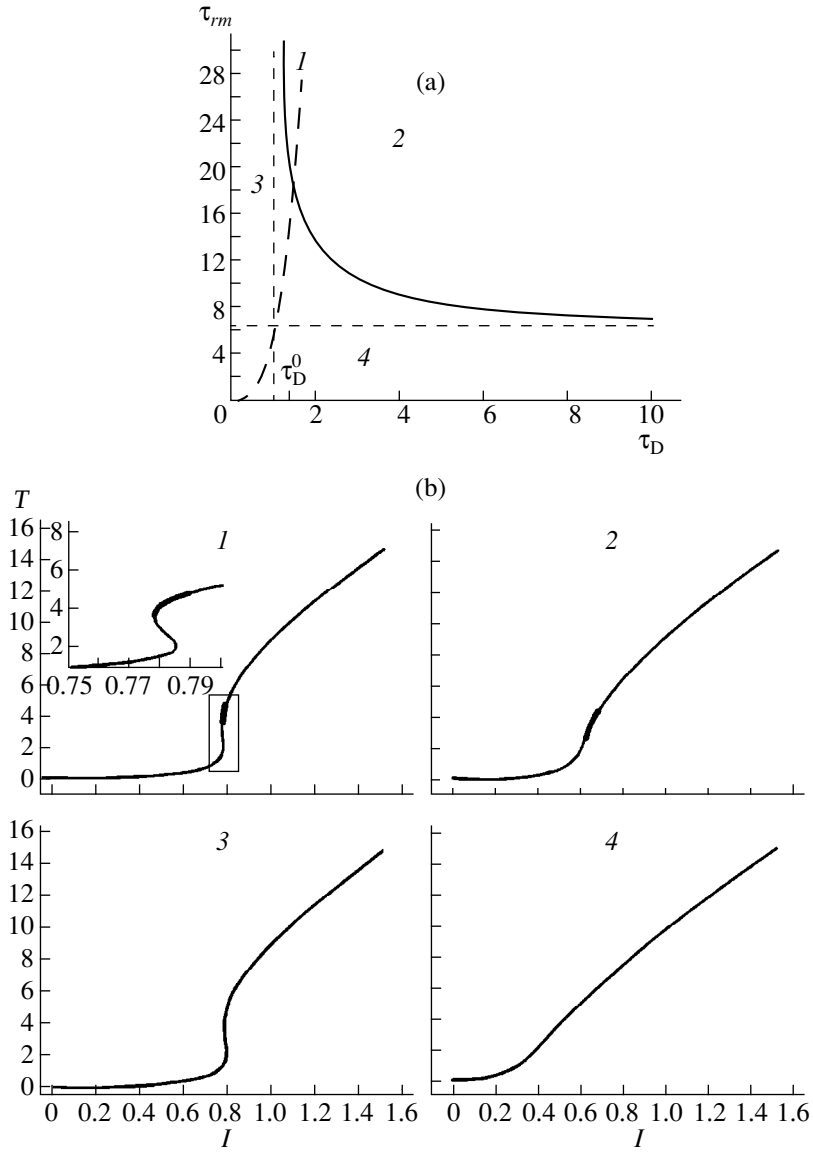

Fig. 3. (a) The domains of existence of instability and optical bistability of the relaxation type in the plane of the parameters τ_{rm} and τ_D for $q = 10$ and $\beta = 1$ in the case of Auger recombination, linear absorption coefficient, and temperature-independent equilibrium electron concentration. The solid, thin-dashed, and thick-dashed lines denote the same as in Fig. 1a. (b) Characteristic dependences $T(I)$ for each of the domains *1–4* (Fig. 3a) for (*1*) $\tau_{rm} = 25$ and $\tau_D = 1.5$; (*2*) $\tau_{rm} = 18$ and $\tau_D = 2$; (*3*) $\tau_{rm} = 18$ and $\tau_D = 1.33$; and (*4*) $\tau_{rm} = 2$ and $\tau_D = 2$. The solid lines with portions of thick lines denote the same as in Fig. 1b.

and bistability regions as the parameter a increases (Tables 6, 7); i.e., the results are similar to those in the case of linear dependence of the recombination rate on concentration.

2.2.2. Nonlinear absorptivity.

A. Constant relaxation time $\tau_p(T) = \tau_{rm} = \text{const}$ and concentration-independent absorption coefficient $\delta(n, T) = \delta(T)$.

In the case where the relaxation time is constant in the absence of transition saturation and the equilibrium concentration of free electrons is temperature-independent, optical bistability in the system occurs if the following inequality is valid:

$$T_0 < 0.75. \tag{13}$$

In this case, the dependence $T(I)$ is bistable for $T_0 < 0.25$ irrespective of the values of the parameters τ_{rm} and τ_D and the coefficient q (the absorption-related optical bistability). In the range of $0.25 < T_0 < 0.75$, the conditions for the emergence of bistability depend on the fraction of energy spent on heating the semiconductor. In order to attain bistability, the following inequality should be fulfilled:

$$\tau_{rm} > \frac{1}{q^2}\left(\frac{3}{\zeta^*(T_0)}\right)^3 \tau_D^3. \tag{14}$$

Here, the function $\zeta^*(T_0)$ is determined from the condition for the existence of a solution to the inequality

$$\zeta^* T^{2/3}\left[1-\frac{T}{(T+T_0)^2}\right]+\left[1-\frac{3T}{(T+T_0)^2}\right]<0. \quad (15)$$

The dependence of the limiting value of ζ on T_0 for which a solution to inequality (15) still exists is shown in Fig. 4 for the sake of illustration. It is important to note that nonlinear dependence of the recombination mechanism on the concentration may widen the range of surrounding-medium temperatures corresponding to the manifestation of absorption-related optical bistability. It was shown previously [11] for the case of the recombination mechanism that is linear in concentration that consideration of the finite rate of thermalization for the absorbed optical energy (finite value of τ_{rm}) results only in narrowing of the range of temperatures T_0 corresponding to bistability as the fraction of energy spent on heating the semiconductor decreases. The possibility of relaxing the conditions for the initiation of the absorption-related optical bistability revealed here makes it possible to appreciably enhance the efficiency of the bistability implementation and reduce the energy spent on switching as a result of a decrease in the energy expenditures for maintaining a specified temperature of the surrounding medium (thermostat). Thus, an increase in the fraction of energy spent on heating the semiconductor results in expanding the existence domain for bistability in the plane of the parameters τ_{rm} and τ_D. If this fraction is small, the condition for the bistability existence is given by $T_0 < 0.25$.

The presence of the temperature dependence of the equilibrium free-electron concentration $n_0(T)$ ($a \neq 0$) leads, as above, to the fact that the switching temperatures approach each other to the point of disappearance of the bistability as parameter a increases (Table 8). However, the value of parameter a for which this occurs is by more than an order of magnitude larger than that calculated for the case of the recombination rate that depends linearly on the concentration.

B. Temperature dependences of the relaxation time and absorption coefficient $\delta(n, T) = \delta(T)$.

The basic conclusions about existence conditions for instability that were made in considering the linear absorption also hold for nonlinear absorptivity. Namely, the instability may occur for any values of the parameter τ_{rm} and for any $\tau_D > 1$. At the same time, as occurred in the case of the recombination rate that depended linearly on concentration, the presence of a nonlinear absorption coefficient brings about a certain narrowing of the domain of existence compared to what is observed for linear absorptivity.

If the equilibrium free-electron concentration is temperature-independent ($a = 0$), the temperature range of instability is no wider than that in the case of linear absorptivity. In the case under consideration, the smallest possible value of the quantity q that is needed to attain instability and defines the fraction of energy spent on heating the semiconductor does not exceed the corresponding value in the case of linear absorptivity. An increase in q brings about an expansion of the instability domain.

Table 6. Dependences of temperatures (radiation intensities) for switching to the upper $T_\uparrow(I_\uparrow)$ and lower $T_\downarrow(I_\downarrow)$ states of the system on parameter a that specifies the temperature dependence of the free-electron equilibrium concentration in the cases of nonlinear temperature dependence of relaxation time $\tau_r(T)$, linear absorptivity $\delta(n, T) \equiv 1$, and the Auger recombination for $T_b = 1$, $q = 50$, $T_0 = 0.16$, $\tau_{rm} = 1$, $\beta = 1$, and $\tau_D = 1$

a	$T_\uparrow$	$T_\downarrow$	$I_\uparrow$	$I_\downarrow$
0	1.47	5.67	0.22	0.18
0.01	1.49	3.88	0.22	0.21
0.1	–	–	–	–

Table 7. Dependences of temperatures (radiation intensities) for switching to the upper $T_\uparrow(I_\uparrow)$ and lower $T_\downarrow(I_\downarrow)$ states of the system, temperature interval ($T_{\omega1}$, $T_{\omega2}$) and the corresponding intensity interval ($I_{\omega1}$, $I_{\omega2}$) on parameter a that specifies the temperature dependence of the free-electron equilibrium concentration in the cases of Auger recombination, linear absorptivity $\delta(n, T) \equiv 1$, and nonlinear temperature dependence of the relaxation time $\tau_r(T)$ for $T_b = 1$, $q = 10$, $\tau_{rm} = 100$, $T_0 = 0.16$, $\beta = 1$, and $\tau_D = 2$

	Bistability				Instability			
a	$T_\uparrow$	$T_\downarrow$	$I_\uparrow$	$I_\downarrow$	$T_{\omega1}$	$T_{\omega2}$	$I_{\omega1}$	$I_{\omega2}$
0	1.70	4.65	0.90	0.84	4.65	7.18	0.840	0.907
0.10	1.77	3.12	0.90	0.89	3.12	3.72	0.900	0.908
0.17	–	–	–	–	2.26	2.55	0.909	0.914
0.20	–	–	–	–	–	–	–	–

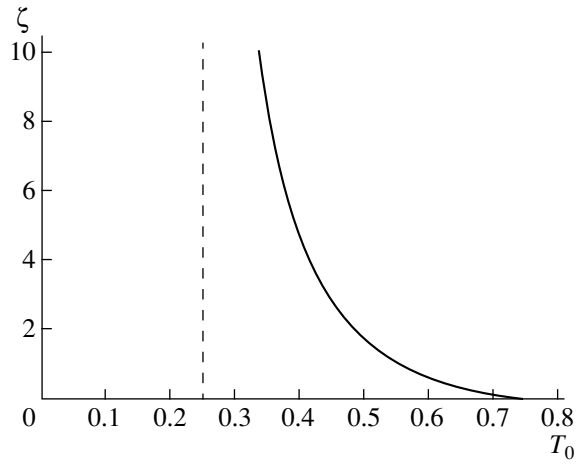

Fig. 4. The domain of existence of absorption-related optical bistability in the plane of the parameters $\zeta \equiv 3\tau_D \tau_{pm}^{-1/3} q^{-2/3}$ and T_0 for the case of Auger recombination, nonlinear absorptivity, the concentration-unsaturable transition, and constant relaxation time.

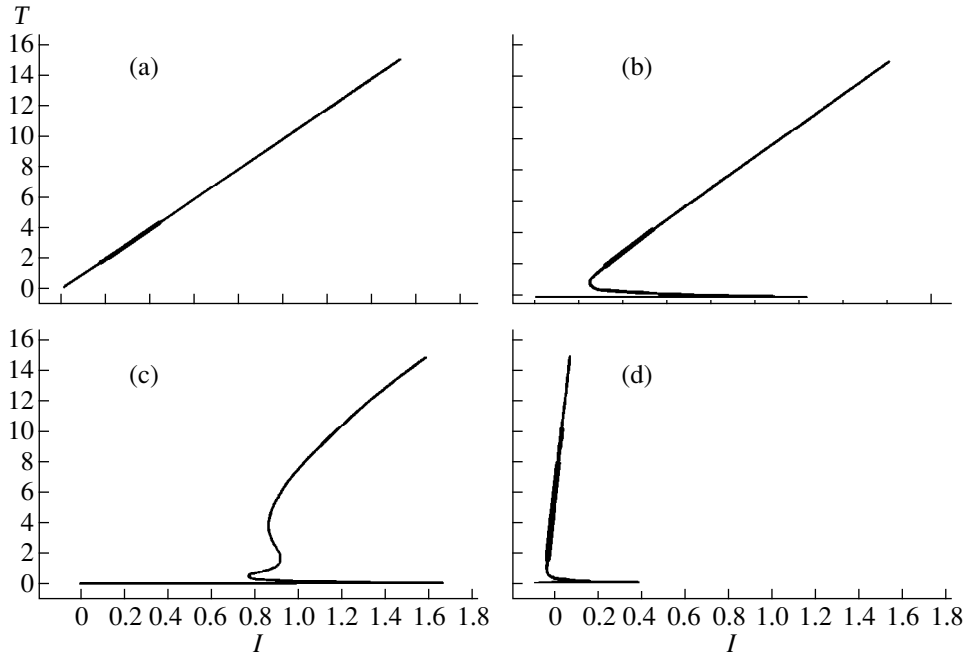

Fig. 5. Variations in the dependence $T(I)$ under changes in absorptivity for the case of Auger recombination, nonlinear temperature dependence of relaxation time, and temperature-independent equilibrium concentration of electrons. The curves shown in different panels correspond to (a) linear absorptivity and $q = 10$; (b) nonlinear absorptivity, concentration-unsaturable transition, and $q = 10$; (c) nonlinear absorptivity, concentration-saturable transition, and $q = 10$; and (d) nonlinear absorptivity, concentration-saturable transition, and $q = 100$. The following values of other parameters were used: $\tau_{rm} = 10$, $T_0 = 0.16$, $\beta = 1$, and $\tau_D = 100$. The solid line with normal thickness corresponds to stable states. The solid-line curves with portions of thick lines denote the same as in Fig. 1b.

The presence of two mechanisms for the initiation of bistability (the relaxation- and absorption-related mechanisms) results, as in the case of the linear recombination rate, in an expansion of the domain of existence of bistability.

Figure 5 shows the aforementioned special features of the intensity dependence of the temperature. The monotone dependence of the temperature on intensity in the presence of temperature dependences of the relaxation time and linear absorptivity (Fig. 5a) transforms into a bistable dependence if there is a nonlinear absorptivity that depends only on temperature. The temperature range of instability remains virtually unchanged, whereas the corresponding intensity range shifts to higher critical values. The instability region belongs now to the upper branch of the bistability curve (Fig. 5b).

Table 8. Dependences of temperatures (radiation intensities) for switching to the upper $T\uparrow(I\uparrow)$ and lower $T\downarrow(I\downarrow)$ states of the system on parameter a that specifies the temperature dependence of the free-electron equilibrium concentration in the case of the constant relaxation time $\tau_r(T) = \tau_{rm}$, the transition unsaturable with respect to concentration $\delta(n, T) \equiv \delta(T)$, and the Auger recombination for $T_b = 1$, $q = 1$, $\tau_{rm} = 1$, $T_0 = 0.16$, $\beta = 1$, and $\tau_D = 10$

a	$T\uparrow$	$T\downarrow$	$I\uparrow$	$I\downarrow$
0	0.02	0.72	12.19	2.52
1000	0.02	0.11	12.19	8.34
10000	–	–	–	–

The fact that the equilibrium concentration of free electrons is temperature-dependent ($a \neq 0$) brings about, as before, a narrowing of the temperature range of instability and the disappearance of instability if parameter a exceeds a certain critical value. In addition, for $a \neq 0$, the temperatures corresponding to switching become close to each other and the subsequent disappearance of the bistability domain is observed as parameter a increases.

C. Temperature dependences of the relaxation time and absorption coefficient with allowance made for dynamic saturation of the latter [$\delta(n, T)$].

Dynamic transition saturation narrows the domain of existence of instability even more than in the absence of this saturation. At the same time, the statement that the effect of parameter q is destabilizing remains valid: an increase in the fraction of absorbed energy spent on heating the semiconductor expands the instability domain. The limiting minimal value of the parameter q for which the dependence $T(I)$ still includes the instability portion is larger in the case of dynamic saturation than in the case where there is no such saturation. Dynamic saturation of the transition may also result in the emergence of multistability (Fig. 5c), which also occurred in the case of the recombination rate that

depends linearly on concentration. The emergence of multistability is accompanied by the disappearance of the region of instability. However, an increase in the parameter q (Fig. 5d) again gives rise to instability; in the latter case, there is also a region of exponential growth of small perturbations along with the region of oscillatory instability.

The presence of temperature dependence of the equilibrium concentration of free electrons causes the temperature range of instability to narrow and the temperatures of switching of bistable states to approach each other. The corresponding values of a in excess of critical values bring about the disappearance of the instability and bistability portions in the curve $T(I)$.

CONCLUSION

As a result of the above analysis, we studied the conditions for the initiation of optical bistability and instability of bistable states for various mechanisms of relaxation of free charge carriers, conditions of absorption of optical energy by a semiconductor, temperature dependence of the relaxation time, and equilibrium concentration of free charge carriers in the conduction band.

It was shown that, in all cases considered, the temperature dependence of the relaxation time is the necessary condition for the initiating instability of bistable states. The instability regions are predominantly localized at the upper branch of the bistability curve. Consideration of the equilibrium concentration of free electrons plays a stabilizing role, because it results in a decrease in the regions of unstable steady states and in the approach to each other of the temperatures corresponding to switching in the bistable dependence.

In the absence of dynamic saturation of the absorption coefficient with respect to concentration, the temperature dependence or independence of this coefficient does not affect the temperature range in which there is no time-independent solution.

In the case of dynamic saturation of the transition, the presence of nonlinear absorptivity brings about a narrowing of the temperature range of instability and a widening of the range of bistability as a result of the simultaneous action of the absorption- and relaxation-related mechanisms of optical bistability initiation.

In the case of Auger recombination, the domain of existence of bistability and instability is larger compared to the case of the relaxation rate that depends linearly on concentration. The fraction of energy q converted to heat plays an important role in the initiation of instability and bistability for the considered dependences of the absorption coefficient on the parameters of the medium. An increase in coefficient q brings about an expansion of the domains of existence of instability and bistability. In the case of Auger recombination, the domain of existence of bistability is larger in the sense that the corresponding range of temperatures of the surrounding medium is wider.

APPENDIX TO THE SECTIONS

2.1. The Recombination Rate That Depends Linearly on Concentration

2.1.1. Linear absorptivity [$\delta(n, T) = \text{const}$].

The boundary of the instability domain in the plane of the parameters τ_{rm} and τ_D (Fig. 1a, solid line) is defined by the following expressions:

$$\tau_{rm} = \tau_{rm}^{(1)}(\tau_D) = \exp\left(2 + \frac{1}{\tau_D}\right) \quad \text{for} \quad \tau_D > \tau_D^*, \tag{A.1.1}$$

$$\tau_{rm} = \tau_{rm}^{(2)}(\tau_D) = \tau_D(\tau_D - 1)\exp\left(\frac{\tau_D}{\tau_D - 1}\right) \quad \text{for} \quad 1 < \tau_D < \tau_D^*. \tag{A.1.2}$$

The value τ_D^* of the parameter τ_D is determined by solving the equation

$$\tau_{rm}^{(2)}(\tau_D) = \tau_{rm}^{(1)}\tau_D.$$

The boundary of the domain of existence of optical bistability in the plane of the parameters τ_{rm} and τ_D (Fig. 1a, dashed line) is defined by the expression

$$\tau_{rm} = \tau_{rm}^{(b)}(\tau_D) = e^2\tau_D. \tag{A.2}$$

2.1.2. Nonlinear absorptivity.

B. Temperature dependences of the relaxation time and the absorption coefficient $\delta(n, T) = \delta(T)$.

The boundary of the instability domain in the plane of the parameters τ_{rm} and τ_D (Fig. 2a, solid line) is defined by the following expressions:

$$\tau_{rm} = \tau_{rm}^{(1)}(\tau_D) = \exp\left(2 + \frac{1}{\tau_D}\right) \quad \text{for} \quad \tau_D > \tau_D^{**}, \tag{A.3.1}$$

$$\tau_{rm} = \tau_{rm}^{(3)}(\tau_D) \quad \text{for} \quad 1 < \tau_D < \tau_D^{**}. \tag{A.3.2}$$

The latter dependence is specified by the following relationships:

$$\tau_D = \frac{\frac{T}{\beta}}{\left(\frac{T}{\beta} - 1\right)\left[1 - \frac{T}{(T + T_0)^2}\right]}, \qquad \tau_{rm} = \frac{\frac{T}{\beta}\exp\left(\frac{T}{\beta}\right)}{\left(\frac{T}{\beta} - 1\right)\left(\frac{T}{\beta} - 1 + \frac{T}{(T + T_0)^2}\right)}. \tag{A.4}$$

The value τ_D^{**} of the parameter τ_D is determined by solving the equation

$$\tau_{rm}^{(3)}(\tau_D) = \tau_{rm}^{(1)}(\tau_D).$$

2.2. The Mechanism of Auger Recombination

2.2.1. Linear absorptivity [$\delta(n, T) = \text{const}$].

For fixed values of the parameters β and q (Fig. 3a, solid line), the boundary of the domain of existence in the plane of the parameters τ_{rm} and τ_D is defined by the following expressions:

$$\tau_{rm} = \tau_{rm}^{(1)}(\tau_D) = \left(\frac{\beta}{q}\right)^2 \frac{e^{\tilde{x}}}{\tilde{x}}(\tilde{x}+2)^3 \quad \text{for} \quad \tau_D > \tau_D^0, \quad \text{(A.5.1)}$$

$$\tau_{rm} = \tau_{rm}^{(2)}(\tau_D) = 3^3\left(\frac{\beta}{q}\right)^2 \exp\left(\frac{\tau_D}{\tau_D - 1}\right) \times \tau_D^5(\tau_D - 1) \quad \text{for} \quad 1 < \tau_D < \tau_D^0. \quad \text{(A.5.2)}$$

Here,

$$\tilde{x} = 1 + \frac{1}{2\tau_D} + \sqrt{\left(1 + \frac{1}{2\tau_D}\right)^2 + 2\left(1 + \frac{1}{\tau_D}\right)}.$$

The value τ_D^0 of the parameter τ_D is determined by solving the equation

$$\tau_{rm}^{(1)}(\tau_D) = \tau_{rm}^{(2)}(\tau_D).$$

The boundary of the bistability domain in the plane of the parameters τ_{rm} and τ_D (Fig. 3a, dashed line) is specified by the expression

$$\tau_{rm} = \tau_{rm}^{(b0)}(\tau_D) = \left(\frac{\beta}{q}\right)^2 (\sqrt{3})^3 (1+\sqrt{3})^2 \tau_D^3 \exp(1+\sqrt{3}). \quad \text{(A.6)}$$

REFERENCES

1. H. Gibbs, *Optical Bistability: Controlling Light with Light* (Academic, New York, 1985; Mir, Moscow, 1988).
2. *Optical Computing: Digital and Symbolic*, Ed. by R. Arratoon (Marcel Dekker, New York, 1989; Mir, Moscow, 1993).
3. N. N. Rozanov, *Optical Bistability and Hysteresis in Distributed Nonlinear Systems* (Nauka, Moscow, 1997).
4. *Oscillations and Traveling Waves in Chemical Systems*, Ed. by R. J. Field and M. Burger (Wiley, New York, 1985; Mir, Moscow, 1988).
5. O. S. Bondarenko, V. A. Trofimov, *et al.*, Bull. Russ. Acad. Sci., Phys., Suppl. Phys. Vibr. **50** (1), 21 (1995).
6. O. S. Bondarenko, S. V. Polyakov, and V. A. Trofimov, Fiz. Tverd. Tela (St. Petersburg) **36** (1), 152 (1994) [Phys. Solid State **36**, 83 (1994)].
7. O. S. Bondarenko and V. A. Trofimov, Dokl. Akad. Nauk **364** (5), 1 (1999).
8. R. A. Smith, *Semiconductors* (Cambridge Univ. Press, Cambridge, 1978; Mir, Moscow, 1982).
9. V. L. Bonch-Bruevich and S. G. Kalashnikov, *The Physics of Semiconductors* (Nauka, Moscow, 1990).
10. Yu. N. Karamzin, S. V. Polyakov, and V. A. Trofimov, Pis'ma Zh. Tekh. Fiz. **18** (24), 38 (1992) [Sov. Tech. Phys. Lett. **18**, 809 (1992)].
11. Yu. N. Karamzin, S. V. Polyakov, and V. A. Trofimov, Preprint No. 62, IPM im. M.V. Keldysha AN SSSR (Keldysh Institute of Applied Mathematics, Russian Academy of Sciences, 1990).

Translated by A. Spitsyn

Semiconductors, Vol. 34, No. 9, 2000, pp. 1045–1051. Translated from Fizika i Tekhnika Poluprovodnikov, Vol. 34, No. 9, 2000, pp. 1086–1092.

ELECTRONIC AND OPTICAL PROPERTIES OF SEMICONDUCTORS

Generalized Multilayer Model for the Quantitative Analysis of the Electromodulation Components of the Electroreflectance and Photoreflectance Spectra of Semiconductors in the Region of the E_0 Fundamental Transition

R. V. Kuz'menko[1]*, A. V. Ganzha[1], É. P. Domashevskaya[1], V. Kircher[2], and S. Hildebrandt[2]

[1]*Voronezh State University, Universitetskaya pl. 1, Voronezh, 394693 Russia*
**e-mail: phssd2@main.vsu.ru*

[2]*Fachbereich Physik der Martin-Luther-Universität Halle-Witteberg, D-06108 Halle/Saale, Germany*

Submitted January 27, 2000;
accepted for publication March 15, 2000

Abstract—With the assumption of the Franz–Keldysh effect as the origination mechanism of the interband electromodulation E_0 component, a generalized multilayer model of this effect was proposed. This model includes such physical parameters as the strength of the surface electric field and its decay profile in the space charge region, energy broadening, and partial modulation of the surface electric field. It was shown that the three regions can be defined in the simulated spectra, namely, the low-energy region, the region of main peak, and the high-energy region of the Franz–Keldysh oscillations. The effect of the model parameters on the line shape in these regions was studied. The ranges of the actual parameters were determined from the quantitative analysis of the experimental photoreflectance spectra of GaAs and InP substrates ($n = 10^{15}$ cm^{-3}–10^{18} cm^{-3}).

INTRODUCTION

Electroreflectance and photoreflectance are the most extensively employed methods of modulation spectroscopy. These techniques are based on the periodic electrical modulation of the reflection signal by the near-surface region of a semiconductor. In the case of electroreflectance, the effect is achieved by application of an external electric field, while for photoreflectance, the inherent surface electric field of the semiconductor is varied due to the illumination of its surface with photon energies higher than the band gap [1]. The electromodulation and photomodulation spectra taken in the region of the E_0 fundamental transition at moderate fields provide the most information because of the pronounced broadening effects in the region of the high-energy transitions [2, 3]. The E_0 spectra can be multicomponent in some cases [4–6]; i.e., along with the E_0 electromodulation component, they can contain the spectral components of the nearest low-energy transitions or E_0 components resulting from the other modulation mechanisms. However, the electromodulation component is dominant for a broad class of specimens. Hence, the problem of correct interpretation of E_0 spectra of these samples can be solved only by performing quantitative analysis in terms of an adequate physical model.

THE ASPNES AND GOBRECHT MODELS

The modulation signal in the most general form is defined as [1]

$$\frac{\Delta R}{R}(E) = \frac{R^*(E) - R(E)}{R(E)}, \quad (1)$$

where $R^*(E)$ is the reflectance signal in the presence of perturbation and $R(E)$ is the reflectance signal without the perturbation. The depth of the informativeness of the modulation signal is defined as the least value of the probing depth of perturbation and the depth of light penetration into the semiconductor. The surface electric field F of the semiconductor is responsible for the variation of the complex permittivity $\varepsilon(E) = \varepsilon_1(E) + i\varepsilon_2(E)$ in the near-surface region of the semiconductor compared to its value in the bulk (the Franz–Keldysh effect). The earliest Aspnes model [7, 8] is based on the assumptions of a homogeneous electric field in the region of the depth of informativeness, total suppression of the surface electric internal field of the semiconductor by the applied external perturbation, and energy broadening Γ independent of the photon energy. In the context of these assumptions, the spectral shape of the

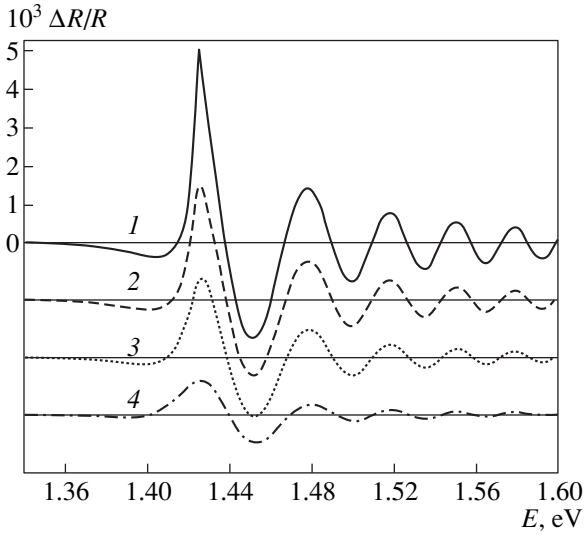

Fig. 1. Electromodulation components calculated in the Aspnes model with the following simulation parameters: $E_0 = 1.424$ eV, $F = 4 \times 10^6$ V/m, $\Gamma' =$ (*1*) 0, (*2*) 0.1, (*3*) 0.2, and (*4*) 0.5.

electromodulation component for the three-dimensional critical point is described by the expressions

$$\frac{\Delta R}{R}(E, F) = \alpha_S(\varepsilon_1, \varepsilon_2)\Delta\varepsilon_1 + \beta_S(\varepsilon_1, \varepsilon_2)\Delta\varepsilon_2, \quad (2)$$

$$\Delta\varepsilon_1(F) = \varepsilon_1(F) - \varepsilon_1(F = 0), \quad (3)$$

$$\Delta\varepsilon_2(F) = \varepsilon_2(F) - \varepsilon_2(F = 0), \quad (4)$$

$$\Delta\varepsilon_1(E) = \frac{\text{const}(\hbar\Theta)^{1/2}}{E^2}G(x, \Gamma'), \quad (5)$$

$$\Delta\varepsilon_2(E) = \frac{\text{const}(\hbar\Theta)^{1/2}}{E^2}F(x, \Gamma'), \quad (6)$$

$$\hbar\Omega = \left[\frac{e^2F^2\hbar^2}{8\mu_\parallel}\right]^{1/3}, \quad (7)$$

$$\mathrm{F}(x, \Gamma') + i\mathrm{G}(x, \Gamma')$$

$$= 2\pi[e^{-i\pi/3}\mathrm{Ai}'(z_0)\mathrm{Ai}'(\omega_0) + \omega_0\mathrm{Ai}(z_0)\mathrm{Ai}(\omega_0)] \quad (8)$$

$$-\left(\frac{-x + (x^2 + \Gamma'^2)^{1/2}}{2}\right)^{1/2} + i\left(\frac{x + (x^2 + \Gamma'^2)^{1/2}}{2}\right)^{1/2}.$$

Here, $\hbar\Theta = 2^{2/3}\hbar\Omega$, $x = (E_0 - E)/\hbar\Theta$, $\Gamma' = \Gamma/\hbar\Theta$, $z_0 = x + i\Gamma'$, $\omega_0 = z_0\exp(-2\pi i/3)$, E is the photon energy, E_0 is the energy of the fundamental transition, α_S and β_S are the Seraphin factors [9] (in the region of the fundamental transition, $\alpha_S \gg \beta_S$, $\alpha_S \approx$ const), $\Delta\varepsilon_1 + i\Delta\varepsilon_2$ are the changes of the real and imaginary parts of the complex permittivity induced by the electric field, $\hbar\Omega$ is the electrooptical energy, $\mu_\parallel$ is the reduced effective mass of the electron and hole in the direction of the electric field, and Ai and Ai' are the Airy function and its derivative.

The spectra simulated with this model for different energy broadenings are shown in Fig. 1. The electromodulation component contains a weak negative peak below the transition energy, a main peak in the region of transition, and high-energy oscillations called the Franz–Keldysh oscillations. The period of the latter in terms of the electrooptical energy is defined by the strength of the surface electric field [10]. The effect of the energy broadening Γ manifests itself in the decay of the signal and flattening of the main peak. It is well known that, for $\Gamma' > 1$, the oscillations disappear and the spectrum is transformed into a resonance structure, which consists of positive and negative extrema (the so-called low-field case) [3]. In this case, the informativeness of the spectrum decreases drastically.

The Aspnes model was developed on the assumption of electric field homogeneity in the region of origination of the electromodulation signal. At the same time, the decay of the surface electric field in the space-charge region leads to the depth dependence of the complex permittivity. The effect of a decaying electric field on the shape of the electromodulation component is characterized by the ratio of the depth of light penetration $d_L(E)$ to the skin depth d_F. For $d_F \gg d_L$, the variation of the permittivity across the entire depth of light penetration is virtually constant. Thus, the spectra can be simulated under the assumption that $F =$ const. This condition is no longer valid for $d_F \leq d_L$. Since this inequality holds for direct gap semiconductors near the fundamental transition for practically significant charge carrier densities ($n > 10^{15}$ cm^{-3}), the inhomogeneity of the electric field has to be taken into account.

The problem of calculating the electromodulation signal in a spatially inhomogeneous medium was solved by Gobrecht and coauthors in the context of the multilayer model. In this model, the surface layer of the semiconductor is divided into j plane-parallel layers. The field F_ν is assumed to be constant within each layer. Then the complex refractive index $\bar{n}_\nu(n, k)$ in each layer ν is defined as

$$\bar{n}_\nu = \bar{n}(F = 0, E) + \Delta\bar{n}_\nu(F_\nu, E). \quad (9)$$

Let us assume that $\Delta\varepsilon_1$ and $\Delta\varepsilon_2$ are the changes of the real and imaginary parts of the complex permittivity induced by the electric field. Then, we obtain for the layer ν

$$\Delta\bar{n}_\nu = \frac{n\Delta\varepsilon_{1\nu} + k\Delta\varepsilon_{2\nu} - i(n\Delta\varepsilon_{2\nu} - k\Delta\varepsilon_{1\nu})}{2(n^2 + k^2)}, \quad (10)$$

where $\Delta\varepsilon_1$ and $\Delta\varepsilon_2$ are calculated in the model through the use of the unbroadened electrooptic functions $F_\nu(F_{\nu,0})$ and $G_\nu(F_{\nu,0})$.

Thus, the space charge region in the multilayer model is represented by a system of homogeneous, plane-parallel, and isotropic layers with different complex refractive indices. The amplitude of the reflected wave $\bar{r}_0$ can be calculated by considering multiple reflections in the system of plane-parallel layers. This amplitude is defined by the recursion formula

$$\bar{r}_{\nu-1} = \frac{\bar{f}_{\nu-1} + \bar{r}_\nu \exp(-2i\varphi_\nu)}{1 + \bar{f}_{\nu-1}\bar{r}_\nu \exp(-2i\varphi_\nu)} \quad (11)$$

with

$$\varphi_\nu = 2\pi(d_\nu/\lambda)(\bar{n} + \Delta\bar{n}_\nu). \quad (12)$$

The Fresnel coefficients for the interface between the layers ν, $\nu - 1$ and j, $j - 1$ are calculated by the formulas

$$\bar{f}_{\nu-1} = \frac{\Delta\bar{n}_{\nu-1} - \Delta\bar{n}_\nu}{2\bar{n} + \bar{n}_{\nu-1} + \bar{n}_\nu}, \quad \bar{r}_j = \frac{\Delta\bar{n}_j}{2\bar{n} + \Delta\bar{n}_j}. \quad (13)$$

For the latter coefficient at the semiconductor–air interface, we have

$$\bar{f}_0 = \frac{\bar{n}_L - (\bar{n} + \Delta\bar{n}_1)}{\bar{n}_L + (\bar{n} + \Delta\bar{n}_1)}, \quad \bar{n}_L = 1, \quad (14)$$

where the coefficient $\bar{n}_L$ is the refractive index of air. In this case, the electroreflectance signal is calculated from the formula

$$\frac{\Delta R}{R}(E) = \frac{|r_0|^2 - \mathrm{Re}(R_0)}{\mathrm{Re}(R_0)}, \quad (15)$$

$$R_0 = \left(\frac{\bar{n} - \bar{n}_L}{\bar{n} + \bar{n}_L}\right)^2. \quad (16)$$

The results of calculations in the context of the multilayer model are shown in Fig. 2. As can be seen, consideration of the inhomogeneity of the electric field gives rise to a negative low-energy peak, a flattening and energy shift of the main peak, and additional damping of the Franz–Keldysh oscillations.

For comparison with the model calculations, the experimental E_0-spectrum of photoreflectance typical of GaAs samples with moderate doping is shown by the solid line in Fig. 3. The phase analysis of the spectrum [11] shows that it contains only a single electromodulation component, E_0. The additional structure in the region of the low-energy shoulder of the main peak and the rapidly damped Franz–Keldysh oscillations are the specific features of this spectrum. Simulation of this spectrum in the context of the models discussed above is impossible, since they reproduce neither the additional structure in the region of the main peak nor the rapid damping of the Franz–Keldysh oscillations.

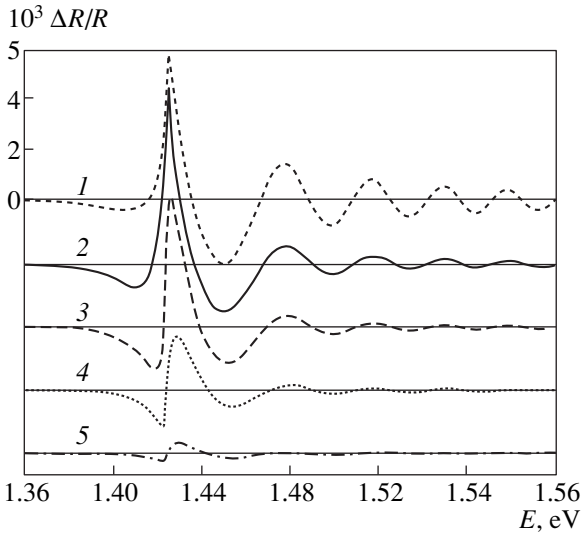

Fig. 2. Electromodulation components calculated in the context of the multilayer model for various skin depths (d_F) of the electric field with the strength $F = 4 \times 10^6$ V/m and $\Gamma = 0$: d_F = (*1*) 1000, (*2*) 100, (*3*) 50, (*4*) 20, and (*5*) 10 nm.

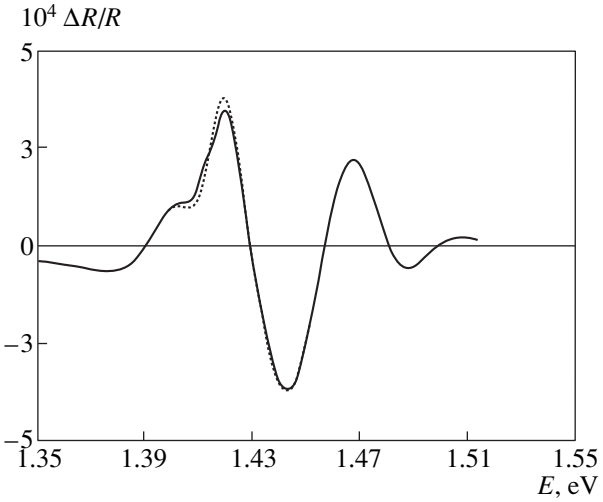

Fig. 3. Experimental E_0-spectrum of photoreflectance of *n*-GaAs with $n = 10^{16}$ cm^{-3} (solid line) and the result of its simulation in the context of the generalized multilayer model (dashed line).

GENERALIZED MULTILAYER MODEL

There is no way to reproduce the experimental spectral features in the context of the models discussed above. This leads us to the conclusion that these theoretical models do not account for a number of physical effects that affect the formation of the modulation spectrum. The experience that has accumulated over more than 30 years since the emergence of modulation spectroscopy allows one to suggest the following effects as possible reasons for the disagreement between the exper-

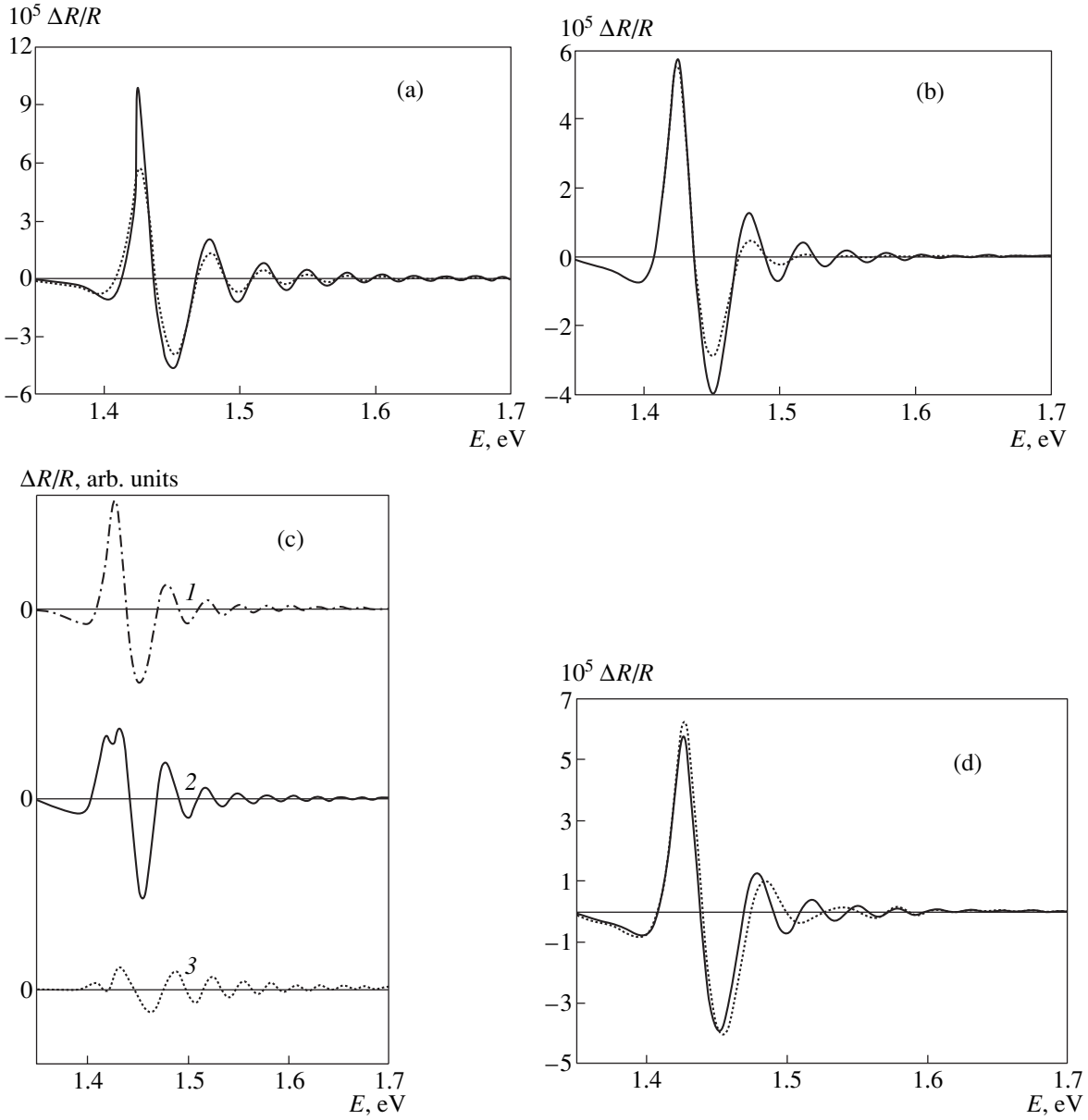

Fig. 4. Electromodulation components calculated in the context of the generalized multilayer model for the following simulation parameters: E_0 = 1.424 eV, $F = 4 \times 10^6$ V/m, d_F = 150 nm, and (a) Γ = 0 meV (solid line), Γ = 6 meV (dashed line); (b) constant Γ = 6 meV (solid line), energy-dependent $\Gamma(E) = 0.006 + 0.1(E - 1.424)$ (dashed line); (c) Γ = 6 meV, ξ = (*1*) 1, (*2*) 0.5, and (*3*) 0.05; (d) Γ = 6 meV, ξ = 1, $a_{lh}/a_{hh} = 0$ (solid line), and $a_{lh}/a_{hh} = 0.5$ (dashed line).

imental spectra and the results of simulation with the Aspnes and Gobrecht models:

incomplete suppression of the surface electric field (partial modulation) [12];

spectral broadening Γ and the dependence of the broadening energy on the photon energy [13–15]; and

neglect of the degeneracy of the band structure [16].

The multilayer model was chosen as a basis for consideration of the effects mentioned above. This choice is due to the fact that the multilayer model is based on first principles, i.e., on the electric-field-induced change of the permittivity and interference in a multilayer system.

A. Consideration of Broadening

Unbroadened electrooptical functions are used by Gobrecht and coauthors in the multilayer model. The broadening can be introduced into the model using the broadened electrooptic functions F and G (8). The inclusion of broadening leads to the flattening and energy shift of the negative low-energy peak, as well as a positive main peak, and to additional damping of the Franz–Keldysh oscillations (see Fig. 4a).

B. Energy Dependence of the Broadening Parameter

The electrooptical energy represents the additional energy acquired by a quantum particle in an electric field. Thus, the high-energy limit of the Franz–Keldysh oscillations observed in the experiment can be explained to a first approximation by the existence of some scattering mechanism with a scattering time τ. We define δE as the energy separation of the last oscillation and the transition energy, and we assume that the scattering time is independent of the electric field strength. In this case, the propagation range of the Franz–Keldysh oscillations can be defined as [13]

$$\delta E = \frac{(eF\tau)^2}{2m}. \quad (17)$$

The electroreflectance measurements performed previously [13] show that, as the strength of the surface electric field increases, the region of observation of the Franz–Keldysh oscillations is extended to the high energies. This extension is described by a linear dependence rather than by a square law, as one might expect from the relationship (17). This means that damping of the Franz–Keldysh oscillations cannot be described with the constant broadening parameter and requires the introduction of the energy dependence $\Gamma(E)$. The increased probability of the scattering of charge carriers excited to the higher states in the energy bands was considered [14] as a possible reason for the energy dependence $\Gamma(E)$. In this case, the following empirical dependence was proposed [14]:

$$\Gamma(E) = \Gamma_0 \exp[a(E - E_0)], \quad E > E_0. \quad (18)$$

An alternative possibility consists in the employment of the linear dependence [15]

$$\Gamma(E) = \Gamma_0 + a(E - E_a), \quad E_a \geq E_0. \quad (19)$$

The introduction of the dependence $\Gamma(E)$ enables the high-energy Franz–Keldysh oscillations to be efficiently damped (see Fig. 4b). In this way, one of the major contradictions of the simulated and experimental spectra is eliminated.

C. Consideration of the Partial Modulation of the Surface Electric Field on Exposure to Light

The effect of partial modulation of the surface electric field has long been known in electroreflectance spectroscopy. However, for a long time, the surface electric field in photoreflectance spectroscopy was assumed to be completely suppressed at a reasonably high illumination level of the semiconductor surface. This assumption was based on the hypothesis that the drift of the minority charge carriers to the surface and their recombination with the majority carriers captured by the surface states constituted the mechanism responsible for the modulation of the surface electric field. This mechanism provides complete suppression of the surface electric field if there is a sufficient number of nonequilibrium minority charge carriers. However, this assumption is not supported by the experimental data [12, 17]. The existence of a different process, along with the drift and capture of the minority charge carriers by the surface states, was demonstrated in studies of the photoreflectance dynamics [12]. This compensating process consists in the capture of the majority charge carriers thermally emitted from the bulk of a semiconductor by the surface states. The lower the height of the surface potential barrier, the more active this process. The relation between the two competing processes defines the modulation level of the surface field.

Thus, in the simulation of the electromodulation component, consideration must be given to partial modulation of the surface field. The transformation which follows demonstrates how the spectrum may be simulated in the case of the partial modulation $F_i \longrightarrow F_f$ using the formalism of the complete modulation. We define the level of modulation of the surface electric field as

$$\xi = (F_i - F_f)/F_i, \quad 0 \leq \xi \leq 1. \quad (20)$$

Then, the electromodulation component is defined as

$$\frac{\Delta R}{R}(E, F_i, F_f)$$

$$= \frac{1}{R}[R(E, F_i) - R(E, 0) - R(E, F_f) + R(E, 0)] \quad (21)$$

$$= \frac{\Delta R}{R}(E, F_i) - \frac{\Delta R}{R}(E, F_f).$$

The skin depth d_f of the electric field F_f is defined in the Schottky approximation as

$$d_f = F_f d_i / F_i. \quad (22)$$

Consideration of the partial modulation in the mathematical formalism of the multilayer model gives rise to an additional structure in the region of the main peak (see Fig. 4c). However, its appearance in the spectrum depends on the broadening parameter Γ used in the calculations. We discovered the following law: the higher the value of Γ, the smaller the values ξ at which the additional structure is observable.

D. Consideration of the Band-Structure Degeneracy

Such direct gap semiconductors as GaAs, InP, and the like are characterized by degeneracy of the valence band in the region of the fundamental transition. As a result, two subbands with equal transition energies occur for heavy ($|3/2, \pm 3/2\rangle$) and light ($|3/2, \pm 1/2\rangle$) holes. In most of the models suggested thus far, either this circumstance is ignored due to a smaller matrix element of the transition for the light hole subband (in this case, only the transition from the heavy hole subband is considered) or the averaged hole effective mass is introduced into the simulation to take into account the existence of two subbands [18]. However, the beats of the

Parameters of the generalized multilayer model determined from the quantitative analysis of the photoreflectance spectra of moderately doped GaAs and InP substrates ($n = 10^{15}$–10^{18} cm^{-3})

Parameter	GaAs		InP	
Carrier density, cm^{-3}	10^{15}	10^{18}	10^{15}	10^{18}
Transition energy E_0, eV	1.422–1.425	1.408–1.420	1.343–1.345	1.330–1.340
Energy broadening Γ, meV	0.1–5	30–100	0.1–3	30–80
Electric field strength F, V/m	10^6–3×10^6	2×10^7–4×10^7	7×10^5–1×10^6	2×10^7–3×10^7
Ratio of the amplitudes a_{lh}/a_{hh}	0.3–0.7		0.1–0.3	
Modulation level ξ for the density of laser excitation of 10 W/cm^2	0.4–1		0.7–1	
Skin depth d_F, nm	800	10	600	10

Franz–Keldysh oscillations observed by van Hove [16] testify that both of these approximations are incorrect.

The degeneracy of the valence band implies the existence of two electron optical transitions from the heavy and light hole subbands and, thus, of two electromodulation components in the E_0-spectrum:

$$\frac{\Delta R}{R}(E) = a_{hh}\frac{\Delta R}{R}(E)_{hh} + a_{lh}\frac{\Delta R}{R}(E)_{lh}. \qquad (23)$$

Both of the transitions have the same energy but different matrix elements a_{lh} and a_{hh} ($a_{hh} > a_{lh}$), which account for different probabilities of the optical transitions from the light- and heavy hole subbands to the conduction band and define the absolute amplitudes of the components. The difference between the reduced electron–hole masses $\mu_{\parallel}^{e-lh}$ and $\mu_{\parallel}^{e-hh}$ leads to a small distinction between electrooptic energies for both subbands, which manifests itself in different periods of the Franz–Keldysh oscillations. For a reasonably large value of the parameter a_{lh}/a_{hh} ($a_{lh}/a_{hh} > 0.4$), the beats can be observed in the region of the high-energy Franz–Keldysh oscillations (see Fig. 4d).

The comparison of the simulated spectra (see Figs. 4a–4d) allows the three spectral regions to be distinguished according to the specific features of the spectral lines:

1. The low-energy region of the negative $\Delta R/R$ preceding the first (main) peak in the spectrum. The degree of inhomogeneity of the near-surface electric field can be inferred from the extent to which this region affects the spectral structure.

2. The region of the main peak. The main peak at low levels of modulation of the surface field can be so radically modified that additional spectral structures can arise even in the region of this peak. These structures are sometimes erroneously interpreted as the result of superposition of the low-energy spectral components.

3. The region of high-energy Franz–Keldysh oscillations.

The effect of the simulation parameters can be either restricted to one of these regions or extended to all three spectral regions discussed.

A comparison of the simulated spectra allows one to infer that the variation of just one of the parameters may strongly affect the resulting shape of the moderate-field component. Different combinations of parameters will sometimes result in the same effect and, as a consequence, in similar spectral structures. For example, damping of the high-energy Franz–Keldysh oscillations can be caused both by the dependence of the broadening parameter on the photon energy and by the superposition of the electromodulation components corresponding to the transitions from different subbands. Nevertheless, the results of the quantitative analysis of the experimental spectra performed by us in the context of the discussed model appear to be unambiguous if the experimental E_0-spectrum contains only electromodulation components of E_0 subbands (such a spectrum is perceived as a single-component one) and the resulting spectral structure exhibits at least two pronounced Franz–Keldysh oscillations.

ANALYSIS OF THE EXPERIMENTAL SPECTRA IN THE CONTEXT OF THE GENERALIZED MULTILAYER MODEL

More than 100 experimental single-component E_0-spectra of photoreflectance were analyzed by us in the context of the outlined model. These spectra were measured at room temperature using GaAs and InP substrates with various dopants and charge-carrier densities in the range $n = 10^{15}$–10^{18} cm^{-3}. Nearly perfect agreement of the simulated and experimental spectral structures is achieved in most cases. In other cases, the disagreement is only slight. The use of the linear dependence $\Gamma(E)$, at least for GaAs, was found to provide the best fit to the experimental spectra. The representative result of the simulation performed is shown in Fig. 3. We performed the simulation of the spectra both manually by choice of the parameters and by the algorithm of nonlinear regression. The latter procedure was found to be efficient only if the starting value of the electric field strength was not too different from the true one.

The ranges of the experimental parameters of the GaAs and InP samples studied were determined by comparison of the results of quantitative analysis (see table). The results correlate well with the published

data for similar samples gained by different experimental techniques [19].

CONCLUSION

In this paper, we showed that a realistic model describing the spectral shape of the electromodulation component has to take into account such parameters as the transition energy, electric-field strength, modulation level of the field, skin depth, energy broadening, its dependence on the photon energy, and the ratio of the amplitudes for heavy- and light-hole subbands. The proposed generalized multilayer model was developed on the basis of the multilayer model of Gobrecht and coauthors by considering a number of parameters mentioned above that were missing in the initial model. The model was verified by quantitative analysis of the experimental photoreflectance spectra of GaAs and InP substrates with the charge carrier densities in the range $n = 10^{15}$–10^{18} cm^{-3}. The ranges of parameters of the multilayer model for the samples studied were determined from a comparison of the results of quantitative analysis. We may conclude from the results that the generalized multilayer model proposed in this paper provides an accurate description of the real spectral structures obtained by electromodulation and photomodulation spectroscopy.

REFERENCES

1. M. Cardona, *Modulation Spectroscopy* (Academic, New York, 1969; Mir, Moscow, 1972).
2. P. Lautenschlager, M. Garriga, S. Logothetidis, and M. Cardona, Phys. Rev. B **35**, 9174 (1987).
3. D. E. Aspnes, Surf. Sci. **37**, 418 (1973).
4. R. L. Tober and J. D. Bruno, J. Appl. Phys. **68**, 6388 (1990).
5. S. F. Pond and P. Handler, Phys. Rev. B **8**, 2869 (1973).
6. R. Kuz'menko, A. Ganzha, J. Schreiber, and S. Hildebrandt, Fiz. Tverd. Tela (St. Petersburg) **39**, 2123 (1997) [Phys. Solid State **39**, 1900 (1997)].
7. D. E. Aspnes, Phys. Rev. **147**, 554 (1966).
8. D. E. Aspnes, Phys. Rev. **153**, 972 (1967).
9. B. O. Seraphin and N. Bottka, Phys. Rev. **145**, 628 (1966).
10. D. E. Aspnes, Phys. Rev. B **10**, 4228 (1974).
11. A. Ganzha, W. Kircher, R. Kuz'menko, *et al.*, Fiz. Tekh. Poluprovodn. (St. Petersburg) **32**, 272 (1998) [Semiconductors **32**, 245 (1998)].
12. H. Shen, M. Dutta, R. Lux, *et al.*, Appl. Phys. Lett. **59**, 321 (1991).
13. A. Jaeger, G. Weiser, and P. Wiedemann, IEEE J. Sel. Top. Quantum Electron. **1**, 1113 (1995).
14. J. M. A. Gilman, A. Hamnett, and R. A. Batchelor, Phys. Rev. B **46**, 13363 (1992).
15. U. Behn and H. Roeppischer, J. Phys. C **21**, 5507 (1988).
16. C. van Hoof, K. Deneffe, J. de Boeck, *et al.*, Appl. Phys. Lett. **54**, 608 (1989).
17. T. Kanata, M. Matsunaga, H. Takakura, *et al.*, J. Appl. Phys. **69**, 3691 (1991).
18. P. L. Jackson and E. G. Seebauer, J. Appl. Phys. **69**, 943 (1991).
19. Landolt-Börnstein: *Numerical Data and Functional Relationships in Science and Technology* (Springer-Verlag, Berlin, 1984).

Translated by Yu. Aleshchenko

Semiconductors, Vol. 34, No. 9, 2000, pp. 1052–1053. Translated from Fizika i Tekhnika Poluprovodnikov, Vol. 34, No. 9, 2000, pp. 1093–1094.

ELECTRONIC AND OPTICAL PROPERTIES OF SEMICONDUCTORS

Thermal EMF in a Bipolar Semiconductor with Phonon Drag of Carriers

A. Konin and R. Raguotis

Institute for Physics of Semiconductors, Vilnius, 2600 Lithuania

Submitted January 27, 2000; accepted for publication March 16, 2000

Abstract—An expression is derived for thermal emf in a semiconductor sample for small deviations of the carrier concentrations from the equilibrium values and an arbitrary extent of the phonon drag of electron–hole pairs. With thermal drag, the thermal emf changes substantially in a sample of arbitrary dimensions. Under certain conditions, the thermal emf sign may also change. © *2000 MAIK "Nauka/Interperiodica".*

It was shown previously [1] that calculation of the thermal emf of a bipolar semiconductor differs fundamentally from the case of a monopolar semiconductor. The theoretical model [1] generalized in [2] confirmed the dependence of the thermal emf on surface parameters of a semiconductor in a sample of arbitrary dimensions.

However, the above publications investigated the case in which there is no influence of the anisotropic part of the phonon distribution function on the anisotropy of electron and hole distributions, i.e., on the thermal phonon drag of electron–hole pairs [3]. This is true for wide-gap semiconductors at relatively high temperatures [3]. In narrow-gap semiconductors, substantial thermal drag is quite possible at relatively low temperatures and weak phonon scattering by defects, resulting in an increase in the thermoelectric power for electrons and holes [4]. This, in turn, must change the thermal emf.

This study is aimed at extending the theoretical model [2] to the case of thermal phonon drag of electron–hole pairs.

In what follows, we consider the temperature range in which the condition $\nu_{ff} \gg \nu_{fe}$ is met [3], where ν_{ff} and ν_{fe} are the phonon–phonon and phonon–carrier collision frequencies, respectively. In this case, the system of kinetic equations for electrons, holes, and phonons is solved analytically [3] and thermal drag occurs provided that

$$B_{(n)p} = \frac{es^2}{\mu_{n(p)}kT\nu_{fd}} \gg 1, \tag{1}$$

where $B_{n(p)}$ is the drag factor for electrons (holes), $\mu_{n(p)}$ is the mobility of electrons (holes), e is the hole charge, s is the speed of sound in the semiconductor, k is the Boltzmann constant, T is the lattice temperature, and ν_{fd} is the frequency of phonon–defect collisions.

Let us consider a semiconductor wafer whose $x = a$ surface is in thermal contact with a thermostat having temperature T_2 and whose $x = -a$ surface is in contact with a thermostat maintaining the temperature T_1. We assume that the sample thickness substantially exceeds the cooling length for electrons and holes [5]. Then the temperatures of all quasiparticles coincide [6] and

$$T(x) = T_0 + \Delta T\frac{x}{2a}, \tag{2}$$

where $T_0 = (T_1 + T_2)/2$, $\Delta T = T_2 - T_1$ and $2a$ is the sample thickness.

According to [2], determination of thermal emf amounts to solving the system of equations

$$\frac{1}{e}\frac{dj_n^x}{dx} - \frac{\delta n}{\tau_n} = 0, \quad \frac{1}{e}\frac{dj_p^x}{dx} + \frac{\delta p}{\tau_p} = 0,$$
$$\frac{d^2(\delta\varphi)}{dx^2} = \frac{e}{\varepsilon\varepsilon_0}(\delta n - \delta p) \tag{3}$$

with the boundary conditions

$$\frac{1}{e}j_n^x\Big|_{x=\pm a} = \mp S_n^{\pm}\delta n|_{x=\pm a}, \quad \frac{1}{e}j_p^x\Big|_{x=\pm a} = \pm S_p^{\pm}\delta p|_{x=\pm a},$$
$$\frac{1}{e}(\xi_p^{\pm}\delta F_p - \xi_n^{\pm}\delta F_n)\Big|_{x=\pm a} = (\xi_n^{\pm} + \xi_p^{\pm})(\varphi_{\pm} - \delta\varphi)\Big|_{x=\pm a}. \tag{4}$$

Here j_n^x and j_p^x are the electron and hole current densities; δn, δp, δF_n, and δF_p are the nonequilibrium concentrations and the corresponding electron and hole chemical potentials; $S_{n,p}^{\pm}$ are the surface-recombination rates for the same quasiparticles; $\xi_{n,p}^{\pm} = \lim_{x\to\pm a}\sigma_{n,p}$ are the surface conductivities due to electrons and holes; $\delta\varphi$ is the electric potential due to nonequilibrium carriers; $\varphi_+ = \varphi(a + 0)$, $\varphi_- = \varphi(-a - 0)$; and $\tau_{n,p}$ is the lifetime of nonequilibrium electrons (holes).

1063-7826/00/3409-1052$20.00 © 2000 MAIK "Nauka/Interperiodica"

In an approximation linear in ΔT, the expressions for the electron and hole currents have the form [1, 4]

$$j_n^x = en_0\mu_n\left[\frac{1}{e}\frac{d}{dx}(\delta F_n - e\delta\varphi) - \tilde{\alpha}_n\frac{\Delta T}{2a}\right],$$
$$j_p^x = -ep_0\mu_p\left[\frac{1}{e}\frac{d}{dx}(\delta F_p + e\delta\varphi) + \tilde{\alpha}_p\frac{\Delta T}{2a}\right], \quad (5)$$

where $\tilde{\alpha}_{n,p}$ are the thermoelectric powers with regard to the phonon drag of electron–hole pairs. In a nondegenerate semiconductor,

$$\tilde{\alpha}_n = -\frac{k}{e}\left(q_n + \frac{5}{2} - \frac{F_n}{kT} + B_n\right),$$
$$\tilde{\alpha}_p = \frac{k}{e}\left(q_p + \frac{5}{2} - \frac{F_p}{kT} + B_p\right), \quad (6)$$

where q_n and q_p are parameters characterizing the mechanisms of electron and hole momentum relaxation [3], with q_n commonly equal to q_p; $F_{n,p}$ are the chemical potentials for the same quasiparticles; and $\xi^+_{n,p} = \xi^-_{n,p} = \xi_{n,p}$.

Further, we consider the case of minor deviations of carrier concentrations from equilibrium values n_0 and p_0: $\delta n \ll n_0$ and $\delta p \ll p_0$. In this case, $\delta F_n = kT\delta n/n_0$ and $\delta F_p = kT\delta p/p_0$. In addition, we assume for simplicity that the boundary conditions are symmetric; i.e., $S_n^+ = S_n^- = S_n$, $S_p^+ = S_p^- = S_p$, $\xi_n^+ = \xi_n^- = \xi_n$, $\xi_p^+ = \xi_p^- = \xi_p$.

Solving Eqs. (3)–(5), we obtain for the thermal emf $\Delta\varphi = \varphi_+ - \varphi_-$

$$\Delta\varphi = -D^{-1}\Delta T[(1+\theta)(\tilde{\alpha}_n + \beta\eta\gamma\tilde{\alpha}_p) + (\tilde{\alpha}_n - \tilde{\alpha}_p)(\beta\gamma\eta - \theta)u^{-1}\tanh u + (1+\beta)(\tilde{\alpha}_n\nu_p + \gamma\eta\theta\tilde{\alpha}_p\nu_n)\tanh u], \quad (7)$$

where

$$D = (1+\theta)(1+\beta\gamma\eta) + (1+\beta)(\nu_p + \gamma\eta\theta\nu_n)\tanh u,$$

$\beta = p_0/n_0$, $\gamma = \mu_p/\mu_n$, $\eta = \tau_p/\tau_n$, $\theta = \xi_p/\xi_n$, $u = a/\lambda$, $\nu_{n,p} = S_{n,p}\tau_{n,p}/\lambda$, and λ is the diffusion length [2].

As can be seen from (6), the phonon drag of electron–hole pairs results in an increase in the thermoelectric powers $\tilde{\alpha}_n$ and $\tilde{\alpha}_p$ and, consequently, in a change in the thermal emf (7), with μ_n often not being equal to μ_p. Therefore, changes in $\tilde{\alpha}_n$ and $\tilde{\alpha}_p$ are variable. For example, in InSb, $B_p \approx 100B_n$ and, at $B_n = 1$–$5|\tilde{\alpha}_p| \gg |\tilde{\alpha}_n|$, whereas, in the absence of drag, $|\tilde{\alpha}_p| \approx |\tilde{\alpha}_n|$.

To conclude, we note that, in this study, the thermal emf was determined at small deviations of carrier concentrations from the equilibrium values. At the same time, it is known [4] that, in an intrinsic semiconductor, the drag may cause a substantial redistribution of the electron–hole-pair concentration across the sample thickness. This markedly changes the carrier chemical potentials and, consequently [1], the thermal emf.

REFERENCES

1. Yu. G. Gurevich, O. Yu. Titov, G. N. Logvinov, and O. I. Lyubimov, Phys. Rev. B **51**, 6999 (1995).
2. A. M. Konin and R. Raguotis, Semicond. Sci. Technol. (in press).
3. F. G. Bass, V. S. Bochkov, and Yu. G. Gurevich, *Electrons and Photons in Bounded Semiconductors* (Nauka, Moscow, 1984).
4. A. M. Konin, Fiz. Tekh. Poluprovodn. (St. Petersburg) **31**, 692 (1997) [Semiconductors **31**, 590 (1997)].
5. F. G. Bass, V. S. Bochkov, and Yu. G. Gurevich, Fiz. Tekh. Poluprovodn. (Leningrad) **7**, 3 (1973) [Sov. Phys. Semicond. **7**, 1 (1973)].
6. V. S. Bochkov and Yu. G. Gurevich, Fiz. Tekh. Poluprovodn. (Leningrad) **17**, 728 (1983) [Sov. Phys. Semicond. **17**, 456 (1983)].

Translated by M. Tagirdzhanov

Semiconductors, Vol. 34, No. 9, 2000, pp. 1054–1057. Translated from Fizika i Tekhnika Poluprovodnikov, Vol. 34, No. 9, 2000, pp. 1095–1098.

SEMICONDUCTOR STRUCTURES, INTERFACES, AND SURFACES

Electrical Conductivity of Silicon-on-Insulator Structures Prepared by Bonding Silicon Wafers to a Substrate Using Hydrogen Implantation

I. V. Antonova, V. F. Stas', V. P. Popov, V. I. Obodnikov, and A. K. Gutakovskiĭ

Institute of Semiconductor Physics, Siberian Division, Russian Academy of Sciences, pr. akademika Lavrent'eva 13, Novosibirsk, 630090 Russia

Submitted February 9, 2000;
accepted for publication February 28, 2000

Abstract—Silicon-on-insulator structures were prepared by exfoliating a thin layer from a silicon wafer owing to hydrogen implantation, transferring this layer to another substrate, and bonding to it. The influence of hydrogen and the doping level in the original wafers on the free-carrier concentration and the conductivity type in the split-off silicon layer was investigated. A high boron concentration in the original material, together with a high concentration of residual hydrogen in the silicon layer exfoliated from the wafer, was shown to result in *n*-type conduction, which is retained up to annealing temperatures of 1100°C in these structures. A decrease in the residual hydrogen concentration owing to additional annealing creates the conditions under which the conductivity of resulting structures corresponds to the conductivity type of the original material. © *2000 MAIK "Nauka/Interperiodica".*

1. INTRODUCTION

Currently, the technology of bonding silicon wafers with their preliminary exfoliation over a hydrogen-implanted layer is a promising method of preparing silicon-on-insulator (SOI) structures with thin silicon layers [1, 2]. The method of preparing the SOI structures used in this study represents a variant of the known Smart-Cut method based on exfoliating a thin silicon film from a wafer owing to hydrogen implantation, annealing at relatively low temperatures, and transferring the exfoliated film to another substrate. As a rule, the temperature of foliation is 400–600°C. The subsequent annealing of the SOI structure at a temperature of ~1100°C makes it possible to reinforce the bonds between the transferred film and the substrate and also to remove the radiation defects and hydrogen still retained in the split-off silicon layer. The purpose of this study is to investigate the influence of residual hydrogen on the electrical conductivity of the split-off silicon layer in SOI structures.

2. EXPERIMENTAL PROCEDURE

The wafers used to prepare the SOI structures were 100 μm thick and produced from *p*-type silicon grown by the Czochralski method (Cz-Si). The wafers were of two types according to the doping level: with hole concentrations of 2×10^{18} and 2×10^{15} cm^{-3}. In Table 1, we list certain parameters of the original material. The H_2^+ ions were implanted in the dose range of (4–6) × 10^{16} cm^{-2}, and the ion energy was 110 keV, which corresponded to the ion range of 0.5 μm. The temperature of splicing (bonding) was 450°C. For exfoliating the film from the donor wafer and transferring it to the substrate, a time of 15–20 min was sufficient; however, the actual annealing time amounted to 0.5 and 3 h at 450°C (Table 2). Henceforth, we will refer to this time as the bonding time. Usually, as a final operation in the preparation of the SOI structures, annealing is performed at 1100°C, which makes it possible to reinforce the bonds between the transferred film and the substrate and to

Table 1. Basic parameters of the original material

Original Si	Conductivity type	Carrier concentration, cm^{-3}	Oxygen concentration, cm^{-3}	Mobility, cm^2/(V s)	Orientation
Cz–Si–1	*p*	2×10^{15}	7×10^{17}	350	⟨100⟩
Cz–Si–2	*p*	2×10^{18}	8×10^{17}	106	⟨111⟩

1063-7826/00/3409-1054$20.00 © 2000 MAIK "Nauka/Interperiodica"

Table 2. Combination of wafers used to prepare the SOI structures, the bonding conditions, and the conductivity type of the split-off silicon layer

Structure	Designation	Bonding conditions	Conductivity type	
			after bonding	after annealing at 1100°C
Cz–Si–1/SiO_2/*Cz*–Si–1	SOI–I	450°C, 0.5 h	*n*	*n*
Cz–Si–2/SiO_2/*Cz*–Si–1	SOI–II	450°C, 0.5 h	*n*	*n*
Cz–Si–1/SiO_2/*Cz*–Si–1	SOI–III	450°C, 3 h	*n*	*p*
Cz–Si–2/SiO_2/*Cz*–Si–1	SOI–IV	450°C, 3 h	*p*	*p*

Note: The SiO_2-layer thickness is 4000 Å.

remove the radiation defects and hydrogen still retained in the split-off silicon layer. However, according to the purpose of this study, we annealed the bonded wafers isochronously for 30 min in the temperature range of 450–1100°C. For the investigations, we used the methods of the Hall-effect measurement, the capacitance–voltage (*C–V*) characteristics, secondary-ion mass spectrometry (SIMS), and transmission electron microscopy (TEM). In the course of the *C–V* measurements, a barrier on the surface of the split-off silicon layer was formed by a mercury probe. The other contact was also formed on the film surface and had a radial symmetry with respect to the probe. Several measurements were carried out with wafers irradiated with hydrogen and subjected to thermal treatment under the same conditions as the SOI structures.

3. RESULTS

In Fig. 1 and Table 2, we give the results of determining the conductivity type and of measuring the mobile-carrier concentration (*N*) (Hall-effect method) in the split-off silicon layer as a function of the annealing temperature T_a of an SOI structure prepared from wafers with various levels of doping using two bonding times. It can be seen that, for a bonding time of 30 min (SOI-I, SOI-II), the *p*-type conduction in the original material changes to *n*-type conduction in the split-off silicon layer and is retained up to an annealing temperature of T_a = 1100°C. A high boron concentration in the original material leads to a higher electron concentration in the silicon film. The carrier mobility in the split-off layer produced from a low-doped original material amounts to 440 $cm^2/(V\ s)$. Values of the mobility in the original material are listed in Table 1.

For a prolonged bonding regime (SOI-III,IV), *n*-type conduction can manifest itself only for annealing temperatures below 500°C. At higher annealing temperatures, *p*-type conduction is observed with a concentration close to that in the original material, especially when heavily doped original material is used. In the last case, the mobility of the charge carriers amounts to 80 $cm^2/(V\ s)$ (106 $cm^2/(V\ s)$ in the original material).

In Fig. 2, we show the depth distribution of electrons in the split-off silicon layer for the SOI-II structure obtained from the *C–V* measurements. For all annealing temperatures, the carrier concentration in the silicon film increases as the surface or the Si/SiO_2 boundary is approached. At the same time, we observed a decrease in electron concentration for a film at reasonably high temperatures.

In Fig. 3, we show the hydrogen distributions measured by SIMS in the SOI structures immediately after bonding and subsequent annealing at various temperatures. The bonding time amounts to 2 h in these structures. The hydrogen concentration in the SOI structure after bonding is fairly high and decreases below the

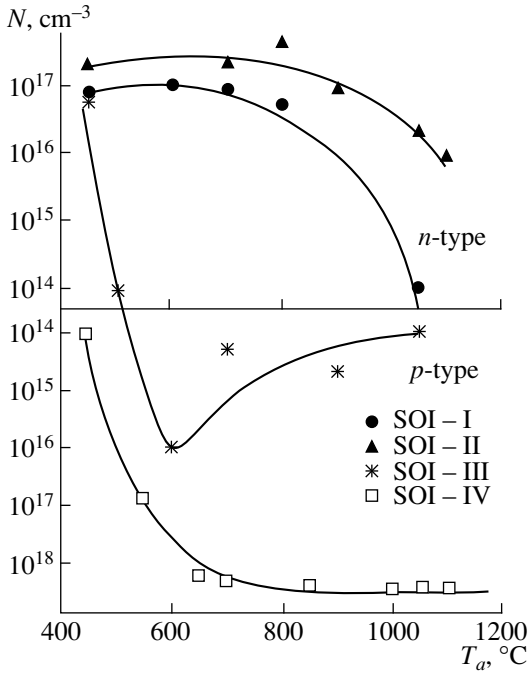

Fig. 1. Concentration (*N*) of the charge carriers according to the Hall measurements in the split-off layer of SOI structures obtained using original wafers with a boron concentration of 2×10^{18} (SOI-II,IV) and 2×10^{15} cm^{-3} (SOI-I,III) as a function of annealing temperature T_a. The bonding was performed at 450°C for 0.5 (SOI-I,II) and 3 h (SOI-III,IV).

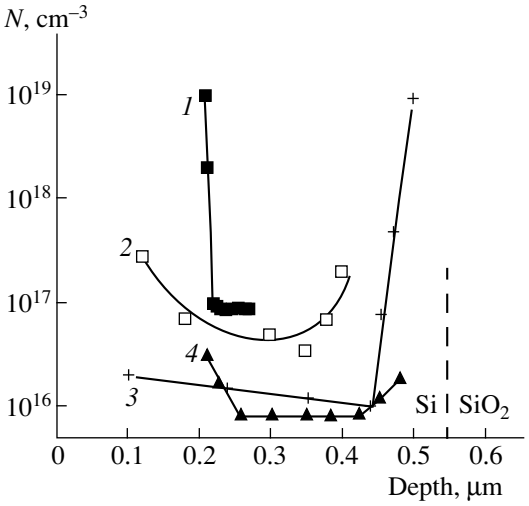

Fig. 2. Depth distribution of the electron concentration for SOI-II (*1*) after bonding and subsequent annealing for 30 min at T_a = (*2*) 900, (*3*) 1050, and (*4*) 1100°C.

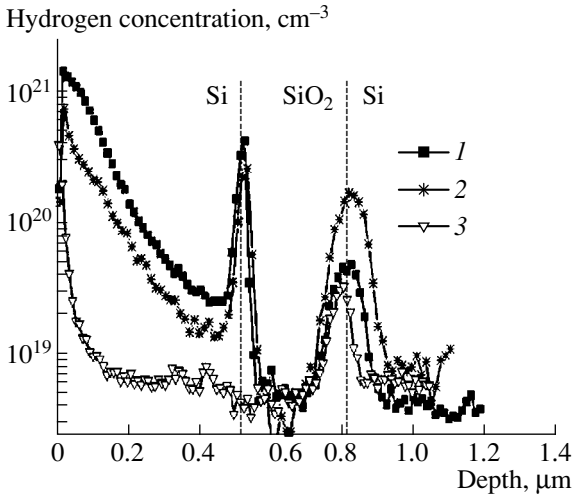

Fig. 3. Depth distribution of the hydrogen concentration in the SOI structures (*1*) immediately after bonding and also after annealing for 30 min at T_a = (*2*) 650 and (*3*) 1100°C. The bonding time is 2 h.

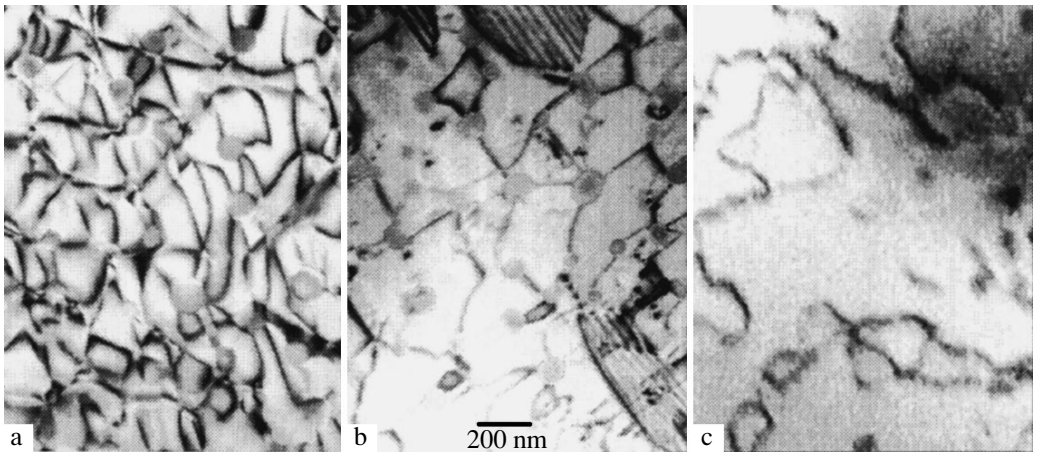

Fig. 4. TEM images of the samples with an original boron concentration of (a) 1×10^{15}, (b) 1×10^{18}, and (c) 1×10^{20} cm^{-3} after hydrogen-ion implantation with a dose of 4.5×10^{16} cm^{-2}and annealing at T_a = 1050°C.

SIMS sensitivity limit only at annealing temperatures $T_a \approx 1100$°C. It is evident that an increase in the bonding time results in a decrease of the residual hydrogen concentration in the structure [3].

The TEM images of the silicon crystals with various original boron concentrations implanted by hydrogen ions in the same regimes as the wafers used for preparing the SOI structures are shown in Fig. 4. All the crystals were annealed at a temperature of 1100°C for 30 min. It is known that hydrogen-filled blisters are formed in the course of annealing the hydrogen-implanted silicon and then are destroyed [1, 2, 4, 5]. To obtain these images, we used the crystal areas between blisters. The main defects observed in this figure are dislocation loops and pores. It can be seen that an increase in the boron concentration results in a decrease in the concentration of dislocations and pores in the irradiated layers. Similar results are also obtained when lower annealing temperatures (450 and 650°C) are used: the concentration of dislocation loops and point-defect clusters also decreases with an increase in the doping level of the material.

4. DISCUSSION

The donor centers in the silicon layer of the SOI structure after bonding represent the combination of oxygen quenched-in donors, donor centers related to hydrogen, and unknown donors that are stable up to high temperatures. Judging from the annealing temperature, it is possible to observe only the first two types of donors in SOI-III,IV: these are the quenched-in donors

and the hydrogen donors, which, as is known, are stable up to temperatures of ~520°C [6, 7]. In contrast, the third type of donors predominates in SOI-I,II.

The principal difference between SOI-I,II and SOI-III,IV is a different bonding time and, as a consequence, a different residual hydrogen concentration. It is known that the bonding temperature (450°C) is the most efficient temperature for the escape of hydrogen from silicon [5]. As follows from the above results, a decrease in the residual hydrogen concentration in the SOI structures is conducive to producing the same conductivity type as that in the original material (*p*-type). In the structures with a high residual hydrogen concentration, the formation of donors that are stable up to a temperature of ~1000°C is observed.

Another point of importance for the formation of donors is the boron-doping level in the material. At the same time, an increase in the boron concentration by three orders of magnitude is accompanied by a threefold increase in the donor concentration. It is known that the boron atoms at the interstices can give rise to donor centers [8], but they are stable only at low temperatures. Various donor centers associated with hydrogen have annealing temperatures lower than ~520°C [9]. The H–B complex, which is stable up to temperatures of ~250–300°C, also belongs [9] to these centers.

The experimental results presented above enable us to assume that hydrogen and boron are involved in the formation of donor centers that are stable up to high temperatures. Moreover, a high annealing temperature is likely associated with the participation of large structural defects (for example, dislocation loops, dangling bonds at an interface, etc.) in the formation of donors, and the stability of a given center is most probably controlled directly by the stability of the structural defects. An increase in the donor concentration, along with that of hydrogen towards the surface or the Si/SiO_2 interface, also agrees with the proposed assumption.

An efficient interaction between boron and point defects (vacancies and interstitials) causes boron to convert into an electrically passive state and to form complexes with hydrogen and defects. As a result, as can be seen from Fig. 4, the concentration of interstitial structural defects (dislocation loops) decreases with an increasing boron concentration. This can be the cause of a weak growth of the donor concentration in a heavily doped material in the context of the proposed assumption about the possible components of the center.

5. CONCLUSION

A high boron concentration in the original material, in combination with a high residual hydrogen concentration, results in *n*-type conduction of the split-off silicon layer in the SOI structure. The donor centers are assumed to be formed with the participation of hydrogen and boron atoms and with the structural defects retained in the silicon film.

ACKNOWLEDGMENTS

We thank E.P. Neustroev and D.V. Kilanov for their help in carrying out the measurements.

REFERENCES

1. M. Bruel, B. Aspar, C. Maleville, H. Moriceau, *et al.*, Proc.-Electrochem. Soc. **17-23**, 3 (1997).
2. M. Bruel, Nucl. Instrum. Methods Phys. Res. B **108**, 313 (1996).
3. V. P. Popov, E. P. Neustroev, I. V. Antonova, *et al.*, Physica B (Amsterdam) **270**, 1 (1999).
4. Q.-Y. Tong, R. Scholz, U. Goesele, *et al.*, Appl. Phys. Lett. **72**, 49 (1998).
5. T. Hara, Y. Kakizaki, S. Oshima, and T. Kitamura, Proc.-Electrochem. Soc. **97-23**, 33 (1998).
6. M. Bruni, D. Bisero, R. Tonini, *et al.*, Phys. Rev. B **49**, 5291 (1994).
7. C. P. Ewels, R. Jones, S. Öberg, *et al.*, Phys. Rev. Lett. **77**, 865 (1996).
8. J. W. Corbett, J. C. Bourgoin, L. J. Cheng, *et al.*, in *Radiation Effects in Semiconductors*, Conf. Ser.-Inst. Phys., No. 31, 1 (1977).
9. H. J. Stain and S. Hahn, J. Electrochem. Soc. **142**, 1242 (1995).

Translated by V. Bukhanov

Semiconductors, Vol. 34, No. 9, 2000, pp. 1058–1061. Translated from Fizika i Tekhnika Poluprovodnikov, Vol. 34, No. 9, 2000, pp. 1099–1102.

SEMICONDUCTOR STRUCTURES, INTERFACES, AND SURFACES

Fabrication and Photoelectric Properties of Oxide/CdTe Structures

G. A. Il'chuk*, V. I. Ivanov-Omskiĭ*, V. Yu. Rud'**, Yu. V. Rud'***, R. N. Bekimbetov***, and N. A. Ukrainets***

** State University "Lvivs'ka Politekhnica," Lviv, 79013 Ukraine*

*** St. Petersburg State Technical University, ul. Politekhnicheskaya 29, St. Petersburg, 195251 Russia*

**** Ioffe Physicotechnical Institute, Russian Academy of Sciences, ul. Politekhnicheskaya 26, St. Petersburg, 194021 Russia*

Submitted March 2, 2000; accepted for publication March 16, 2000

Abstract—A new technological process is proposed for forming an energy barrier in cadmium telluride crystals, and rectifying photosensitive anisotype and isotype structures are obtained. The photoelectric properties of the obtained structures and their dependence on the geometry of illumination with natural or linearly polarized light were investigated and are discussed. The new technology can be applied to the fabrication of different kinds of photoconversion structures based on cadmium telluride. © *2000 MAIK "Nauka/Interperiodica".*

1. INTRODUCTION

Cadmium telluride CdTe is recognized as one of the most promising semiconductor materials for the production of low-cost large-area solar cells [1]. Photoconversion efficiencies of up to 15% have been achieved in these devices, while theoretical estimations yield substantially higher values, up to 25% [2–4]. For this reason, new technologies are being intensively developed and photoelectric processes are being studied in different types of photosensitive CdTe structures. This paper follows this line of investigation and is the first study of photoelectric properties of the oxide/CdTe structures produced using the new approach to formation of photosensitive CdTe structures, which substantially simplifies the technology involved and, correspondingly, leads to lower fabrication cost.

2. EXPERIMENTAL PROCEDURE

Photosensitive structures were fabricated from electrically uniform *n*- and *p*-type CdTe single crystals with a free carrier concentration of 10^{16}–10^{17} cm^{-3} at T = 300 K. Single crystals were grown by planar crystallization from a nearly stoichiometric CdTe melt under controlled cadmium-vapor partial pressure that directly governed the type and concentration of majority carriers [5].

In a set of physical-technological studies, single-crystal *n*- and p-type CdTe wafers with specular (100) natural cleavage surfaces, and also with mechanically and then chemically polished surfaces of arbitrary crystallographic orientation, were subjected to thermal treatment in atmospheric air. This led to the formation of uniformly colored thin (~0.5 μm) *n*-type films on the crystal surface. These films exhibit good adhesion to the substrate, and their thickness and color are governed by the temperature and time of thermal treatment under conditions chosen as a result of detailed studies.

No colored film at all was formed on the surface of *n*- and *p*-type CdTe crystals when thermal treatment was performed in an evacuated ampule (P = 10^{-2}–10^{-5} Torr), all other technological conditions being the same. Thus, there is good reason to believe that thermal treatment of cadmium telluride wafers in air gives rise to thin interference films of a native oxide. This technological process is very simple and can be easily controlled by varying the temperature and time of thermal treatment.

The obtained native oxide layer (hereinafter denoted by *Ox*) was mechanically removed from all sides of the CdTe substrate except one. Steady-state current–voltage (*I–V*) characteristics and spectral dependences of the relative quantum efficiency η of photoconversion in natural and linearly polarized light were measured for the obtained *Ox*/*n*-CdTe and *Ox*/*p*- CdTe structures.

3. RESULTS AND DISCUSSION

As can be seen from the *I–V* characteristics, all the anisotype (*n*-*Ox*/*p*-CdTe) and isotype (*n*-*Ox*/*n*-CdTe) structures clearly demonstrate rectification. Figure 1 shows a typical *I–V* characteristic of an anisotype structure. As can seen, the forward-to-reverse current ratio for a bias $|U| \simeq 2$ V is typically no less than 10^3, and the forward bias corresponds to a positive voltage at the *p*-CdTe substrate. For these structures, the initial portion of the *I–V* characteristic is described by the conventional diode equation with nonideality factor $n \simeq 4.5$, which may be due to the effect of the series resistance.

In the bias range $U > 1.2$ V, the forward *I–V* characteristic satisfies the relation

$$U = U_0 + R_0 I. \quad (1)$$

The residual resistance of these structures is $R_0 \simeq 10^4\ \Omega$, and the cutoff voltage is $U_0 \simeq 0.75$ V. The reverse steady-state *I–V* characteristic of anisotype structures follows a power law $I_{oc} \propto U^{\alpha}$, where $\alpha \simeq 0.85$ at $U < 3$ V, whereas the current rise is characterized by α approaching unity at $U > 3.5$ V. The reverse current in the anisotype structures, $I_r \simeq 3 \times 10^{-8}$ A at $U \simeq 1$ V, and its increase with increasing bias are presumably due to imperfections at the sample periphery.

Isotype *n*-*Ox*/*n*-CdTe structures also exhibit rectification, with the forward bias corresponding to the negative voltage applied to the *n*-CdTe substrate. Photosensitivity rectifying properties of the isotype structures are much inferior to those of the anisotype structures.

A photovoltaic effect is observed in both structural types under nonpolarized illumination, irrespective of the incident beam localization on the surface, with polarity corresponding to rectification polarity. For example, in the case of anisotype *n*-*Ox*/*p*-CdTe structures, the oxide layer is always negatively charged, with the photovoltage sign remaining the same over the entire photosensitivity region. For the structures of highest quality, the open-circuit photovoltage is ~0.2 V and the short-circuit photocurrent is ~0.3 μA for the oxide layer illuminated with unfocused light of a ~100-W incandescent lamp. The maximum voltage ($S_u \simeq 2000$ V/W) and current ($S_i = 5$ mA/W) photosensitivities are achieved in anisotype structures.

Figure 2 presents a typical spectral dependence of the relative quantum photoconversion efficiency η, defined as the ratio of the short-circuit photocurrent to the number of incident photons, for an anisotype *n*-*Ox*/*p*-CdTe structure. For structures of this kind, the long-wavelength photosensitivity edge for illumination from the oxide film or the CdTe substrate sides coincide and follow an exponential law. The slope of the long-wavelength photosensitivity edge η is $S = \delta(\ln\eta)/\delta(\hbar\omega) \simeq 65\ \text{eV}^{-1}$, corresponding to direct band-to-band transitions in CdTe [6]. The energy position of the long-wavelength photosensitivity edge η and the bend in the spectral dependence of photosensitivity at $\hbar\omega_1 \simeq 1.44$ eV for illumination from the oxide side (Fig. 2, curve *1*) correlate with the CdTe band gap [7]. The sharp short-wavelength drop of η at $\hbar\omega > 1.41$ eV under illumination from the substrate side (Fig. 2, curve *2*) is directly associated with strong interband absorption in the substrate crystal. With increasing $\hbar\omega > 1.41$ eV, the photogeneration region nears the outer surface of the substrate, thus moving away from the active region of the structure to a distance exceeding the photoelectron diffusion length in CdTe and eventually causing a photosensitivity "dip" ($\eta \longrightarrow 0$). For *n*-*Ox*/*p*-CdTe structures illuminated from the substrate side, the η spectra are usually highly selective and their characteristic full

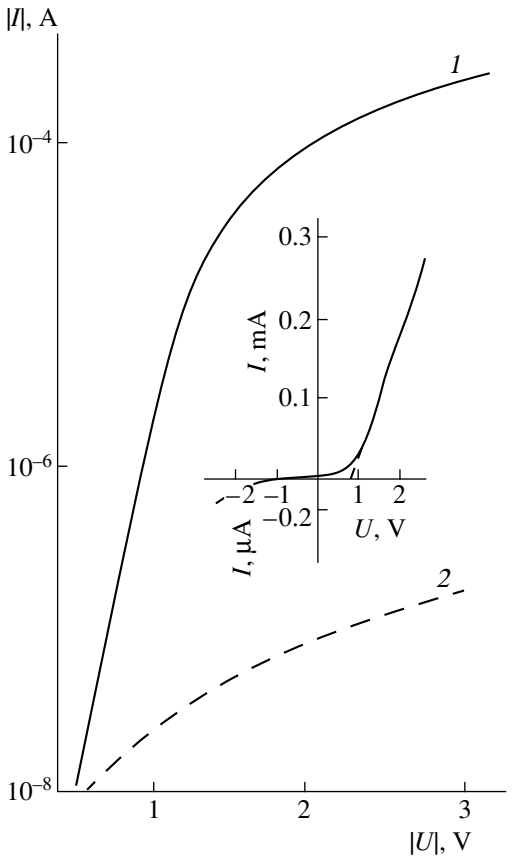

Fig. 1. Steady-state *I–V* characteristic of an *n*-*Ox*/*p*-CdTe structure at $T = 300$ K (sample no. 1). Forward bias corresponds to negative voltage on the oxide film. (*1*) corresponds to the forward and (*2*), to the reverse *I–V* characteristic.

width at half-maximum is $\delta_{1/2} \simeq 25$ meV. Under illumination from the oxide side, the photosensitivity spectra become wide-band, with $\delta_{1/2} \simeq 390$–400 meV. This suggests that a thin film of a wide-gap oxide is formed on the CdTe surface during heat treatment in air. The short-wavelength drop of η under nonpolarized illumination from the oxide side is gradual as far as 3.2 eV. Therefore, the absence of pronounced features in the short-wavelength photosensitivity spectra under nonpolarized-light illumination from the oxide side presents no serious grounds to even evaluate the band gap of the oxide film formed in thermal treatment of CdTe in air.

No dependence of the short-circuit photocurrent *i* on the orientation of the light-wave electric vector **E** was found in the *Ox*/CdTe structures illuminated with linearly polarized light incident normal to the surface for illumination from both the oxide and substrate sides. This suggests that the photoactive absorption is isotropic in both materials and, therefore, the natural photopleochroism coefficient P_N is zero [8].

At oblique incidence of linearly polarized light, as soon as the angle θ of incidence becomes other than 0°,

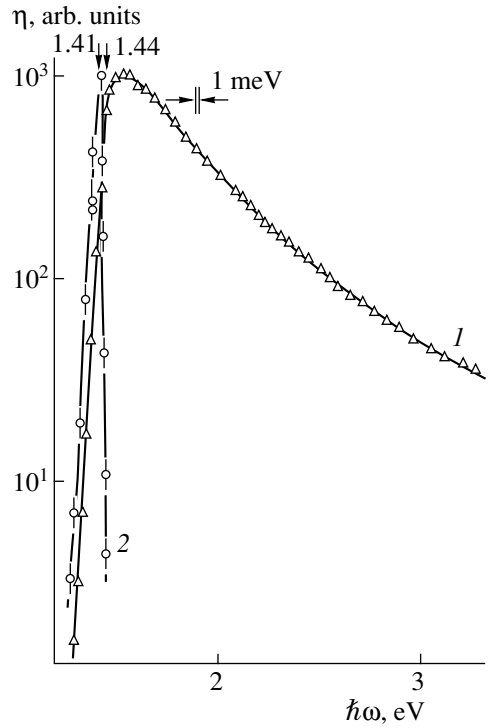

Fig. 2. Spectral dependences of the relative quantum efficiency of photoconversion of an *n*-*Ox*/*p*-CdTe structure illuminated with nonpolarized light at T = 300 K (sample no. 3). (*1*) from the oxide film side and (*2*) from the CdTe substrate side.

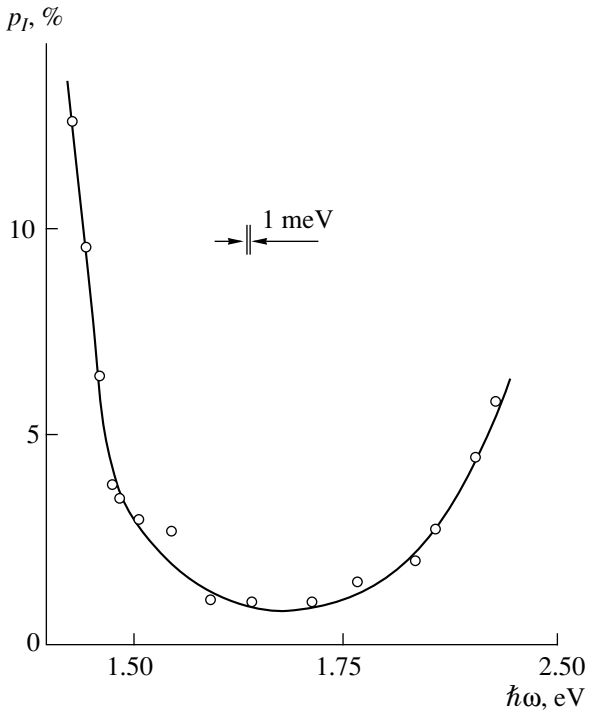

Fig. 3. Spectral dependence of the induced photopleochroism coefficient for an *n*-*Ox*/*p*-CdTe structure at T = 300 K, θ = 70° (sample no. 3). Illumination from the oxide film side.

Ox/CdTe structures exhibit induced photopleochroism [9] whose magnitudes and angular dependences vary substantially between the illumination configurations studied. In the case of illumination from the CdTe side, the angular dependences of the short-circuit photocurrents i^P (with the **E** vector parallel to the plane of incidence of light) and i^S (with **E** perpendicular to the plane of incidence) are similar to those observed previously in Schottky barriers on CdTe [10].

In the case of illumination from the oxide-film side, the angular dependence of i^S changes radically and becomes similar to that of i^P. Such a transformation has been found previously in a variety of heterojunction systems and in thin silicon films. When linearly polarized light enters a thin film from air, there is interference and the induced photopleochroism coefficient decreases sharply, i.e., $P_I \longrightarrow 0$, if the antireflection conditions are met [9, 11–14]. It is this effect that is observed in the spectral dependence of the induced photopleochroism coefficient for the *n*-*Ox*/*p*-CdTe structure illuminated from the oxide side (Fig. 3). In the region of high photosensitivity of these structures (Fig. 2, curve *2*), the induced photopleochroism coefficient falls to 1–2% (a value that is too low and untypical of CdTe) indicating the high antireflection quality of the oxide film in a wide spectral range. The strong "response" of the induced photopleochroism to the reconstruction of the CdTe surface during its interaction with air becomes understandable if we take into account that $P_I \simeq 50\%$ for the same structure illuminated from the CdTe substrate side and for a similar angle of incidence of linearly polarized light $\theta \simeq 70°$. Indeed, the value of P_I decreases from 50 to 1–2% upon such oxidation of CdTe, and this effect can be employed in fast diagnostics of the antireflection coating fabrication on the cadmium telluride surface.

4. CONCLUSION

The performed physicotechnological investigations showed that thermal treatment of cadmium telluride in air can be used to develop high-efficiency low-cost photoconversion devices and that polarization dependences of photosensitivity can be used in diagnostics of CdTe oxidation processes.

REFERENCES

1. *Proceedings of the 5th International Conference on Polycrystalline Semiconductors V—Bulk Materials, Thin Films and Devices, Schwabich Gmund, Germany, Sept. 13–18, 1998*, Ed. by J. H. Werner, H. P. Strunk and H. W. Schock (Scitec, Switzerland, 1999).
2. H. S. Ullal, K. Zweibel, and B. von Roedern, in *Proceedings of the 26th IEEE PVSC, Anaheim, 1997*, p. 301.
3. H. Ohyama, T. Aramoto, S. Kumazawa, *et al.*, in *Proceedings of the 26th IEEE PVSC, Anaheim, 1997*, p. 343.

4. R. W. Brirkmize and E. Elser, Annu. Rev. Mater. Sci. **27**, 625 (1997).
5. O. A. Matveev, S. V. Prokof'ev, and Yu. V. Rud', Izv. Akad. Nauk SSSR, Neorg. Mater. **5**, 1175 (1969).
6. *Physics and Chemistry of II–VI Compounds*, Ed. by M. Aven and J. S. Prener (North-Holland, Amsterdam, 1967).
7. *Physicochemical Properties of Semiconductors: A Reference Book* (Nauka, Moscow, 1979).
8. F. P. Kesamanly, V. Yu. Rud', and Yu. V. Rud', Fiz. Tekh. Poluprovodn. (St. Petersburg) **33**, 513 (1999) [Semiconductors **33**, 483 (1999)].
9. G. A. Il'chuk, N. A. Ukrainets, V. I. Ivanov-Omskiĭ, *et al.*, Fiz. Tekh. Poluprovodn. (St. Petersburg) **33**, 553 (1999) [Semiconductors **33**, 518 (1999)].
10. V. Yu. Rud', Yu. V. Rud', and H. W. Schock, Solid State Phenom. **67/68**, 421 (1999).
11. V. Yu. Rud' and Yu. V. Rud', Fiz. Tekh. Poluprovodn. (St. Petersburg) **33**, 954 (1999) [Semiconductors **33**, 870 (1999)].
12. V. Yu. Rud' and Yu. V. Rud', Fiz. Tekh. Poluprovodn. (St. Petersburg) **33**, 425 (1999) [Semiconductors **33**, 412 (1999)].

Translated by D. Mashovets

Semiconductors, Vol. 34, No. 9, 2000, pp. 1062–1063. Translated from Fizika i Tekhnika Poluprovodnikov, Vol. 34, No. 9, 2000, pp. 1103–1104.

SEMICONDUCTOR STRUCTURES, INTERFACES, AND SURFACES

The Transient Photomagnetic Effect in Multilayer Structures with *p–n* Junctions

V. N. Agarev and V. I. Stafeev

Orion Scientific and Industrial Association, Moscow, 111123 Russia

Submitted March 6, 2000;
accepted for publication March 16, 2000

Abstract—A transient voltage occurring after bias switching in a supermultilayer structure consisting of series-connected *p–n* junctions is analyzed. It is shown that a transient photomagnetic effect of a very high magnitude can be induced in such structures by illumination in the presence of a magnetic field.

A supermultilayer structure is a structure consisting of a large number of *p–n* junctions connected in opposite directions to each other; i.e., it is a structure of the *p–n–p–n–p–n*… type [1]. When a bias voltage $V \gg 2mkT/q$ is applied to a supermultilayer structure ($2m$ is the number of *p–n* junctions, T is the temperature, q is the elementary charge), it will drop mainly across the reverse-biased *p–n* junctions. The charge stored at their capacitances will greatly exceed the charge on the forward-biased *p–n* junctions.

Shorting the supermultilayer structure generates a current that equalizes the charges of all *p–n* junctions (provided all are identical). An excess charge will be discharged by the reverse currents of the *p–n* junctions. Since these currents are small, the discharge time will be much longer than the bulk lifetime of the nonequilibrium charge carriers in this semiconductor [1].

Because no totally identical junctions exist in a supermultilayer structure, the relaxation process brings about a potential difference, the value of which depends on the initial charges of the barrier capacitances and the difference of the reverse currents of counterconnected *p–n* junctions [2–4]. The limiting value of the generated transient potential difference can be written as $V_{\max} = m\varphi$, where φ is a contact potential difference between *p*- and *n*-regions. The supermultilayer structure contains 10^3–10^4 barrier/cm, $\varphi \sim 1$ V; therefore, a transient potential difference may be as high as 10^3–10^4 V/cm.

We now consider a supermultilayer structure in the open-circuit conditions with preliminarily charged capacitances of the *p–n* junctions. A transient charge at the *p–n* junctions in such conditions is much larger than the equilibrium charge of the ionized donors: $Q(0) \gg Q_0$. At an arbitrary time t, the charge at the barrier capacitances in the nth region between the jth and $(j + 1)$th junctions is

$$Q(t) = Q_j(t) + Q_{j+1}(t) = (1/2)Q_0\sqrt{1 + V_j(t)/\varphi} + (1/2)Q_0\sqrt{1 + V_{j+1}(t)/\varphi}, \quad (1)$$

where V_j and V_{j+1} are the voltages on the jth and $(j + 1)$th *p–n* junctions.

The total voltage across the supermultilayer structure in the open-circuit conditions is then

$$V = m(V_{j+1} - V_j). \quad (2)$$

Under illumination of the supermultilayer structure in a transverse magnetic field B, the change of the charge at the barrier capacitances occurs due to the effect of thermal generation–recombination, $-I_s$; the generation under the action of light, $-I_f$; and the photomagnetic current, $-I_{fm}$, [5]:

$$dQ_j/dt = -I_s - I_f - I_{fm} = -I_j, \quad (3)$$

$$dQ_{j+1}/dt = -I_s - I_f + I_{fm} = -I_{j+1}. \quad (4)$$

Since V_j and V_{j+1} are negative and much greater in magnitude than kT/q, the currents I_f and I_{fm} may be assumed to be constant, because the concentration of nonequilibrium holes at the boundaries with the *p–n* junctions is much lower than the concentration of equilibrium holes. If thermal generation occurs predominantly in a quasi-neutral region, the current I_s may also be assumed to be constant. Simultaneous solution of Eqs. (1), (3), and (4) yields the total voltage drop [2]

$$V(t) = 4m\varphi[Q(0)/Q_0]^2 \times [2t(I_j - I_{j+1})/Q(0) - t^2(I_j^2 - I_{j+1}^2)/Q(0)^2]. \quad (5)$$

The highest photovoltage is attained at $t = t_{\max} = Q(0)/(I_j + I_{j+1})$ and is equal to

$$V_{\max} = 4m\varphi[Q(0)/Q_0]^2(I_j - I_{j+1})/(I_j + I_{j+1}). \quad (6)$$

For $I_f \gg I_s$ and $\mu B \ll 1$, i.e., when $I_{fm} \ll I_f$, the condition for the maximum value of the photovoltage is

$$V_{\max} = 4m\varphi[Q(0)/Q_0]^2 I_{fm}/I_f = (4m\varphi/\pi)[Q(0)/Q_0]^2 2\mu B, \quad (7)$$

because, according to [5], $I_{fm}/I_f = 2\mu B/\pi$.

1063-7826/00/3409-1062$20.00

The anomalous effect of a photomagnetic voltage in CdTe has been studied previously [6]. According to the suggested model [6], this effect can be described by the expression

$$V_0 = 4mkT\mu B/q\pi. \quad (8)$$

Comparing (7) and (8), we obtain

$$V_{max}/V_0 = 2q\varphi[Q(0)/Q_0]^2/kT \gg 1. \quad (9)$$

The room temperature data for CdTe are $q\varphi/kT \approx 60$, $[Q(0)/Q_0]^2 \approx 10$; therefore, $V_{max}/V_0 \approx 600$. Thus, a transient photomagnetic effect is quite possible in a supermultilayer structure with preliminarily charged barrier capacitances of the *p–n* junctions. The magnitude of this effect can be several times greater than that of the "giant photomagnetic effect in semiconductor films" [6] occurring under steady-state conditions.

REFERENCES

1. V. I. Stafeev, Fiz. Tekh. Poluprovodn. (Leningrad) **6**, 2134 (1972) [Sov. Phys. Semicond. **6**, 1811 (1972)].
2. V. N. Agarev, Pis'ma Zh. Tekh. Fiz. **3** (13), 626 (1977) [Sov. Tech. Phys. Lett. **3**, 256 (1977)].
3. V. N. Agarev, Fiz. Tekh. Poluprovodn. (Leningrad) **14**, 1018 (1980) [Sov. Phys. Semicond. **14**, 607 (1980)].
4. V. N. Agarev, Fiz. Tekh. Poluprovodn. (St. Petersburg) **31**, 920 (1997) [Semiconductors **31**, 784 (1997)].
5. É. I. Adirovich, D. A. Aronov, É. M. Mastov, and Yu. M. Yuabov, Fiz. Tekh. Poluprovodn. (Leningrad) **8**, 354 (1974) [Sov. Phys. Semicond. **8**, 226 (1974)].
6. É. I. Adirovich, É. M. Mastov, and Yu. M. Yuabov, Fiz. Tekh. Poluprovodn. (Leningrad) **5**, 1415 (1971) [Sov. Phys. Semicond. **5**, 1241 (1971)].

Translated by A. Zalesskiĭ

Semiconductors, Vol. 34, No. 9, 2000, pp. 1064–1067. Translated from Fizika i Tekhnika Poluprovodnikov, Vol. 34, No. 9, 2000, pp. 1105–1108.

SEMICONDUCTOR STRUCTURES, INTERFACES, AND SURFACES

Photovoltaic Effect in *a*-Si:H/*n*-InSe Heterostructures

R. N. Bekimbetov*, Yu. A. Nikolaev*, V. Yu. Rud', Yu. V. Rud'*, and E. I. Terukov***

** Ioffe Physicotechnical Institute, Russian Academy of Sciences, Politekhnicheskaya ul. 26, St. Petersburg, 194021 Russia*

*** St. Petersburg State Technical University, Politekhnicheskaya ul. 29, St. Petersburg, 195251 Russia*

Submitted March 21, 2000; accepted for publication March 21, 2000

Abstract—Heterostructures in an *a*-Si:H/InSe system were grown by the deposition of *a*-Si:H films onto the surface (001) of InSe single-crystal wafers and also by deposition of pure indium films with their subsequent selenization, in which case InSe films were synthesized at the *a*-Si:H surface. The photovoltaic effect was observed and studied for both types of heterostructures. It was concluded that the heterostructures obtained may be used as wide-band photoconverters of radiation. © *2000 MAIK "Nauka/Interperiodica".*

INTRODUCTION

Production of heterostructures by bringing various semiconductors into optical contact finds ever wider use in studies of photovoltaic capabilities of novel systems; the specific value of this method consists in the fact that it does not require growth-related studies and thus prevents the transformation of the properties of the contacting phases under the effect of technological processes of heterostructure fabrication [1–5]. It was this method, which we have recently applied in studies of the photoelectric properties of a contact between *a*-Si:H and InSe materials obtained separately, that allowed us to demonstrate experimentally the potential of the new system for use in solar cells [6]. This study continues this line of research. It is devoted to the development of physicotechnological basics of the preparation processes and to the first studies of heterostructures in which a heteroboundary is formed by the conventional growth of one semiconductor on the initial substrate of another [7].

EXPERIMENT

Heterostructures of two types were grown. The single-crystal InSe wafers were used in one type (type A) as substrates; these wafers were obtained by cleaving over the (001) cleavage plane from an ingot grown by planar crystallization of the melt, which was close in stoichiometry to that of this compound. The electron concentration in the InSe wafers used, which had mean dimensions of $5 \times 5 \times 0.05$ mm^3, in the absence of doping was typically $n \cong 10^{15}$ cm^{-3} at T = 300 K. Then, *a*-Si:H films with a resistivity of ~10^9 Ω cm at T = 300 K were grown on the specular surface of *n*-InSe wafers by the method of glow discharge in a mixture of silane with hydrogen (~12%). The substrate temperature was 230°C during the growth process. As a result, *a*-Si:H films with a thickness of ~1 μm were obtained on the InSe (001) surface; these films demonstrated high adhesion with respect to the InSe (001) surface.

In *B*-type heterostructures, *a*-Si:H films with thicknesses of about 1 μm were used as substrates; these films were grown on silica wafers by the same method as *A*-type heterostructures. Then, a layer of pure indium with a thickness of ~1 μm was deposited by vacuum thermal evaporation onto the surfaces of *a*-Si:H films; this layer was subsequently used for synthesis of InSe layers. InSe synthesis occurred as a result of interaction of a pure indium film, which was on the surface of *a*-Si:H, with selenium vapors. The temperature of the *a*-Si:H films during the process was ~400°C. This method allowed us to produce, at the *a*-Si:H surface, thin (≅0.5 μm) InSe films, which had a specular outer surface and possessed high adhesion with respect to the postgrown surface of *a*-Si:H films. The area of the heterostructures of the *A*- and *B*-types obtained was $\approx 5 \times 5$ mm^2. It should be noted, in this case, that neither method imposes serious limitations on an increase in the heterostructure area.

EXPERIMENTAL RESULTS AND DISCUSSION

We consider the main results of photoelectric studies of the heterostructures obtained. The typical parameters for both types of heterostructures are given in the table. As the studies of steady-state current–voltage (*I–V*) characteristics show, the heterostructures feature a weak rectification. The ratio of photocurrents in the forward and reverse directions usually does not exceed 2–3 ($U \cong 5$ V), with the residual resistance R_0 of *A*-type heterostructures always being much lower than that for *B*-type (see table). This difference is likely caused by the features of interphase interactions during the processes of preparation of these heterostructures. In the case of *B*-type structures, the residual resistance corresponds to that characteristic of those structures obtained by bringing InSe into optical contact with *a*-Si:H [6], whereas, for the *A*-type heterostructure, a strong reduction of R_0 is observed. In connection with this fact, there are grounds to believe that, in the process

Photoelectric properties of *a*-Si:H/InSe heterostructures at $T = 300$ K (illumination from the *a*-Si:H side)

Type of heterostructure	R_0, Ω	$\Delta\hbar\omega^m$, eV	$\delta_{1/2}$, meV	S_D, eV^{-1}	S_u^m, V/W	S_i^m, μA/W
A	$\sim 10^4$	1.2–1.75	780	42	0.2	25
B	$\sim 10^7$	2.05–2.15	500	35	200	2

of *a*-Si:H deposition onto the InSe surface, the doping of contacting phases occurs. This experimental fact requires special study.

Both types of heterostructures, as in the case of attaining an optical contact [6], reveal a photovoltaic effect. The sign of the photovoltages of these heterostructures agrees with the direction of rectification and corresponds to negative polarity of the photovoltage at their narrow-gap *n*-InSe component. At present, *a*-Si:H/InSe heterostructures even now are significantly superior to an optical heterocontact for these semiconductors [6] with respect to the maximum values of voltage S_u and current S_i photosensitivity (see table). If one takes into account that the electrical properties of heterostructures are still considerably inferior to those observed in optical heterocontacts [6], one can hope that the quantum efficiency of photoconversion for heterostructures will considerably improve, provided the parameters of their *I–V* characteristics are optimized.

Typical spectral dependences of the relative quantum efficiency of photoconversion η for the *A*-type heterostructures are shown in Fig. 1 in comparison with *a*-Si:H/InSe optical heterocontact. Under illumination of *A*-type heterostructures, the "window effect" [7] distinctly manifests itself, which is characteristic of ideal heterostructures, when a high photosensitivity is realized in the range between the band gaps of contacting semiconductors. In this case, a film of amorphous hydrogenated silicon is grown on a single-crystal substrate of the layered InSe semiconductor, and this basic difference in the structures of contacting materials, as follows from Fig. 1 (curve *1*), results in a narrowing of the photosensitivity spectral range. Such a feature usually appears in the case of a high concentration of defects at the heteroboundary.

The maximum photosensitivity in *B*-type heterostructures under illumination from the *a*-Si:H side is attained in the range of photon energies $\Delta\hbar\omega^m$ from 1.2 to 1.75 eV (see table and Fig. 1). The long-wavelength edge of the photosensitivity for these heterostructures has an exponential shape, and its slope $S_D = \delta(\ln\eta)/\delta(\hbar\omega)$ has high values (see table) that correspond to direct interband transitions in InSe [8]. The full width of the photosensitivity spectra for *B*-type heterostructures $\delta_{1/2}$ is as large as 780 meV (see table), and the short-wavelength falloff of η for $\hbar\omega > 1.7$ eV is caused by the influence of optical absorption in the *a*-Si:H film, through which the radiation enters the active region. We should emphasize that the spectral contour of photosensitivity for *B*-type heterostructures turns out to be close to that characteristic of an optical heterocontact between InSe and *a*-Si:H (Fig. 1, curves *1*, *3*). This can serve as grounds for the assumption about the similarity of the quality of amorphous hydrogenated silicon on the crystalline InSe substrate and on silica glass. The observation of a set of equidistant peaks in the photosensitivity spectra for *B*-type heterostructures testifies in favor of the assumption considered above; these

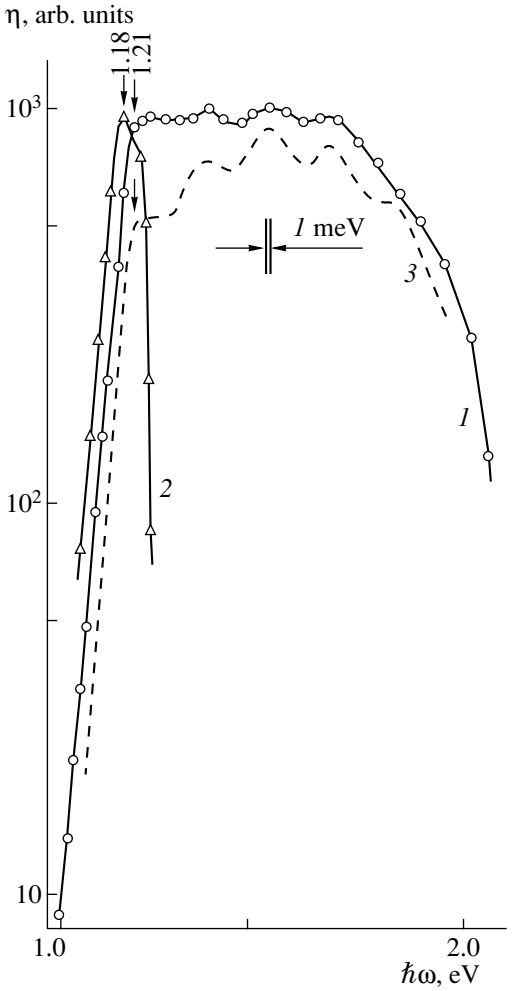

Fig. 1. Spectral dependences of the relative quantum efficiency of *a*-Si:H/InSe heterostructure photoconversion at $T = 300$ K. (*1*, *2*) Heterostructure is obtained by the growth of *a*-Si:H film at the surface of InSe wafers (type A); (*3*) heterostructure is obtained by bringing the *n*-InSe wafer into optical contact with *a*-Si:H film. The structure was illuminated (*1*, *3*) from the *a*-Si:H side and (*2*) from the side of an *n*-InSe wafer ≈50 μm thick.

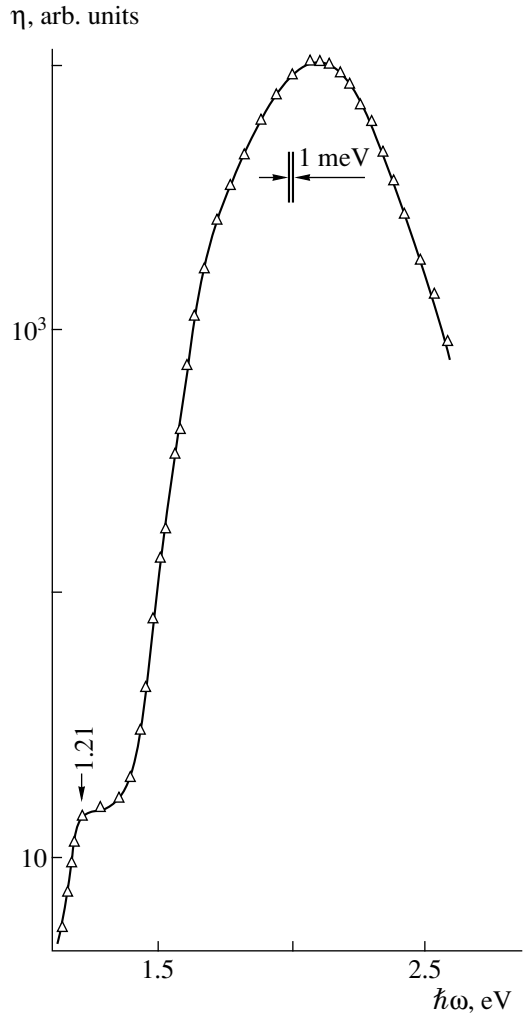

Fig. 2. Spectral dependence of the relative quantum efficiency of photoconversion of the InSe/*a*-Si:H heterostructure obtained by InSe film growth at the surface of *a*-Si:H film (type B), at $T = 300$ K.

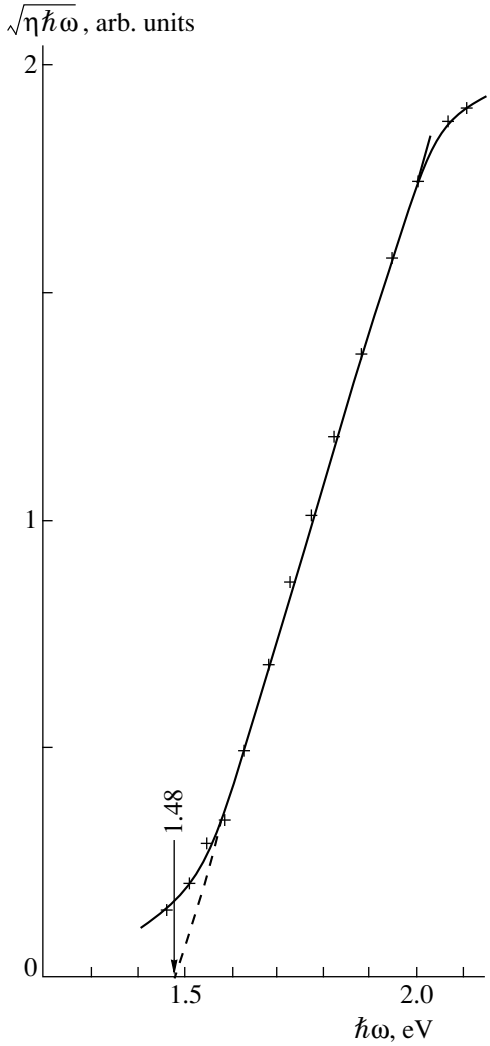

Fig. 3. Spectral dependence of the relative quantum efficiency of photoconversion of InSe/*a*-Si:H heterostructures (type B) in coordinates $\sqrt{\eta\hbar\omega} - \hbar\omega$ at $T = 300$ K.

peaks, which are similar to the case of optical heterocontacts, can be explained by radiation interference in the *a*-Si:H films.

A transition to the illumination of *B*-type heterostructures from the side of their narrow-band component shifts the short-wavelength cutoff of the photosensitivity to the region of interband absorption in InSe (Fig. 1, curve *2*). Therefore, the photosensitivity spectrum becomes a narrow-band one and, correspondingly, $\delta_{1/2}$ decreases to values of ≅100 meV for the thickness of InSe wafers used. The energy position of a distinct step in the η spectra in the case of illumination of the *A*-type heterostructures from the *a*-Si:H side for $\hbar\omega \cong 1.21$ eV, as in the case of short-wavelength cutoff of photosensitivity under conditions of the illumination from the InSe side, corresponds to the band gap of InSe [8]. The correlation observed for the spectral contour and energy position of the short-wavelength decay of η in *A*-type heterostructures and optical *a*-Si:H/InSe heterocontacts (Fig. 1, curves *1*, *3*) should be considered in the context of quantitative correspondence in the edge absorption spectra of *a*-Si:H films grown on different substrates.

In the case of *B*-type heterostructures, the spectral dependences of η under illumination from the *a*-Si:H side testify that the photosensitivity remains wide-band; however, its peak shifts to the fundamental absorption region of their *a*-Si:H wide-band component (Fig. 2). A long-wavelength edge of photosensitivity similar to that for *A*-type heterostructures is determined as before by the absorption in InSe; however, the contribution of this absorption decreases by 2–3 orders of magnitude with respect to the fundamental absorption in *a*-Si:H. The photosensitivity of *A*-type heterostructures prevails under their illumination from the wide-band window side. In this case, a spectral contour

of η is practically independent of the orientation of illumination with respect to a sample, which can be caused by the predominant localization of the active region of heterostructure in the high-resistivity *a*-Si:H film. It is this difference in the doping levels of a heterostructure components of *A*- and *B*-types that reduces the contribution of the fundamental absorption in InSe in the photosensitivity of the *B*-type heterostructures. Taking this fact into account, the long-wavelength edge of high photosensitivity of a *B*-type heterostructure is plotted in coordinates $\sqrt{i\hbar\omega} - \hbar\omega$ in Fig. 3. It can be seen that the photosensitivity spectrum for a *B*-type heterostructure in the range from 1.6 eV up to 1.9 eV is well approximated by a straight line in the coordinates used, which corresponds to the indirect interband transitions in *a*-Si:H [9]. The extrapolation of this dependence to $\eta\hbar\omega = 0$ yields the energy value of ≈1.48 eV, which is assumed to be the band gap of the *a*-Si:H films on which the heterostructures of *A*- and *B*-types were formed. We should emphasize that this value agrees satisfactorily with the photon energies above which photosensitivity falloff occurs in heterostructures in the case of illumination from the *a*-Si:H side (Fig. 1, curves *1*, *2*). A natural photopleochroism is absent in both types of heterostructures, which corresponds to an isotropic character of absorption in their components [10].

CONCLUSION

Thus, the growth technologies of *a*-Si:H/InSe heterostructures of two types are developed. The first studies of the photovoltaic properties of new heterostructures were performed; they open possibilities of developing wide-band photoconverters of natural radiation with the use of this system.

REFERENCES

1. I. V. Bodnar, V. Yu. Rud', and Yu. V. Rud', Cryst. Res. Technol. **31**, 261 (1996).
2. V. Yu. Rud', Yu. V. Rud', S. Iida, *et al.*, Inst. Phys. Conf. Ser. **152**, 967 (1997).
3. M. C. Ohmer, V. Yu. Rud', Yu. V. Rud', and P. G. Schuhemann, in *Abstracts 24th International Conference on the Physics of Semiconductors, Jerusalem, Aug. 2–7, 1998*, Vol. 2, Th-P213.
4. A. A. Lebedev, V. Yu. Rud', and Yu. V. Rud', Fiz. Tekh. Poluprovodn. (St. Petersburg) **32**, 353 (1998) [Semiconductors **32**, 320 (1998)].
5. V. Yu. Rud', Yu. V. Rud', V. F. Gremenok, *et al.*, Fiz. Tekh. Poluprovodn. (St. Petersburg) **33**, 1205 (1999) [Semiconductors **33**, 1097 (1999)].
6. Yu. A. Nikolaev, V. Yu. Rud', Yu. V. Rud', and E. I. Terukov, Fiz. Tekh. Poluprovodn. (St. Petersburg) **34**, 818 (2000) [Semiconductors **34**, 677 (2000)].
7. B. L. Sharma and R. K. Purohit, *Semiconductor Heterojunctions* (Pergamon, Oxford, 1974; Sov. Radio, Moscow, 1979).
8. *Physicochemical Properties of Semiconductors: A Reference Book* (Nauka, Moscow, 1979).
9. *Amorphous and Microcrystalline Semiconductor Devices II—Materials and Device Physics*, Ed. by J. Kamaki (Artech Hause, London, 1992).
10. F. P. Kesamanly, V. Yu. Rud', and Yu. V. Rud', Fiz. Tekh. Poluprovodn. (St. Petersburg) **30**, 1921 (1996) [Semiconductors **30**, 1001 (1996)].

Translated by T. Galkina

Semiconductors, Vol. 34, No. 9, 2000, pp. 1068–1072. Translated from Fizika i Tekhnika Poluprovodnikov, Vol. 34, No. 9, 2000, pp. 1109–1113.

LOW-DIMENSIONAL SYSTEMS

Accumulation of Majority Charge Carriers in GaAs Layers Containing Arsenic Nanoclusters

P. N. Brunkov*, V. V. Chaldyshev*, A. V. Chernigovskiĭ*, A. A. Suvorova*, N. A. Bert*, S. G. Konnikov*, V. V. Preobrazhenskiĭ, M. A. Putyato**, and B. R. Semyagin****

** Ioffe Physicotechnical Institute, Russian Academy of Sciences, Politekhnicheskaya ul. 26, St. Petersburg, 194021 Russia*
e-mail: brunkov@pop.ioffe.rssi.ru

*** Institute of Semiconductor Physics, Siberian Division, Russian Academy of Sciences, pr. akademika Lavrent'eva 13, Novosibirsk, 630090 Russia*

Submitted February 29, 2000;
accepted for publication March 1, 2000

Abstract—The accumulation of electrons and holes in GaAs layers that contained As clusters and were sandwiched between *n*- and *p*-type buffer GaAs layers was revealed by capacitance–voltage measurements. As a result of majority-carrier accumulation, expansive depletion regions are formed in the adjoining buffer layers. Simulation of the capacitance–voltage characteristics, based on a numerical solution of the Poisson equation, shows that the accumulated charge density is $\sim 1 \times 10^{12}$ cm^{-2}, which is comparable with the concentration of As nanoclusters determined by transmission electron microscopy. *© 2000 MAIK "Nauka/Interperiodica".*

INTRODUCTION

Gallium arsenide containing arsenic nanoclusters [low-temperature-grown GaAs (LT-GaAs)] attracts a lot of attention because of its unique properties, such as a high electrical resistivity and the femtosecond lifetimes of nonequilibrium charge carriers [1–4]. Despite the fact that this material has already found quite a number of device applications (see, e.g., [5]), the nature of its electronic properties still remains a matter of discussion. In particular, the precise energy position and parameters of local levels related to As clusters in the band gap of GaAs are still unclear. The presence of a high concentration of localized states pinning the Fermi level deep within the band gap and ensuring the fast recombination of nonequilibrium carriers is the basic feature distinguishing this material from a conventional semi-insulating or high-resistivity GaAs. It was shown in our previous publications [6, 7] that an LT-GaAs layer containing As clusters can accumulate electrons from the adjacent *n*-type GaAs layers, inducing space-charge regions (SCRs) there. The charge distribution in the LT-GaAs/*n*-GaAs structure is similar to that in an asymmetric *p*–*n* junction in which LT-GaAs plays the part of a *p*-type region heavily doped with deep acceptors.

In this communication, we report the results obtained in capacitance–voltage (*C*–*V*) studies of structures with a Schottky barrier, in which the LT-GaAs layer containing As clusters is inserted between *p*-type GaAs layers. The *C*–*V* characteristics of this structure are compared with those of structures with *n*-type layers. It is shown that the LT-GaAs layer accumulates majority carriers in both kinds of structures.

EXPERIMENTAL

Samples of *n*- and *p*-types (henceforth, *N* and *P* structures) were grown by molecular beam epitaxy in a Katun' two-chamber installation on n^+- and p^+-GaAs (100) substrates, respectively. The *N* structure comprised three layers: an *n*-GaAs layer ~0.5 μm thick (epitaxy temperature $T_s = 580$°C), an LT-GaAs layer ~0.1 μm thick ($T_s = 200$°C), and a second *n*-GaAs layer ~0.5 μm thick ($T_s = 580$°C). The epilayers of the *N* structure were uniformly doped with Si to a concentration of $\approx 2 \times 10^{16}$ cm^{-3}.

In the case of a *P* structure, layers were grown on a p^+ substrate in the following order: a buffer GaAs layer heavily doped with beryllium; a *p*-GaAs layer ~0.5 μm thick (Be concentration $\approx 2 \times 10^{16}$ cm^{-3}, $T_s = 580$°C); an LT-GaAs layer ~0.1 μm thick ($T_s = 200$°C); a *p*-GaAs layer ~0.5 μm thick (Be concentration $\approx 2 \times 10^{16}$ cm^{-3}, $T_s = 580$°C); and, finally, on the surface of the *P* structure, a short-period GaAs/AlAs superlattice (1 nm/1 nm) of a total thickness of 38 nm.

The low temperature of the epitaxial growth of LT-GaAs layers ensured an ~0.5-at. % excess of arsenic in such layers [4]. The growth of the upper layers of the structures at high temperature for 0.5 h led to precipitation of the excess arsenic and gave rise to a system of arsenic nanoclusters in the LT-GaAs layer. The crystal structure of the samples and the spatial arrangement, concentrations, and sizes of the clusters were studied by transmission electron microscopy (TEM) in cross section and in the growth plane. A Philips EM 420 electron microscope at an accelerating voltage of 100 keV was used.

1063-7826/00/3409-1068$20.00

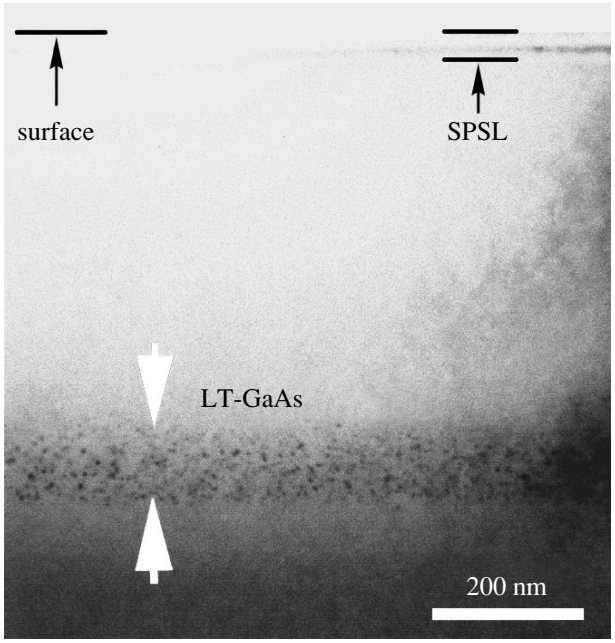

Fig. 1. Cross-sectional light-field TEM image (**g** = 220) of a *P* structure.

Schottky barriers were formed by vacuum evaporation of Au onto the sample surface, with an electrode diameter of 0.4 and 0.5 mm for the *N* and *P* structures, respectively. Ohmic contacts to n^+ and p^+ substrates were formed using AuGe and AuZn alloys, respectively. The contacts were formed at a temperature of 400°C.

C–V characteristics were measured with an E7-14 capacitance bridge at a frequency of 10 kHz in the temperature range from 77 to 400 K. The amplitude of the probing signal was 40 mV.

RESULTS AND DISCUSSION

Figure 1 shows a cross-sectional TEM image of a *P* structure. It can be seen that the LT-GaAs layer containing arsenic clusters has a thickness $d_{LT} \approx 0.1$ μm and is sandwiched between two *p*-GaAs layers containing no clusters. The density of As clusters (N_{CL}) in the LT-GaAs layer is about 6×10^{11} cm^{-2} with their average diameter (d_{CL}) in the range from 5 to 7 nm. TEM images of an *N* structure were reported previously [7]. For the *N* structure with $d_{LT} \approx 0.1$ μm, $N_{CL} \approx 4 \times 10^{11}$ cm^{-2} and d_{CL} = 6–8 nm. Thus, the *P* and *N* structures are close in their geometric characteristics, the parameters of their cluster systems, and the doping levels of, respectively, *p*- and *n*-type regions adjacent to the LT-GaAs layer. It should be noted that there are no extended lattice defects in both types of structures.

The *C–V* characteristics of *P* and *N* structures, measured at a frequency of 10 kHz, are shown in Figs. 2a and 3a, respectively. The depletion-layer approximation was used to calculate the effective concentration profiles of free carriers ($N_{CV} - W$) from the *C–V* characteristics (Figs. 2b and 3b) [8]:

$$N_{CV}(W) = \frac{C^3}{q\varepsilon\varepsilon_0\left(\frac{dC}{dV}\right)}, \quad W = A\frac{\varepsilon\varepsilon_0}{C}, \qquad (1)$$

where q is the elementary charge, ε_0 is the permittivity of free space, ε is the relative permittivity of the semiconductor, W is the SCR width, and A is the Schottky barrier area.

As the reverse voltage (V_{rev}) increases, the capacitance of the *P* structure at T = 77 K decreases gradually in the range V_{rev} = 0–0.2 V with an abrupt drop at $V_{rev} \approx$ 0.3 V (Fig. 2a). As the reverse voltage increases further (V_{rev} = 0.4–6 V), the capacitance of the *P* structure again decreases gradually. At $V_{rev} > 6$ V, the capacitance of the *P* structure remains virtually unchanged. Calculation of the effective carrier-concentration profile N_{CV}–W for the *P* structure shows (Fig. 2b) that the regions of gradual variation of the structure capacitance are associated with the uniform doping of the *p*-GaAs buffer layers to $(1–3) \times 10^{16}$ cm^{-3}. The region in which there is an abrupt drop in the capacitance at $V_{rev} \approx 0.3$ V is due to the presence of a wide (≈0.7 μm) SCR within

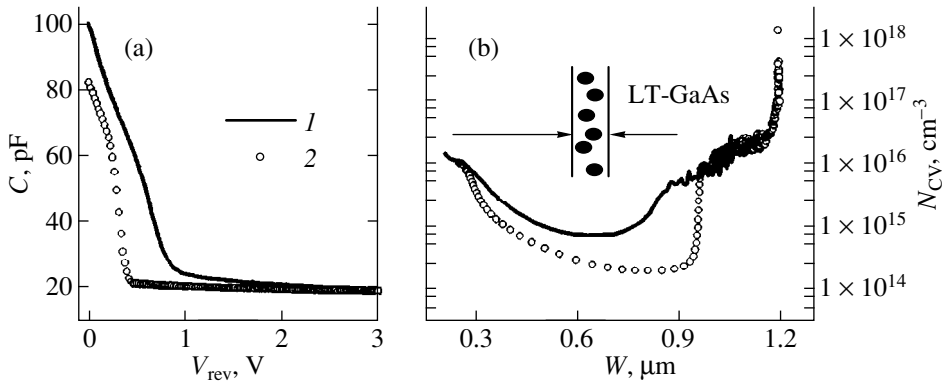

Fig. 2. (a) *C–V* and (b) $N_{CV} - W$ characteristics of a *P* structure, measured at 10 kHz at (*1*) 290 and (*2*) 77 K. The insert here (as in Figs. 3–5) shows the position of the LT-GaAs layer.

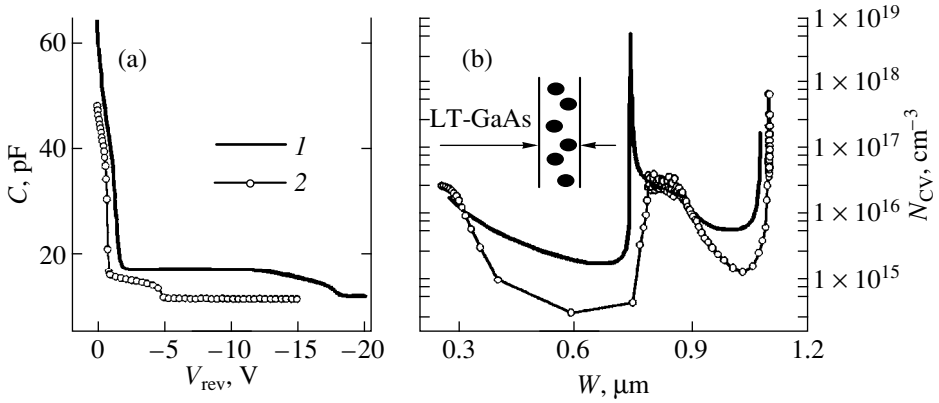

Fig. 3. (a) *C–V* and (b) $N_{CV} - W$ characteristics of an *N* structure, measured at 10 kHz at (*1*) 290 and (*2*) 94 K.

which lies the 0.1-μm-thick LT-GaAs layer (Fig. 2b). Such a carrier distribution N_{CV}–*W* across the *P* structure is presumably due to a substantial positive charge that accumulates in the LT-GaAs layer containing As clusters and induces a wide built-in SCR. The region in which there is an abrupt drop in the *P* structure capacitance is observed when, at $V_{rev} \approx 0.3$ V, the SCR of the Schottky barrier merges with the SCR induced about the LT-GaAs layer. At $V_{rev} > 6$ V, the boundary of the Schottky barrier SCR reaches the heavily doped p^+ substrate. Therefore, the *P* structure capacitance remains virtually unchanged and the N_{CV}–*W* characteristic shows a rise in the concentration for $W = 1.2$ μm corresponding to the total thickness of the epilayers of the *P* structure (Fig. 2b).

With the temperature raised to 290 K, the shape of the *C–V* characteristic of the *P* structure is virtually unchanged; however, the entire curve shifts to higher reverse voltages (Fig. 2a) because of the decreasing built-in potential of the Schottky barrier [7]. At 290 K, the *C–V* and N_{CV}–*W* characteristics become smoother, since the Debye screening length, determining the resolution of the *C–V* method, increases with increasing temperature [7]. It should be noted that the free-carrier concentration in the *p*-GaAs buffer layers of the structure, determined from the N_{CV}–*W* characteristics (Fig. 2b), is virtually independent of temperature, which points to a low concentration of electrically active defects in these epitaxial layers.

The *C–V* characteristic of the *N* structure at $T = 94$ K shows two portions of gradually changing capacitance (for $V_{rev} = 0$–0.5 V and $V_{rev} = 1.0$–4.2 V) (Fig. 3a), which are associated with uniform doping of the *n*-GaAs buffer layers to $\approx 3 \times 10^{16}$ cm^{-3} (Fig. 3b). For $V_{rev} > -5$ V, the capacitance of the *N* structure is virtually constant, since the boundary of the Schottky barrier SCR has already reached the heavily doped n^+ substrate at a depth of 1.1 μm (Fig. 3b) corresponding to the total thickness of epilayers of the *N* structure. The abrupt drop in the capacitance at $V_{rev} \approx 0.7$ V is associated with the accumulation of negative charge of electrons in the LT-GaAs layer and is observed when the SCR of the Schottky barrier merges with the SCR formed about the LT-GaAs layer (Fig. 3b). Calculation of the effective free-carrier concentration profile N_{CV}–*W* by formula (1) shows that a 0.45-μm-thick SCR is formed in the *N* structure at 94 K about the 0.1-μm-thick LT-GaAs layer (Fig. 3b).

The second abrupt change in the capacitance at $V_{rev} \approx 5$ V is due to the presence of an SCR located at the interface between the first *n*-GaAs buffer layer and the n^+ substrate (Fig. 3b) in the *N* structures. In our opinion, this is due to the presence of electrically active defects at the metallurgical junction between the n^+ substrate and the first epilayer. In the case of a *P* structure, a GaAs layer heavily doped with Be was deposited onto the p^+ substrate prior to growing the first *p*-type GaAs buffer. As can be seen from the effective concentration profile N_{CV}–*W* (Fig. 2b), there is no SCR at the interface between the first buffer layer and the p^+ substrate, since electrically active defects at the surface of the p^+ substrate are neutralized.

Thus, the *C–V* characteristics of the *P* and *N* substrates are qualitatively similar at low temperature. However, at $T = 290$ K, a broad plateau of quasi-constant capacitance appears in the *C–V* characteristic of the *N* structure in the V_{rev} range from –1.8 to –11.5 V (Fig. 3a). It has been shown previously that this plateau is associated with the emission of electrons accumulated in the LT-GaAs layer [6, 7]. The emission rate decreases as the temperature is lowered. As can be seen from Fig. 3a, the electron emission from the LT-GaAs layer in the *N* structure is completely suppressed at 94 K, so that no plateau is observed in the *C–V* characteristic. The absence of a quasi-constant capacitance portion in the *C–V* characteristic of the *P* structure not only at low temperature but also at room temperature (Fig. 2a) means that the rate of hole emission from the LT-GaAs layer in the *P* structure is much lower than the rate of electron emission from the same layer in the *N* structure.

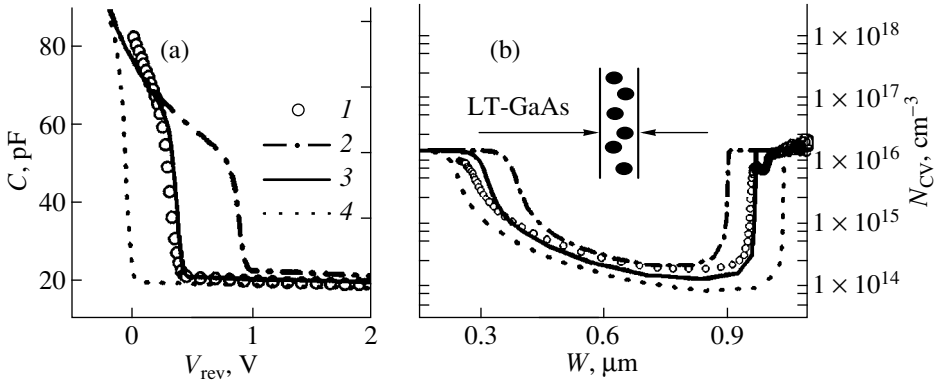

Fig. 4. (a) *C–V* and (b) $N_{CV} - W$ characteristics of a *P* structure, measured at 10 kHz at 77 K (*1*). Simulations of the *C–V* and $N_{CV} - W$ characteristics of the *P* structure were performed for density of charge accumulated in the LT-GaAs layer N_Q^{LT} = (*2*) 6.0×10^{11}, (*3*) 8.0×10^{11}, and (*4*) 1.0×10^{12} cm^{-2}.

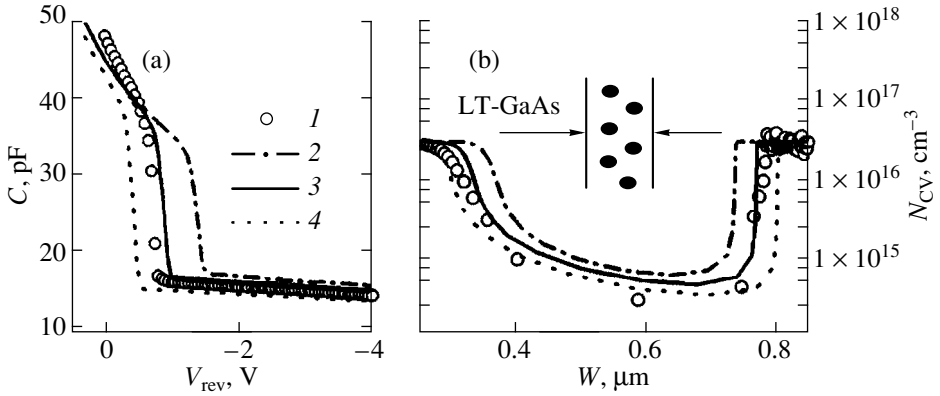

Fig. 5. (a) *C–V* and (b) $N_{CV} - W$ characteristics of an *N* structure, measured at 10 kHz at 94 K (*1*). Simulations of the *C–V* and $N_{CV} - W$ characteristics of the *N* structure were performed for the density of the charge accumulated in the LT-GaAs layer N_Q^{LT} = (*2*) 0.8×10^{12}, (*3*) 1.0×10^{12}, and (*4*) 1.2×10^{12} cm^{-2}.

To evaluate the charge accumulated in the LT-GaAs layer, the *C–V* and N_{CV}–*W* characteristics of *P* and *N* structures were simulated at low temperature. The simulation was based on a numerical solution of the one-dimensional Poisson equation by the finite-difference method [9, 10]. It was assumed that the emission rate of the accumulated carriers is low, so that the concentration of electrons or holes (N_Q^{LT}) localized in the LT-GaAs layer is independent of the reverse voltage V_{rev} across the structure.

A quantitative analysis of the *C–V* and N_{CV}–*W* characteristics of the *P* structure at *T* = 77 K (Figs. 4a, 4b) demonstrates that a charge corresponding to a hole density of $N_Q^{LT} = 0.8 \times 10^{12}$ cm^{-2} is accumulated in the LT-GaAs layer. Comparison of the results of calculations with experimental data for the *N* structure shows (Figs. 5a, 5b) that the best agreement is observed for $N_Q^{LT} = 1.0 \times 10^{12}$ cm^{-2}.

Thus, the investigation performed demonstrated that the LT-GaAs layer containing arsenic clusters accumulates electrons when sandwiched between *n*-GaAs layers and holes when sandwiched between *p*-GaAs layers. A broad SCR is formed about the LT-GaAs layer. A numerical analysis of *C–V* and N_{CV}–*W* characteristics on the basis of a one-dimensional solution of the Poisson equation shows that both electrons and holes are accumulated in local levels lying somewhat higher than the midgap of GaAs. Such levels may be related both to point defects and to nanoclusters. The concentrations of the latter ($N_{CL} \approx 4 \times 10^{11}$ cm^{-2} for the *N* structure and $N_{CL} \approx 6 \times 10^{11}$ cm^{-2} for the *P* structure), determined by TEM, are close to the concentrations of charge

carriers accumulated in the LT-GaAs layer (N_Q^{LT} = 1.0×10^{12} cm^{-2} and $N_Q^{LT} = 8 \times 10^{11}$ cm^{-2}, respectively).

CONCLUSION

The investigation of *C–V* characteristics of *n*-LT-*n* and *p*-LT-*p* structures with a Schottky barrier suggests that the LT-GaAs layers containing arsenic nanoclusters accumulate electrons or holes, respectively, and induce expansive depletion regions in the adjoining *n*- or *p*-type layers. The concentration of the accumulated majority carriers [$(8–10) \times 10^{11}$ cm^{-2}] is close to the concentration of As clusters in the LT-GaAs layer. The levels at which electrons and holes are accumulated lie somewhat higher than the midgap of GaAs. When a reverse voltage is applied, the rate of hole emission from the LT-GaAs layer in the *P* structure is much lower than that of electrons from the LT-GaAs layer in the *N* structure.

ACKNOWLEDGMENTS

This work was supported by the Ministry of Science of the Russian Federation, programs "Fullerenes and Atomic Clusters" and "Physics of Solid-State Nanostructures" (project no. 97-1035); the Russian Foundation for Basic Research (project no. 98-02-17617); and INTAS (grant no. 97-30930).

REFERENCES

1. F. W. Smith, A. R. Calawa, C. L. Chen, *et al.*, IEEE Electron Device Lett. **9**, 77 (1988).
2. M. Kaminska, Z. Liliental-Weber, E. R. Weber, *et al.*, Appl. Phys. Lett. **54**, 1881 (1989).
3. M. R. Melloch, K. Mahalingam, N. Otsuka, *et al.*, J. Cryst. Growth **111**, 39 (1991).
4. N. A. Bert, A. I. Veĭnger, M. D. Vilisova, *et al.*, Fiz. Tverd. Tela (St. Petersburg) **35**, 2609 (1993) [Phys. Solid State **35**, 1289 (1993)].
5. V. V. Chaldyshev, M. A. Putyato, B. R. Semyagin, *et al.*, Élektron. Prom-st., Nos. 1/2, 154 (1998).
6. P. N. Brounkov, V. V. Chaldyshev, A. A. Suvorova, *et al.*, Appl. Phys. Lett. **73**, 2796 (1998).
7. P. N. Brunkov, V. V. Chaldyshev, N. A. Bert, *et al.*, Fiz. Tekh. Poluprovodn. (St. Petersburg) **32**, 1170 (1998) [Semiconductors **32**, 1044 (1998)].
8. S. Sze, *Physics of Semiconductor Devices* (Wiley, New York, 1981; Mir, Moscow, 1984).
9. P. N. Brunkov, S. G. Konnikov, V. M. Ustinov, *et al.*, Fiz. Tekh. Poluprovodn. (St. Petersburg) **30**, 924 (1996) [Semiconductors **30**, 492 (1996)].
10. P. N. Brunkov, A. A. Suvorova, N. A. Bert, *et al.*, Fiz. Tekh. Poluprovodn. (St. Petersburg) **32**, 1229 (1998) [Semiconductors **32**, 1096 (1998)].

Translated by M. Tagirdzhanov

Semiconductors, Vol. 34, No. 9, 2000, pp. 1073–1078. Translated from Fizika i Tekhnika Poluprovodnikov, Vol. 34, No. 9, 2000, pp. 1114–1119.

LOW-DIMENSIONAL SYSTEMS

Diagnostics of the Hot-Hole Distribution Function in Quantum Wells in a Strong Electric Field

V. Ya. Aleshkin*, D. M. Gaponova*, V. I. Gavrilenko*, Z. F. Krasil'nik*, D. G. Revin*, B. N. Zvonkov, and E. A. Uskova****

**Institute for Physics of Microstructures, Russian Academy of Sciences, Nizhni Novgorod, 603600 Russia*
e-mail: aleshkin@ipm.sci-mnov.ru

*** Physicotechnical Research Institute, Nizhni Novgorod State University, Nizhni Novgorod, 603600 Russia*

Submitted March 6, 2000; accepted for publication March 16, 2000

Abstract—Modulation of the fundamental absorption edge by a high lateral electric field in a *p*-type $In_{0.21}Ga_{0.79}As/GaAs$ heterostructure with quantum wells was studied at 4.2 K and electric fields as high as 1.9 kV/cm. The field-induced change in the symmetric part of the hole distribution function was measured.

1. INTRODUCTION

Two experimental methods for measurement of the hot-carrier distribution function in bulk semiconductors are currently known. One of these was proposed by W. Pinson and R. Bray [1] and developed by L.E. Vorob'ev and coworkers [2, 3]. This method is based on monitoring the changes in the light-absorption coefficient under the action of an applied electric field in the wavelength range corresponding to the optical transitions from the light- and heavy-hole subbands into the spin-split subband. It has been used with success to determine both the symmetric part of the hot-hole distribution function in *p*-Ge [1, 2] and its anisotropy [3]. The second method was used to determine changes in the electron distribution function induced by a high electric field in thin samples of degenerate III–V semiconductors (see, e.g., [4, 5]). This method is based on observing the fundamental-absorption edge modulation by the electric field as a result of the "disruption" of the Burstein–Moss effect. As is known, the effect consists in a short-wavelength shift of the fundamental-absorption edge because of the carrier degeneracy in heavily doped semiconductors. An electric field leads to carrier heating and thereby depopulates the states that lie below the Fermi level and can be involved in optical transitions, which smears the short-wavelength fundamental-absorption edge. However, light absorption in a bulk semiconductor for frequencies corresponding to the final electron states lying above the Fermi level is very high. That is why this method has been successfully used to observe light-absorption modulation only for frequencies corresponding to transitions to final states lying below the Fermi level. As a result, the field-induced changes in the distribution function could only be determined for energies lower than the Fermi energy.

The possibility of applying the second method to measure the hot carrier distribution function in quantum wells (QWs) was demonstrated experimentally in our previous study [6]. In contrast to a bulk sample, the interband light-absorption coefficient in QWs is small (on the order of one percent in a single QW) and, therefore, its modulation can be easily detected for transitions to states lying both below and above the Fermi level. Consequently, a change in the carrier-distribution function under the action of an electric field can also be easily detected for carriers with energy exceeding the Fermi energy. However, only the effective hole temperature was estimated by comparing the measured and calculated light-transmission modulation for equilibrium distribution functions at different temperatures; the distribution function itself was not determined [6].

In this study, we determined the changes induced by an electric field in the symmetric part of the hole distribution function in QWs of the $In_{0.21}Ga_{0.79}As/GaAs$ heterostructure. This was done by measuring the light-transmission modulation by a pulsed strong electric field in the QW interband-absorption range, with subsequent mathematical processing of the experimental data.

2. EXPERIMENTAL PROCEDURE AND RESULTS

The heterostructure under the study was grown under atmospheric pressure by MOC hydride epitaxy on (001) semi-insulating GaAs and contained 20 105-Å-wide $In_{0.21}Ga_{0.79}As$ QWs separated by barrier GaAs layers with a width of 600 Å. The GaAs barriers were δ-doped with Zn to a distance of 50 Å from the boundary of each QW. Hall measurements yielded a hole density within a single QW of $p_s \approx 1.7 \times 10^{11}$ cm^{-2} and the mobility $\mu \approx 315$ cm^2/(V s) at 300 K.

Photoluminescence (PL) and light-transmission modulation were measured at 4.2 K. Voltage pulses with an amplitude of up to 600 V and a duration of

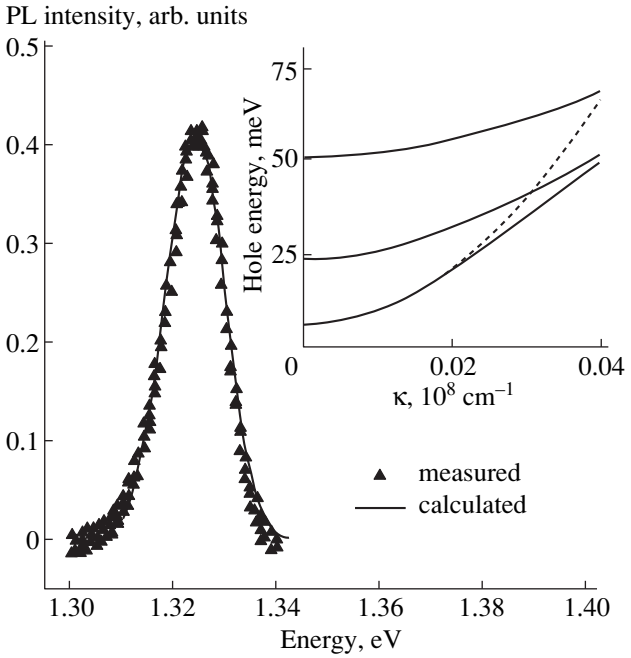

Fig. 1. Measured (triangles) and calculated (solid line) PL spectra for an $In_{0.21}Ga_{0.79}As/GaAs$ heterostructure with QWs 150 Å thick. The insert shows the calculated hole spectrum in a QW. Dashed line represents $\varepsilon_{hh1} + \hbar^2k^2/2m_h$; $m_h = 0.1m_0$.

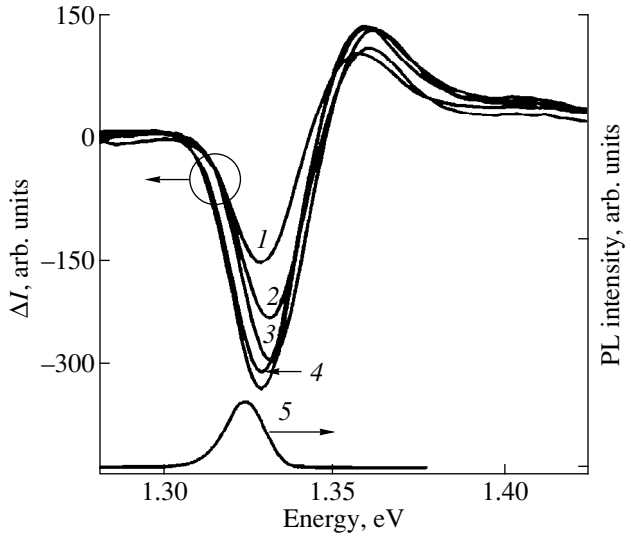

Fig. 2. Measured spectra of light transmission modulation by an electric field E for an $In_{0.21}Ga_{0.79}As/GaAs$ heterostructure with QWs 105 Å thick. A PL spectrum at $E = 0$ (curve *5*) is presented in the lower part of the figure. E = (*1*) 380, (*2*) 630, (*3*) 1260, (*4*) 1580, and (*5*) 1900 V/cm.

3–10 μs were applied to a sample under study via ohmic stripe contacts deposited on its surface. The highest electric-field strength in the sample was 1900 V/cm. Voltage pulse-repetition frequencies (3–10) Hz and pulse widths were chosen so that the crystal lattice did not heat up noticeably during a pulse and cooled completely between pulses. Interband PL was excited by the 514-nm spectral line of a CW Ar^+ laser; the radiation emitted by the sample was passed through a monochromator and detected by a photomultiplier. An opaque diaphragm with an aperture ~1.5 mm in diameter was installed in front of the sample and screened the contacts from the incident light to prevent light-induced carrier injection.

A quartz halogen lamp was used as a light source in studying the transmission modulation. Radiation with the required photon energy ($\hbar\omega$ = 1.25–1.45 eV, $\Delta\hbar\omega \approx$ 3 meV) was separated from the wide emission spectrum using a monochromator. This radiation was directed onto the sample via an optical fiber. The light transmitted through the sample was detected with a germanium photodiode mounted immediately behind the sample. The output signal of the photodiode was proportional to the difference of the transmitted-light intensities in the absence and presence of an applied electric field. In addition, the signal induced by light modulated by a mechanical chopper and incident on the photodiode was measured in order to determine the sign of the transmission change induced by the applied electric-field pulses.

The PL spectra of the heterostructure under study, measured in the absence of an applied electric field (see Fig. 1), comprise a single line corresponding to transitions between the first size-quantization subbands of electrons and holes (*e*1–*hh*1). The fairly large half-width of the line at 4.2 K (~18 meV) is mainly due to the scatter of QW parameters in the heterostructure. A PL spectrum calculated with account of the QW-material composition fluctuations is shown in Fig. 1. We assumed the fluctuations to be Gaussian, and therefore the PL intensity spectrum was calculated by the formula

$$I_{PL}(\hbar\omega) \sim \int_{-\infty}^{\infty} \exp\left(-\frac{(x-\bar{x})^2}{2\sigma_x}\right) \times f_e\left([\hbar\omega - \varepsilon_{e1-hh1}(x)]\frac{m}{m_c}\right), \quad (1)$$

where $\bar{x}$ and σ_x are, respectively, the mean and variance of the indium content in the QW and $f_e(\varepsilon)$ is the unnormalized distribution function of photoelectrons in the conduction band:

$$f_e(\varepsilon) = \Theta(\varepsilon)\exp\left(-\frac{\varepsilon}{T}\right). \quad (2)$$

Here, ε is the electron kinetic energy, $\Theta(\varepsilon)$ is the Heaviside function, T is the temperature in energy units (T = 4.2 K), and $\varepsilon_{e1-hh1}(x)$ is the minimal transition energy between the first electron and hole subbands. The $\bar{x}$ and σ_x values were chosen to ensure the best possible agreement between the calculated and measured PL line shapes. It can be seen from Fig. 1 that these spectra practically coincide for $\bar{x}$ = 0.21 and σ_x = 0.006.

Transmission modulation spectra measured for the heterostructure subjected to an electric field of varied strength are shown in Fig. 2. A PL spectrum measured in the absence of the field is shown for comparison. It can be seen that application of the electric field may increase or decrease the light transmission. A change in light transmission is noticeable even in rather weak electric fields of ~40 V/cm. Both positive and negative transmission modulations increase with increasing electric field, being approximately the same at moderate fields. The negative modulation starts to dominate over the positive modulation in strong fields. The field dependence of the transmission tends to level off at field strengths exceeding 1.2 kV/cm. The positions of peaks and dips in the transmission modulation spectra are virtually independent of the electric field.

3. DISCUSSION

The dimensionless absorption coefficient (the ratio of absorbed power to the sum of absorbed and transmitted powers) of a single QW for normal radiation incidence can be written as

$$\alpha(\omega) = \frac{2e^2}{m_0^2 \omega c \sqrt{\varepsilon_\infty}} \int d^2k \left|\langle \psi_c^* | \hat{p}_x | \psi_v \rangle\right|^2 \times \delta(\varepsilon_c(\mathbf{k}) - \varepsilon_v(\mathbf{k}) - \hbar\omega) f_{v(\mathbf{k})}[1 - f_c(\mathbf{k})], \quad (3)$$

where ω is the circular frequency of the incident radiation; e and m_0 are the charge and mass of a free electron, respectively; c is the speed of light; ε_∞ is the high-frequency dielectric constant of the QW; $\mathbf{k}$ is the electron wave vector in a lateral direction; $\psi_i(\mathbf{k})$, $\varepsilon_i(\mathbf{k})$, and $f_i(\mathbf{k}, E)$ are, respectively, the wave function, dispersion law, and distribution function of electrons in the ith band; the subscripts c and v refer to the conduction and valence bands; and p_x is the momentum-operator component aligned with the electric-field vector of light. Using the Kane model [7], the matrix element of the momentum operator may be written as (see, e.g., [8])

$$\left|\langle \psi_c^* | \hat{p}_x | \psi_v \rangle\right|^2 = \chi^2 \frac{3E_g(E_g + \Delta)}{2m_0(3E_g + \Delta)}\left(\frac{m_0}{m_c} - 1\right), \quad (4)$$

where χ is the overlap integral of wave function envelopes in the valence and conduction bands and E_g, Δ, and m_c are the band gap, spin–orbit splitting, and effective electron mass in the conduction band of the QW material. Since we are dealing with a p-type material, $f_c \approx 0$. Moreover, we are interested in the frequency range where the photon energy does not significantly exceed the onset energy of interband transitions and where, therefore, the following expressions can be used to describe electron dispersion in the conduction and valence bands:

$$\varepsilon_c(\mathbf{k}) = \frac{\hbar^2 k^2}{2m_c} + \varepsilon_{e1}, \quad \varepsilon_v(\mathbf{k}) = -\frac{\hbar^2 k^2}{2m_h} + \varepsilon_{hh1}, \quad (5)$$

where ε_{e1} and ε_{hh1} are the first electron size-quantization energy levels in the bands and m_h is the hole mass at the first subband bottom. We used the following values for the electron and hole masses in the QWs of the heterostructure under study: $m_c = 0.067m_0$, $m_h = 0.1m_0$, where m_0 is the free electron mass (see the insert of Fig. 1). Using formulas (4) and (5) and assuming that $f_c = 0$, we obtain the following expression for the absorption coefficient [9]:

$$\alpha(\omega) = A\left\{1 - \bar{f}_h\left[\varepsilon_h = (\hbar\omega - \varepsilon_{e1-hh1})\frac{m^*}{m_h}\right]\right\}, \quad A = \gamma \frac{2\pi|\chi|^2}{\sqrt{\varepsilon_\infty}} \frac{3(E_g + \Delta)}{(3E_g + \Delta)}\left(\frac{m_0}{m_c} - 1\right)\frac{m^*}{m_0}. \quad (6)$$

Here, $\gamma = e^2/\hbar c$ is the fine structure constant; $m^* = m_h m_c/(m_h + m_c)$ is the reduced mass;

$$\bar{f}_h(\varepsilon_h) = \frac{1}{2\pi}\int_0^{2\pi} d\varphi [1 - f(\mathbf{k})] \quad (7)$$

is the hole-distribution function in the first size-quantization subband of the valence band, averaged over the angle φ determining the direction of the wave vector in the QW plane; and $\varepsilon_h = \hbar^2 k^2/2m_h$ is the hole kinetic energy. We note that, in the two-dimensional case, the hole-energy distribution $f_h(\varepsilon)$ differs from $\bar{f}_h(\varepsilon)$ only by a constant coefficient $f_h(\varepsilon) = \bar{f}_h(\varepsilon)2\pi m_h/h^2$.

The change in the absorption coefficient induced by an electric field is related to the change in the hole-distribution function

$$\Delta\alpha(\omega) = -A\Delta\bar{f}_h\left[(\hbar\omega - \varepsilon_{e1-hh1})\frac{m^*}{m_h}\right], \quad \Delta\bar{f}_h(\varepsilon_h) = \bar{f}_n(\varepsilon_h) - f_0(\varepsilon_h), \quad (8)$$

where $f_0(\varepsilon_h)$ is the equilibrium hole distribution function

$$f_0(\varepsilon_h) = \frac{1}{1 - \exp\left(\dfrac{\varepsilon_h - \varepsilon_{hh1} - F}{T}\right)}, \quad (9)$$

with F standing for the chemical potential. The change in the reflection coefficient for the QW is appreciably smaller than that in the absorption coefficient [8]. Therefore, the field-induced modulation of the intensity of light transmitted through the QW is controlled by the change in absorption and is proportional to a change in the hole distribution function:

$$\Delta T(\hbar\omega) = \frac{\Delta I(\hbar\omega)}{I} = (1 - R)A\Delta\bar{f}_h\left[\frac{m^*}{m_h}(\hbar\omega - \varepsilon_{e1-hh1})\right], \quad (10)$$

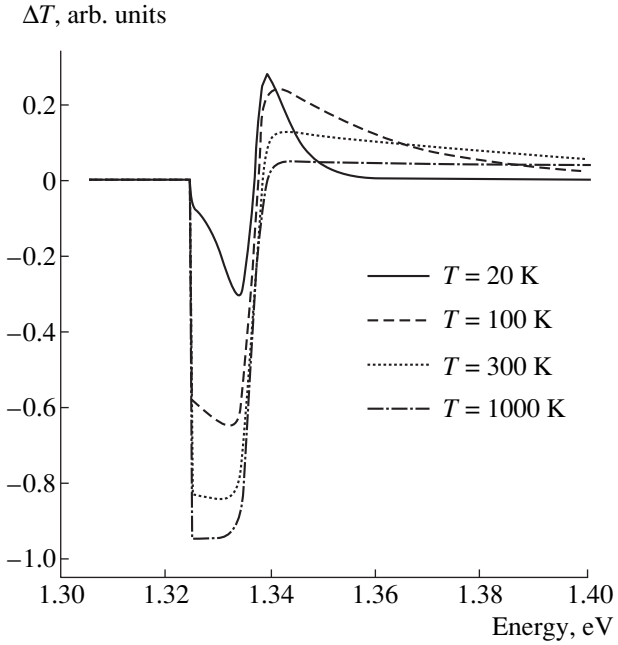

Fig. 3. Calculated spectra of the light-transmission modulation induced by hole-gas heating in an $In_{0.21}Ga_{0.79}As/GaAs$ heterostructure with QWs 105 Å thick and a hole density of 2×10^{11} cm^{-2} (without parameter fluctuations). The hole distribution functions were assumed to be described by the Fermi–Dirac distribution with effective temperature *T*.

where *R* is the total reflection coefficient of the whole structure. Therefore, by measuring the field dependence of the transmission $\Delta I(\hbar\omega)/I$, we can determine changes in the hole distribution function on applying an electric field. We note that the energy scale for ΔI differs from that for $\Delta \bar{f}_h$ by a factor $m_h/m^* = (1 + m_h/m_c)$.

Formula (10) can be illustrated by a simple example. Let the hole-gas temperature in the absence of electric field be 4.2 K. Let us also assume that the electric field merely raises the effective hole-gas temperature, with the distribution function shape (9) and the hole density in the first subband preserved. Figure 3 shows $\Delta T(\hbar\omega)$ dependences at different effective hole temperatures for an $In_{0.21}Ga_{0.79}As/GaAs$ heterostructure with a QW width of 105 Å, in which case $m_h = 0.1m_0$, $m_c = 0.067m_0$, and $p_s = 2 \times 10^{11}$ cm^{-2}. It can be seen that hole-gas heating causes the light transmission to increase in the short-wavelength range of the absorption spectrum and to decrease at long wavelengths. The reason is that the heating tends to increase the occupation of electron states above the Fermi level in the valence band and to decrease the occupation of electron states below the Fermi level. As mentioned in the Introduction, the modulation of light transmission is associated with the "disruption" of the Burstein–Moss effect as a result of carrier heating.

We now take into account the effect of fluctuations on the modulation of light transmission by an electric field. For the structures under study, the most important fluctuations are those of composition [10]. Typically, these fluctuations can be described by a Gaussian distribution. The validity of this description can be verified by comparing the calculated PL spectrum with that observed experimentally (see Fig. 1). For the Gaussian fluctuations of the composition, the transmission modulation can be described as

$$\Delta T(\hbar\omega) \approx \frac{(1-R)AN}{\sqrt{2\pi\sigma_x}} \int_{-\infty}^{\infty} \exp\left[-\frac{(x-\bar{x})^2}{2\sigma_x^2}\right] \Delta \bar{f}_h \times \left(\frac{m^*}{m_h}[\hbar\omega - \varepsilon_{e1-hh1}(\bar{x}) - B(x-\bar{x})]\right) dx, \quad (11)$$

where $B = d\varepsilon_{e1-hh1}(x)/dx$ for $x = \bar{x}$ and *N* is the number of QWs. Formula (11) is valid if the variance of *x* is small and the regions with constant *x* are much larger than the space charge regions between them. The latter condition means that the effect of fluctuations in *x* on the charge-carrier density may be neglected. In what follows, we assume that both of these conditions are satisfied. It can also be shown that the dopant-concentration fluctuations affect the light transmission to a much lesser extent than do the composition fluctuations. For example, Gaussian fluctuations with a hole density variance of 10% in an $In_{0.21}Ga_{0.79}As$ structure with a QW thickness of 105 Å and a mean hole density of 2×10^{11} cm^{-2}, studied experimentally, lead to a relative change of light transmission that amounts to several percent. For this reason, we neglect the hole-density fluctuations induced by dopant concentration fluctuations.

Integral Eq. (11) has to be solved to find the distribution function $\Delta \bar{f}_h(\varepsilon_h)$ from an experimental $\Delta T(\hbar\omega)$ dependence. However, it is impossible to exactly solve this equation for nonzero σ_x. The reason is that the integral operator with such a kernel (11) has eigenfunctions $\exp ikx$ with eigenvalues $(1 - R)A\exp(-k^2\sigma_x/2)$ vanishing in the limit of $k \longrightarrow \pm\infty$. This means that $\Delta T(\hbar\omega)$ is "insensitive" to the changes $\Delta \bar{f}_h(\varepsilon_h)$ on a length scale less than $m_h B\sigma_x/m$; i.e., $\Delta \bar{f}_h(\varepsilon_h)$ cannot be determined with the described accuracy. Formally, this manifests itself in the fact that the operator with zero eigenvalues has no inverse operator.

An approximate solution to Eq. (11) can be found. The Green function of the integral operator (11) can be written as a limit for $a \longrightarrow 0$:

$$G(y-y') = \lim[G_a(y-y')],$$

$$G_a(y) = \frac{1}{2\pi(1-R)A} \int_{-\infty}^{\infty} dk \frac{\exp iky}{\exp\left[-\frac{(k\sigma_x Bm)^2}{2m_h^2}\right] + ak^2}. \quad (12)$$

Using Eq. (12), we can write the following solution to Eq. (11), considering G_a as an approximate Green's function:

$$\Delta \bar{f}_h(\varepsilon_h) = \int_{-\infty}^{\infty} dy G_a(y-\varepsilon_h)\Delta T\left[\frac{y m_h}{m} + \varepsilon_{e1-hh1}(\bar{x})\right]. \quad (13)$$

We note that a in (12) cuts off the contribution from higher harmonics to Green's function. For $a \longrightarrow 0$, G_a tends to infinity and, therefore, we cannot choose a value for a that is too small. Too small a value of a leads, on the one hand, to calculation errors and, on the other, to a strong influence of $\Delta T(\hbar\omega)$ measurement errors on the result obtained. It should be noted that the $G_a(y)$ function falls fast with increasing y on a characteristic scale of $B\sigma_x$. Therefore, a region with a size on the order of $B\sigma_x$ in the vicinity of the $y = \varepsilon_h$ point contributes to integral (13).

Figure 4 shows both the dependence $\Delta \bar{f}_h(\varepsilon_h)$ calculated from the Fermi–Dirac distribution (for electron temperatures in the range from 4.2 to 150 K) and the dependence $\Delta f_n(\varepsilon_h)$ reconstructed from $\Delta T(\hbar\omega)$ for two $In_{0.21}Ga_{0.79}As/GaAs$ structures with QWs 105 Å wide and hole density $p_s = 2 \times 10^{11}$ cm^{-3}, differing in x variance: $\sigma_x = 0.003$ and $\sigma_x = 0.006$. It is evident that the reconstructed dependence $\Delta f_h(\varepsilon_h)$ agrees well with the dependence obtained from the Fermi–Dirac distribution for the structure with $\sigma_x = 0.003$ and much worse for that with $\sigma_x = 0.006$.

The dependences $\Delta f_h(\varepsilon_h)$ calculated by (13) from the experimental data are shown in Fig. 5 (experimental data shown in Fig. 2 were used). The value of a was chosen to be 0.03. Since the absolute value of the absorptivity was not measured, the change in $\Delta \bar{f}_h(\varepsilon_h)$ was determined, strictly speaking, to within a constant factor. We used the following reasoning to estimate it. The magnitude of the dip in $\Delta \bar{f}_h(\varepsilon_h)$ obviously tends to a constant value at high electric fields (see Fig. 5). It is clear that the limit this dip approaches equals –1. The limiting case occurs when all holes leave the states with corresponding energy. For this reason, we chose the constant in such a way that the change in the distribution function at low energies and an electric field strength of 1900 V/cm was on the order of unity.

It can be seen in Fig. 5 that, in moderate electric fields (380 V/cm), the integrated (over the hole energy) positive and negative modulations $\Delta \bar{f}_h(\varepsilon_h)$ have approximately equal magnitudes, which reflects the conservation of the total number of holes in the first size-quantization subband. With increasing electric field strength, the negative modulation of the distribution function begins to dominate over the positive one and this integral becomes negative, which corresponds to a decrease in the hole density in the first subband. We note that holes in the second hole subband, lying 0.19 meV higher than the first one, make only a minor contribution to the absorption in the measured spectral region, since a transition from the second hole subband to the first electron subband is forbidden. Holes in the

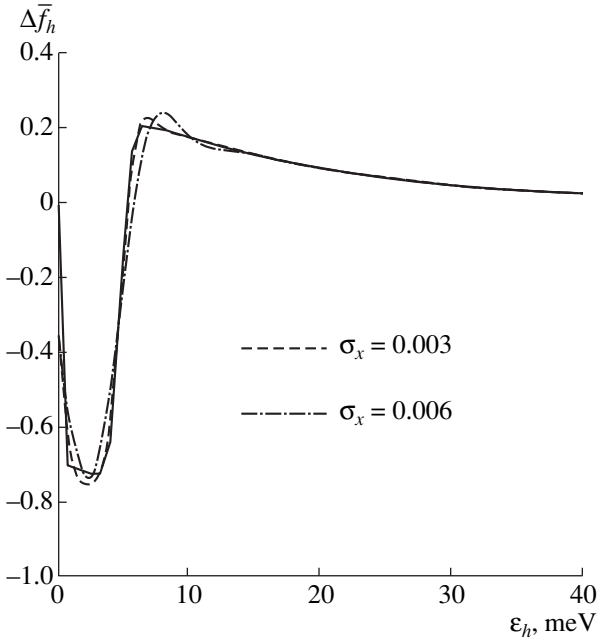

Fig. 4. Changes in the hole-distribution function, obtained by means of Eq. (13) from the calculated transmission modulation for two $In_{0.21}Ga_{0.79}As$ QWs with different σ_x. The light transmission modulation is due to a hole temperature rise from 4.2 to 150 K. The hole density is 2×10^{11} cm^{-2}. The solid line corresponds to a change in the hole-distribution function calculated from the Fermi–Dirac distribution.

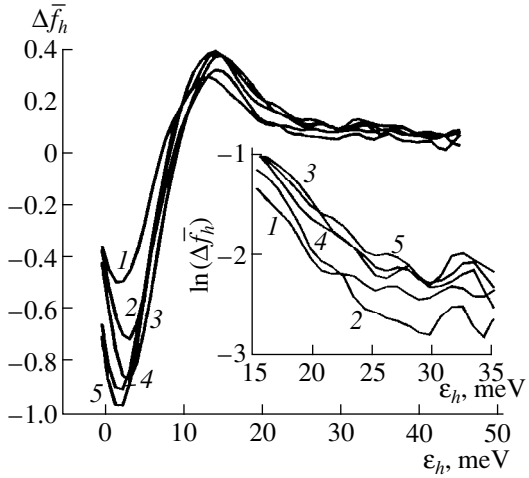

Fig. 5. Changes in the hole distribution function $\Delta \bar{f}_h(\varepsilon_h)$ induced by the electric field E and calculated from the measured light-transmission modulation spectra. E = (*1*) 380, (*2*) 630, (*3*) 1260, (*4*) 1580, and (*5*) 1900 V/cm. The insert shows the dependences $\Delta \bar{f}_h(\varepsilon_h)$ on the logarithmic scale for energies higher than 15 meV.

third subband also contribute only slightly to the absorption in the measured spectral range because of the small overlap integral χ for the transition to the first electron subband. Thus, it follows from Fig. 5 that the escape of holes from the lower subband is noticeable at fields exceeding 380 V/cm.

In the insert in Fig. 5, the dependences $\Delta \bar{f}_h(\varepsilon_h)$ are shown on a logarithmic scale for energies higher than the peak energy Δf_h. It can be seen that this dependence is almost linear for low energies (below 20–30 meV) and $\Delta \bar{f}_h(\varepsilon_h)$ behaves irregularly for higher energies. The linear dependence corresponds to the Maxwell distribution of holes. The effective hole temperature determined from this linear portion has the following values: $T(E = 380$ V/cm) = (110 ± 30) K, $T(E = 630$ V/cm) = (90 ± 25) K, $T(E = 1260$ V/cm) = (110 ± 15) K, $T(E = 1580$ V/cm) = (125 ± 15) K, $T(E = 1900$ V/cm) = (127 ± 20) K.

For high energies, the function $\Delta \bar{f}_h(\varepsilon_h)$ is determined with a large error that is probably related to gross experimental errors in measuring the transmission modulation in the corresponding spectral range, which occurs because of the small signal amplitude.

A nonparabolicity of the hole spectrum (see the insert in Fig. 1) becomes noticeable at high energies, and the proposed method for reconstructing the distribution-function change should be modified. We note also that the accuracy of reconstruction of the distribution-function change is low because of the large scatter in x (the variance $\sigma_x = 0.006$, which corresponds to PL line half-width of 17 meV).

Thus, we have determined the changes induced by an electric field in the hole distribution function in QWs by measuring the light transmission modulation near the fundamental-absorption edge.

ACKNOWLEDGMENTS

The work was supported by the Russian Foundation for Basic Research (project no. 00-02-16159), the Interdisciplinary Program "Physics of Solid-State Nanostructures" (project nos. 97-2022 and 99-1128), the Interdisciplinary Program "Physics of Microwaves" (project no. 3.17), the State Scientific and Technological Program "Physics of Quantum and Wave Processes/Fundamental Spectroscopy" (project no. 8/02.08), the Federal Special Program "Integration" (project nos. 540 and 541), and the Russian National Program for Support of Leading Scientific Schools.

REFERENCES

1. W. E. Pinson and R. Bray, Phys. Rev. A **136**, 1449 (1964).
2. L. E. Vorob'ev, Yu. K. Pozhela, A. S. Reklaĭtis, *et al.*, Fiz. Tekh. Poluprovodn. (Leningrad) **12**, 742 (1978) [Sov. Phys. Semicond. **12**, 433 (1978)].
3. L. E. Vorob'ev, Yu. K. Pozhela, A. S. Reklaĭtis, *et al.*, Fiz. Tekh. Poluprovodn. (Leningrad) **12**, 754 (1978) [Sov. Phys. Semicond. **12**, 440 (1978)].
4. W. Jantsch and H. Heinrich, Solid State Commun. **13**, 715 (1973).
5. W. Jantsch and H. Brücker, Phys. Rev. B **15**, 4014 (1977).
6. V. Ya. Aleshkin, A. A. Andronov, A. V. Antonov, *et al.*, in *Proceedings of the International Symposium on Nanostructures: Physics and Technology, St. Petersburg, 1998*, p. 168.
7. E. O. Kane, J. Phys. Chem. Solids **1**, 249 (1957).
8. G. Bastard, *Wave Mechanics Applied to Semiconductor Heterostructures* (Les Editions de Physique, 1988).
9. D. G. Revin, Author's Abstract of Candudate's Dissertation (Nizhni Novgorod, 1999).
10. I. A. Avrutskiĭ, O. P. Osaulenko, V. G. Plotnichenko, and Yu. N. Pyrkov, Fiz. Tekh. Poluprovodn. (St. Petersburg) **26**, 1907 (1992) [Sov. Phys. Semicond. **26**, 1069 (1992)].

Translated by S. Ktitorov

Semiconductors, Vol. 34, No. 9, 2000, pp. 1079–1084. Translated from Fizika i Tekhnika Poluprovodnikov, Vol. 34, No. 9, 2000, pp. 1120–1124.

LOW-DIMENSIONAL SYSTEMS

Size-Quantization Stark Effect in Quasi-Zero-Dimensional Semiconductor Structures

S. I. Pokutniĭ

Illichivsk Educational Research Center, Odessa State University, Illichivsk, 68001 Ukraine
e-mail:wladik@tecom.odessa.ua

Submitted November 24, 1999;
accepted for publication March 23, 2000

Abstract—A theory of the size-quantization Stark effect in semiconductor nanocrystals under conditions in which the polarization interaction of an electron (hole) with a nanocrystal surface plays the dominant role is developed. It is shown that, in the region of interband absorption, the shifts of electron (hole) size-quantization levels in a nanocrystal subjected to an external homogeneous electric field are governed by the quadratic Stark effect. A new electrooptical method is proposed furnishing an opportunity to determine the critical radii of nanocrystals in which bulk excitons can appear. © *2000 MAIK "Nauka/Interperiodica".*

1. INTRODUCTION

Nowadays, optical [1–4] and electrooptical [5–7] properties of quasi-zero-dimensional (quasi-0D) structures [quantum dots (QDs)] comprising semiconductor nanocrystals (SNCs) of a spherical shape with radii $a \simeq 1–10^2$ nm grown in transparent dielectric matrices are being studied intensively. The reason for this is that such heterosystems are new promising materials for new elements of nonlinear optoelectronics (in particular, elements for optical-signal control in optical computers and QD lasers).

Since the band gap of a semiconductor is much narrower than that of dielectric matrices, the carrier motion in an SNC is confined to within its volume. The optical and electrooptical properties of such heterosystems are controlled by the energy spectrum of the confined electron–hole pair (exciton) [1–7]. Methods of optical spectroscopy have been used to detect the size quantization of electron [1, 2] and exciton [3, 4] energy spectra in such quasi-0D structures.

Interest in studying electrooptical effects in quasi-0D semiconductor systems is due to the fact that the Stark shift of energy levels of confined electron–hole pairs (excitons) is not accompanied by any abrupt drop in the oscillator strength of the corresponding transitions in SNCs [5]. This parameter has high values exceeding those typical of the oscillator strength of optical transitions in semiconductors [8, 9]. As a result, exciton states remain stable in electric fields much stronger than the ionization field in the bulk semiconductor at Stark shifts that exceed the exciton binding energy [6, 7].

The effect of electric fields with strength as high as 10^7 V/m on the absorption spectra of glasses doped with CdS and CdSSe SNCs in the region of the interband-absorption edge has been studied previously [5, 10]. The observed dependence of the Stark shift of electron (hole) energy levels on the SNC size is governed by specific features of the energy spectrum of a confined electron–hole pair (exciton) in a homogeneous external electric field. The problem of the occurrence of bulk excitons in SNCs subjected to a homogeneous external electric field has not been discussed in [5, 10]. By a bulk exciton in an SNC we mean an exciton whose structure (reduced effective mass, Bohr radius, and binding energy) is the same as that of an exciton in the bulk semiconductor material.

In this study, a theory is developed on the size-quantization Stark effect in SNCs under the conditions in which the polarization interaction of an electron (hole) with the SNC surface plays the dominant role. It is shown that the shifts of electron (hole) size-quantization levels in an SNC subjected to an external homogeneous electric field in the region of interband absorption are governed by the quadratic Stark effect. A new electrooptical method is proposed, furnishing an opportunity to determine the critical radii of nanocrystals in which bulk excitons may appear.

2. THE STARK SHIFT OF THE ELECTRON–HOLE-PAIR ENERGY LEVELS IN A SEMICONDUCTOR NANOCRYSTAL SUBJECTED TO A HOMOGENEOUS EXTERNAL ELECTRIC FIELD

A simple model of a quasi-0D structure in the form of a neutral spherical SNC with radius a and permittivity ε_2, surrounded by a medium with permittivity ε_1, has been considered previously [11–13]. An electron e and a hole h having effective masses m_e and m_h, respectively, move inside such an SNC, with r_e (r_h) being the distance from the electron (hole) to the SNC center. The

1063-7826/00/3409-1079$20.00

permittivities of the SNC and the surrounding medium are supposed to be significantly different ($\varepsilon_1 \ll \varepsilon_2$). It is also assumed that the electron and hole energy bands are parabolic.

The characteristic dimension parameters of the problem are as follows: a, a_e, a_h, a_{ex}, where $a_e = \varepsilon_2\hbar^2/m_e e^2$, $a_h = \varepsilon_2\hbar^2/m_h e^2$, $a_{ex} = \varepsilon_2\hbar^2/\mu e^2$ are the electron, hole, and exciton Bohr radii in a semiconductor with permittivity ε_2, respectively; $\mu = m_e m_h/(m_e + m_h)$ is the reduced exciton effective mass; and e is the elementary charge. The fact that all the characteristic dimension parameters of the problem significantly exceed the lattice constant a_0 (a, a_e, a_h, $a_{ex} \gg a_0$) allows the electron and hole motion to be considered within the framework of the effective-mass approximation.

In the model in question, considered in the context of the above-mentioned approximations, the Hamiltonian of an electron–hole pair in an SNC subjected to a homogeneous external electric field F has the form

$$H = -(\hbar^2/2m_e)\Delta_e - (\hbar^2/2m_h)\Delta_h + E_g + V_{hh'}(r_h, a) + V_{eh}(r_e, r_h) + V_{ee'}(r_e, a) + V_{eh'}(r_e, r_h, a) + V_{he'}(r_e, r_h, a) + eFr_e - eFr_h, \quad (1)$$

where the first two terms determine the kinetic energy of the electron and the hole, $V_{eh}(r_e, r_h)$ is the energy of the electron–hole Coulomb interaction

$$V_{eh}(r_e, r_h) = -\frac{e^2}{2\varepsilon_2 a}\frac{2a}{(r_2^2 - 2r_e r_h\cos\theta + r_h^2)^{1/2}}, \quad \theta = \widehat{r_e r_h}, \quad (2)$$

$V_{ee'}(r_e, a)$ ($V_{hh'}(r_h, a)$) is the energy of the interaction of an electron (hole) with its own image, and $V_{eh'}(r_e, r_h, a)$ ($V_{he'}(r_e, r_h, a)$) is the energy of the interaction of an electron (hole) with an image of an oppositely charged carrier. The last two terms in expression (1) describe the energy of interaction of an electron (hole) with the applied electric field of strength F, E_g is the band gap of a bulk semiconductor with permittivity ε_2.

For arbitrary ε_1 and ε_2, the terms $V_{hh'}(r_h, a)$, $V_{ee'}(r_e, a)$, $V_{eh'}(r_e, r_h, a)$, and $V_{he'}(r_e, r_h, a)$ in (1), which describe the energy of the polarization interaction of an electron and a hole with the SNC surface, can be presented in analytical form [14], which becomes particularly simple in the case of $\varepsilon_1 \ll \varepsilon_2$ [11–13]:

$$V_{hh'}(r_h, a) = \frac{e^2}{2\varepsilon_2 a}\left(\frac{a^2}{a^2 - r_h^2} + \frac{\varepsilon_2}{\varepsilon_1}\right), \quad (3)$$

$$V_{ee'}(r_e, a) = \frac{e^2}{2\varepsilon_2 a}\left(\frac{a^2}{a^2 - r_e^2} + \frac{\varepsilon_2}{\varepsilon_1}\right), \quad (4)$$

$$V_{eh'} = V_{he'} = -\frac{e^2}{2\varepsilon_2 a}\frac{a}{[(r_e r_h/a)^2 - 2r_e r_h\cos\theta + a^2]^{1/2}}. \quad (5)$$

Let us study the effect of an applied electric field F on the energy spectrum of an electron–hole pair confined in an SNC whose size is limited by the condition

$$a_0 \ll a_h \ll a \le a_e \le a_{ex}. \quad (6)$$

When this condition is met, the polarization interaction makes the main contribution to the potential energy of the Hamiltonian (1). The fulfillment of the condition (6) (i.e., $m_e \ll m_h$) makes it possible to consider the motion of a heavy hole in a potential averaged over the electron motion (adiabatic approximation).

First, we present the spectrum of an electron–hole pair in the state n_e, $l_e = 0$, t_h confined to an SNC whose radius satisfies condition (6), obtained previously [11–13] in terms of the adiabatic approximation and the first-order perturbation theory in the functions of an infinitely deep spherical potential well (using the Hamiltonian (1) with the last two terms neglected):

$$E^{t_h}_{n_e,0}(S) = E_g + \frac{\pi^2 n_e^2}{S^2} + \frac{1}{S}\left[Z_{n_e,0} + \frac{\varepsilon_2}{\varepsilon_1}\right] + \lambda^{t_h}_{n_e,0}(S). \quad (7)$$

Here, n_e (t_h) is the electron (hole) principal quantum number and l_e is the electron orbital quantum number. The last term in Eq. (7) represents the energy spectrum of a heavy hole

$$\lambda^{t_h}_{n_e,0}(S) = \frac{P_{n_e,0}}{S} + \omega(S, n_e)(t_h + 3/2), \quad (8)$$

which oscillates with a frequency [12]

$$\omega(S, n_e) = 2[1 + (2/3)\pi^2 n_e^2]^{1/2} S^{-3/2} \quad (9)$$

in the adiabatic potential of an electron confined to an SNC. The parameters $Z_{n_e,0}$ and $P_{n_e,0}$ take the values

$$Z_{n_e,0} = 2\int_0^1 \frac{dx\sin^2(\pi n_e x)}{1 - x^2},$$

$$P_{n_e,0} = 2\mathrm{Ci}(2\pi n_e) - 2\ln(2\pi n_e) - 2\gamma + (\varepsilon_2/\varepsilon_1) - 1,$$

where $\mathrm{Ci}(y)$ is the integral cosine and $\gamma = 0.577$ is the Euler constant. Henceforth, the energy is measured in units of $\mathrm{Ry}_h = \hbar^2/2m_h a_h^2$ and the dimensionless lengths $x = r_h/a$ and $S = a/a_h$ are used.

It is worth noting that the energy spectrum of an electron–hole pair in an SNC described by Eqs. (7)–(9) has been obtained [11–13] for SNCs of size S that satisfy the condition (6) and the following inequality:

$$S^{1/2} \gg (t_h + 3/2)[1 + (2/3)\pi^2 n_e^2]^{-1/2}. \quad (10)$$

The energy spectrum of an electron–hole pair in an SNC, described by Eqs. (7)–(9), is only valid for the lowest states of the electron–hole pair (n_e, $l_e = 0$; t_h), which satisfy the following inequality:

$$E^{t_h}_{n_e,0}(S) - E_g \ll \Delta V_0(S). \tag{11}$$

Here, $\Delta V_0(S)$ is the depth of the potential well for electrons in an SNC; for example, ΔV_0 = (2.3–25) eV for CdS SNCs in the size range given by (6) [15].

For the sake of simplicity, we assume that the applied electric field **F** is directed along the axis 0*Z* of the electron coordinate system. On averaging the potential energy in the Hamiltonian (1) over the electron wave functions of an infinitely deep spherical well [12], we obtain an expression for the potential energy of a heavy hole moving in an SNC in the adiabatic potential of an electron in the state n_e, $l_e = 0$:

$$U_{n_e,0} = \frac{1}{S}\left[\frac{1}{1-x^2} + 2\mathrm{Ci}(2\pi n_e) - 2\mathrm{Ci}(2\pi n_e x) + \frac{\sin(2\pi n_e x)}{\pi n_e x} + 2\ln x + \frac{\varepsilon_2}{\varepsilon_1} - 4\right] - \frac{eFa}{\mathrm{Ry}_h}x. \tag{12}$$

The last term in (12) leads to a shift in the bottom of the hole potential well in an SNC (compared with the minimum of the hole potential energy at the point $x = 0$ [12] in the absence of an electric field) by

$$\Delta x = \frac{(\varepsilon_2/e)}{1 + (2/3)\pi^2 n_e^2} Fa^2 \tag{13}$$

and to the corresponding shift of all the hole size-quantization levels $\lambda^{t_h}_{n_e,0}(S)$ (8) by

$$\Delta\lambda^{t_h}_{n_e,0}(a, F) = -\frac{\varepsilon_2}{2[1 + (2/3)\pi^2 n_e^2]} F^2 a^3. \tag{14}$$

Here, the shift of the hole energy levels $\Delta\lambda^{t_h}_{n_e,0}(a, F)$ (14) is independent of the principal hole quantum number t_h, being determined solely by the principal electron quantum number n_e.

Thus, Eq. (14) describes the size-quantization quadratic Stark effect according to which the hole size-quantization levels $\lambda^{t_h}_{n_e,0}(S)$ (8) are shifted by $\Delta\lambda^{t_h}_{n_e,0}(a, F) \simeq a^3F^2$ (14) under the action of an electric field *F*.

Formulas (13) and (14) are valid if, in addition to inequalities (6), (10), and (11), the following conditions are satisfied:

$$E^{t_h}_{n_e,0}(S) + \Delta\lambda^{t_h}_{n_e,0}(S, F) - E_g \ll \Delta V_0(S), \tag{11a}$$

$$\frac{\left|\Delta\lambda^{t_h}_{n_e,0}(S, F)\right|}{E_e} \ll 1, \tag{15}$$

$$\left(\frac{\Delta r_h}{a}\right)^2 = (\Delta x)^2 \ll 1. \tag{16}$$

Here, $E_e = \pi^2 n_e^2/S^2$ is the kinetic energy of an electron confined to an SNC. The fulfillment of inequality (15) makes it possible to consider the effect of an applied electric field *F* on the electron–hole-pair energy spectrum (7) in a SNC in terms of the adiabatic approximation. Condition (16) determines the smallness of the shift Δr_h (13) of the hole potential-well bottom under the action of the applied electric field, compared with the SNC radius *a*.

Taking into account expressions (13) and (14), we can readily show that the condition of the simultaneous fulfillment of inequalities (15) and (16) reduces to the condition

$$(F/e)^2 \ll \frac{[1 + (2/3)\pi^2 n_e^2]^2}{S^4} \frac{1}{\varepsilon_2^2 a_h^4}, \tag{17}$$

which defines the allowed electric-field strengths *F*. We also assume that, apart from the fulfillment of inequality (11a), which allows us to study the effect of the applied electric field only on the lowest states (n_e, 0; t_h) of an electron–hole pair confined to an SNC, the broadening of the hole levels (8) under the action of the applied electric field *F* (17) is fairly small compared with the distance $\omega(S, n_e)$ (9) between the equidistant hole levels.

3. THE OCCURRENCE OF A BULK EXCITON IN A SEMICONDUCTOR NANOCRYSTAL SUBJECTED TO A HOMOGENEOUS EXTERNAL ELECTRIC FIELD

It has been shown theoretically [16–18] that, as the SNC radius *a* increases so that $a \geq a_c$, a bulk exciton appears in a CdS SNC embedded in a borosilicate glass matrix (under the experimental conditions of [1, 2]). The bulk exciton formation has a threshold nature and is possible only in those SNCs whose radii *a* exceed some critical SNC radius a_c.

The following critical radii have been obtained for CdS SNCs $a_c^{(1)} = 2.8a_{ex}$ (in the adiabatic approximation for an infinitely deep spherical potential well associated with an SNC) [16] and $a_c^{(2)} = 1.7a_{ex}$ (in the adiabatic approximation with allowance for the finite depth of the spherical SNC potential well) [17]. The value $a_c^{(3)} = 3.48a_{ex}$ for CdS nanocrystal was found by going beyond the adiabatic approximation and using a variational method for an infinitely deep spherical SNC potential well [18]. The critical radii $a_c^{(1)} = 2.8a_{ex}$ and $a_c^{(3)} = 3.48a_{ex}$ for CdS nanocrystals are in good agreement with each other, differing by ≅20%. As for the

critical radius $a_c^{(2)} = 1.7a_{ex}$ for CdS nanocrystal it is smaller, as would be expected, than the values $a_c^{(1)} = 2.8a_{ex}$ and $a_c^{(3)} = 3.48a_{ex}$.

The above-listed critical radii for CdS SNCs $a_c^{(1)}$, $a_c^{(2)}$, and $a_c^{(3)}$ were obtained using a new optical method proposed by the author [16–18] and based on a comparison of the theoretical dependence of the exciton (electron–hole pair) spectrum $E_{n_e,0}^{t_h}(a)$ (7) on the parameters of the problem with experimental exciton-absorption spectra in SNCs.

The action of a weak homogeneous external electric field F (17) on an SNC of size $a \geq a_c$, in which a bulk exciton occurs, leads to a shift in the exciton size-quantization levels that coincides with the Stark shift in the exciton ground-state energy in a semiconductor with permittivity ε_2

$$\Delta V = -(9/4)\varepsilon_2 a_{ex}^3 F^2. \quad (18)$$

As the SNC radius a increases, the shift of the hole energy levels (14) coincides, for some critical value of the radius $a = \bar{a}_c$, with the shift of the exciton ground-state energy ΔV (18). This allows us to determine the critical radius $\bar{a}_c$ such that, for $a \geq \bar{a}_c$, the bulk exciton can appear in an SNC subjected to a homogeneous external electric field F (17)

$$(\bar{a}_c/a_{ex}) = [(9/2)(1 + (2/3)\pi^2 n_e^2)]^{1/3}. \quad (19)$$

Formula (19) yields the critical radius $\bar{a}_c$ such that, for $a \geq \bar{a}_c$, a bulk exciton can appear in the ground state

$$\bar{a}_c(n_e = 1, l_e = 0; t_h = 0) = 3.24a_{ex}. \quad (20)$$

A comparison of $\bar{a}_c(1, 0; 0)$ (20) with the critical radius $a_c^{(2)}(1, 0; 0) = 3.48a_{ex}$ obtained by the author [18] using the new optical method shows good agreement (these values differ by no more than 6.9%). Such a difference is presumably due to the fact that the variational method used by the author [18] to calculate the exciton spectrum can yield an overestimated energy, which in its turn leads to an overestimated value of the SNC critical radius $a_c^{(2)}$.

In determining $\bar{a}_c$ (20), one of the applicability conditions of the developed theory [inequality (6)] is violated. Nevertheless, we consider that formulas (13), (14), (19), and (20) are valid for SNCs of radius $a \geq a_{ex}$. The reason why this can be done is the good agreement of the exciton spectrum (calculated by the author [18] for an SNC of radius $a \geq a_{ex}$ using the variational method) with the electron–hole pair spectrum (obtained [16] in terms of the adiabatic approximation with the condition (6) for the SNC radii a met) and, consequently, the closeness of critical SNC radii: $\bar{a}_c = 3.24a_{ex}$ (20) and $a_c^{(2)} = 3.48a_{ex}$ [18].

Thus, a new electrooptical method can be proposed for determining the critical SNC radii $\bar{a}_c$ by means of equation (19); this method is based on the equality of the Stark shift of the hole size-quantization levels $\Delta\lambda_{n_e,0}^{t_h}(a, F)$ (14) and that of the exciton ground-state energy ΔV (18). The new electrooptical method yields a critical SNC radius $\bar{a}_c$ (20) differing by no more than 6.9% from $a_c^{(2)} = 3.48a_{ex}$ obtained by the author [18] with the use of the new optical method.

4. CONCLUSION

To conclude, let us briefly discuss the possible experimental verifications of the new electrooptical method proposed in this paper. Spectra of interband absorption by CdS nanocrystals ($\varepsilon_2 = 9.3$) with radius a in the range from 1 to 100 nm, embedded in a transparent borosilicate glass matrix ($\varepsilon_1 = 2.25$), were studied by Ekimov *et al.* [1, 2]. The electron and hole effective masses in CdS are $m_e/m_0 = 0.205$ and $m_h/m_0 = 5$, respectively; i.e., $m_e \ll m_h$. The theoretical spectrum of an exciton confined to a CdS SNC, calculated by me [16–18], describes with high accuracy the observed dependence of the exciton spectrum on the SNC radius a [1, 2] in the SNC size region of $a \geq a_{ex} = 2.5$ nm.

The transparency peaks associated with the transitions between the exciton size-quantization levels were observed by Vandyshev *et al.* [3] in the transmission spectra of CdSe ($\varepsilon_2 = 9.4$) SNCs of radius $a = 5.0$ nm embedded in a silicate-glass matrix ($\varepsilon_1 = 2.25$). The electron and hole effective masses in CdSe are $m_e/m_0 = 0.13$ and $m_h/m_0 = 2.5$, respectively; i.e., $m_e \ll m_h$. The positions of the transparency peaks of the CdSe SNCs as a function of the NC radius at $a \simeq a_{ex} = 4.55$ nm are described with high accuracy by the exciton spectrum [19].

Let us subject the quasi-0D systems studied in experiments [1–3] to a homogeneous external electric field F (17). Consideration of the local field effect [20] results in the fact that, in the quasi-0D systems [1–3], the SNCs are subjected to the field

$$F_{ins} = f^{-1}F, \quad f = 3/[2 + (\varepsilon_2/\varepsilon_1)], \quad (21)$$

where the coefficient $f = 0.489$ for CdS and CdSe SNCs. F in expressions (13), (14), and (17) should be replaced by F_{ins} (21).

Figures 1 and 2 show the shifts $\Delta\lambda_{1,0}^{t_h}(a, F)$ (14) of the size-quantization levels of a hole in the states $n_e = 1$, $l_e = 0$, and t_h in the electric field F for CdS and CdSe SNCs, respectively. In the calculations, the conditions (6), (10), (11a), and (17) were assumed to be satisfied. From

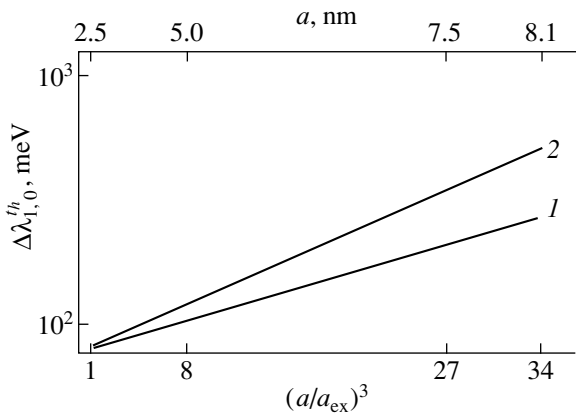

Fig. 1. Shift of the hole size-quantization levels $\Delta\lambda^{t_h}_{1,0}(a, F)$ (14) under the action of a homogeneous external electric field F as a function of the CdS nanocrystal radius a (upper scale) or the parameter $(a/a_{ex})^3$ (lower scale), where a_{ex} is the exciton Bohr radius in CdS. Lines *1* and *2* correspond to electric field strengths F of 10^3 and 1.23×10^3 V/m, respectively.

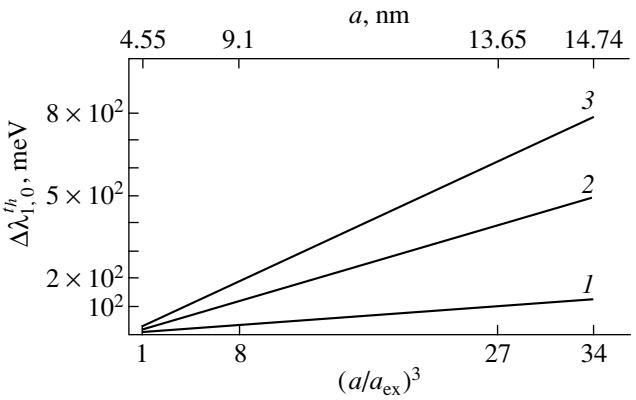

Fig. 2. Shift of the hole size-quantization levels $\Delta\lambda^{t_h}_{1,0}(a, F)$ (14) under the action of a homogeneous external electric field F as a function of the CdSe nanocrystal radius a (upper scale) or the parameter $(a/a_{ex})^3$ (lower scale), where a_{ex} is the exciton Bohr radius in CdSe. Lines *1*, *2*, and *3* correspond to electric field strengths F of 210, 410, and 510 V/m, respectively.

the dependence of $\Delta\lambda^{t_h}_{1,0}(a, F)$ on the SNC radius a and the electric field F it follows that, with increasing SNC radius $a > a_{ex}$, the Stark shifts of the hole size-quantization levels increase in proportion to a^3 and approach the Stark shifts of the exciton ground-state energy ΔV (18). This occurs for $\bar{a}_c$ values coinciding with the SNC critical radii $\bar{a}_c(1, 0; 0) = 3.24a_{ex}$ (20) ($\bar{a}_c(1, 0; 0) = 8.1$ nm for CdS NCs and $\bar{a}_c(1, 0; 0) = 14.74$ nm for CdSe SNCs) such that, for $a \geq \bar{a}_c(1, 0; 0)$, the bulk exciton may come into existence in CdS and CdSe nanocrystals.

In addition, as the strength of the homogeneous external electric field F increases, the quadratic Stark effect is observed, according to which the shifts $\Delta\lambda^{t_h}_{1,0}(a, F)$ (14) and $\Delta V(F)$ (18) increase in proportion to F^2. For CdS SNCs, with F increasing from 10^3 to 1.23×10^3 V/m, the Stark shift of the exciton ground-state energy $\Delta V(F)$ (18) increases from 4.87×10^2 to 7.37×10^2 meV. For CdSe SNCs, with electric field strength F increasing from 2.1×10^2 to 5.1×10^2 V/m, $\Delta V(F)$ (18) increases from 1.25×10^2 to 7.78×10^2 meV (see Figs. 1, 2).

Thus, it has been ascertained that the electrooptical properties of SNC-containing quasi-0D systems in the interband-absorption region are governed by the size-quantization quadratic Stark effect. A new electrooptical method is proposed, furnishing an opportunity to determine the critical radii of nanocrystals in which bulk excitons can appear.

5. ACKNOWLEDGMENT

This work was supported in part by the International Science Foundation “Vidrodzhennya.”

REFERENCES

1. A. I. Ekimov and A. A. Onushchenko, Pis’ma Zh. Éksp. Teor. Fiz. **40** (8), 337 (1984) [JETP Lett. **40**, 1136 (1984)].
2. A. I. Ekimov, A. A. Onushchenko, and Al. L. Éfros, Pis’ma Zh. Éksp. Teor. Fiz. **43** (6), 292 (1986) [JETP Lett. **43**, 376 (1986)].
3. Yu. V. Vandyshev, V. S. Dneprovskiĭ, and V. I. Klimov, Pis’ma Zh. Éksp. Teor. Fiz. **53** (6), 301 (1991) [JETP Lett. **53**, 314 (1991)].
4. A. D. Yoffe, Adv. Phys. **42**, 173 (1993).
5. A. I. Ekimov, P. A. Skvortsov, and T. V. Shubina, Zh. Tekh. Fiz. **59** (3), 202 (1989) [Sov. Phys. Tech. Phys. **34**, 371 (1989)].
6. K. Bajema and R. Merlin, Phys. Rev. B **36**, 1300 (1987).
7. T. Wood and S. Burrus, Appl. Phys. Lett. **44**, 16 (1984).
8. S. I. Pokutniĭ, Fiz. Tverd. Tela (St. Petersburg) **39** (4), 606 (1997) [Phys. Solid State **39**, 528 (1997)].
9. S. I. Pokutniĭ, Fiz. Tverd. Tela (St. Petersburg) **39** (4), 720 (1997) [Phys. Solid State **39**, 634 (1997)].
10. S. Nomura and T. Kobayashi, Solid State Commun. **74** (10), 1153 (1990).
11. N. A. Efremov and S.I. Pokutniĭ, Fiz. Tverd. Tela (Leningrad) **32** (6), 1637 (1990) [Sov. Phys. Solid State **32**, 955 (1990)].

12. S. I. Pokutniĭ, Fiz. Tekh. Poluprovodn. (Leningrad) **25** (4), 628 (1991) [Sov. Phys. Semicond. **25**, 381 (1991)].
13. S. I. Pokutnyi, Phys. Lett. A **168** (5–6), 433 (1992).
14. N. A. Efremov and S. I. Pokutniĭ, Fiz. Tverd. Tela (Leningrad) **27** (1), 48 (1985) [Sov. Phys. Solid State **27**, 27 (1985)].
15. V. Ya. Grabovskis, Ya. Ya. Dzenis, and A. I. Ekimov, Fiz. Tverd. Tela (Leningrad) **31** (1), 272 (1989) [Sov. Phys. Solid State **31**, 149 (1989)].
16. S. I. Pokutniĭ, Fiz. Tekh. Poluprovodn. (St. Petersburg) **30** (11), 1952 (1996) [Semiconductors **30**, 1015 (1996)].
17. S. I. Pokutnyi, Phys. Lett. A **203** (5–6), 388 (1995).
18. S. I. Pokutniĭ, Fiz. Tverd. Tela (St. Petersburg) **38** (9), 2667 (1996) [Phys. Solid State **38**, 1463 (1996)].
19. S. I. Pokutniĭ, Fiz. Tverd. Tela (St. Petersburg) **34** (8), 2386 (1992) [Sov. Phys. Solid State **34**, 1278 (1992)].
20. S. Schmitt-Rink, D. Miller, and D. Chemla, Phys. Rev. B **35**, 8113 (1987).

Translated by S. Goupalov

Semiconductors, Vol. 34, No. 9, 2000, pp. 1085–1089. Translated from Fizika i Tekhnika Poluprovodnikov, Vol. 34, No. 9, 2000, pp. 1125–1129.

AMORPHOUS, VITREOUS, AND POROUS SEMICONDUCTORS

Nanostructured *a*-Si:H Films Obtained by Silane Decomposition in a Magnetron Chamber

O. A. Golikova, M. M. Kazanin, A. N. Kuznetsov, and E. V. Bogdanova

Ioffe Physicotechnical Institute, Russian Academy of Sciences, Politekhnicheskaya ul. 26, St. Petersburg, 194021 Russia

Submitted February 29, 2000; accepted for publication March 1, 2000

Abstract—Nanostructured *a*-Si:H films grown by the MASD method at various deposition temperatures (T_s = 300–390°C) were studied. Among these films, those "on the verge of crystallinity" are of particular interest, because they tend to crystallize. In addition, although their electron-transport parameters are slightly inferior to those of conventional device-grade *a*-Si:H, they are preferable because of the higher stability of their photoconductivity under exposure to light. © *2000 MAIK "Nauka/Interperiodica".*

1. INTRODUCTION

We demonstrated in our previous papers [1, 2] that the magnetron-assisted decomposition of SiH_4 (MASD) provides wide possibilities for controlling structure and properties when obtaining *a*-Si:H films. Thus, for a constant hydrogen content (C_H), the microstructure parameter (R) can vary from zero to unity; i.e., in limiting cases, the films contain either monohydride complexes (SiH) or dihydride complexes (SiH_2) only. It is important that these variations in R are attained at high deposition temperatures, which provide low C_H (up to 3 at. %). This was considered as the specific feature of the MASD technique [2].

We paid most of our attention to films with $R \cong 0$, since their electronic parameters corresponded to the parameters of the device-grade *a*-Si:H [1, 2]. However, films having high R = 0.65–1.0 are of interest in their own right.

Indeed, it was found [3] that, in contrast with films with $R \cong 0$[4], films with R = 0.65–0.75 begin to crystallize under the effect of fairly "soft" Si^+ implantation (the ion energy was 70 keV, the dose $D = 10^{13}$ cm^{-2}, and T = 300 K). The implanted films were annealed in vacuum at a pressure of $(3–4) \times 10^{-6}$ Torr at 200°C for 1 h. Thus, starting films with R = 0.65–0.75 were actually nanostructured. However, the volume fraction of the crystalline phase (X_c) in them is so small that it is undetectable by known methods [3, 5]. According to the terminology of the authors [5], these films are "on the verge of crystallinity." It is these very small-sized crystals, which are formed in the film in the course of deposition, that act as the crystallization nuclei during subsequent treatments. Indeed, subsequent to the implantation of Si^+, the microstructure parameter becomes equal to unity. This is observed with increasing X_c, in which case the SiH_2 complexes are found mainly at the boundaries of nanocrystals [6].

However, judging from the value R = 1, MASD enables us to obtain films having a similar structure formed directly in the course of deposition, i.e., without any additional treatments.

The purpose of this study was to determine the specific features of the charge transport in various nanostructured *a*-Si:H films obtained using the MASD method.

2. EXPERIMENTAL RESULTS AND DISCUSSION

The MASD method combines two processes, namely, silane decomposition in the dc-discharge plasma of the 25% SiH_4–75% Ar gas mixture and cathode magnetron sputtering of the crystalline Si target.

The films were obtained under the following conditions: the anode voltage was V_A = 500 V, the magnetic field was H = 500 G, the gas-mixture pressure was $P \cong$ 3 mTorr, and the mixture pumping rate was r = 1 sccm. The deposition temperature was varied in the range T_s = 300–390°C, the deposition rate was r = 0.8–1.2 Å s^{-1}, and the film thickness was d = 0.8–1.0 μm.

Let us consider the specific features of the MASD method from the standpoint of the possibility of obtaining nanostructured *a*-Si:H films containing inclusions of Si nanocrystals in the amorphous matrix.

First, it was noted earlier [7] that Si nanocrystallites up to 2 nm in size, which can contribute to film formation, were found among various Si–H radicals during investigations of the silane–argon plasma composition.

Second, the growing film is also exposed to the particle beam from the sputtering target—Si atoms and ions.

If the deposition temperature is sufficiently high, the mobility of all these particles on the surface of the growing film increases. We note that the energy transfer to the film from the atoms and Ar ions reflected from

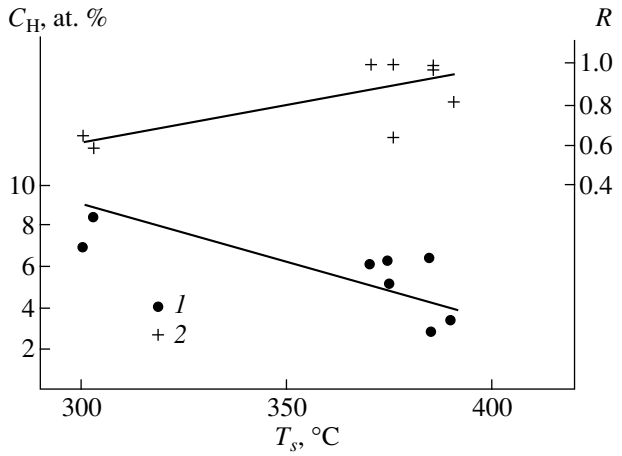

Fig. 1. Dependences of the hydrogen content (C_H) and microstructure parameter (R) on the film deposition temperature (T_s). Gas pressure 3 mTorr, pumping rate 1 sccm.

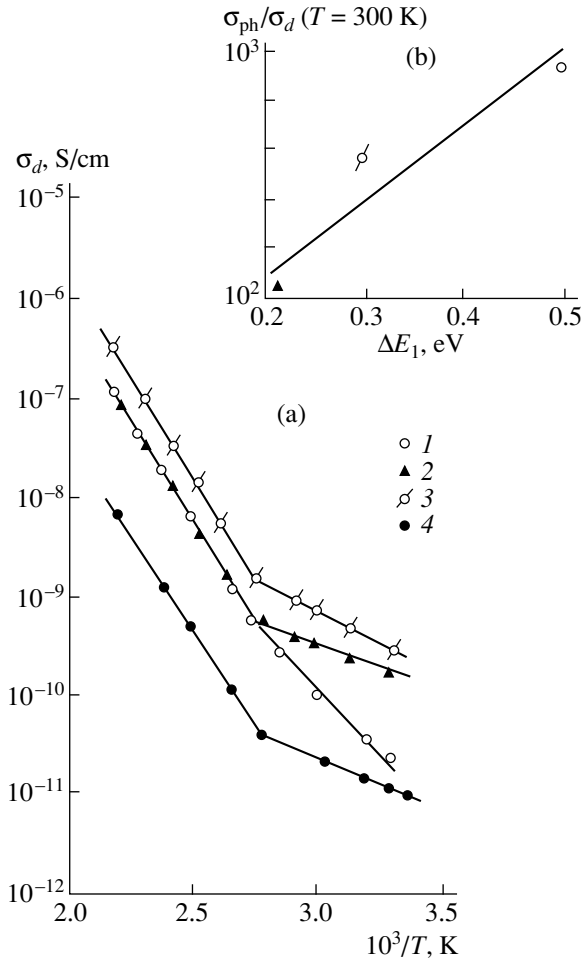

Fig. 2. (a) Temperature dependences of the dark conductivity of nanostructured films with R = 1, which were obtained (*1–3*) in the deposition process and (*4*) after Si^+ implantation. (b) Ratio of photoconductivity to dark conductivity (σ_{ph}/σ_d) at T = 300 K as a function of the activation energy ΔE_1 of σ_d at lowered temperatures.

the Si target actually signifies an increase in the effective deposition temperature. This phenomenon is also favorable for the formation of Si nanocrystals in the amorphous matrix of the film.

On the other hand, high deposition temperatures lead to a low hydrogen content in the films, which is apparently favorable for the growth of Si nanocrystallites. Indeed, according to [6], a high hydrogen content (~20 at. %) leads to the formation of a specific shell around growing nanocrystallites, which hinders their growth.

To determine the T_s dependences of C_H and R at $P \cong$ 3 mTorr (Fig. 1), data reported previously [2] were used. It can be seen that $R \cong 1$ is attained for the films deposited at T_s = 370–390°C. According to the Raman spectroscopy data, the volume fraction of the crystalline phase (X_c) in the films is no more than 20% and the size of nanocrystallites (d_{Raman}) is no larger than 5 nm. For this reason, the structure of these two-phase films comprises the amorphous matrix with inclusions of Si nanocrystals, which are distributed over the matrix.

Indeed, it can be seen from the temperature dependences of the dark electrical conductivity of these nanostructured films that two activation energies of conductivity σ_d are observed. The values ΔE_1 and ΔE_2 correspond to room temperature and to elevated temperatures, respectively (Fig. 2a). The data for the films having closely matched values ΔE_2 (0.76–0.80 eV) are given in Fig. 2a. It can be seen that the charge transport at elevated temperatures is determined by the major high-resistivity amorphous phase. However, the contribution to the charge transport from the second phase, which has a much lower resistivity, becomes evident at lowered temperatures. In this case, since $\Delta E_2 \cong$ const, we can immediately assess the influence of the second phase from the values of ΔE_1.

It was demonstrated [6] that the room temperature photosensitivity (σ_{ph}/σ_d) for films that were obtained by the plasma-enhanced chemical vapor deposition (PECVD) under high dilution of SiH_4 with hydrogen decreased with an increase in the crystalline phase contribution to the charge transport. The data shown in Fig. 2b are consistent with the data reported previously [6] (films *1–3*). As for the photoconductivity of films *1–3*, it is on the order of 10^{-8} S/cm at room temperature. The measurements were carried out at the incident photon energy ε = 2 eV and photocarrier generation rate $G \cong 10^{19}$ cm^{-3} s^{-1}. In the temperature range of 200–300 K, σ_{ph} increased with ΔE on the order of several hundredths of an electron-volt.

We note that the comparison of σ_d and σ_{ph} and their activation energies for PECVD films [6] with the MASD films considered above would be incorrect. The reason for this is that the hydrogen content in these films is different ($C_H \cong$ 20 at. % and 5–6 at. %, respectively), which affects both the resistance of the bound-

aries between the amorphous and crystalline phases and the σ_{ph} magnitude.

The temperature dependence of the dark conductivity for one of the films implanted with 30–120-keV Si^+ ions [3] is also shown in Fig. 2a. Prior to implantation, the parameters were C_H = 7 at. % and R = 0.75. After implantation, this film contained 5.6 at. % hydrogen and had R = 1; i.e., in this respect, it was identical to films (*1–3*) (Fig. 2a). Two slopes are also observed in the $\log\sigma_d(1/T)$ curve for this film: ΔE_1 = 0.3 eV and ΔE_2 = 0.75 eV. However, first, the σ_d value was underestimated for this film, and, second, photoconductivity was not observed for it. We assign these specific features to the influence of radiation defects, whose annealing was incomplete.

Let us now consider the specific features of the charge transport in the nanostructured films with $R < 1$, which are on the verge of crystallinity. The temperature dependences of the dark conductivity and photoconductivity for one of these films and the same dependences, which were determined for the film with R = 1 after deposition, are shown in Fig. 3. In this case, films that have almost identical activation energies of dark conductivity at high temperatures $\Delta E \cong 0.90$ eV are chosen. It can be seen that ΔE = 0.90 eV is also observed for the film with R = 0.65 at lowered temperatures, while the lower activation energy of 0.42 eV is observed for the film with R = 1 as well as for other films (Fig. 2a) with a similar structure. Thus, for the film with R = 0.65, the contribution of the second crystalline phase to the charge transport is not distinguishable, whereas this contribution is rather significant for the film with R = 1 (Fig. 3). The photoconductivity at room temperature for this film is even lower than for other films with a similar structure described above ($\sigma_{ph} \cong 10^{-9}$ S/cm). This is apparently caused by a lower hydrogen content (3 at. %).

The temperature dependences of photoconductivity for the films with R = 0.65 and R = 1 are also different. In the former case, the region of temperature quenching of photoconductivity is observed, while in the latter case, as well as for other films with R = 1, σ_{ph} increases steadily and slightly with increasing temperature (Fig. 3).

The temperature quenching of photoconductivity, which is observed for a series of semiconductor materials, is often explained in the context of the well-known Rose model [8]. This model implies the existence of two photoelectron recombination levels with radically different trapping sections ($S_{n1} \gg S_{n2}$). Level 1 lies close to the middle of the mobility gap, while level 2 lies close to the valence band top. In this case, for fairly large intensities of incident light (F), the superlinearity of the photocurrent–illuminance characteristics $I_{ph} \sim F^n$, where $n > 1$, is observed. For *a*-Si:H, which falls "on the verge of crystallinity," photocurrent–illuminance characteristics of this type are actually observed for $F = 10^{13}$–10^{15} cm^{-2} s^{-1} in contrast with the linear photocurrent–illuminance characteristics for the highly photosensitive *a*-Si:H [9, 10] (Fig. 4).

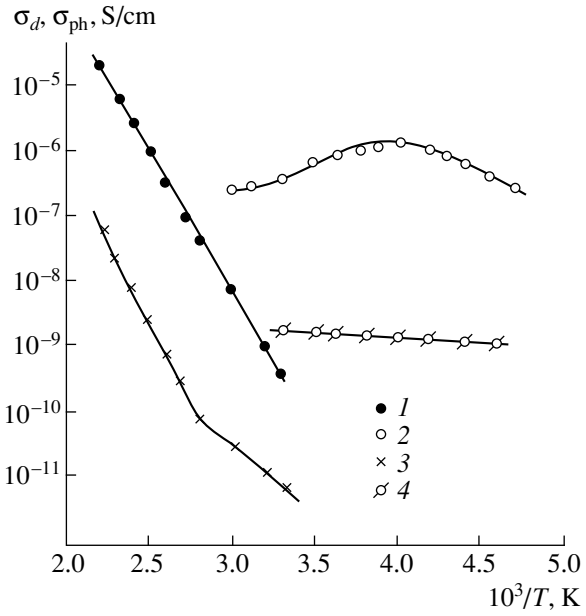

Fig. 3. Temperature dependences of (*1*, *3*) the dark conductivity and (*2*, *4*) photoconductivity for films with R = 0.65 and R = 1, respectively.

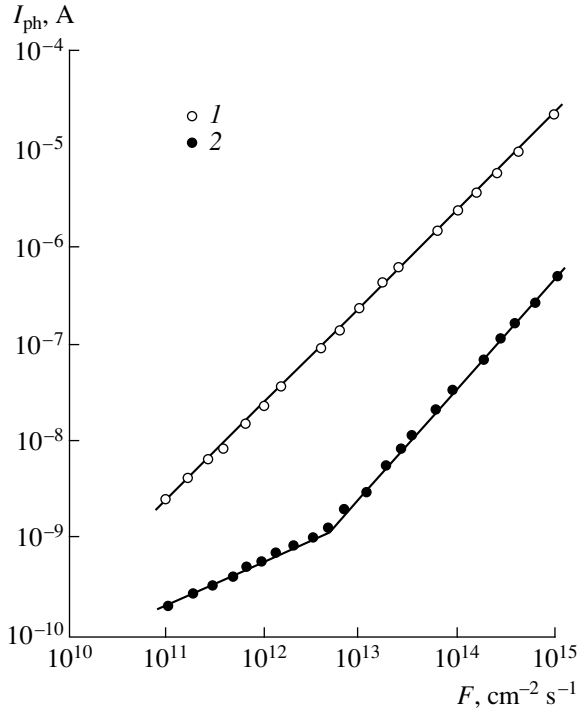

Fig. 4. Current–illuminance characteristics for nanostructured *a*-Si:H films (λ= 630 nm, T = 300 K), (*1*) from [9] and (*2*) our data.

While on the subject of two different photoelectron recombination levels, recombination via the levels of

Parameters of the films (T_s = 380°C, ΔE = 0.9 eV)

Film material	Device-grade *a*-Si:H	Nanostructured *a*-Si:H (this study)	Nanostructured *a*-Si:H [7, 9, 10]
σ_d, S/cm (T = 300 K)	10^{-10}	4×10^{-10}	10^{-9}
σ_{ph}, S/cm (T = 300 K, λ = 630 nm, $G = 10^{19}$ cm^{-3} s^{-1})	1.5×10^{-6}	4×10^{-7}	6×10^{-5}
σ_{ph}/σ_d	1.5×10^4	10^3	6×10^4
Thermal quenching of photoconductivity	Absent	Present	Present
Exponent of the photocurrent–illuminance characteristic (T = 300 K, λ = 630 nm, $F = 10^{11}$–10^{15} cm^{-2} s^{-1})	0.9	0.42 and 1.15 before and after $F = 4 \times 10^{12}$ cm^{-2} s^{-1}, respectively	1.0
Exponent in the expression $\sigma_{ph} \sim t^{-\gamma}$ under illumination, 300 K	0.1	0.0	γ = 0.6 and $\gamma \longrightarrow 0$ before and after $t = 3.5 \times 10^3$ s, respectively
N_D, cm^{-3} (CPM)	3×10^{16}	4×10^{16}	1.6×10^{16}
E_u, meV (CPM)	53	63	62
C_H, at. %	4	5.6	8.3
Infrared-absorption major modes, cm^{-1}	2000 (R = 0)	2090, 2000 (R = 0.65)	2000, 2030

Note: CPM stands for constant photoconductivity method.

the dangling Si–Si bonds, which are present in the amorphous matrix and at the boundaries of nanocrystals, should apparently be taken into account. However, this issue, as well as the question about the causes of distinctions between the photocurrent–illuminance characteristics for $F < 10^{13}$ cm^{-2} s^{-1} (Fig. 4), requires additional examination.

Let us now consider the photoconductivity kinetics for the nanostructured *a*-Si:H films with R = 0.65 under illumination (the flux power W = 100 mW/cm^2, wavelength $\lambda < 0.9$ μm, illumination time 5 h, and T = 300 K) compared to the photoconductivity kinetics for films of "conventional" *a*-Si:H with R close to zero. If $\sigma_{ph} \sim t^{-\gamma}$, the parameter γ characterizes the degradation rate of photoconductivity.

It was demonstrated for the conventional *a*-Si:H [11] that γ increases with the Fermi-level shift from the middle of the mobility gap towards the conduction band. Thus, for two films deposited at T_s = 300°C and having C_H = 8–9 at. % and R = 0, the activation energies of dark conductivity equal 0.84 and 0.75 eV, and γ equals 0.20 and 0.46, respectively. However, for "intrinsic" *a*-Si:H, in which case $\Delta E \cong 0.85$ eV, while the C_H values are different, γ decreases with a decrease in C_H (down to 0.1 at $T_s \cong 300$°C and C_H = 4 at. %).

In contrast with the above, the γ magnitudes determined for *a*-Si:H nanostructured films with R = 0.65 turned out to be "insensitive" to variations in both C_H and ΔE. For each case, $\gamma \cong 0$; i.e., the Staebler–Wronski effect is actually absent. At present, it is generally accepted that the formation of metastable defects (dangling bonds) under intense illumination necessarily proceeds via hydrogen diffusion. In this case, the result obtained can be explained. Indeed, more than half the amount of hydrogen in the films with R = 0.65, which are on the verge of crystallinity, is in the form of SiH_2 complexes. Second, the SiH_2 complexes are located at the boundaries of nanocrystals, whose content in the films is very small. Since these complexes are widely separated, they thereby hinder hydrogen diffusion.

3. CONCLUSION

A comparison of properties of various nanostructured films, which were investigated in this study, demonstrated that films on the verge of crystallinity are of the most interest.

First, these films crystallize easily. Because of this, they can be considered as the base material for polysilicon (*pc*-Si) films, which constitute a promising material for many practical applications. These are, for example, photovoltaic devices, field transistors, and integrated circuits [12], as well as hybrid *a*-/*pc*-Si devices of a large area [13].

Second, having somewhat inferior electronic parameters compared to device-grade *a*-Si:H films, they have a certain advantage, namely, they are highly stable under intense illumination. This is very important for photovoltaic applications. However, the photosensitivity (σ_{ph}/σ_d) of the nanostructured MASD *a*-Si:H films is significantly lower than that of the PECVD nanostructured films obtained with both undiluted silane [8, 9] and silane mixtures with H_2, He, and Ar [7] as the source.

Certain data that characterize the films of conventional device-grade *a*-Si:H films and nanostructured MASD and PECVD *a*-Si:H films are listed in the table. The films were deposited at the same temperature (T_s = 380°C) and had the identical activation energy of the

dark conductivity (ΔE = 0.9 eV). Thus, the Fermi level position in the mobility gap in relation to the conduction-band bottom was identical for all cases. However, the structural and electronic properties of the films were markedly different. We cannot identify the reasons for these distinctions here; this will undoubtedly require further investigations in the field of technology and physics of nanostructured films.

REFERENCES

1. O. A. Golikova, A. N. Kuznetsov, V. Kh. Kudoyarova, and M. M. Kazanin, Fiz. Tekh. Poluprovodn. (St. Petersburg) **30**, 1879 (1996) [Semiconductors **30**, 983 (1996)].
2. O. A. Golikova, A. N. Kuznetsov, V. Kh. Kudoyarova, and M. M. Kazanin, Fiz. Tekh. Poluprovodn. (St. Petersburg) **31**, 816 (1997) [Semiconductors **31**, 691 (1997)].
3. O. A. Golikova, A. N. Kuznetsov, V. Kh. Kudoyarova, *et al.*, Fiz. Tekh. Poluprovodn. (St. Petersburg) **34**, 86 (2000) [Semiconductors **34**, 87 (2000)].
4. O. A. Golikova, Fiz. Tekh. Poluprovodn. (St. Petersburg) **33**, 464 (1999) [Semiconductors **33**, 447 (1999)].
5. A. H. Mahan, W. Beyer, L. M. Williamson, *et al.*, ICAMS-18 Abstracts (USA, 1999), p. 147.
6. Yu. He, Ch. Yin, G. Cheng, *et al.*, J. Appl. Phys. **75**, 797 (1994).
7. P. Roca i Cabarrocas, Mater. Res. Soc. Symp. Proc. **507**, 1855 (1998).
8. A. Rose, *Concept of Photoconductivy and Allied Problems* (Interscience, New York, 1963; Mir, Moscow, 1966).
9. O. A. Golikova and M. M. Kazanin, Fiz. Tekh. Poluprovodn. (St. Petersburg) **33**, 110 (1999) [Semiconductors **33**, 97 (1999)].
10. O. A. Golikova and M. M. Kazanin, Fiz. Tekh. Poluprovodn. (St. Petersburg) **33**, 336 (1999) [Semiconductors **33**, 335 (1999)].
11. O. A. Golikova, M. M. Kazanin, and V. Kh. Kudoyarova, Fiz. Tekh. Poluprovodn. (St. Petersburg) **32**, 484 (1998) [Semiconductors **32**, 434 (1998)].
12. K. Pangal, J. C. Sturm, and S. Wagner, Mater. Res. Soc. Symp. Proc. **507**, 277 (1998).
13. P. Mei, J. B. Boyce, D. K. Folk, *et al.*, Mater. Res. Soc. Symp. Proc. **507**, 3 (1998).

Translated by N. Korovin

Semiconductors, Vol. 34, No. 9, 2000, pp. 1090–1093. Translated from Fizika i Tekhnika Poluprovodnikov, Vol. 34, No. 9, 2000, pp. 1130–1134.

AMORPHOUS, VITREOUS, AND POROUS SEMICONDUCTORS

On the Mechanism of Porous Silicon Formation

D. N. Goryachev, L. V. Belyakov, and O. M. Sreseli

Ioffe Physicotechnical Institute, Russian Academy of Sciences, Politekhnicheskaya ul. 26, St. Petersburg, 194021 Russia

Submitted April 20, 2000;
accepted for publication April 24, 2000

Abstract—A new qualitative mechanism of pore nucleation and initial stages of porous silicon (*por*-Si) growth was proposed. The emphasis was on the charge exchange between Si^{2+} ions generated by electrolytic or chemical oxidation of initial silicon (disproportionation reaction). The mechanism eliminates, to a large extent, the contradictions typical of earlier proposed schemes of *por*-Si growth; in particular, it explains the morphological features of *por*-Si produced under various experimental conditions. The impact of light in these processes was also considered. © *2000 MAIK "Nauka/Interperiodica".*

INTRODUCTION

A dark-colored film formed at the single-crystal silicon surface electrolytically etched in HF solutions was first described in 1956 [1] and afterwards was studied by many teams. The relevant publications were reviewed, for example, in [2]. The film formation mechanism attracted considerable interest after the publication [3] by Canham (1990). He observed strong red-orange photoluminescence (PL) of these films and explained this by the quantum-size effect in silicon nanocrystallites. He also proposed a new formation mechanism for luminescent films referred to as porous silicon (*por*–Si).

According to the concepts of [3] (and as was also shown earlier in [4]), anodic oxidation of silicon in HF solutions forms narrow "etch channels" extending into the silicon bulk. Further etching lengthens and gradually expands these pores until the thin separating walls are partially destroyed. Thus, etching produces a large number of threadlike wall residues arranged mainly perpendicular to the silicon surface or along the crystallographic axes. The thread thickness mostly does not exceed a few nanometers, which initiates various quantum-size effects; in particular, the band gap is widened and, hence, the probability of PL excitation in the visible region of the spectrum becomes higher.

Later, new experimental facts somewhat changed Canham's concepts. Nevertheless, most available theories of *por*-Si formation are, as before, based on the idea of etched threadlike pores. More detailed studies of this process revealed at least two general problems. First, formation of areas of more intense etching, which causes pore nucleation on the initially homogeneous surface of silicon single crystal, should be understood. Second, the fact that silicon is predominantly dissolved deep into the substrate, rather than laterally, should be explained.

As for the initial pore formation stage, the pore nucleation was earlier assumed to be caused by etching of defects (dislocation outcrops, impurities, etc.) at the single-crystal silicon surface. Chemical or electrolytic etching of such surfaces readily forms so-called etch pits. As is known, spatial scales of this phenomenon (micrometers [5]) are not comparable at all to scales of silicon fragments formed when "growing" *por*-Si (a few nanometers). It is also well known that *por*-Si forms readily on *p*- and *n*-Si with various doping levels. It is difficult to relate these experimental facts to surface structural defects. Finally, direct observations *in situ* by scanning tunneling microscopy showed silicon surface pitting to occur at initial electrolysis stages irrespective of the atomic-defect arrangement [6].

Recently, a number of new approaches to the problem of pore nucleation have been outlined. First, these are theoretical studies demonstrating possible instability of the semiconductor–electrolyte planar interface with respect to weak perturbations arising in the course of electrolysis. The optimal wavelength of these perturbations is assumed to define the order of magnitude of the distances between pores [7, 8]. Many authors relate the initial stage of pore nucleation to gaseous hydrogen release during Si electrolytic dissolution; this hydrogen is produced in oxidation of bivalent silicon compounds by hydrogen ions [2].

However, numerous methods are known to produce *por*-Si using pure chemical etching rather than electrolytic etching. Together with HF, any strong oxidizer, for example, KNO_2, HNO_3, etc., is added to the etchant. Under these conditions, Si^{2+} is finally oxidized to Si^{4+} by stronger oxidizers, rather than by hydrogen ions, and without hydrogen release.

Currently, the number of studies dedicated to the second stage of *por*–Si formation (i.e., to the pore growth into the silicon substrate depth) is very great. Early papers along this line of inquiry were briefly reviewed in [2]. Many publications were dedicated to the idea of the collapse of the space charge region (SCR) when pore walls are thinned, in which case free charge carriers disappear. The pore-wall electrical resistance correspond-

ingly increases; therefore, the etching process is localized mainly at the pore bottom, deepening the pores. However, a doubled width of the silicon SCR is mostly of the order of tenths of a micrometer [11], while the cross-sectional size of pore-wall residues should not exceed ten nanometers.

All the aforesaid demonstrates that the considered problem is still under discussion and that pore formation theories are diverse, complex, and contradictory [7, 12–14]. It is evident that the *por*-Si formation mechanisms cannot be understood if specific chemical properties of silicon are ignored [9, 10, 12, 15]. This is evidenced by numerous attempts to produce other porous semiconductors that have not confirmed the manifestation of quantum-size effects in their properties [9, 13, 16].

In early studies [17–19] of *por*-Si formation, the emphasis was evidently on chemical rather than semiconductor properties of silicon. Instability of Si^{2+} ions produced by silicon anodic oxidation was taken into account, as well as their subsequent disproportionation (mutual exchange of electrons) with the formation of secondary (predominantly amorphous) silicon and Si^{4+} ions. Thus, the case in point was not only pore etching in the silicon substrate bulk, but also buildup of a new amorphous or finely crystalline layer at the silicon surface. Nevertheless, disproportionation reactions were later considered only as a side process accounting for, e.g., an amorphous phase in the *por*-Si composition [19] or pore wall protection against lateral etching [2].

A detailed analysis of the available (including the authors') experimental data allows us to revise some commonly accepted concepts of the *por*-Si formation mechanism. We infer that disproportionation reactions play a rather significant role in nanocrystalline *por*–Si formation and propose a new qualitative mechanism of initial pore growth. Disproportionation reactions are shown to be promoted by illumination during silicon anodic oxidation. The proposed model eliminates many of the above contradictions in conventional theories.

CHEMICAL PROCESSES DURING *por*–SI FORMATION

We consider processes at the silicon surface etched electrolytically or chemically in more detail, in particular, the probability of secondary crystallization due to disproportionation of Si^{2+} ions.

Electrolytic- and chemical-etching processes in silicon are similar in many respects. These are multistage processes represented by a great number of consecutive and parallel reactions [20]. Two consecutive reactions are fundamental. One is directly related to charge transport through the silicon–solution interface and proceeds with hole h^+ consumption. In the ionic form, this reaction can be written as

$$Si + 2h^+ \longrightarrow Si^{2+}. \quad (1)$$

The Si^{2+} ions are not very stable and are further oxidized (for example, by hydrogen ions) as

$$Si^{2+} + 2H^+ \longrightarrow Si^{4+} + H_2 \quad (2a)$$

or participate in the disproportionation reaction as

$$Si^{2+} + Si^{2+} \longrightarrow Si + Si^{4+}. \quad (2b)$$

The latter reaction yields secondary atomic silicon in amounts equal to a halved number of participating silicon ions. Its second part is bound by F^- ions (existing in the solution) and forms stable complex ions $[SiF_6]^{2-}$ that pass into the solution. In fact, both secondary reactions (2a) and (2b) proceed in parallel. The contribution of both reactions is controlled by specific experimental conditions.

Among the variety of semiconductor materials, only silicon exhibits the reaction of ion disproportionation with mutual exchange of electrons and transformation into a neutral atom and an ion with an increased valence. This is a serious chemical factor distinguishing silicon from other semiconductors and maintaining the porous layer formation. Germanium, which is closest in properties, can also be dissolved, yielding divalent and tetravalent ions. However, bivalent germanium compounds are less stable than bivalent silicon ones, and the plausible reaction of their disproportionation is totally suppressed by Ge^{2+} ion oxidation by hydrogen ions.

PORE NUCLEATION AND GROWTH

We consider the first stage (pore nucleation) during the electrolytic (i.e., under the action of an external current source) formation of *por*-Si. Immediately after applying the external voltage to an electrolytic cell in the absence of surface defects, uniform (isotropic) dissolution of silicon begins according to reaction (1) and Si^{2+} ions begin to accumulate. At this initial stage, *por*–Si is not formed. This is the so-called incubation period observed experimentally [21].

The Si^{2+} ions produced by reaction (1) can be adsorbed by the silicon surface at points of their formation or can diffuse in the solution as complex $[SiF_4]^{2-}$ ions and be adsorbed at a certain distance from the formation site. Then reactions (2a) and (2b) become efficient. The disproportionation reaction requires a charge exchange between two Si^{2+} ions. It is known that the probability of charge exchange between separate ions or molecules containing them is much higher when these are adsorbed at solid conducting surfaces than when the ions are in the solution. In the former case, this is caused by free carriers in the solid phase; thus, a direct charge exchange can proceed between particles separated by a significant distance. In the case of solution, the preliminary direct approach of particles is required; furthermore, potential barriers related to deformation or removal of solvate shells surrounding particles should be overcome.

Thus, ions adsorbed at the silicon surface are subject to disproportionation. Secondary neutral Si atoms formed by reaction (2b) are also initially adsorbed at the silicon substrate surface containing specific initial defects, i.e., "excess" surface silicon atoms.

We estimate the concentration of these new silicon atoms in a specific case. Let the current density be 10 mA/cm^2, which is a typical value when manufacturing *por*-Si. At a 100% current efficiency, about 3×10^{16} Si^{2+} ions per 1 cm^2 per second are formed. If we assume that only 1% of the Si^{2+} ions decay, then by reaction (2b), this corresponds to the formation of about 10^{14} neutral silicon atoms. Recall that the surface concentration of Si atoms in the lattice is on the order of 3×10^{14} cm^{-2}. Thus, the concentration of atoms repeatedly crystallized per second at the silicon substrate surface is comparable to, or exceeds, the surface concentration of the "parent" lattice. Under these conditions, newly formed silicon atoms have no time to uniformly complete the initial silicon lattice. A chaotic distribution of secondary silicon atoms over the substrate surface becomes more probable, including distribution with the formation of aggregates consisting of a few atoms of secondary silicon.

These aggregates can again be dissolved according to reaction (1). However, due to quantum-size widening of the band gap, their resistance can greatly exceed that of the initial silicon, which increases the aggregate stability against dissolution. Thus, statistically distributed islands (surface nanocrystallites) with increased stability against dissolution emerge at the silicon surface. Thus, the first stage of porous-silicon formation is completed (i.e., surface inhomogeneities of quantum-size scale come into existence).

In later stages, silicon is dissolved predominantly in the spaces between crystalline aggregates; i.e., the formation and deepening of pores begin. Simultaneously, secondary silicon grows over the entire *por*-Si surface, including pore walls. Its high resistivity, along with quantum-size effects in thin pore walls, maintains increased stability of the walls against dissolution and promotes large pore growth into the substrate depth [3]. Secondary silicon also precipitates on pore walls as separate aggregates, which allows the formation of small lateral branches of pores.

Thus, according to our concepts, two pore systems are formed in *por*-Si: (i) large main pores of micrometer width, propagating into the substrate depth to tens of micrometers and clearly observed by optical microscopes and (ii) much shorter "nanopores" branched from large pores. Such a porous structure maintains transport of initial reactants and reaction products over the entire *por*-Si volume and conforms well to microscopic studies of the *por*-Si surface [11]. Possible formation of secondary silicon aggregates with a crystalline structure (nanocrystallites) was indirectly confirmed by luminescence (in the visible region of the spectrum) of porous layers on amorphous silicon substrates (see [23]).

ROLE OF LIGHT IN DISPROPORTIONATION REACTIONS

Numerous experiments show that the contribution of the disproportionation reaction to porous silicon formation is enhanced by illumination [24].

Porous layers on *n*-Si substrates are nearly always produced under illumination. In this case, light should produce a sufficient hole concentration at the silicon–electrolyte interface. The *por*-Si consists of two layers: the upper nanocrystalline layer featuring an intense visible PL and the lower macrocrystalline layer at the layer–substrate interface [11, 25]. Thicknesses of both layers depend on substrate parameters and grow as the anodic oxidation time (the amount of passed electric charge) increases. It is assumed that incident light (more precisely, its short-wavelength component) is absorbed in the growing nanocrystalline layer and the macrocrystalline layer grows in the absence of, or at low-intensity, illumination [25]. A sharp interface is observed between the two layers. We emphasize that only a macrocrystalline layer (exhibiting no visible photoluminescence) is, as a rule, formed on n^+-Si substrates without illumination, in spite of a sufficient subsurface hole concentration.

As is known, illumination during *por*-Si growth on *p*-Si substrates has virtually no effect on electrical parameters of the process (cell voltage and current density) but substantially changes the formed *por*-Si layer structure. The layer becomes more light-colored, its surface becomes more porous and dim, and PL of the layer produced on illumination is shifted to shorter wavelengths and has a much higher intensity than that of layers manufactured in the dark [24]. Cleavages of such samples also exhibit two pronounced layers with a distinct interface; the upper layer is more light-colored and homogeneous.

We consider reaction (2b) and the impact of light on its kinetics in more detail. As was mentioned above, this reaction proceeds with participation of a solid phase, i.e., the silicon substrate or porous layer. In the ionic form, the reaction can be written as two coupled reactions of charge transport through the Si/Si^{2+} interface:

$$Si^{2+} + 2e^- \longrightarrow Si \qquad (3a)$$

and

$$Si^{2+} + 2h^+ \longrightarrow Si^{4+}. \qquad (3b)$$

The resulting rate of reaction (2b) is controlled by the rate of the slower reaction from (3a) and (3b).

The impact of illumination on the rate of reaction (2b) can be understood if we assume that reactions (3a) and (3b) proceed via the conduction and valence bands, respectively. Such an assumption is valid, since the two reactions are related to different electrochemical systems (Si^{2+}/Si and Si^{4+}/Si^{2+}, respectively) and have different electrochemical potentials in a solution. As is known, these potentials are specific analogues of the semiconductor Fermi levels and it is their position rel-

ative to the semiconductor band diagram that controls the interphase charge transport. In this case, the reaction kinetics is affected by the semiconductor's parameters: the concentration of majority and minority carriers, their mobility, and the surface recombination rate. Therefore, as illumination increases the concentration of minority carriers in both *n*- and *p*-type substrates, it promotes the disproportionation reaction (2b) at the expense of reaction (2a). Correspondingly, the *por*-Si structure and luminescence are changed. A finely crystalline layer with efficient PL is formed at the *por*-Si surface.

CONCLUSION

A mechanism of pore nucleation and initial growth stage of pores during porous silicon (*por*–Si) formation is proposed. The reaction of mutual charge exchange between Si^{2+} ions (disproportionation reaction) has a dominant role in this process. The Si^{2+} ions are formed at the first stage of the electrolytic or so-called "chemical" methods of *por*–Si production. The disproportionation leads to the production of secondary Si neutral atoms and Si^{4+} ions. Taking into account this process, the following disputable and unclear aspects in the *por*-Si formation mechanism were explained:

(i) the high concentration of pore nucleation centers that depends weakly on the conduction type, doping level, and defect density in the initial silicon matrix;

(ii) formation of two pore types having micrometer and nanometer thicknesses and different lengths; and

(iii) the impact of light on the *por*-Si morphology; in particular, the formation of the two-layer *por*-Si structure during anodic oxidation of silicon substrates of both conduction types exposed to illumination.

ACKNOWLEDGMENTS

The work was supported in part by the Federal Program "Physics of Solid-State Nanostructures," project nos. 99-1107 and 97-1035.

REFERENCES

1. A. Uhlir, Bell Syst. Tech. J. **35**, 333 (1956).
2. R. L. Smith and S. D. Collins, J. Appl. Phys. **71**, R1 (1992).
3. L. T. Canham, Appl. Phys. Lett. **57**, 1046 (1990).
4. M. J. J. Theunissen, J. Electrochem. Soc. **119**, 351 (1972).
5. *Silicon, Collection of Articles*, Ed. by D. A. Petrov (Inostrannaya Literatura, Moscow, 1960).
6. P. Allongue, V. Costa-Keiling, and H. Gerischer, J. Electrochem. Soc. **140**, 1009 (1993).
7. Y. Kang and J. Jorne, J. Electrochem. Soc. **140**, 2258 (1993).
8. A. Valance, Phys. Rev. B **52**, 8323 (1995); Phys. Rev. B **55**, 9706 (1997).
9. P. Allongue, C. H. de Villeneuve, L. Pinsard, and M. C. Bernard, Appl. Phys. Lett. **67**, 941 (1995).
10. J. E. Peou, C. H. de Villeneuve, F. Boutry-Forveille, *et al.*, in *Pits and Pores: Formation, Properties, and Significance for Advanced Luminescent Materials*, Ed. by P. Schmuki *et al.* (Pennington, 1997), Proc.-Electrochem. Soc. **97-7**, 83 (1997).
11. C. Levy-Clement, A. Logoubi, and M. Tomkiewicz, J. Electrochem. Soc. **141**, 958 (1994).
12. E. S. Kooij, D. Vanmaekelbergh, and J. J. Kelly, in *Pits and Pores: Formation, Properties, and Significance for Advanced Luminescent Materials*, Ed. by P. Schmuki *et al.* (Pennington, 1997), Proc.-Electrochem. Soc. **97-7**, 70 (1997).
13. A. G. Cullis, L. T. Canham, and D. J. Calcott, J. Appl. Phys. **82**, 909 (1997).
14. P. M. Faushet, in *Pits and Pores: Formation, Properties, and Significance for Advanced Luminescent Materials*, Ed. by P. Schmuki *et al.* (Pennington, 1997), Proc.-Electrochem. Soc. **97-7**, 27 (1997).
15. O. Teschke, M. S. dos Santos, M. U. Kleinke, *et al.*, J. Appl. Phys. **78**, 590 (1995).
16. D. N. Goryachev and O. M. Sreseli, Fiz. Tekh. Poluprovodn. (St. Petersburg) **31**, 1383 (1997) [Semiconductors **31**, 1192 (1997)].
17. D. R. Turner, in *The Electrochemistry of Semiconductors*, Ed. by P. J. Holms (Academic, London, 1962).
18. R. Memming and G. Schwandt, Surf. Sci. **4**, 109 (1966).
19. L. M. Peter, D. J. Blackwood, and S. Pons, Phys. Rev. Lett. **62**, 308 (1989).
20. J. Eddowes, J. Electroanal. Chem. **280**, 297 (1990).
21. D. Brumhead, L. T. Canham, D. M. Seekings, and P. J. Tufton, Electrochim. Acta **38**, 191 (1993).
22. F. Kozlowski and W. Lang, J. Appl. Phys. **72**, 5401 (1992).
23. R. B. Wehrspohn, J.-N. Chazalviel, F. Ozanam, and I. Solomon, Thin Solid Films **297**, 5 (1997).
24. L. V. Belyakov, D. N. Goryachev, O. M. Sreseli, and I. D. Yaroshetskiĭ, Fiz. Tekh. Poluprovodn. (St. Petersburg) **27**, 1961 (1993) [Semiconductors **27**, 1078 (1993)].
25. P. Steiner, F. Kozlovski, and W. Lang, IEEE Electron Device Lett. **14**, 317 (1993).

Translated by A. Kazantsev

Semiconductors, Vol. 34, No. 9, 2000, pp. 1094–1099. Translated from Fizika i Tekhnika Poluprovodnikov, Vol. 34, No. 9, 2000, pp. 1135–1141.

PHYSICS OF SEMICONDUCTOR DEVICES

Elemental Composition and Electrical Properties of (*a*-C:H):Cu Films Prepared by Magnetron Sputtering

T. K. Zvonareva[1], V. M. Lebedev[2], T. A. Polyanskaya[1], L. V. Sharonova[1]*, and V. I. Ivanov-Omskiĭ[1]

[1]*Ioffe Physicotechnical Institute, Russian Academy of Sciences, Politekhnicheskaya ul. 26, St. Petersburg, 194021 Russia*
**e-mail: shar@nano.ioffe.rssi.ru*

[2]*Konstantinov Institute of Nuclear Physics, Russian Academy of Sciences, Gatchina, 188850 Russia*

Submitted March 14, 2000;
accepted for publication March 16, 2000

Abstract—Amorphous hydrogenated carbon films with varied copper concentration were prepared by dc co-sputtering of graphite and copper targets in an argon–hydrogen atmosphere. The relative atomic concentrations of carbon, copper, and oxygen were determined using proton Rutherford backscattering and the method of nuclear reactions. The dc conductivity of the films was studied in the in-plane and transverse geometries. The conductivity data are discussed in terms of the model of a medium in the form of a dielectric matrix containing two types of conducting inclusions in the form of graphite-like and copper nanoclusters. © *2000 MAIK "Nauka/Interperiodica".*

1. INTRODUCTION

Fabrication of systems of metal nanoclusters in dielectric matrices and investigation of their properties reflect the general interest of modern condensed-matter physics in limited-dimensionality structures. In this field, mention should be made of recent efforts directed at embedding the metal nanoclusters in carbon [1, 2]. In such a material, the metal concentration is comparable with that of carbon, and, in fact, we are dealing with a system of metal nanoclusters (precipitates) distributed in a carbon matrix [1], or with metal drops in carbon envelopes [2]. Nanocluster systems based on amorphous carbon appear to be promising media for information recording and storage, especially if the clusters are formed from magnetic metals. Electronic effects (in particular, electron transport) in these systems, which are mesoscopic media, are of considerable interest for nanoelectronics. Nevertheless, the relation of their conductivity to the material structure and composition has not yet been adequately studied, especially if the metal concentration is high.

In this paper, we report the results of studying amorphous hydrogenated carbon films (*a*-C:H):Cu having Cu concentrations of several to tens of atomic percent and belonging to nanocluster mesoscopic systems. Previous investigations of similar samples [3–8] have shown that, for high Cu concentrations, copper is partially embedded as separate atoms in the carbon network, intercalating in the graphite nanoclusters present in the film, and partially precipitates as metal drops randomly distributed in the carbon network. In other words, a mesoscopic nanocluster medium is formed. The electrical conductivity of similar samples was studied previously [3], but the distinctive feature of the present investigation is that a detailed analysis of the elemental composition of the films was performed and the conductivity was measured in different geometries, both over the surface and across the film. The data on conductivity in different geometries may be important in view of the fact that the films are grown under profoundly nonequilibrium conditions, and thus an anisotropy would be expected, as determined by the orientation of the conducting channels relative to the film plane.

2. FABRICATION OF THE (*a*-C:H):Cu FILMS

The (*a*-C:H):Cu films were prepared by magnetron dc co-sputtering of the graphite and copper targets in an argon–hydrogen plasma (80% Ar + 20% H_2) [9]. The concentration of copper introduced into the carbon films was varied by changing the copper-to-graphite target-area ratio $\Sigma = S[\mathrm{Cu}]/S[\mathrm{C}]$.

Films were deposited onto substrates heated to 200°C. Preliminarily, the sputtering chamber was evacuated to 10^{-6} Torr. The film deposition was performed in a working gas flow at 10^{-2} Torr, with the ion current density 10^{-1} A/cm^2. All the films were obtained at a negative substrate self-bias of no higher than 10 V. The film growth rate depended on the copper concentration introduced (i.e., on Σ) [9] and was 3–7 nm/min in our experiments.

The film deposition time t and the copper-to-graphite target-area ratio $\Sigma = S[\mathrm{Cu}]/S[\mathrm{C}]$ are given in the table (henceforth, technological sample numbers are used). Two main sets of samples obtained at deposition times t = 0.5 and 5.25 h, as well as one film on a glass

Parameters of (*a*-C:H):Cu samples

Sample no.	$\Sigma = S$[Cu]/S[C]	t, h	Thickness, nm	Density, g/cm^3	[Cu]/[C]	[O]/[C]
365	0	0.5	70		0.028	0.11
366	0.021	0.5	105		0.17	0.35
370	0.067	0.5	160		0.37	0.43
408	0.108	0.5	250		0.62	0.54
368	0.134	0.5	230		0.76	0.55
357	0	1.0	240			
374	0	5.25	780	1.79	0.005	0.11
375	0.091	5.25	1850	3.62	0.90	0.82
383	0.108	5.25	1900	3.58	1.02	0.89
407	0.116	5.25	1720	3.49	1.00	0.90
386	0.125	5.25	1730	3.53	0.94	0.96
410	0.134	5.25	1820	3.46	0.96	0.91
376	0.143	5.25	2180	3.81	1.30	0.91

Note: [Cu]/[C] is the ratio of atomic concentrations of Cu and C; [O]/[C] is the same for O and C.

substrate with deposition time t = 1 h (sample 357), were investigated. In each sputtering belonging to the two main runs, the films were deposited simultaneously onto fused quartz and KDB-20 (*p*-Si:B, ρ = 20 Ω cm *c*-Si(100) crystalline silicon substrates. The thicknesses of the films on quartz substrates, given in the table, were determined using an MII-11 interference Linnik microscope for the films with a deposition time of 5.25 h, and ellipsometrically using an LEF-3M ellipsometer for thinner films.

3. ELEMENTAL COMPOSITION OF (*a*-C:H):Cu FILMS

The elemental composition, i.e., the relative content of carbon, oxygen, and copper, was determined for (*a*-C:H):Cu films on silicon substrates by nuclear methods of elemental analysis: Rutherford backscattering and nuclear reactions [10]. The analysis was performed on an analytical complex designed for the study of materials and developed on the basis of an electrostatic accelerator at the Konstantinov Institute of Nuclear Physics, Russian Academy of Sciences, Gatchina, Leningrad oblast [11].

Figure 1 shows typical spectra of protons (p) scattered to an angle of 135° for (*a*-C:H):Cu films. The proton energy in the beam was E_p = 1 MeV. The silicon signal appears in these spectra owing to scattering from the substrate atoms. For thin films, the relative concentrations of carbon, oxygen, and copper were determined from the areas under the spectral peaks corresponding to these elements (Fig. 1a); for thicker films, they were determined from the height of steps (Fig. 1b) proportional to the scattering cross section and the concentration of a given type of atoms in the target [10]. In the spectra measured for thick (~2 μm) films under nor-

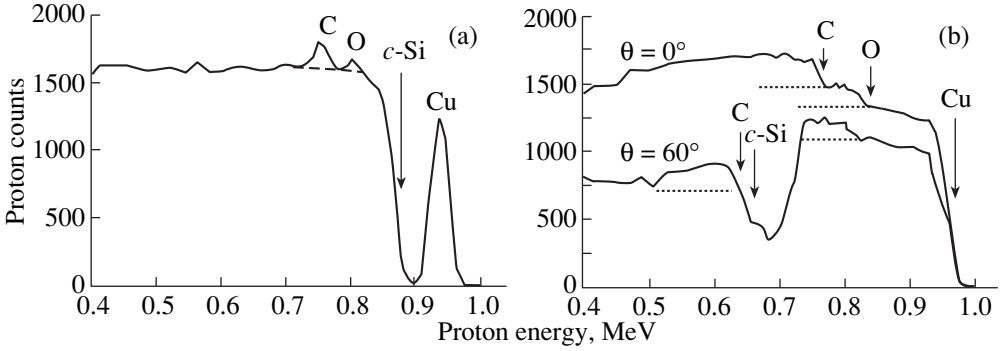

Fig. 1. Spectra of protons scattered at an angle of 135° from carbon, oxygen, copper, and silicon atoms in (*a*-C:H):Cu films on *c*-Si substrates: (a) film 408, thickness 250 nm at normal incidence of the beam (θ = 0°); (b) film 407, thickness 1720 nm at normal (θ = 0°) and oblique (θ = 60°) beam incidence. Initial proton energy E_p = 1 MeV. Partial contributions from separate elements (carbon, oxygen, copper, and silicon) to the overall spectrum are shown.

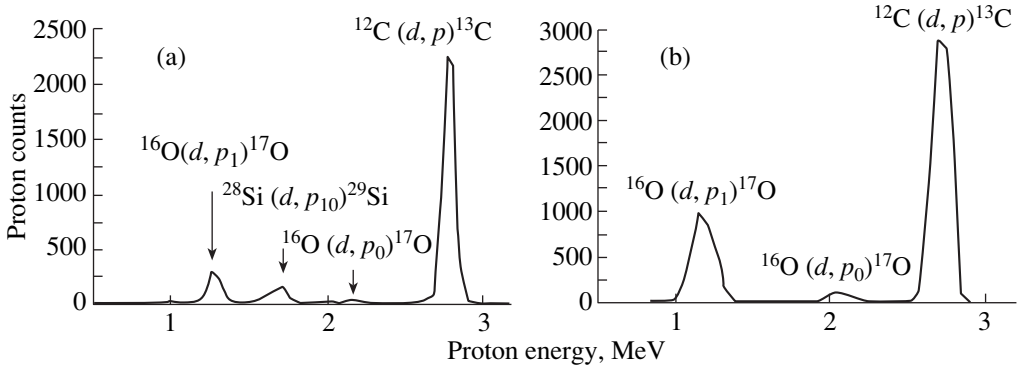

Fig. 2. Spectra of protons generated in nuclear reactions ^{12}C(d, p)^{13}C, ^{16}O(d, p)^{17}O, and ^{28}Si(d, p)^{29}Si with carbon, oxygen, and silicon atoms in (*a*-C:H):Cu films on *c*-Si substrates at normal ($\theta = 0°$) incidence of a deuteron beam with initial energy $E_d = 1$ MeV: (a) film 408, thickness 250 nm; (b) film 407, thickness 1720 nm. The proton detector was mounted at an angle of 135° to the beam direction and was shielded with an 11-μm-thick aluminum absorbing filter.

mal incidence of the beam ($\theta = 0°$), the step produced by proton scattering from carbon atoms coincides in energy with the edge of the silicon-substrate scattering spectrum. For this reason, oblique ($\theta = 60°$) incidence of protons onto the target was also used (Fig. 1b).

The carbon and oxygen content of the films was also determined by means of nuclear reactions involving deuterons (d): ^{12}C(d, p)^{13}C and ^{16}O(d, p)^{17}O [10]. Figure 2 displays characteristic spectra of protons generated by nuclear reactions involving carbon and oxygen atoms for films 407 and 408. The initial deuteron energy was $E_d = 1$ MeV. An ion detector mounted at an angle of 135° to the beam direction was shielded from deuterons scattered into the back hemisphere with an 11-μm-thick aluminum absorbing filter. Reference SiO_2 and Al_2O_3 films were used to evaluate the oxygen content of the films.

Data on the relative content of carbon, copper, and oxygen in (*a*-C:H):Cu films, obtained by two different techniques, practically coincide with the average values given in the table.[1]

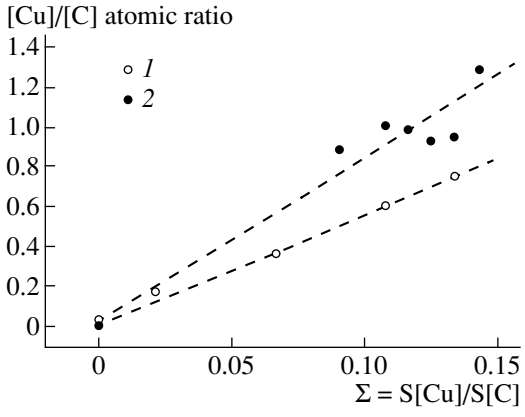

Fig. 3. Atomic concentration ratio [Cu]/[C] in (*a*-C:H):Cu films as a function of the area ratio of the targets being sputtered $\Sigma = S$[Cu]/S[C] for two sets of samples with deposition times t = (*1*) 0.5 and (*2*) 5.25 h.

Figure 3 shows the ratio of atomic concentrations of copper and carbon incorporated in the film, [Cu]/[C], as a function of the area ratio of the targets being sputtered, Σ. Two basic conclusions can be made. First, no single calibration dependence can be obtained for films obtained at different sputtering times. Although these dependences can be regarded in both cases as linear (with higher precision for thin films and lower precision for thick films), the slopes of the straight lines differ by a factor of ~1.3. Second, the actual ratio of the atomic concentrations [Cu]/[C] exceeds that of the target areas by a factor of 6–8, owing to the difference in the copper and graphite sputtering rates.

As can be seen from the table, a high oxygen content is characteristic of the films. Its presumed origin is the residual atmosphere in the growth chamber. Similarly to copper, oxygen is introduced into thin and thick films in different concentrations under the same technological conditions (with only the sputtering times being different). The oxygen concentration grows with increasing copper concentration in both types of samples (Figure 4).

The mass thickness of the films was also determined in the Rutherford backscattering experiments. For films up to several micrometers thick, the energy width of the part of the spectrum corresponding to scattering from the film is proportional to the film thickness. The proportionality factor depends on the elemental composition of the target and the scattering kinematics and stopping losses for protons entering and leaving the sample [10]. Combined with the known linear thicknesses of the films, these data allow an evaluation of the mass densities. Since the mass thickness is determined with an accuracy of 5% for thick films and ~50% for

[1] Hydrogen effusion experiments performed with copper-free *a*-C:H films indicate that the hydrogen concentration in these films is ~25 at. %.

thin films, density data are given in the table for the former films only. In copper-free *a*-C:H, the density is 1.7 g/cm^3; this value is typical of amorphous hydrogenated carbon [12]. The values of about 3.5 g/cm^3 for films with copper are directly due to the copper contribution (the bulk copper density is ~9 g/cm^3). Strictly speaking, the mentioned densities of thick films should be regarded as estimates rather than as precise values. The reason is that the linear thicknesses were determined for films on quartz substrates and the mass thicknesses were determined for films on silicon, while the growth rates may vary between films on different substrates even in a single deposition run.

4. ELECTRICAL CONDUCTIVITY OF (*a*-C:H):Cu FILMS

The conductivity was measured at room temperature with a dc voltage of ≤0.5 V across the sample [in the linear portion of the current–voltage (*I–V*) characteristic]. Films on silicon, quartz, and glass substrates were studied, with preference given to the results obtained with insulating substrates (quartz and glass). The films were provided with nickel electrodes. Prior to film growth, parallel 0.7-mm-wide Ni strips spaced 3 mm apart were deposited onto a ~1 × 2 cm^2 substrate by rf ion-plasma sputtering. After a film was deposited, the strips were used as electrodes for the in-plane conductivity measurements. Next, using the same method, nickel strips of the same width were deposited onto the film surface perpendicularly (in the film plane) to the bottom strips. The intersections of the bottom and upper electrodes formed, in fact, a set of samples for conductivity measurements across the film at different points (5–6 points per film), with the area of each sample being equal to ~0.5 mm^2. To exclude possible artifacts related to the upper Ni electrodes (for example, metal atoms may penetrate deep inside the film or even through the film as far as the substrate), an alternative kind of upper electrode was used, with In + Ga eutectic drops deposited directly onto the carbon film at room temperature. In both cases, the general pattern of the film electrical properties was the same.

The obtained data are shown in Figure 5 as a dependence of the electrical resistivity on the ratio of the atomic concentrations of copper and carbon. Figure 5a shows data for all the films on quartz and glass substrates in the entire range of compositions studied (see table), with open and full symbols corresponding to conduction across the film and over the surface of the film, respectively. Figure 5b compares the data for films deposited for 5.25 h onto silicon and quartz substrates. It can be seen that the conductivity patterns are the same in these two cases. The substrate material exerts little or no effect on the electrical properties of the films, even though insulating substrates (quartz and glass) are preferable to silicon in measuring the conductivity of carbon films. The in-plane conductivity measurements for films on silicon substrates are impossible because of the effect of shunting by the substrate. For films on silicon substrates, data on the transverse conductivity were also not always reliable. As a reliability criterion, the linearity of the *I–V* characteristics was adopted. Evidently, with the chosen geometry of electrodes, the distribution of potential in the film is affected by the substrate if the resistivity of the latter is not sufficiently high.

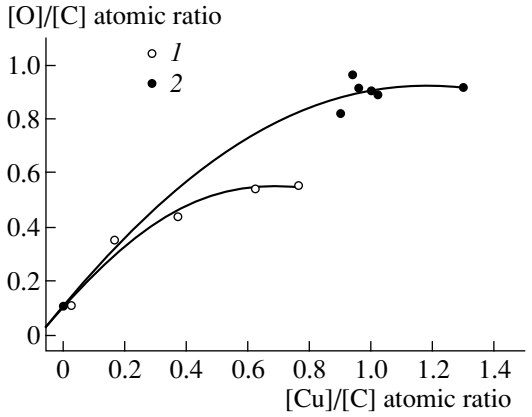

Fig. 4. Correlation of oxygen (O) and copper (Cu) atomic concentrations in (*a*-C:H):Cu films for two sets of samples with deposition times *t* = (*1*) 0.5 and (*2*) 5.25 h.

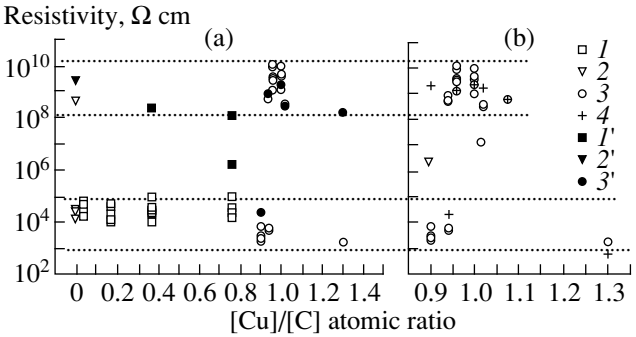

Fig. 5. Resistivity of (*a*-C:H):Cu: (a) transverse (*1–3*) and in-plane (*1*'–*3*') measurements with films on (*1*, *1*', *3*, *3*') quartz and (*2*, *2*') glass substrates; (b) transverse measurements with films on (*3*) quartz and (*4*) silicon substrates. Deposition times *t* = (*1*, *1*') 0.5, (*2*, *2*') 1, and (*3*, *4*, *3*') 5.25 h (see table).

It can be seen from Fig. 5 that all the values of resistivity obtained in the transverse measurements fall into two ranges, $\rho = 10^3$–10^5 and 10^8–10^{10} Ω cm (conductivity $\sigma = 10^{-3}$–10^{-5} and 10^{-8}–10^{-10} Ω^{-1} cm^{-1}, respectively). These ranges refer to both thin (*t* = 0.5 h) and thick (*t* = 5.25 h) films and in no way correlate with the copper content in the studied range of concentrations. Both resistivity levels can be observed in the same film. The data obtained in planar geometry correspond to the higher resistivity range, except for a single point (sample 375).

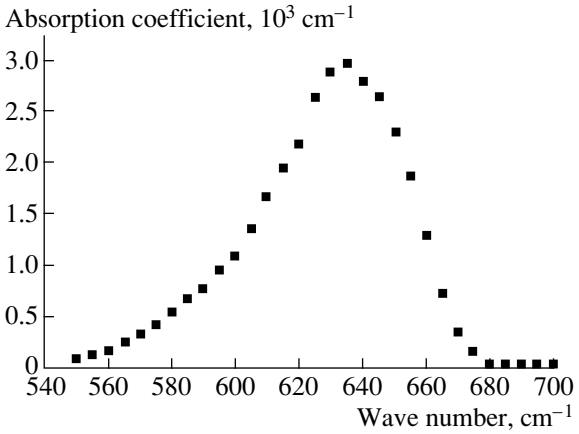

Fig. 6. Absorption coefficient of an (*a*-C:H):Cu film in the spectral range of the Cu_2O vibrational mode (sample 376).

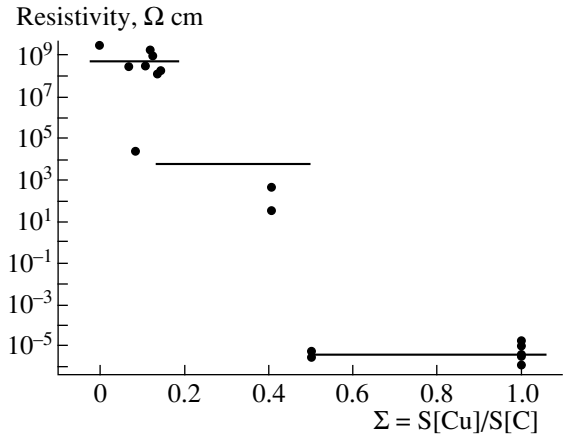

Fig. 7. In-plane resistivity of (*a*-C:H):Cu films as a function of a technological parameter (copper content Σ). Data sets *1*'–*3*' from Fig. 5 are supplemented with data for (*a*-C:H):Cu films on different insulating substrates (glass and quartz), with high copper content and varied thickness.

This situation can be simulated by a high-resistivity matrix (higher resistivity range) with nanometer inclusions of a conducting phase. When the dimensions of separate inclusions or chains of these are comparable with the film thickness and are found in the contact region, "punctures" with lower resistivity are observed in the film.

Which conducting phase corresponds to the lower resistivity level remains unknown. It seems unlikely that it consists of pure copper clusters: first, no appreciable influence of the copper concentration on the conductivity is observed, since the "punctures" are also observed in *a*-C:H samples without copper; second, even the lowest experimental values of resistivity are substantially larger than the bulk copper resistivity. We may suppose that the "puncture" conduction is controlled by graphite-like clusters existing in copper-free *a*-C:H films, and, in (*a*-C:H):Cu, they can be modified (intercalated) with copper atoms [8]. Cross-sectional scanning electron microscopy images of cleaved films [9] demonstrate structural inhomogeneities directed from the substrate toward the surface and developed to the greatest extent in copper-containing samples. With such a structural anisotropy, it is reasonable to also expect an anisotropy of the electrical properties. It is quite possible that the conducting channels are elements of the inhomogeneities observed previously [9].

As mentioned above, copper in (*a*-C:H):Cu films can also precipitate in the form of pure copper drops (copper nanoclusters). If such nanoclusters have a high concentration, they can form conducting chains and percolation along these chains is bound to occur, with the conductivity becoming comparable with that of copper. Based on the data given in the table and on the assumption that the hydrogen content in all the samples is at the level of 25 at. %, we estimate the volume content of copper in the second set of samples (the deposition time $t = 5.25$ h) at ~30%, a value on the order of the critical concentration in the percolation theory [13]. Nevertheless, no transition to metallic conduction is observed in Fig. 5. This may occur for several reasons. First, the percolation-theory inferences are based on the assumption of a chaotic distribution of impurity atoms (in our case, copper). At the same time, we assume that the formation of metallic clusters in the films results from correlated atomic distribution under nonequilibrium growth conditions. In this situation, the percolation threshold should be determined by considering a random distribution of clusters, rather than atoms, and this yields higher critical concentrations for copper. Second, we believe (as stated above) that some copper atoms are incorporated into the graphite network (intercalation) and therefore are not involved in the formation of metallic percolation channels; i.e., the effective concentration of copper atoms in these channels is lower than the total copper concentration.

In addition, it should be noted that the role of oxygen in the films is not clear yet. The most likely conjecture is that copper enters into chemical combination with oxygen and forms Cu_2O or CuO oxides. Figure 6 shows IR absorption spectra of (*a*-C:H):Cu films, measured using a Specord-75IR spectrometer. An absorption band peaked at ~635 cm^{-1} can be ascribed to Cu_2O [14]. An absorption band of CuO at ~510 cm^{-1}[14] was not detected. However, even taking into account the presence of Cu_2O in the films, we can state that copper is far from being totally oxidized. This is confirmed by direct observations of copper clusters in similar (*a*-C:H):Cu films [6, 7].

In order to observe the transition to metallic conduction via copper and determine real technological conditions (the values of parameter Σ) necessary for this transition to occur, we combined in Fig. 7 the data on lateral conductivity in the film plane for different samples, including those not belonging to the sets under study and having high copper concentrations ($\Sigma \longrightarrow 1$). It can

be seen that transition to a third conductivity level ($\sigma = 10^5$–10^6 Ω^{-1} cm^{-1}), corresponding to metallic copper conductivity, does occur for $\Sigma \gtrsim 0.4$.

5. CONCLUSION

The data obtained in studying the elemental composition of (*a*-C:H):Cu films prepared by magnetron sputtering show that the relative content of carbon, copper, and oxygen depends on the duration of film growth under the same technological conditions.

The conductivity data demonstrate an anisotropy associated with the geometry of the (*a*-C:H):Cu-film growth process. Conducting channels of the "puncture" type across the film are observed in a wide range of copper concentrations (estimated at the range from 0 to ~30 at. %), while the in-plane conductivity is low. The whole set of conductivity data for copper concentrations $\gtrsim$50 at. % (estimate) can be interpreted in terms of the insulator-matrix model ($\sigma = 10^{-10}$–10^{-8} Ω^{-1} cm^{-1}) with inclusions of two different conducting phases with conductivities of $\sigma = 10^{-5}$–10^{-3} and 10^{-5}–10^{-6} Ω^{-1} cm^{-1}. The first of these is assumed to be composed of graphite-like nanoclusters, including those intercalated with copper atoms (a contribution from conduction via Cu_2O is also possible), whereas the second phase is formed by copper nanoclusters.

Thus, electrical properties of the films prepared by magnetron sputtering are consistent with the interpretation of (*a*-C:H):Cu as a mesoscopic medium. Furthermore, *a*-C:H (copper-free amorphous hydrogenated carbon) is a mesoscopic medium as well. The point is that, depending on the copper concentration in (*a*-C:H):Cu films, different systems of clusters play a key role in conduction. We note that mesoscopic effects have been observed in similar films in a study of *I*–*V* characteristics measured with a tunnel microscope probe [15].

ACKNOWLEDGMENTS

The authors are grateful to G.S. Frolova for placing at our disposal IR spectroscopic data and to A.V. Nashchekin for his participation in conductivity measurements of (*a*-C:H):Cu films.

The work was supported by the State Program "Integration" (project no. 75) and the Russian Foundation for Basic Research (project nos. 00-02-16994 and 00-02-17004).

REFERENCES

1. T. Cabioc'h, A. Naudon, M. Jaouen, *et al.*, Philos. Mag. **79** (3), 501 (1999).
2. J. Jiao and S. Seraphin, J. Appl. Phys. **83** (5), 2442 (1998).
3. V. I. Ivanov-Omskiĭ, A. B. Lodygin, and S. G. Yastrebov, Fiz. Tverd. Tela (St. Petersburg) **37** (6), 1693 (1995) [Phys. Solid State **37**, 920 (1995)].
4. V. I. Ivanov-Omskiĭ, A. B. Lodygin, and S. G. Yastrebov, Mol. Mater. **8**, 95 (1996).
5. V. I. Ivanov-Omskiĭ, A. I. Tolmatchev, and S. G. Yastrebov, Philos. Mag. B **73**, 715 (1996).
6. V. I. Ivanov-Omskiĭ, V. I. Siklitskiĭ, and S. G. Yastrebov, Fiz. Tverd. Tela (St. Petersburg) **40** (3), 568 (1998) [Phys. Solid State **40**, 524 (1998)].
7. A. V. Kolobov, H. Oyanagi, S. G. Yastrebov, *et al.*, J. Surf. Anal. **4** (2), 377 (1998).
8. V. I. Ivanov-Omskiĭ and É. A. Smorgonskaya, Fiz. Tekh. Poluprovodn. (St. Petersburg) **32** (8), 931 (1998) [Semiconductors **32**, 831 (1998)].
9. T. K. Zvonareva, V. I. Ivanov-Omskiĭ, A. V. Nashchekin, and L. V. Sharonova, Fiz. Tekh. Poluprovodn. (St. Petersburg) **34** (1), 96 (2000) [Semiconductors **34**, 98 (2000)].
10. *Ion Beam Handbook for Material Analysis*, Ed. by J. M. Mayer and E. Rimini (Academic, New York, 1977).
11. V. M. Lebedev and V. A. Smolin, 1994–1995 PNPI Research Report (Gatchina, 1996), p. 296.
12. F. Jansen, M. Machonkin, S. Kaplan, and S. Hark, J. Vac. Sci. Technol. A **3** (3), 605 (1985).
13. B. I. Shklovskiĭ and A. L. Éfros, *Electronic Properties of Doped Semiconductors* (Nauka, Moscow, 1979; Springer-Verlag, New York, 1984).
14. D. Kember and N. Sheppard, Appl. Spectrosc. **29** (6), 496 (1975).
15. A. O. Golubok, O. M. Gorbenko, T. K. Zvonareva, *et al.*, Fiz. Tekh. Poluprovodn. (St. Petersburg) **34** (2), 223 (2000) [Semiconductors **34**, 217 (2000)].

Translated by D. Mashovets

Semiconductors, Vol. 34, No. 9, 2000, pp. 1100–1102. Translated from Fizika i Tekhnika Poluprovodnikov, Vol. 34, No. 9, 2000, pp. 1142–1144.

PHYSICS OF SEMICONDUCTOR DEVICES

Tunable InAsSb/InAsSbP Laser with a Low Radiation Divergence in the *p–n*-Junction Plane

A. P. Astakhova, T. N. Danilova, A. N. Imenkov, N. M. Kolchanova, V. V. Sherstnev, and Yu. P. Yakovlev*

Ioffe Physicotechnical Institute, Russian Academy of Sciences, Politekhnicheskaya ul. 26, St. Petersburg, 194021 Russia

** e-mail: jak@itopt.ioffe.rssi.ru*

Submitted March 3, 2000; accepted for publication March 7, 2000

Abstract—On the basis of the InAsSb/InAsSbP double heterostructure, lasers with a thick active region (3 μm) and a wide cavity (40 μm) were fabricated that operated near 3.3 μm and were intended for obtaining a low radiation divergence in the *p–n*-junction plane. Laser emission spectra and radiation patterns for different currents were studied. The current-induced shift of the laser emission line reaches 24 Å. The half-width of the radiation pattern is 9° in the *p–n*-junction plane and 63° in the perpendicular plane. The experimental data on the radiation pattern are compared with the theoretical results expected in the case where two in-phase waves with the same amplitude are formed in a cavity. © *2000 MAIK "Nauka/Interperiodica"*.

1. INTRODUCTION

Tunable lasers on the basis of III–V solid solutions show considerable promise for high-resolution diode laser spectroscopy [1–3]. A narrow emission line, a large current-induced change of laser wavelength, high intensity, fast response, and stability render tunable lasers suitable for other applications.

Previously, we studied current-induced wavelength tuning and the spatial distribution of radiation in the far field of diode InAsSb/InAsSbP heterolasers having a stripe 10–12 μm wide and emitting in the 3.3-μm region. The best lasers had a single-mode spectrum and a wide range of current-induced wavelength tuning, which was as wide as 60–100 Å. The spatial distribution of laser radiation intensity in the *p–n*-junction plane for currents I close to the threshold value I_{th} corresponds to a single mode with a full angular width at half maximum $\Delta\theta \approx 22°$ corresponding to the cosine distribution of light intensity at the output cavity mirror. As the current is increased up to $2.5I_{th}$, $\Delta\theta$ increases up to 17° [4], which formally corresponds to a uniform distribution of the electric field in the light wave at the output mirror, with the light-wave amplitude virtually vanishing at the stripe edges. The realization of such a distribution is highly improbable. An assumption was made that, in the case of an anomalously narrow radiation pattern, we have propagation of two parallel light waves (instead of a single one) that oscillate in phase from one edge to another and change places. Theoretical calculations supported this assumption [5]. Later, we studied lasers with a wider stripe (18–20 μm). For some lasers with a stripe of this width, the radiation pattern in the *p–n*-junction plane corresponded to a single mode, but the distribution was broadened at its base because of the appearance of low-intensity first-order transverse modes [6]. However, the central mode split into two with increasing current. For the majority of lasers with a stripe 18 μm wide, the radiation pattern had two maxima separated by an angle of ~11°. In the case of a single transverse mode, the angular spacing should be ~20°. A theoretical analysis assuming oscillations in a waveguide in the form of two parallel out-of-phase radiation waves gives good agreement with the anomalous radiation pattern in the *p–n*-junction plane experimentally obtained for lasers with this stripe width. An additional increase of the stripe width by a factor of two (up to 40 μm) led to the fact that the second-order transverse mode became dominant in the radiation pattern in the *p–n*-junction plane for currents close to the threshold value, and the total half-width of the radiation pattern was $\Delta\theta \approx 23°$ [6]. The dependence of spectral and spatial characteristics of these lasers on current was not studied. However, such studies are of considerable importance, because lasers with a wide stripe have a larger output power and a narrower spectral line.

The aim of this study was to determine and analyze the dependence of spectral and spatial characteristics of lasers with a stripe 40 μm wide on current.

2. LASER DIODES

Laser diodes on the basis of *P*-$InAs_{0.48}Sb_{0.17}P_{0.35}$/*n*-$InAs_{0.95}Sb_{0.05}$/*N*-$InAs_{0.48}Sb_{0.17}P_{0.35}$ double heterostructures were produced by liquid-phase epitaxy on an InAs (100) substrate doped with Zn up to a hole concentration of 5×10^{18} cm^{-3}. An active region 3 μm thick was not doped intentionally. It was of *n* type and had an

electron concentration of ~10^{16} cm^{-3}. Each confining layer was 3 μm thick. The *n*-InAsSbP layer was doped with Sn up to an electron concentration of ~(3–5) × 10^{18} cm^{-3}. The *p*-InAsSbP layer was doped with Zn up to a hole concentration of ~1×10^{18} cm^{-3}.

On the grown structures, we formed photolithographically stripes 40 μm thick. Fabry–Perot cavities 250 μm long were produced by cleaving. In the lasers studied by us, substrates were ~500 μm wide and ~100 μm thick.

3. EXPERIMENTAL TECHNIQUE

We studied the laser-structure emission spectra and radiation patterns, both in the *p*–*n*-junction plane and in the perpendicular plane, as functions of current at a temperature of 77 K. The lasers were pumped by rectangular current pulses with an off-duty ratio of two and a repetition rate of 80 Hz.

4. EXPERIMENTAL RESULTS

The laser emission spectrum consists of several modes whose relative intensities depend on current. In the range of currents from $I = 1.5I_{th}$ to $3I_{th}$, it always has a dominant mode. The intensity of this mode exceeds the sum of intensities of other modes in a somewhat narrower range of currents. In this range, a laser may be treated as a single-mode device. As the current is increased, wavelengths of all laser modes linearly shift to lower values. Figure 1 shows the dependence of the wavelength λ of the dominant mode on the current. The maximum current-induced wavelength change is 24 Å, with intermode spacing being equal to 62 Å. For larger currents, long-wavelength modes are observed, which is associated with heating of the active region.

For all currents, the far-field distribution in the *p*–*n*-junction plane is represented by a single lobe with a sharp peak and a somewhat broadened base. Near the threshold current ($I/I_{th} = 1.2$), $\Delta\theta \approx 23°$, and the radiation pattern becomes sharper. With increasing current, so that $\Delta\theta \approx 9°$ for $I/I_{th} = 1.44$. In the plane perpendicular to the *p*–*n*-junction plane, $\Delta\theta \approx 63°$ (Fig. 2).

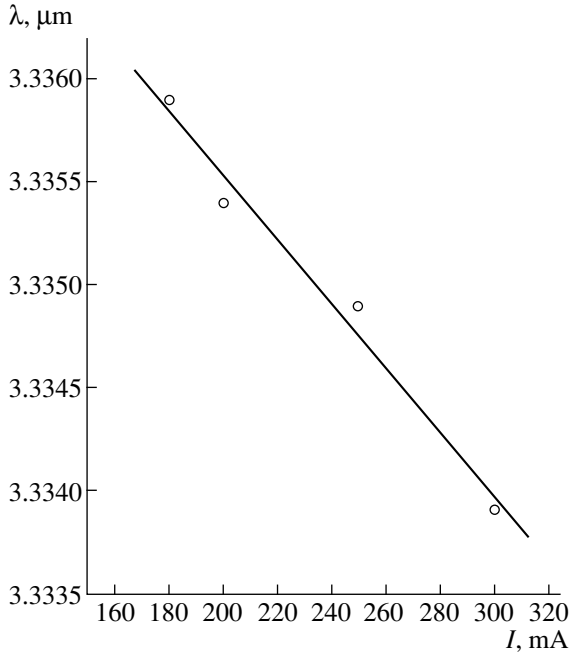

Fig. 1. Dependence of the wavelength λ of the dominant mode on the current *I* for the laser *V*-1109-1-15 at a temperature of 77 K.

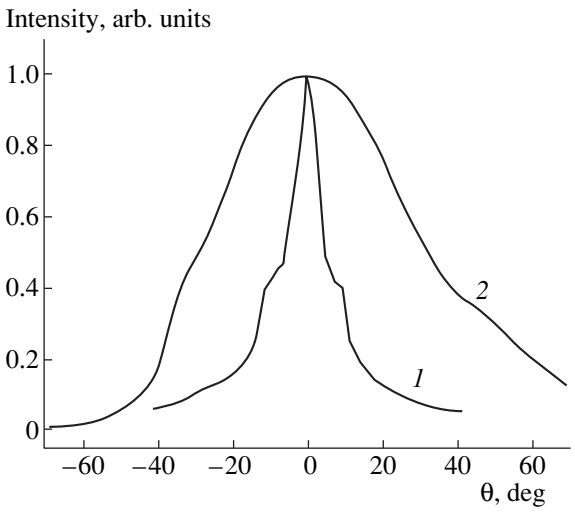

Fig. 2. Laser radiation patterns in the planes (*1*) parallel and (*2*) perpendicular to the *p*–*n* junction for the laser *V*-1109-1-15 for the current $I/I_{th} = 1.44$ and a temperature of 77 K.

5. DISCUSSION OF RESULTS

The main unexpected result was that an increase in the stripe width from 10–20 to 40 μm had almost no adverse effect on spectral laser characteristics. There exists a range of currents where the laser may be thought of as a single-mode device. The 24-Å current-induced wavelength shift, with intermode spacing being equal to 62 Å, is an average value for InAsSb/InAsSbP heterolasers with a stripe 10–20 μm wide.

The radiation pattern of the lasers under study in the *p*–*n*-junction plane is unusual. For near-threshold currents, Δθ has the same value as that in the lasers with a stripe 40 μm thick whose intensity distribution at the output cavity mirror corresponds to the second transverse mode [6], but it represents a single lobe with a sharp peak. As the current is increased, Δθ decreases, like in the case of lasers with a stripe 10–20 μm wide, but the decrease is larger than in the case of narrow-stripe lasers, and Δθ reaches 9°. For the lasers under study, like in the case of lasers with a stripe 10–20 μm wide, the experimental radiation pattern agrees well

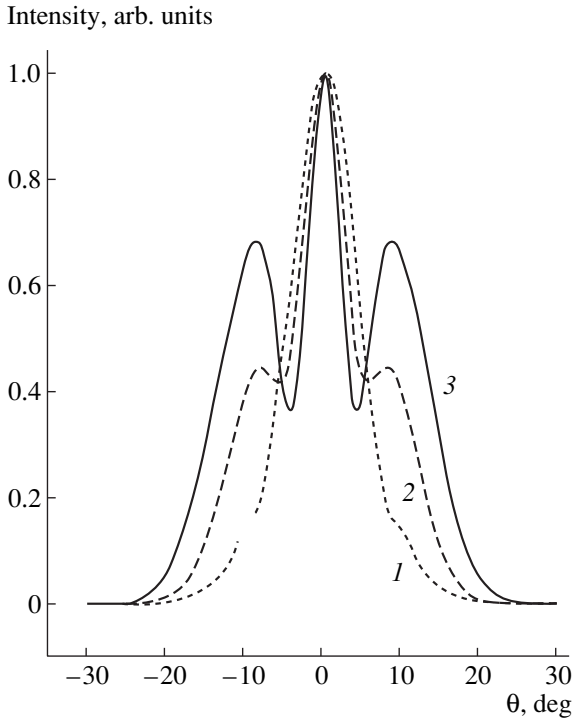

Fig. 3. Radiation patterns in the *p–n*-junction plane calculated by formulas [5] for the case where two in-phase waves of equal amplitude are formed in the cavity. The waves are displaced from the stripe center by (*1*) 5, (*2*) 8, and (*3*) 10 μm.

with the theoretical pattern obtained under the assumption that oscillations in a cavity represent two in-phase waves, but taking into account the fact that a waveguide of a wide-stripe laser contains second-order modes. Figure 3 shows radiation patterns in the *p–n*-junction plane calculated for two waves of equal amplitude and the same dependence of the refractive index on the coordinate as the one used in [5]. Curve *1* corresponds to the radiation flux whose centroid is displaced from the stripe center to the point corresponding to the coordinate of the first transverse mode. Curves *2* and *3* correspond to the waves oscillating between the extreme maximums of the second and third transverse modes, respectively. The experimental radiation pattern agrees well with theoretical curve *2* in accordance with the observation of the second-order transverse mode in lasers with a stripe 40 μm wide in the case of propagation of a single light wave [6]. In the case of wide stripes, side wings appear in the pattern, but their intensity is low.

In the plane perpendicular to the *p–n*-junction plane, the radiation pattern has a cosine intensity distribution. Its half-width is close to the value determined by the relationship $\Delta\theta = \lambda/d = 63°$, where d is the width of the active region. Most likely, the beam does not oscillate in this direction. We also note that the fulfillment of this relation for $\Delta\theta$ suggests that, in the case of an active region 3 μm thick, the light beam does not enter wide-gap regions. This is indicative of a good optical confinement, which is close to unity.

6. CONCLUSION

Thus, the study of laser diodes based on InAsSb/InAsSbP junctions with a stripe 40 μm wide showed a wide-range linear current-induced wavelength tuning, which enables one to use them for high-resolution diode laser spectroscopy. The comparison of the experimental dependence of the radiation pattern in the *p–n*-junction plane with the theoretical distribution suggests that two in-phase waves are formed in lasers of the given type, which leads to a low divergence of laser radiation.

ACKNOWLEDGMENTS

This work was supported in part by INCO-Copernicus under contract no. N1C15-CT97-0802 (DG12-CDPF) and the Russian Foundation for Basic Research (project no. 99-02-18019).

REFERENCES

1. Yu. P. Yakovlev, A. N. Baranov, A. N. Imenkov, *et al.*, Kvantovaya Élektron. (Moscow) **20**, 839 (1993).
2. A. P. Danilova, A. N. Imenkov, N. M. Kolchanova, *et al.*, Fiz. Tekh. Poluprovodn. (St. Petersburg) **33**, 1469 (1999) [Semiconductors **33**, 1322 (1999)].
3. A. P. Danilova, A. N. Imenkov, N. M. Kolchanova, *et al.*, Fiz. Tekh. Poluprovodn. (St. Petersburg) **34**, 115 (2000) [Semiconductors **34**, 237 (2000)].
4. T. N. Danilova, A. P. Danilova, O. G. Ershov, *et al.*, Fiz. Tekh. Poluprovodn. (St. Petersburg) **32**, 373 (1998) [Semiconductors **32**, 339 (1998)].
5. A. P. Danilova, T. N. Danilova, A. N. Imenkov, *et al.*, Fiz. Tekh. Poluprovodn. (St. Petersburg) **33**, 1014 (1999) [Semiconductors **33**, 924 (1999)].
6. A. N. Baranov, T. N. Danilova, O. G. Ershov, *et al.*, Pis'ma Zh. Tekh. Fiz. **19** (17), 30 (1993) [Tech. Phys. Lett. **19**, 543 (1993)].

Translated by A. Kirkin

Semiconductors, Vol. 34, No. 9, 2000, pp. 983–988. Translated from Fizika i Tekhnika Poluprovodnikov, Vol. 34, No. 9, 2000, pp. 1025–1029.

ATOMIC STRUCTURE AND NONELECTRONIC PROPERTIES OF SEMICONDUCTORS

Long-Range Effects of Ion Irradiation, Chemical Etching, and Mechanical Grinding on Relaxation of a Solid Solution of Iron in Gallium Phosphide

E. S. Demidov, A. B. Gromoglasova*, and V. V. Karzanov

Nizhni Novgorod State University, pr. Gagarina 23, Nizhni Novgorod, 603600 Russia

**e-mail: anna@phys.unn.runnet.ru*

Submitted February 25, 2000;
accepted for publication March 14, 2000

Abstract—Electron spin resonance was used to study directly the influence of external factors on a system of defects in gallium phosphide crystals doped nonuniformly with iron. The Fe_s^{3+} (Ga) ions replacing Ga atoms (the *A* centers) and Fe_i^0 interstitial atoms (the *B* centers) are considered as indicators and participants in rearrangement of the crystal's defect system. Long-range effects of ion irradiation with argon, chemical etching, or mechanical grinding on the *A* and *B* centers are observed. The long-range effect is explained by plastic deformation of the GaP:Fe crystal and by interaction of dislocations with *A* and *B* centers when the crystal is modified by ion irradiation or by removal of a layer that is saturated with Fe_s^{3+} (Ga) centers and gives rise to stresses from one of the sample surfaces. In the case of ion irradiation, the role of elastic waves that are generated in the stopping zone of argon ions and that interact with *B* centers and dislocations is apparently important. © *2000 MAIK "Nauka/Interperiodica".*

INTRODUCTION

The Fe impurity in gallium phosphide is a convenient indicator of the rearrangement of a defect structure under external effects on the crystal of this wide-gap III–V semiconductor. At the liquid-nitrogen temperature, the following electron spin resonance (ESR) spectra related to 3*d*-impurity centers are easily detected: spectrum *A* originating from substitutional (Me_s) triply ionized Fe centers at the gallium sites Fe_s^{3+} (Ga) and spectrum *B* originating from interstitial (Me_i) neutral Fe_i^0 centers, as was established elsewhere [1–3]. In this case, according to [3], the solubility of the interstitial component may be as high as 2×10^{17} cm^{-3}. This value is larger by an order of magnitude than that for the Me_i component in silicon and is comparable to a solubility equal to ~10^{18} cm^{-3} for Fe_s^{3+} (Ga) in GaP. The Fe-Me_i component in gallium phosphide is bound to a lesser extent and, consequently, is more mobile compared to Me_s. Therefore [3], low-temperature relaxation of a solid solution is characteristic of Fe_i^0; in the course of this relaxation, solid-state reactions occurring in GaP:Fe are of the same type that proceed in silicon with 3*d* Fe_i^0 or Cr_i^+ centers, in which case these impurities are predominantly dissolved in the form of Me_i. It was shown previously [4–6] that bombardment of the crystal surface with argon ions can be used to control the processes of complex formation and decomposition of a 3*d*-impurity solid solution in the bulk of silicon at distances of hundreds of micrometers from the surface (i.e., far beyond the stopping range of Ar^+ ions). It is also reasonable to expect a manifestation of such a long-range effect in the case of ion implantation of argon into gallium phosphide in view of the aforementioned similarity in the behavior of the interstitial fraction of Fe impurity in GaP to that of Cr and Fe in Si. It is noteworthy that indirect indications of the long-range effect in III–V semiconductors have been previously observed in the case of irradiation of semi-insulating GaAs:Cr and InP:Fe crystals [7, 8]. This paper is devoted to a study of the long-range effect in GaP:Fe irradiated with argon ions; the ESR method is used to directly monitor the Fe_s^{3+} (Ga) and Fe_i^0 states. We observed the long-range effect in the cases of both irradiation of the crystals with argon ions and chemical or mechanical removal of near-surface layers of the crystal. The origin of the long-range effect is discussed.

1063-7826/00/3409-0983$20.00

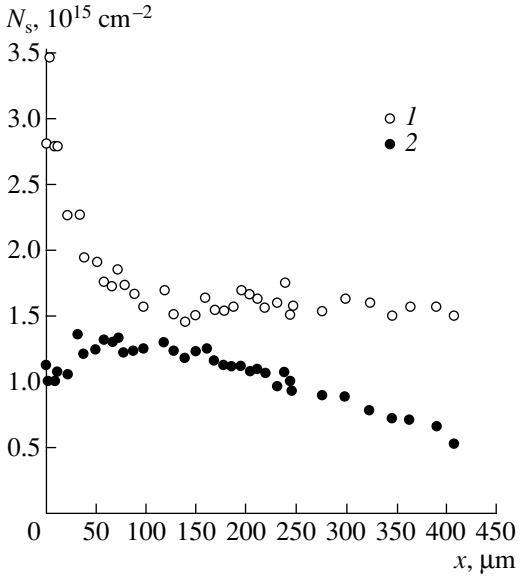

Fig. 1. Integral distribution of concentration N_s for (*1*) *A* and (*2*) *B* Fe centers over the depth x in the GaP:Fe sample irradiated with argon ions; the distribution was obtained by chemical layer-by-layer etching.

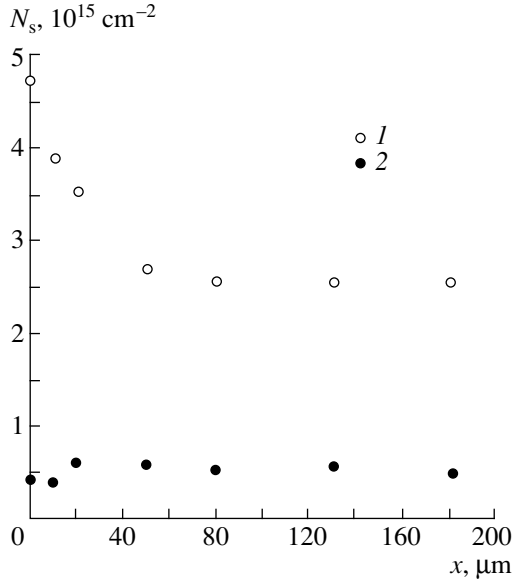

Fig. 2. The same as in Fig. 1, but for an unirradiated sample in the case of layer-by-layer removal of GaP by mechanical grinding.

EXPERIMENTAL

As starting samples, we used wafers of GaP single crystals cut in the (111) plane that were approximately 700 μm thick and had a concentration of shallow-level donors of 2×10^{17} cm^{-3} and a dislocation density of 10^4 cm^{-2}. Doping of GaP samples with Fe has been described elsewhere [3, 7]. The samples were irradiated with Ar^+ ions with an energy of 40 keV and a dose of $F = 10^{17}$ cm^{-2}; the ion-current density was $j = 7$ μA/cm^2. The temperature of the GaP sample during irradiation was no higher than 70°C.

The ESR spectra were recorded using an *EPA-2M* Russian-made modernized 3-cm spectrometer [7] at a temperature of 80 K in a cryostat [8]. As a standard of intensity, we used the traces of Cr^{3+}-ion impurity in a sapphire rod on which the sample was mounted in the cryostat. The standard was calibrated with a weighed copper sulfate ($CuSO_4 \cdot 5H_2O$) crystal. The sample under investigation was always fastened with equal rigidity to the sapphire rod in the cryostat with respect to the cavity and the magnetic field in the ESR spectrometer. Possible variations in temperature of ±2 K were identical for the sample and the standard. According to [2, 9], excited states are not yet important for Fe_s^{3+} (Ga) and Fe_i^0 centers in GaP at 80 K; i.e., small relative temperature-related variations in the ESR-signal intensity were identical due to the Curie law for active centers in the sample and the Cr^{3+} standard. Therefore, an error in the intensity of ESR spectra of Fe centers in relation to the standard was mainly defined by the noise in the ESR spectrometer. In order to reduce the contribution of the $1/f$ noise, the ESR spectra were recorded with a short scan period of 30 s. Using multiple recording of the spectra, we reduced the relative error to a value no larger than 2.5% in the case of measuring the depth distribution of Fe centers and detecting the ESR-signal intensity in GaP:Fe before and after irradiation. The error in determining the concentration of *A*- and *B*-Fe centers was no larger than 20%.

After diffusion-induced doping, the crystals were subjected to scribing and mechanical grinding of the peripheral sides in order to obtain samples with uniform impurity distribution over the depth. As a result, the samples had an area of 4.5×7 mm^2. The distribution of *A* and *B* centers over the depth was detected using either mechanical grinding or chemical etching in a $HBr : K_2Cr_2O_7 : CCl_3COOH = 1 : 2 : 0.5$ solution. The rear surface of the sample was protected with a chemically stable nitrovarnish during etching. In view of the strong dependence of the etching rate on the Fe content, the thickness of the crystals was checked after each removal of a layer by two methods, i.e., by measuring the thickness at five points and by weighing.

RESULTS AND DISCUSSION

Relative intensities of ESR spectra for the *A* and *B* centers of Fe in a GaP sample before and after irradiation with Ar ions are listed in the table. For the same sample, the results of measuring the *A*- and *B*-spectrum intensities converted to the concentrations of active centers are shown in Figs. 1–3. Figure 1 corresponds to the case where the layers were removed chemically from the irradiated side; Fig. 2 represents the case where the layers were removed by mechanical grinding for the unir-

radiated GaP:Fe sample; and Fig. 3 shows the results obtained for an unirradiated GaP:Fe sample in the case of chemical etching, with a 15-μm-thick layer removed preliminarily from the rear side by grinding. In Figs. 1–3, it is the integrated concentrations that are shown in view of positive peaks in the *A* and *B* spectra; these peaks exceed the experimental error, and their conventional differentiation would yield physically meaningless negative concentrations of the *A* and *B* centers.

It can be seen from the table that the intensity of the ESR signal related to both the *A* and *B* centers decreased as a result of irradiation. The changes amounted to 10 and 12%, respectively, which exceeds the experimental error. In contrast to thermal relaxation processes at 300–800 K [3], ion irradiation modifies the states of the Fe-related centers; this is true for both the Fe_i^0 and Fe_s^{3+} (Ga) centers. The mean projected range of Ar ions in GaP is ~30 nm, which, according to [3] and Fig. 1, is much smaller than the depth of location of the *A* and *B* Fe centers; a possible decrease in the concentration of these centers in the amorphized layer owing to their recharging or to the rearrangement of chemical bonds should not exceed 0.1%. Thus, the data listed in the table are indicative of a long-range effect for both substitutional (in the Ga sublattice) and interstitial Fe centers.

Unfortunately, due to the wide scatter (larger than 10%) of the Fe content in available GaP crystals, we could not confidently detect the irradiation-induced changes in the shape of the depth distribution for the *A* and *B* centers. The *A*- and *B*-center distributions shown in Fig. 1 for an irradiated sample is similar to that reported previously [3] for an unirradiated sample, if we leave aside the abrupt changes in the ESR-signal intensity in a thin (~5 μm) near-surface layer and an increase in the ESR-signal intensity of 33% at a depth of ~30 μm for the *B* centers. As reported previously [3], the largest decrease in the *A*-center concentration occurs in a layer ~50 μm thick, although the leveling-off of the concentration, which corresponds to the *A*-center signal from the rear side of the sample, occurs at a depth of ~90 μm. The horizontal portion of the *B*-center distribution extends to a depth of ~150 μm. Thus, the layer of the Fe interstitial component (Fe_i^0) also begins at a point deep in the sample (as in Fig. 1 in [3]), i.e., at a depth of ~180 μm. At depths > 150 μm, the intensity of the ESR signal related to *B* centers decreases linearly with depth, which corresponds to the uniform distribution of these centers (again, similar to what was shown in Fig. 1 in [3]). The halved value of concentration is observed at a depth of ~350 μm; i.e., the *B*-center layer, as expected [3], is located within the crystal almost symmetrically relative to the initial surfaces.

An increase in the *A*-spectrum intensity and a decrease in the *B*-spectrum intensity in a thin (~5 μm) near-surface layer are also observed in unirradiated crystals. A decrease in the *B*-spectrum intensity is probably related to removal of the near-surface *n*-type layer [3] in which the *B* centers are present. An abrupt increase in the *A*-spectrum intensity is apparently due to redistribution of the space charge; a drop of the Fermi level below the acceptor level E_v + 0.7 eV in the near-surface region; and recharging of the Fe_s(Ga) defects after the removal of the *n*-layer, which contributes to a certain increase in the number of triply ionized Fe centers with five unpaired electrons in the 3*d* shell.

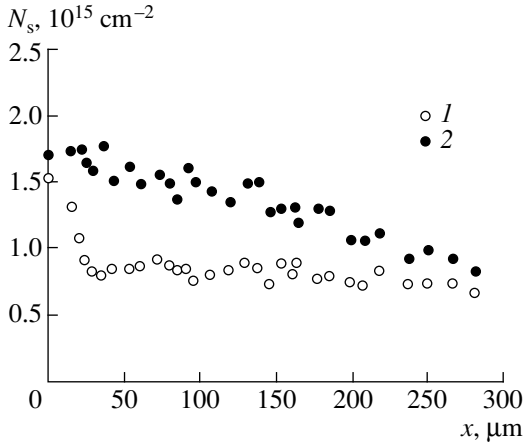

Fig. 3. The same as in Fig. 1 but for an unirradiated sample in the case of layer-by-layer chemical etching.

An increase in the *B*-spectrum intensity of 30% at a depth of ~30 μm (see Fig. 1) appears to be of fundamental importance; there is no reason to believe that this increase is due to the effect of ion irradiation, because a similar increase is also observed in the case of an unirradiated sample (see Fig. 2). We relate the physical cause of such behavior of the Fe_i^0 centers to plastic deformation of the crystal under the effect of chemical or mechanical one-sided thinning of the sample. Such a drastic change in the integrated intensity of the *B* spectrum can be reduced by alternate removal of the layers from opposite sides of the crystal (as was done in [3]). This increase may diminish or become nonexistent if the near-surface concentration of *A* centers is low. This is evidenced by the distribution shown in Fig. 3, where the concentration of *A* centers in the 30-μm-thick near-surface layer is much lower than that in Figs. 1 and 2 and, in addition, where a 15-μm layer with the Fe_s^{3+} (Ga) *A* centers was removed from the

Variation in the ESR-spectrum intensities as a result of irradiation of GaP:Fe crystal with argon ions

Relative intensity	Before irradiation	After irradiation	Variation in intensity, %
B/standard	1.846 + 0.005	1.616 + 0.022	12.4
A/standard	1.509 + 0.009	1.355 + 0.016	10.2

opposite side of the sample. After diffusion of Fe in GaP and quenching, strong stresses arise in the crystal; these stresses are apparently tensile, because, according to [10], the ionic radius of Fe^{3+} (0.067 nm) is larger than that of Ga^{3+} (0.062 nm). As experiments show, such crystals withstand much lower impact loads than GaP samples that are not doped with Fe. A similar phenomenon has also been previously observed in GaAs samples doped nonuniformly with Fe. The presence of highly stressed near-surface layers in the case of one-sided etching or grinding gives rise to bending of the crystal due to the effect of the Fe_s^{3+} (Ga) layer from the opposite side of the sample. It is unlikely that elastic deformation would cause the point defects to move. It is more reasonable to assume that there is a plastic, stress-relieving strain due to the motion of dislocations into the bulk of the crystal. As of now, it is hard to determine which contribution is larger: the climb of edge dislocations or the glide of edge, screw, or mixed dislocations. In the case of pure dislocation climb, interstitials or vacancies are generated [11]. However, in the case of such intrinsic defects, a decrease in the *B*-center ESR signal would be rather observed owing to the formation of complexes with *B* centers and their recharging or owing to the formation of substitutional Fe centers according to the reaction $Fe_i + V_{Ga} \longrightarrow Fe_s(Ga)$. The reaction $Fe_s(Ga) \longrightarrow Fe_i + V_{Ga}$ is ruled out in the region where the Fe_i centers are concentrated on account of negligibly low concentrations of $Fe_s(Ga)$ at a large depth (see [3] and the distributions shown in Figs. 1–3). Most probably, the major contribution is made by the motion of dislocations whose vicinities were initially enriched with interstitial atoms and corresponded to the regions with the Fermi level lying below the donor level of Fe_i; therefore, this interstitial Fe fraction did not contribute to the *B* spectrum. As a result of plastic deformation, the dislocation moves rapidly away from the region enriched with Fe_i defects; the latter transform into the neutral state and enhance the *B*-spectrum intensity. Here, any motion of dislocations can make a contribution, ranging from a climb to a glide. Only the climb accompanied with generation of vacancies and their association with Fe_i defects has an adverse effect.

Naturally, the motion of dislocations is also bound to affect the *A* centers. The $Fe_s(Ga)$ defects are virtually immobile at temperatures near 300 K; therefore, in this case, an important role is played by the dislocation climb accompanied either by mere generation of Fe_i defects, by formation of complexes of Fe_i defects with the point defects that are inherent in the matrix (this would necessarily result in the decay of the *A* spectrum), or by the reaction $Fe_i + V_{Ga} \longrightarrow Fe_s(Ga)$ with the ensuing increase in the ESR *A*-signal intensity. However, detection of the "self-effect" of the layer enriched with $Fe_s(Ga)$ defects on their distribution observed using ESR calls for special experiments that involve a small difference in the concentration profiles of the centers and mechanical blocking of plastic deformation in a part of the crystal. In connection with this, a simpler experimental study of the influence of external deformation on the ESR signals of the *A* and *B* centers is of interest; the results will be reported in our next publication. Nevertheless, evidence of such an influence can still be detected in Figs. 1–3. This influence manifests itself in appreciable (exceeding the experimental error) oscillations in the measured ESR-signal intensities for both spectra (particularly in Fig. 3); we believe that these oscillations are caused by deformation of the crystals. In measuring the thickness of the samples with a thickness gage, the mechanical contact of the indenter with a force amounting to tens of grams resulted in bending of the crystals and their plastic deformation. The oscillations indicate that partially reversible changes are possible. This means that reverse motion of dislocations to the region that they previously left and that is enriched with Fe_i defects is possible for the *B* centers; for the *A* centers, generation of interstitial atoms instead of vacancies and vice versa is feasible. An asymmetry of the point-defect generation during the dislocation climb should exist in the case of bending a crystal cut in the (111) plane owing to the natural asymmetry of a III–V compound in the $\langle 111 \rangle$ direction.

In light of the above-suggested mechanism of long-range influence of chemical or mechanical removal of near-surface layers on both ESR spectra, it can not be excluded that, in the long-range effect of Ar-ion irradiation as well, plastic deformation of the crystal is involved (at least for the *A* centers); i.e., we may assume that here we are dealing with the mechanism discussed previously [12] and proposed [13] as a basis for explanation of the long-range effect observed in germanium and silicon. At the same time, for the *B* centers (see table), the long-range effect in the case of irradiation with argon ions resulted only in a decrease in the *B*-spectrum intensity in GaP:Fe. Most probably, as was previously assumed by us when interpreting the long-range effect in silicon, elastic waves are generated in the stopping zone of argon ions; these waves enhance the mobility of Fe_i defects, which is conducive to accumulation of these defects near dislocations, to the recharging process $Fe_i^0 \longrightarrow Fe_i^+$, and to a decrease in the ESR-signal intensity. Recent experiments performed with silicon using atomic-force microscopy [14] showed that the craters of argon-blister ruptures were formed at the silicon surface for the irradiation doses used in this study. These ruptures may also act as the source of elastic waves in GaP as well.

It is noteworthy that, in the course of low-temperature relaxation of the *B* centers [3], dislocations apparently play the role of *X* defects. Up to the saddle point (773 K), heating resulted in accumulation of interstitial Fe in the vicinity of dislocations. At temperatures higher than 773 K, diffusion-related leveling-off of the

interstitial-Fe distribution occurred with an increasing fraction of Fe_i^0.

The above data indicate that it is necessary to take into account plastic deformation of the crystal in the case where the depth distribution of defects is measured by removing the near-surface layers of the crystal. In connection with this, the reasoning [15] that the *B* spectrum can be assigned to the Ga-substituting defect Fe_s^+ (Ga) ($3d^7$) in the $^4S_{3/2}$ state needs additional clarification or experiments; this reasoning is based on matching the depth distributions of the *A* and *B* centers. If we reduce the values of N_s for *B* centers by 15/8 times [in order to treat the *B* centers as Fe_s^+ (Ga) defects] in Figs. 1–3, the integral distributions do not form a unified curve for the dependence of $N_s(A + B)$ on the thickness of the removed layer when the diffusion coefficient is the same for the *A* and *B* centers. The extended portions, which are almost linear after the oscillations have been smoothed, are indicative of the uniform distribution of the *B* centers in the middle of the crystal. The temperature dependence of the diffusion coefficient D [cm^2/s] = $10^4\exp\{-(3.47 \pm 0.01)/kT$ [eV]$\}$ obtained previously [15] is at variance with the formula D [cm^2/s] = $0.16\exp\{-(2.32 \pm 0.2)/kT$ [eV]$\}$ derived elsewhere [16]. In addition, there is an error in Fig. 3b in [15]. The value of $D = 3.6 \times 10^{-10}$ cm^2/s at 1153 K should lie above the straight line in Fig. 3 in [15] by an order of magnitude according to the text and Fig. 1 in [15]. Thus, there is no simple (common to the *A* and *B* centers) Arrhenius dependence $D(T)$. It appears strange that the authors of [15] excluded from consideration the data on the low-temperature relaxation of the *B* centers [1, 2] on the grounds that this relaxation did not affect the magnitude and type of electrical conductivity. In [3], the results of electrical measurements and their interpretation were reported. The absence of the *B* spectra in the case of semi-insulating materials reported in [15] was observed earlier by us [2]. This absence can be easily accounted for [2, 15] by the fact that crystals compensated with chromium and nickel [15] or copper [2] were used; in such crystals, the Fermi level was located at E_v + (0.4–0.5) eV, which was below the donor level E_v + 1 eV presumed in [3], so that all the Fe_i centers were ionized. It is this circumstance that accounts for the absence of the *B* spectrum. Moreover, if the *B* centers were Fe_s^+ (Ga) ($3d^7$) defects, the *B* spectrum should be observed in overcompensated semi-insulating GaP crystals with a high Fe concentration [2, 15] in view of the fact that the acceptor level Fe_s^{2+} (Ga) $\longrightarrow$ Fe_x^+ (Ga) lies above the Ni and Cr acceptor levels and above the first acceptor Fe level at E_v + 0.7 eV. The problem associated with observation of the *B* centers in semi-insulating GaP crystals consists in the search for the conditions for pinning the Fermi level above E_v + 1 eV but not too close to the conduction-band bottom in GaP, so that the recharging process $Fe_i^0 \longrightarrow Fe_i^-$ (as in the case of Fe in Si) will not occur. This problem can be solved by overcompensating *p*-GaP crystals (with *p* no higher than 10^{17} cm^{-3} [3]) with Fe or by compensating *n*-type crystals [17] with Ti or Va, which have acceptor levels in the upper half of the band gap. The variant with compensation of donors in GaP by Fe centers residing in the lattice sites is apparently realized in the case represented by curve *1* in Fig. 1 [15], where a nearly linear integral distribution of the *B* centers at 1153 K was observed and corresponded to their almost uniform distribution in a layer ~100 μm thick. This thickness is defined (leaving aside the uncontrolled acceptors) by overcompensation of donors in GaP by Fe centers (Fe_s^{2+}, Fe_s^+, …) at the lattice sites. According to the trends established in [7, 17], the larger band gap of GaP makes possible the existence of six charge states for substitutional Fe centers (from Fe_s^{3+} to Fe_s^{2-}) and four charge states for interstitial centers (Fe_i^+, Fe_i^0, Fe_i^-, and Fe_i^{2-}). In nonuniformly doped crystals with the Fe distribution of the type shown in Fig. 3, we may hope to separate a fairly thick high-resistivity region that contains only the *B* centers and to study the *B*-center recharging spectrum in more detail.

REFERENCES

1. V. F. Masterov, S. I. Markov, L. P. Pasechnik, and V. K. Sobolevskiĭ, Fiz. Tekh. Poluprovodn. (Leningrad) **17**, 1130 (1983) [Sov. Phys. Semicond. **17**, 711 (1083)].
2. E. S. Demidov and A. A. Ezhevskiĭ, Fiz. Tekh. Poluprovodn. (Leningrad) **19**, 1629 (1985) [Sov. Phys. Semicond. **19**, 1003 (1985)].
3. E. S. Demidov, V. V. Karzanov, A. B. Gromoglasova, and O. N. Morozkin, Fiz. Tekh. Poluprovodn. (St. Petersburg) **33**, 385 (1999) [Semiconductors **33**, 377 (1999)].
4. P. V. Pavlov, E. S. Demidov, and G. V. Zorina, Fiz. Tekh. Poluprovodn. (Leningrad) **21**, 984 (1987) [Sov. Phys. Semicond. **21**, 603 (1987)].
5. E. S. Demidov, V. V. Karzanov, and P. V. Pavlov, Fiz. Tekh. Poluprovodn. (Leningrad) **23**, 548 (1989) [Sov. Phys. Semicond. **23**, 342 (1989)].
6. V. V. Karzanov, P. V. Pavlov, and E. S. Demidov, Fiz. Tekh. Poluprovodn. (Leningrad) **23**, 2064 (1989) [Sov. Phys. Semicond. **23**, 1276 (1989)].
7. E. S. Demidov, Author's Abstract of Doctoral Dissertation (Nizhegorod. Gos. Univ., Nizhni Novgorod, 1994).
8. E. S. Demidov and A. A. Ezhevskiĭ, Zavod. Lab. **47**, 42 (1981).
9. E. S. Demidov, A. A. Ezhevskiĭ, and V. V. Karzanov, Fiz. Tekh. Poluprovodn. (Leningrad) **17**, 661 (1983) [Sov. Phys. Semicond. **17**, 412 (1983)].

10. B. F. Ormont, *Introduction to Physical Chemistry and Crystal Chemistry of Semiconductors* (Vysshaya Shkola, Moscow, 1982).

11. P. V. Pavlov and A. F. Khokhlov, *The Physics of the Solid State* (Nizhegorod. Gos. Univ., Nizhni Novgorod, 1993).

12. I. A. Abroyan, A. N. Andronov, and A. I. Titov, *Physical Foundations of Electron- and Ion-Beam Technology* (Vysshaya Shkola, Moscow, 1984).

13. T. A. Kuzemchenko, Author's Abstract of Candidate's Dissertation (Inst. Obshch. Fiz. Akad. Nauk SSSR, Moscow, 1989).

14. V. V. Karzanov, K. A. Markov, S. Yu. Zubkov, *et al.*, in *Proceedings of All-Russia Conference "Microprobe Microscopy–99," Nizhni Novgorod, 1999*, p. 185.

15. N. N. Pribylov, A. I. Spirin, S. I. Rembeza, and V. I. Kirillov, Phys. Status Solidi A **172**, 177 (1999).

16. F. S. Shishiyanu and V. G. Georgiu, Fiz. Tekh. Poluprovodn. (Leningrad) **10**, 2188 (1976) [Sov. Phys. Semicond. **10**, 1301 (1976)].

17. E. S. Demidov, Fiz. Tverd. Tela (St. Petersburg) **34**, 37 (1992) [Sov. Phys. Solid State **34**, 18 (1992)].

Translated by A. Spitsyn

Semiconductors, Vol. 34, No. 9, 2000, pp. 989–993. Translated from Fizika i Tekhnika Poluprovodnikov, Vol. 34, No. 9, 2000, pp. 1030–1034.

ATOMIC STRUCTURE AND NONELECTRONIC PROPERTIES OF SEMICONDUCTORS

Oxygen-Containing Radiation Defects in $Si_{1-x}Ge_x$

Yu. V. Pomozov[1], M. G. Sosnin[1], L. I. Khirunenko[1], V. I. Yashnik[1], N. V. Abrosimov[2, 3], W. Schröder[3], and M. Höhne[3]

[1] *Institute of Physics, National Academy of Sciences of Ukraine, pr. Nauki 144, Kiev, 258650 Ukraine*
e-mail: lukh@iop.kiev.ua

[2] *Institute of Solid-State Physics, Russian Academy of Sciences, Chernogolovka, Moscow oblast, 142432 Russia*

[3] *Institute of Crystal Growth, D-12489 Berlin, Germany*

Submitted February 25, 2000; accepted for publication March 1, 2000

Abstract—The processes of formation and annealing of radiation defects in $Si_{1-x}Ge_x$ samples irradiated with 4-MeV electrons were studied. It is shown that, in the range of Ge contents of 3.5–15 at. %, a reduction in the efficiency of formation of oxygen-containing defects (VO and VO_2) compared to that in silicon is observed. The existence of three types of VO centers, perturbed and unperturbed by neighboring Ge atoms, is detected in $Si_{1-x}Ge_x$. © *2000 MAIK "Nauka/Interperiodica".*

1. INTRODUCTION

$Si_{1-x}Ge_x$ solid solutions are among the most promising materials of modern microelectronics. Devices produced on the basis of $Si_{1-x}Ge_x$ offer considerable advantages (high speed; a low noise level; the possibility of attaining high operating frequencies, from two to tens of gigahertz; and a low manufacturing cost) over Si-based and, in a number of cases, GaAs-based devices. This material also appears promising for the development of devices that feature a higher radiation resistance [1]. In connection with this, it is important to study the processes of production and annealing of radiation defects in bulk single-crystal samples of this material. The processes of production and annealing of radiation defects in $Si_{1-x}Ge_x$ single crystals have been studied inadequately, and the available data have been obtained for samples with a Ge content no higher than 1 at. %. In this paper, we report the data we obtained on the production and annealing of oxygen-containing radiation defects in $Si_{1-x}Ge_x$ single crystals with a Ge content as high as 15 at. %.

It is known that, in Czochralski-grown silicon, a large variety of oxygen-containing radiation defects can be formed, depending on the impurities present [2]. Among these defects, the vacancy + oxygen (VO) center is dominant. As a result of isochronous annealing (at a temperature of $T \geq 300$°C [2–4]), a major portion of the VO centers is transformed into VO_2 centers. As the annealing temperature increases, there is a sequential transformation of the VO_2 to VO_3 complexes (at $T \approx 450$°C), the VO_3 to VO_4 complexes (at $T \approx 450$–485°C), and so on. In this case, the VO_2 centers are formed as a result of the capture of the diffusing VO centers by interstitial oxygen, whereas the centers containing a larger number of O atoms are formed owing to the capture of diffusing oxygen by the VO_2, VO_3, and like centers. Simultaneously with the formation of VO_n complexes, V_nO complexes are formed. The V_2O centers were observed immediately after irradiation, the V_3O centers are formed as a result of annealing out of the VO and V_2O centers (at $T > 300$°C), the V_4O centers emerge when the V_3O centers are annealed out (at $T \approx 450$°C), and so on. The entire process of annealing out the VO centers may be represented by the following scheme:

$$\begin{array}{l} VO \Rightarrow VO_n\ (VO_2 \Rightarrow VO_3 \Rightarrow VO_4 \Rightarrow \text{and so on}) \\ \quad \Downarrow \\ V_nO\ (V_2O \Rightarrow V_3O \Rightarrow V_4O \text{ and so on}). \end{array}$$

Most of the oxygen-containing complexes are optically and electrically active [2, 5] and thus can profoundly affect the properties of Si and Si-based devices.

It is known that the introduction of germanium into silicon affects both the state of interstitial oxygen and the processes of oxygen diffusion and precipitation [6–11]. In connection with this, the processes of production and annealing of O-containing radiation defects in $Si_{1-x}Ge_x$ can also change compared to those in silicon. This paper is devoted specifically to studies of these processes.

2. EXPERIMENTAL

The *p*-$Si_{1-x}Ge_x$ single crystals doped with boron were grown at the Institute of Crystal Growth (Berlin, Germany) by the Czochralski method [12, 13]. The concentrations of oxygen and carbon were determined from the intensities of the infrared-absorption bands peaked at 9 and 16 μm and were found to be $(7–9) \times 10^{17}$ cm^{-3} and $(2–3) \times 10^{16}$ cm^{-3}, respectively. The content of germanium in the samples was determined using an SP-733 X-ray microprobe analyzer and was found to vary from 3.0 to 15 at. %.

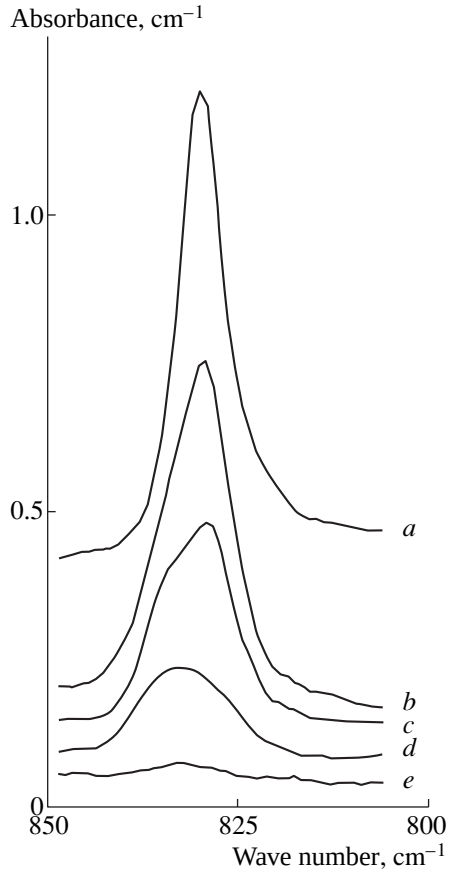

Fig. 1. Differential absorption spectrum of VO centers in $Si_{1-x}Ge_x$ for N_{Ge} = (*a*) 0, (*b*) 3.5, (*c*) 6.5, (*d*) 8.5, and (*e*) 11.5 at. %.

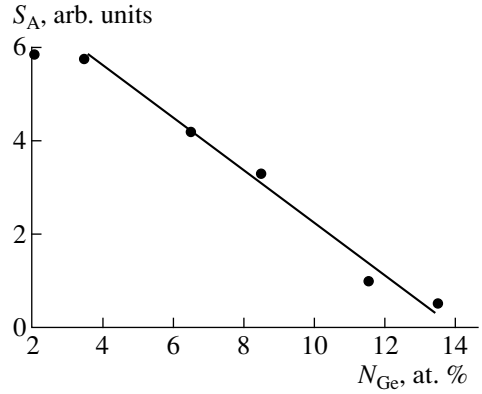

Fig. 2. The area under the VO-absorption band as a function of Ge content in $Si_{1-x}Ge_x$.

The crystals were irradiated with 4-MeV electrons at a temperature of about 300 K. The irradiation dose was (3.5–6) × 10^{17} cm^{-2}. The irradiated samples were annealed isochronously (t = 20 min) in the temperature range of 100–400°C with a step of 10°C. The dependence of the formation and annealing of VO centers on the germanium content in $Si_{1-x}Ge_x$ was studied using infrared Fourier spectroscopy.

3. RESULTS AND DISCUSSION

Differential VO-center absorption spectra measured at $T \approx 300$ K for $Si_{1-x}Ge_x$ samples irradiated with 5×10^{17} cm^{-2} electrons are shown in Fig. 1. As can be seen, as the content of Ge in $Si_{1-x}Ge_x$ increases, a significant decrease in the VO-center absorption-band intensity and an appreciable increase in its half-width are observed. Because of this, the areas under the absorption bands were calculated in order to compare the efficiencies of the introduction of VO centers in the samples with differing germanium content. The results of the calculations are shown in Fig. 2. It can be seen from the dependence obtained that, as the germanium content increases ($N_{Ge} \geq 3.0$ at. %), a decrease in the area under the VO-center band (i.e., a reduction in the efficiency of the production of these centers) is observed. For a germanium content higher than 12 at. %, it is virtually impossible to estimate the area within the limits of experimental accuracy. The X-ray diffraction studies of the samples did not reveal the presence of accumulations of germanium atoms in Si or a significant density of dislocations which could act as sinks for vacancies formed as a result of irradiation. Study of the defect formation in the samples irradiated at a temperature $T \leq 100$ K showed that the process of formation of major radiation defects in crystals with a germanium content as high as 15 at. % is not much different from the corresponding process in crystals with a germanium content of ≤1 at. % [14]. Namely, the VO centers are not observed immediately after irradiation in any of crystals studied; i.e., the vacancies are also effectively trapped by germanium atoms. The absorption band corresponding to VO centers emerges only after annealing the Ge–V centers (at $T \geq 280$ K). These experiments suggest that, as in the case of crystals with a germanium content lower than 1 at. %, the germanium atoms act as annihilation centers for the Frenkel-pair components in the samples under consideration.

We analyzed the half-width of the absorption band corresponding to VO centers. It follows from Fig. 1 that, as the germanium content increases, the absorption band is broadened, predominantly to the high-frequency region of the spectrum and virtually without any variations in the peak position. Decomposition of the band into components for a germanium content of 3.5 at. % (Fig. 3) showed that this band was a superposition of three lines peaked at 830, 834.6, and 839.2 cm^{-1}. The component peaked at 830 cm^{-1} is dominant, and its position coincides with that of the VO-center absorption band in silicon. As the germanium content increases, the ratio of the component intensities changes: the contribution of the bands peaked at 834.6 and 839.2 cm^{-1} increases with a simultaneous decrease in the intensity of the component peaked at 830-cm^{-1}.

It is known that the VO complex may be treated as a vacancy in which one of the reconstructed bonds is "decorated" with an oxygen atom (the bonds in the Si_2O quasi-molecule are not broken in this case); i.e., the oxygen atom is located near the vacancy at the almost substitutional site [2, 5]. Studies of the oxygen absorption spectra in the as-grown $Si_{1-x}Ge_x$ samples show that, as the content of germanium increases, the probability of finding the germanium atoms in the nearest coordination shells around the Si_2O quasi-molecules becomes higher [6, 9, 11]. The resulting perturbations give rise to three additional oxygen-absorption bands peaked at 1130.1, 1118.4, and 1127.2 cm^{-1} and positioned at lower frequencies with respect to the 1136-cm^{-1} absorption band characteristic of undoped silicon. As the germanium content increases, the intensities of these additional bands increase; i.e., the fraction of quasi-molecules "perturbed" by germanium atoms increases.

It is reasonable to assume that the oxygen atom, either unperturbed or perturbed by the near-neighbor germanium atom, may be involved in the formation of VO centers under irradiation; i.e., by analogy with interstitial oxygen (the Si_2O quasi-molecule), VO centers either perturbed or unperturbed by the near-neighbor germanium atoms may form. Most likely, the vibration frequencies would also be different for these centers (as in the case of Si_2O). This makes it possible to suggest that the experimentally observed VO-center absorption band in $Si_{1-x}Ge_x$ is a superposition of the VO-center lines unperturbed (830 cm^{-1}) and perturbed by germanium atoms residing in the nearest coordination shells (834.6 and 839.2 cm^{-1}). This reasoning is supported by the similarity in the behavior of the oxygen-absorption spectrum components and the VO centers with an increase in the germanium content: the fraction of perturbed centers increases with the germanium content.

We then isochronously annealed the irradiated samples. The most representative results obtained for $Si_{1-x}Ge_x$ crystals with a germanium content of 3.5 at. % and a spectral resolution of 1 cm^{-1} are shown in Fig. 4. For the sake of clarity, the spectra are shifted with respect to each other on the vertical axis. As can be seen, as the annealing temperature increases, the VO-center band broadens and splitting of the band into two components peaked at 830 and 834.6 cm^{-1} is observed at the annealing temperature of $T \approx 230$°C (Fig. 4, curve *c*). As the annealing temperature is further increased, the intensity of the component at 834.6 cm^{-1} increases, with a simultaneous decrease in the intensity of the component peaked at 830 cm^{-1}; as a result, the peak of the band shifts to 834.6 cm^{-1} (Fig. 4, curve *d*). In the annealing temperature range of 280–300°C, the components at 839.2 cm^{-1} become more intense and the intensities of the components at 834.6 and 839.2 cm^{-1} become equal after annealing at $T_{ann} \approx 305$°C. As the temperature is

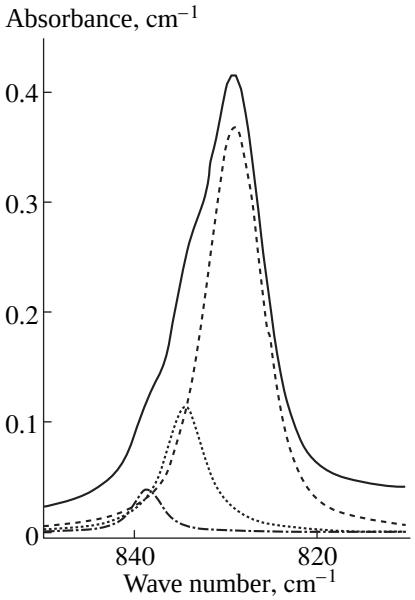

Fig. 3. Decomposition of the VO-center absorption band into components in $Si_{1-x}Ge_x$ with $N_{Ge} \approx 3.5$ at. %.

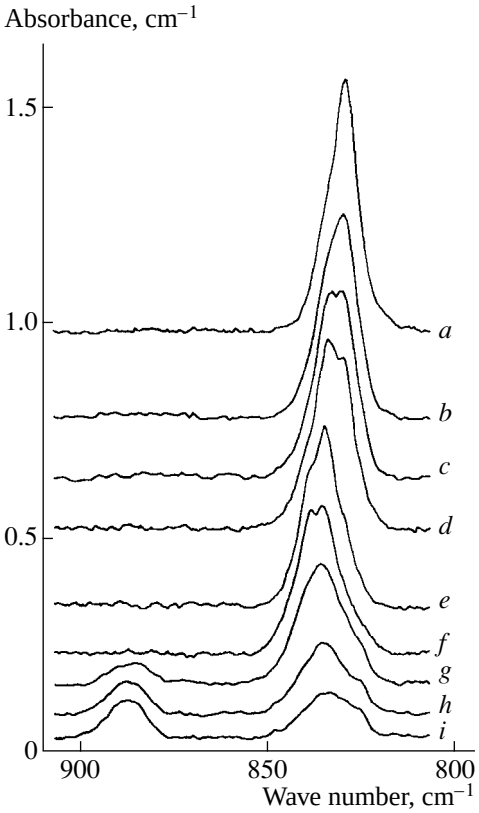

Fig. 4. Variations in VO bands in the spectra of the samples with a Ge content of 3.5 at. % as a result of annealing. (*a*) Before annealing and after annealing at T_{ann} = (*b*) 220, (*c*) 230, (*d*) 240, (*e*) 290, (*f*) 305, (*g*) 330, (*h*) 350, and (*i*) 360°C.

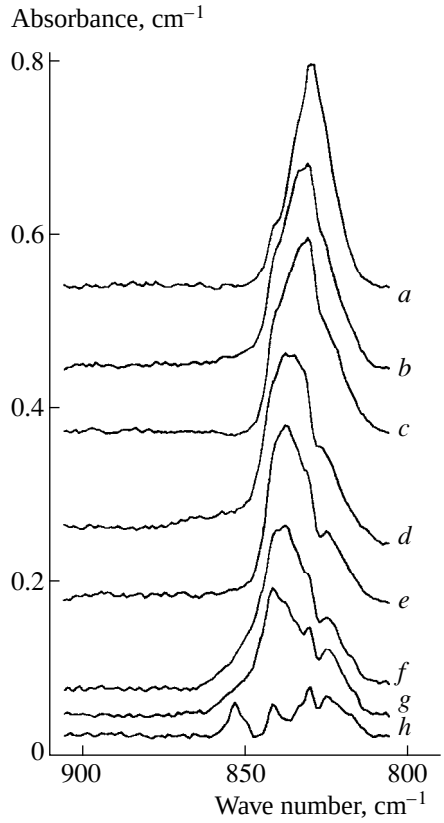

Fig. 5. Annealing of VO centers in $Si_{1-x}Ge_x$ with $N_{Ge} \approx$ 8.5 at. %. The spectrum (*a*) corresponds to an unannealed sample. The samples were annealed at T_{ann} = (*b*) 220, (*c*) 230, (*d*) 260, (*e*) 280, (*f*) 300, (*g*) 320, and (*h*) 370°C.

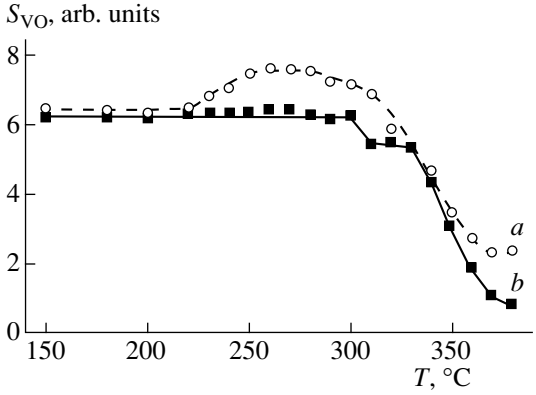

Fig. 6. The area under the VO-center absorption band as a function of annealing temperature for (*a*) Si and (*b*) $Si_{1-x}Ge_x$ with $N_{Ge} \approx$ 3.5 at. %.

raised further, a gradual decrease in the total intensity of the band is observed. The general pattern of annealing the samples with a higher Ge content N_{Ge} is basically similar to that of a sample with N_{Ge} = 3.5 at. %. However, the ratio of the component intensities changes; namely, the contributions of the components at 834.6 and 839.2 cm^{-1} increase. Thus, for example, for a sample with a germanium content of 8.5 at. % (Fig. 5), the peak of the band shifts first to 834.6 cm^{-1} and then to 839.2 cm^{-1}. For all the studied samples (as in the case of silicon as well [15]), residual absorption was observed in the same spectral region after the VO centers were annealed out; this absorption persists up to annealing temperatures of ~600°C. Thus, the studies we performed showed that the spectral components corresponding to VO centers perturbed by Ge atoms that reside in the nearest coordination shells were enhanced in the course of annealing of the VO centers.

The annealing-temperature dependence of the area under the VO-absorption band for $Si_{1-x}Ge_x$ samples with a germanium content of 3.5 at. % is shown in Fig. 6. As can be seen, the area under the band remains unchanged up to the annealing temperature of ~300°C. Intense annealing of VO centers sets in at $T \geq 330$°C. The constancy of the area under the VO band in $Si_{1-x}Ge_x$ subjected to annealing in the temperature range where a structure in this band becomes distinct suggests that an increase in the intensity of the absorption components at 834.6 and 839.2 cm^{-1} under annealing is not related to the emergence of new centers. Apparently, the VO centers that do not have a germanium atom as the nearest neighbor but are in the fields of elastic stresses (which affect the barrier to diffusion of these centers) and acquire energy upon heating start to move over the crystal; encounter germanium atoms, whose concentration exceeds by at least five orders of magnitude the concentrations of oxygen and VO centers; and localize in the vicinity of these atoms. It is to be noted that the VO center is localized first in the vicinity of the germanium atom that resides in a more distant (possibly, the second) coordination shell with respect to Si_2O (the band peaked at 834.6 cm^{-1}) and then gains additional energy upon further heating; as a result, the probability of finding the VO center in the vicinity of a germanium atom that resides in a nearer (probably the first) coordination shell around Si_2O (839.2 cm^{-1}) increases. Thus, in the course of annealing in the temperature range of 220–305°C, localization of unperturbed VO centers in the vicinity of germanium atoms occurs first, whereas the VO centers are annealed out at $T \geq 330$°C.

The observed increase in the area under the VO-absorption band on annealing of Si (for $T \approx 230$°C) corresponds to the "negative" annealing stage caused by additional formation of VO centers due to annealing out of divacancies. In the $Si_{1-x}Ge_x$ sample under consideration, divacancies are annealed out at $T \approx 340$°C; however, the stage of negative annealing is not observed in this case. A slight decrease in the area under the VO band at $T \sim 300$°C in $Si_{1-x}Ge_x$ coincides with the annealing of VO centers in Si and apparently corresponds to the onset of annealing of VO centers that are unperturbed by germanium atoms.

As mentioned above, the large fraction of VO centers annealed out in silicon are transformed into VO_2 centers that give rise to the absorption band peaked at 889 cm^{-1} [2]. Formation of VO_2 centers in the studied $Si_{1-x}Ge_x$ samples differs significantly from that in silicon. More than 50% of the VO centers in silicon are transformed into VO_2 centers as a result of annealing, whereas the fraction of formed VO_2 centers is much less in the case of $Si_{1-x}Ge_x$. Thus, for a Ge content N_{Ge} = 3.5 at. %, the fraction of formed VO_2 centers (determined from the area under the band in Fig. 4) amounts to a mere 20%. As the germanium content increases, the concentration of formed VO_2 centers decreases, and, for N_{Ge} > 8 at. %, the absorption band corresponding to VO_2 centers is no longer observed within the limits of experimental accuracy (Fig. 5). Thus, the experiment shows that, simultaneously with an increase in the concentration of VO centers perturbed by neighboring Ge atoms, the probability of transformation of these centers into VO_2 complexes during annealing decreases. The presence of an additional barrier apparently makes the diffusion of VO centers (located in the vicinity of Ge atoms) over the lattice more difficult; as a result, the formation of VO_2 centers becomes less likely.

Thus, we showed that, for a Ge content in $Si_{1-x}Ge_x$ higher than 3 at. %, the efficiency of formation of oxygen-containing radiation defects (VO and VO_2) decreased. In the studied crystals, we observed three types of VO centers: those unperturbed and perturbed by Ge atoms that resided in the nearest coordination shells.

REFERENCES

1. M. Glück, J. Hersener, H. G. Umbach, *et al.*, Solid State Phenom. **57–58**, 413 (1997).
2. J. Lennart Lindström and Bengt G. Svensson, Mater. Res. Soc. Symp. Proc. **59**, 45 (1986).
3. Y. H. Lee, J. C. Corelli, and J. W. Corbett, Phys. Lett. A **60**, 55 (1977).
4. G. Davies, E. C. Lightowlers, R. C. Newman, and A. S. Oates, Semicond. Sci. Technol. **2**, 524 (1987).
5. B. Pajot, Semicond. Semimet. **42**, 191 (1994).
6. H. Yamada-Kaneta, C. Kaneta, and T. Ogawa, Phys. Rev. B **47**, 9338 (1993).
7. L. I. Khirunenko, Yu. V. Pomozov, V. I. Shakhovtsov, and V. V. Shumov, Mater. Sci. Forum **258–263**, 1773 (1997).
8. L. I. Khirunenko, Yu. V. Pomozov, V. I. Shakhovtsov, and V. V. Shumov, Solid State Phenom. **57–58**, 183 (1997).
9. D. Wauters and P. Clauws, Mater. Sci. Forum **258–263**, 103 (1997).
10. E. Hild, P. Gaworzewski, M. Franz, and K. Pressel, Appl. Phys. Lett. **72**, 1362 (1998).
11. L. I. Khirunenko, Yu. V. Pomozov, M. G. Sosnin, and V. K. Shinkarenko, Physica B (Amsterdam) **273–274**, 317 (1999).
12. N. V. Abrosimov, S. N. Rossolenko, V. Alex, *et al.*, J. Cryst. Growth **166**, 657 (1996).
13. N. V. Abrosimov, S. N. Rossolenko, W. Thieme, *et al.*, J. Cryst. Growth **174**, 182 (1997).
14. L. I. Khirunenko, V. I. Shakhovtsov, V. K. Shinkarenko, *et al.*, Fiz. Tekh. Poluprovodn. (Leningrad) **21**, 562 (1987) [Sov. Phys. Semicond. **21**, 345 (1987)].
15. L. I. Khirunenko, V. I. Shakhovtsov, V. V. Shumov, and V. I. Yashnik, in *Early Stages of Oxygen Precipitation in Silicon* (Kluwer, Dordrecht, 1996), p. 403.

Translated by A. Spitsyn

Semiconductors, Vol. 34, No. 9, 2000, pp. 994–997. Translated from Fizika i Tekhnika Poluprovodnikov, Vol. 34, No. 9, 2000, pp. 1035–1038.

ATOMIC STRUCTURE AND NONELECTRONIC PROPERTIES OF SEMICONDUCTORS

Specific Features of the Behavior of Oxygen in Sn-Doped Silicon

Yu. V. Pomozov, M. G. Sosnin, L. I. Khirunenko*, and V. I. Yashnik

Institute of Physics, National Academy of Sciences of Ukraine, pr. Nauki 144, Kiev, 258650 Ukraine

**e-mail: lukh@iop.kiev.ua*

Submitted February 25, 2000; accepted for publication March 1, 2000

Abstract—The influence of Sn on the absorption spectra of Si and the formation of low-temperature quenched-in donors (T = 450°C) in Si was investigated. The effects of Ge and C were compared. It was found that Sn-doping of Si, similarly to Ge- and C-doping, leads to a decrease in the efficiency of the formation of quenched-in donors. It was demonstrated that the inhibition effect of the formation of quenched-in donors depends on the elastic stresses induced by isovalent impurities in Si. The higher the deformational charge of the impurity, the lower the concentration required for a comparable effect. *© 2000 MAIK "Nauka/Interperiodica".*

The wide application of semiconductor devices in various branches of engineering poses the problem of creating new materials and corresponding devices with a high operation speed, as well as with increased radiation and thermal resistance. In recent years, the investigation of semiconductors doped with isovalent impurities has attracted considerable attention. These impurities are electrically inactive and have no actual influence on the initial parameters of a semiconductor. However, as the source of internal elastic stress, isovalent impurities can efficiently interact either with vacancies or with interstitials, depending on the covalent radius ratio of atoms of the host material and impurity [1–5]. This property of isovalent impurities can be used to purposefully affect the defect–impurity interaction both during the growth of semiconductor crystals and under various external effects (for example, irradiation or thermal treatment).

Isovalent impurities in Si are C, Ge, Sn, and Pb. It is known that C, Ge, and Sn profoundly affect the processes of radiation-defect formation [1–3, 6–8]. In these processes, C effectively interacts with interstitials [2, 8], while Ge and Sn interact with vacancies [1, 3, 6, 8]. As for the influence of these impurities on quenched-in defect formation, it is known that C and Ge suppress the formation of quenched-in donors in Si [9–12]. The influence of Sn on the formation of quenched-in donors in Si was not actually investigated. Thus, for example, it was noted that there was no doping influence on O precipitation for a Sn concentration lower than 5×10^{17} cm^{-3} [13]. To our knowledge, the influence of Pb on defect formation in Si was not investigated, apparently because of difficulties in growing these crystals.

In this paper, the data obtained on the behavior of O and the efficiency of low-temperature quenched-in donor (T = 450°C) formation in Sn-doped Si are reported, and the results are compared with samples doped with Ge and C.

n-Si:(P, Sn) Czochralski-grown single crystals were investigated. The P content was $(2–4) \times 10^{14}$ cm^{-3}. The concentrations of O and C, which were determined from the absorption bands at 9 and 16 μm, were $(7–8) \times 10^{17}$ cm^{-3} and $(2–3) \times 10^{16}$ cm^{-3}, respectively. The Sn content, which was varied from 10^{18} to 2×10^{19} cm^{-3}, was measured by neutron activation analysis and an SP-733 X-ray microprobe analyzer. The as-grown crystals and crystals annealed in air at T = 450°C for a total time of up to 150 h were investigated. Prior to annealing, the samples were treated at T = 770°C for 15 min. Before measurements were taken, the oxide film was removed from the surface of the samples by etching in HF. The absorption spectra for O and quenched-in donors were investigated, and the O content and charge carrier concentrations were measured after each 20 h of thermal treatment using measurements of the infrared absorption and the Hall effect. The absorption spectra were investigated using an IFS-113v infrared Fourier spectrometer at T = 4.2 K and 300 K with a spectral resolution of 0.25–1 cm^{-1}.

It is known that the absorption spectrum for interstitial O in the region of the ν_3 vibration at $T \approx 4.2$ K consists of the band at 1136.4 cm^{-1} with a fine structure on the low-frequency side. This structure is related to the Si isotope composition (^{28}Si, ^{29}Si, ^{30}Si) [14]. It was found that perturbations, which appear in Si doped with isovalent impurities because of their arrangement in the nearest coordination spheres in relation to O, bring about additional absorption lines in the region of the ν_3 vibration [9, 15–17]. The absorption spectra in the region of the ν_3 vibration obtained by us for Si samples with a Sn content of up to 2×10^{19} cm^{-3} are shown in Fig. 1. It can be seen from Fig. 1 that three additional

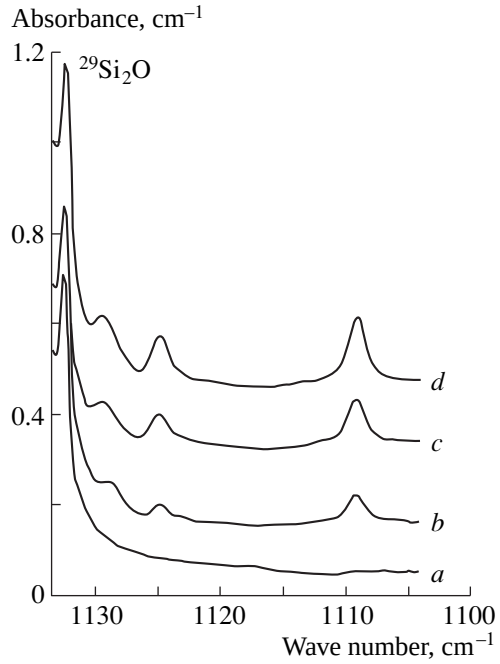

Fig. 1. Absorption spectrum for O in the region of the ν_3 vibration for Si:Sn. N_{Sn} = (*a*) 0, (*b*) 2×10^{18}, (*c*) 6×10^{18}, and (*d*) 19×10^{18} cm^{-3}.

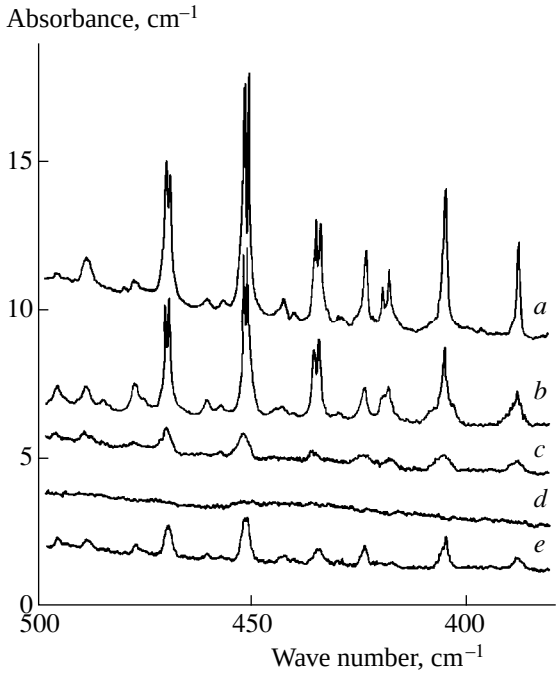

Fig. 2. Absorption spectra for quenched-in donors in Si:Sn and Si:C. N_{Sn} = (*a*, *e*) 0, (*b*) 2, (*c*) 6, and (*d*) 19×10^{18} cm^{-3}. N_C = (*a*) 2×10^{16} and (*e*) 1.5×10^{18} cm^{-3}.

lines, 1129.7, 1124.8, and 1109.2 cm^{-1}, appear in the spectrum on the low-frequency side from the absorption bands of O, which are characteristic of Si, with an increase in Sn content. The intensities of these lines increase with increasing Sn content. According to the model suggested by Yamasda-Kaneta *et al.* [15], these absorption bands can be attributed to vibrations of the O atom, which is perturbed by Sn atoms located in the nearest coordination spheres. We also found a similar three-component structure for the Ge- and C-doped samples [17]. It was also demonstrated that the vibration modes of O in Si shift to lower frequencies for all isovalent impurities, regardless of the sign of strain induced by this impurity. Indeed, the C covalent radius $R_C \leq R_{Si}$, while the Ge and Sn covalent radii R_{Sn}, $R_{Ge} \geq R_{Si}$.

It is known that, if the deformation source appears close to the molecule, quasi-elastic forces appear in the molecule. These forces hinder the variations in the interatomic distance and the bond angle. For the case of a bent triatomic molecule, such as Si_2O, the quasi-elastic forces, which appear because of the angle variation, are considerably weaker compared to quasi-elastic forces hindering the change in the bond lengths [18]. Thus, the variation in the vibration frequency related to the appearance of a deformation source close to the molecule is mainly defined by the variation in the bond angle. The Si_2O quasi-molecule in the Si matrix is "rigidly" bound to the neighboring Si atoms, and the bond angle 2α is about 164° [19]. It is also known that, for example, in organosilicones, where the quasi-molecule Si_2O can be oriented freely, the bond angle 2α in Si_2O is about 148° [20]. The absorption band shifts in the same direction for all isovalent impurities in Si. This indicates that the Si_2O quasi-molecule, which has sixfold orientational degeneracy, tends to orientate with the appearance of the deformation source (regardless of the source sign) in such a manner that the bond angle of the quasi-molecule diminishes. Thus, the sign of the strain, which appears in Si doped by the isovalent impurity, determines the direction of the shift (orientation) for O. This specific influence of all isovalent impurities on the vibration mode of O in Si also implies that their influence on the O diffusion potential barrier is similar. This circumstance can affect the precipitation of O during thermal treatment regardless of the mechanisms of formation of quenched-in donors (for example, the diffusion of the O atoms or dimers).

It is known that Ge and C suppress the formation of O-containing quenched-in donors in Si to a large extent. In this connection, it seems of interest to investigate thermal-defect formation in Si:Sn. The absorption spectra obtained for Si:Sn crystals in the absorption region of quenched-in donors or thermodonors (TD^0) for the samples thermally treated for 150 h are shown in Fig. 2. It can be seen that, for the same thermal treatment time, the absorption-spectrum shape in the thermodonor region for Si:Sn features no actual variations compared to pure Si up to Sn concentrations of (1–2) $\times$ 10^{18} cm^{-3}. Only a slight variation in the

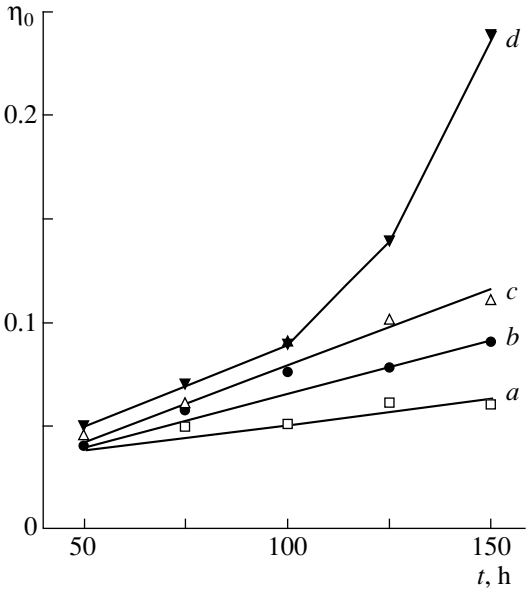

Fig. 3. Dependence of η_0 on the Sn content in Si and annealing duration at $T = 450$°C. N_{Sn}, 10^{18} cm^{-3}: (*a*) 0, (*b*) 2, (*c*) 6, and (*d*) 19.

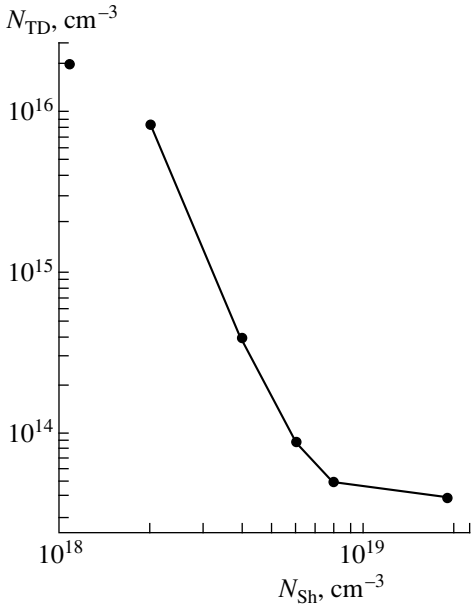

Fig. 4. Dependence of the thermodonor concentration on the Sn content in Si. Annealing duration is 150 h.

intensity of some lines is observed. For Sn concentrations in the samples $N_{Sn} > 2 \times 10^{18}$ cm^{-3}, the absorption lines for quenched-in donors gradually broaden. Because of this, some lines overlap and a considerable decrease in their intensity is observed (Fig. 2*c*). For a Sn content of 2×10^{19} cm^{-3}, no absorption spectra are observed within the limits of experimental sensitivity. Comparison of the results obtained in this study with our preliminary data for Ge-doped Si [16] demonstrate that they are completely identical. It can be seen that an increase in both isovalent impurity contents causes a broadening of the absorption lines and their subsequent overlapping, with the intensity decreasing dramatically. However, the isovalent impurity concentrations at which the comparable effects are observed are different. For Sn, they are lower by an order of magnitude than for Ge. The investigations carried out demonstrated that similar variations in the shape of the absorption spectra are also observed for C-doped crystals (Fig. 2*e*). However, because of the low limiting solubility of C in Si, a wide broadening of the absorption lines is not attained, in contrast with Ge- or Sn-doping. Comparable variations of the thermodonor absorption-spectrum shape are brought about, for example, by C-doping to a concentration of about 1.5×10^{18} cm^{-3}, by Sn-doping to a concentration of 4×10^{18} cm^{-3}, and by Ge-doping to a concentration of 7×10^{19} cm^{-3}. Let us compare the isovalent impurity concentrations, which lead to identical spectral variations, with their deformational charges A, which amount to the variations of the unit cell volume with the introduction of one impurity atom. These charges equal $|A_C| = 16.5 \times 10^{-25}$ cm^{-3}, $|A_{Sn}| = 8 \times 10^{-25}$ cm^{-3}, and $|A_{Ge}| = 1.2 \times 10^{-25}$ cm^{-3}, respectively [21]. It can be seen that the larger this quantity, the lower the isovalent impurity concentration that is necessary to attain the comparable effects. Thus, the investigations carried out indicate that Sn-, Ge-, and C-doping of Si lead to identical variations in the thermodonor absorption spectra. However, the effect depends on the magnitude of elastic stress induced by the isovalent impurity in Si: the larger the deformational charge of the isovalent impurity, the lower the concentrations necessary for comparable effects.

The relative escape of optically active O, i.e., $\eta_0(t) = 1 - N_O(t)/N_O(0)$, where $N_O(0)$ is the initial concentration of O in the samples and $N_O(t)$ is the concentration after t hours of thermal treatment, was also measured for the samples under investigation during their thermal treatment. The results obtained are shown in Fig. 3. As for Si, the escape of optically active O increased with an increase in the thermal treatment time. For an Sn content in Si of $N_{Sn} \geq 10^{18}$ cm^{-3}, O escape from the samples dropped abruptly. No variations in the O concentration with the thermal treatment time were observed for $N_{Sn} \geq 4 \times 10^{18}$ cm^{-3} (the values determined were within the experimental accuracy limits).

The thermodonor concentrations, which were determined for the same crystals from measurements of the Hall effect, are shown in Fig. 4. It can be seen that an increase in the Sn concentration leads to an abrupt decrease in the efficiency of introducing the quenched-in donors. Because of this, for a Sn content of 2×10^{19} cm^{-3}, their concentration is about 4×10^{13} cm^{-1}. This is in agreement with the data obtained from the analysis of the absorption spectra. The concentration of quenched-

in donors in Si for the same duration of the thermal treatment is 2.1×10^{16} cm^{-3} (the point on the ordinate axis in Fig. 4).

Thus, it is found from the investigations carried out that Sn-doping of Si, similarly to Ge- and C-doping, leads to a decrease in the efficiency of introducing low-temperature quenched-in donors. It was demonstrated that the effect of suppressing the formation of quenched-in donors in Si containing isovalent impurities depends on the magnitude of the elastic stress induced by the isovalent impurity in Si. The larger the deformational charge of the isovalent impurity, the lower the concentrations necessary for observation of the comparable effects.

REFERENCES

1. G. D. Watkins, IEEE Trans. Nucl. Sci. **NS-16**, 13 (1969).
2. A. R. Bean, R. C. Newman, and R. S. Smith, J. Phys. Chem. Solids **31**, 739 (1970).
3. G. D. Watkins, Phys. Rev. B **12**, 4383 (1975).
4. V. K. Bazhenov and V. I. Fistul', Fiz. Tekh. Poluprovodn. (Leningrad) **18**, 1345 (1984) [Sov. Phys. Semicond. **18**, 843 (1984)].
5. E. V. Solov'eva and M. G. Mil'vidskiĭ, Fiz. Tekh. Poluprovodn. (Leningrad) **17**, 2022 (1983) [Sov. Phys. Semicond. **17**, 1289 (1983)].
6. V. B. Neĭmash, M. G. Sosnin, B. M. Turovskiĭ, *et al.*, Fiz. Tekh. Poluprovodn. (Leningrad) **16**, 901 (1982) [Sov. Phys. Semicond. **16**, 577 (1982)].
7. G. Davies, A. S. Oates, R. C. Newman, *et al.*, J. Phys. C **19**, 841 (1986).
8. L. I. Khirunenko, V. I. Shakhovtsov, V. K. Shinkarenko, *et al.*, Fiz. Tekh. Poluprovodn. (Leningrad) **21**, 562 (1987) [Sov. Phys. Semicond. **21**, 345 (1987)].
9. A. R. Bean and R. C. Newman, J. Phys. Chem. Solids **33**, 255 (1972).
10. Yu. M. Babitskiĭ, N. I. Gorbacheva, P. M. Grinshteĭn, and M. G. Mil'vidskiĭ, Fiz. Tekh. Poluprovodn. (Leningrad) **18**, 1309 (1984) [Sov. Phys. Semicond. **18**, 818 (1984)].
11. L. I. Khirunenko, V. I. Shakhovtsov, and V. V. Shumov, Mater. Sci. Forum **258**–**263**, 1767 (1997).
12. E. Hild, P. Gaworzewski, M. Franz, and K. Pressel, Appl. Phys. Lett. **72**, 1362 (1998).
13. Yu. M. Babitskiĭ, N. I. Gorbacheva, P. M. Grinshteĭn, *et al.*, Fiz. Tekh. Poluprovodn. (Leningrad) **22**, 307 (1988) [Sov. Phys. Semicond. **22**, 187 (1988)].
14. D. R. Bosomworth, N. Hayes, A. R. L. Spray, and G. D. Watkins, Proc. R. Soc. London **317**, 133 (1970).
15. H. Yamasda-Kaneta, C. Kaneta, and T. Ogawa, Phys. Rev. B **47**, 9338 (1993).
16. I. Khirunenko, V. I. Shakhovtsov, V. J. Shumov, and V. I. Yashnik, *Early Stages of Oxygen Precipitation in Silicon* (Kluwer, Dordrecht, 1996).
17. L. I. Khirunenko, Yu. V. Pomozov, M. G. Sosnin, and V. K. Shinkarenko, Physica B (Amsterdam) **273**–**274**, 317 (1999).
18. G. Herzberg, in *Molecular Spectra and Molecular Structure* (Van Nostrand, New York, 1945; Inostrannaya Literatura, Moscow, 1949), Chap. 1.
19. B. Pajot, Semicond. Semimet. **42**, 191 (1994).
20. A. N. Lazarev, I. S. Lazarev, I. S. Ignat'ev, and T. F. Tenisheva, in *Vibrations of Simple Molecules with Si–O Bonds* (Nauka, Leningrad, 1991), p. 59.
21. V. E. Kustov, M. G. Mil'vidskiĭ, Yu. G. Semenov, *et al.*, Fiz. Tekh. Poluprovodn. (Leningrad) **20**, 270 (1986) [Sov. Phys. Semicond. **20**, 169 (1986)].

Translated by N. Korovin

Semiconductors, Vol. 34, No. 9, 2000, pp. 998–1003. Translated from Fizika i Tekhnika Poluprovodnikov, Vol. 34, No. 9, 2000, pp. 1039–1045.

ATOMIC STRUCTURE AND NONELECTRONIC PROPERTIES OF SEMICONDUCTORS

Early Stages of Oxygen Precipitation in Silicon: The Effect of Hydrogen

V. P. Markevich*, L. I. Murin*, J. L. Lindström, and M. Suezawa*****

**Institute of Solid-State and Semiconductor Physics, Belarussian Academy of Sciences, ul. Brovki 17, Minsk, 220072 Belarus*

***Lund University, Department of Solid State Physics, S-221 00 Lund, Sweden*

****Institute for Materials Research, Tohoku University, Sendai 980-8577, Japan*

E-mail: murin@ifttp.bas-net.by

Submitted March 6, 2000;
accepted for publication March 16, 2000

Abstract—The formation of small oxygen clusters upon heat treatment at 280–375°C was studied in crystalline silicon doped with hydrogen by high-temperature in-diffusion. The presence of hydrogen in concentrations of 10^{15}–10^{16} cm^{-3} significantly enhances (by up to a factor of 10^6 at $T \le 300$°C) the oxygen diffusivity in Si crystals. Possible mechanisms of interaction between O and H impurity atoms and the origin of hydrogen-enhanced oxygen diffusion in silicon are discussed. © *2000 MAIK "Nauka/Interperiodica".*

1. INTRODUCTION

Oxygen is present in high concentrations (~10^{18} cm^{-3}) in the starting Czochralski-grown crystalline silicon (Cz-Si) and can be effectively introduced into Si crystals by various high-temperature technological procedures. Being electrically inactive, oxygen can nevertheless strongly affect the characteristics of a material. Oxygen precipitation has long been used for internal gettering of fast-diffusing metal impurities. On the other hand, even short-term thermal treatment of oxygen-containing Si crystals in the temperature range of 300–700°C gives rise to various electrically active centers (quenched-in donors, etc.). As a result of such thermal treatments commonly used at the final stages of the technological cycle, the electrical properties of the material and, correspondingly, the operating characteristics of the fabricated devices may change markedly. In this connection, the behavior of oxygen impurity atoms in silicon has been studied intensively in recent years.

However, despite extensive studies in this field (see, e.g., [1, 2] and references therein) and the use of a great diversity of investigation techniques, a number of key issues still remain unclarified. This is primarily true for the formation mechanism of thermal donors and processes of in- and out-diffusion of oxygen at $T_a \le 700$°C. While in the temperature range of 700–1300°C the processes of mass transport and oxygen precipitation are limited by the conventional (normal) diffusion of isolated O_i atoms, at T_a = 300–700°C the situation is more complicated. In this temperature range, both oxygen agglomeration and the formation of diffusion profiles are accelerated and can only be described using an effective oxygen diffusivity, exceeding that for normal diffusion by several orders of magnitude. This is supposedly due to the existence of fast-diffusing oxygen-containing complexes. However, both the nature of these complexes and the mechanism of enhanced O diffusion have not been elucidated conclusively.

Recently, it was established that atomic hydrogen introduced into Cz-Si crystals strongly affects oxygen behavior. In particular, a pronounced enhancement of the loss of O_i from a solid solution and the generation of oxygen-containing doubly charged thermal donors (TD) was observed upon thermal treatment of Si:(O, H) crystals in the temperature range of 350–450°C [3–10]. Presumably, this enhancement is due to a significant increase in the mobility of oxygen atoms as a result of their interaction with fast-diffusing H atoms [3, 4, 6].

The mechanisms of interaction between hydrogen and oxygen impurity atoms and the possible structures of O–H complexes, possibly responsible for the enhanced diffusion of O atoms in silicon, have been considered in a number of theoretical studies [11–14]. No stable hydrogen–oxygen complex with a valence O–H bond has been found. However, various energetically favorable configurations of a center including one atom of hydrogen and oxygen each have been derived. According to [11], the energetically favorable configuration of such a center in Si crystals is a complex with hydrogen and oxygen atoms residing at neighboring bond-center sites of a silicon atom. It was found [12] that, in the most stable configuration, the hydrogen and oxygen atoms are bonded to the same silicon atom, but the H atom occupies the antibonding position opposite the bond-centered O atom. An O–H complex in various charge states was considered in [13, 14], and it was found that the configuration with O and H atoms at neighboring bond-center sites is energetically favorable for the neutral and positively charged states, whereas the configuration with a hydrogen atom in the antibonding position is

more stable for the negatively charged state. All calculations demonstrated that the activation energy of oxygen atom migration must decrease as a result of the O–H interaction.

Two types of complexes incorporating a hydrogen atom and an oxygen atom have been found experimentally in Cz-Si crystals implanted with protons at $T = 20$ K [15]. It was shown that the structure of these complexes differed from the theoretically derived structures [11–14]. In addition, it was established that these complexes are unstable. On raising the temperature of a crystal to 200 K, they disappear and can hardly be responsible for the enhanced diffusion of oxygen at temperatures higher than 300°C. Thus, it may be concluded that there is still no universally accepted model of interaction between hydrogen and oxygen atoms that would describe the available experimental data on the hydrogen-enhanced diffusion of oxygen.

Recently, two important results were obtained, inspiring hope that the problem in question could be solved. Firstly, local vibration modes of a complex incorporating two oxygen atoms (oxygen dimer O_{2i}) were identified [16–18] together with the local vibration modes of the first three centers belonging to the family of doubly charged oxygen-containing thermal donors [19, 20]. Secondly, IR absorption lines associated with hydrogen molecules (H_2) at a tetrahedral interstitial site in the Si lattice and O_i–H_2 complexes were observed [21–24]. The spectroscopy of local vibration modes is used in this work to study the formation of small oxygen clusters in hydrogenated silicon in order to elucidate the mechanism of hydrogen-enhanced diffusion and clustering of oxygen.

2. EXPERIMENTAL

Czochralski-grown phosphorus-doped *n*-type silicon crystals ($\rho_0 = 10$–$20\ \Omega$ cm) were studied. The oxygen concentration in the samples was determined from optical absorption [25] to be 5×10^{17}–12×10^{17} cm^{-3}. The concentration of carbon was lower than 10^{16} cm^{-3}. Hydrogen was introduced into the samples by high-temperature (1200–1300°C) treatment in a H_2 atmosphere for 1 or 0.5 h. The gas pressure was 1.0 or 1.5 atm. After thermal treatment, the samples were cooled by submerging ampules with the samples into water. The hydrogenated and control untreated samples were isothermally annealed in dry nitrogen at various temperatures in the range of 280–375°C. Optical absorption spectra were measured at 10 and 295 K with a resolution of 0.5 or 1.0 cm^{-1} using a Bruker IFS-113v Fourier spectrometer.

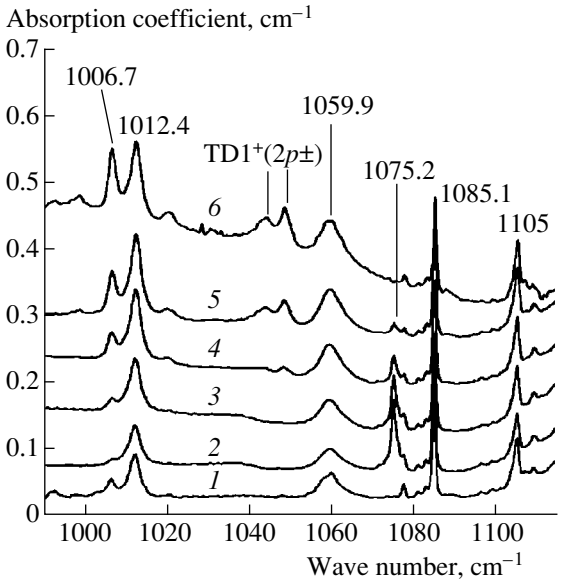

Fig. 1. Absorption spectra of silicon crystals with an oxygen content of 1.15×10^{18} cm^{-3} at 10 K: (*1*) initial crystal; (*2*) after thermal treatment at 1200°C for 1 h in hydrogen; and (*3*)–(*6*) after thermal treatment of sample 2 at 300°C for 45, 185, 360, and 1200 min, respectively.

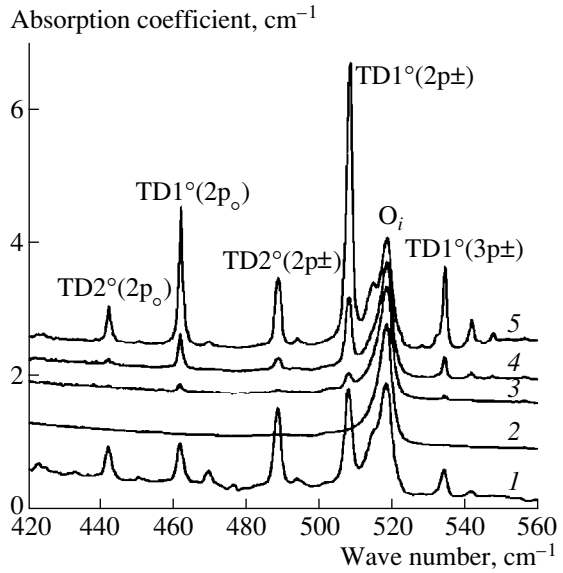

Fig. 2. Absorption spectra of silicon crystals with an oxygen content of 1.15×10^{18} cm^{-3}at 10 K: (*1*) initial; (*2*) after thermal treatment at 1200°C for 1 h in hydrogen; and (*3*)–(*5*) after thermal treatment of sample 2 at 300°C for 90, 185, and 360 min, respectively.

3. RESULTS AND DISCUSSION

Figures 1 and 2 show the absorption spectra in the wave-number ranges of 990–1115 and 420–560 cm^{-1} for a silicon sample that had an initial oxygen concentration of 1.15×10^{18} cm^{-3} and was treated with hydrogen at $T = 1200$°C and then annealed at $T = 300$°C for varied times. For comparison, the absorption spectra of the initial sample are also shown. The absorption lines at 1012.4 and 1059.9 cm^{-1} observed for the starting material have been assigned previously to local vibration modes of a center incorporating two oxygen

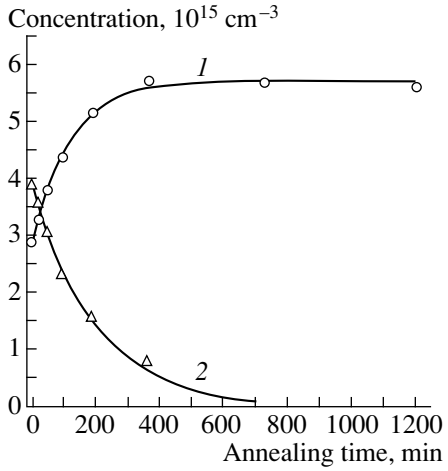

Fig. 3. Concentration of (*1*) oxygen dimers and (*2*) H_2 molecules vs. time of annealing at 300°C for a silicon sample that had an oxygen concentration $N_O = 1.15 \times 10^{18}$ cm^{-3} and was thermally treated at 1200°C in hydrogen. The solid lines in the figure are calculated by fitting simple exponential dependences to experimental data.

atoms [16, 17]. The possible structures of complexes responsible for these bands have been considered theoretically [18, 26]. The absorption bands at 1105.4 and 1006.8 cm^{-1} are also due to vibrations of O atoms in complexes supposedly incorporating two and three oxygen atoms, respectively [16, 27]. However, the bands have not been positively identified. The absorption band at 1085.1 cm^{-1} is related to vibrations of the interstitial natural oxygen isotope ^{18}O in the silicon lattice [28]. Absorption bands in the range of 420–540 cm^{-1} are due to electron transitions from the ground 1*s* state to excited states of doubly charged quenched-in donors of various types in the neutral charge state [29].

High-temperature treatment in hydrogen reduces the intensity of the bands at 1012.4, 1059.9, and 1105.4 cm^{-1}, with the band at 1006.7 cm^{-1} nearly completely disappearing. The lines associated with electron transitions in quenched-in donors also disappear. At the same time, the intensity of the band at 1085.1 cm^{-1} changes only slightly, which indicates that the concentration of isolated oxygen atoms at interstitial sites is not changed significantly by short-term high-temperature treatments. Hydrogenation leads to the appearance of an intense band at 1075.2 cm^{-1} in the spectra of oxygen-containing samples [21, 30]. This band has been identified as resulting from stretching vibrations of an oxygen atom in a complex incorporating a bond-center oxygen atom and a hydrogen molecule at the nearest tetrahedral (T_d) interstitial site [21–24, 31].

The interaction of free hydrogen molecules with O_i atoms in silicon has been studied in detail [22–24]. It was found that practically the whole amount of hydrogen introduced into Cz-Si crystals of the *n*-type conductivity by high-temperature in-diffusion with subsequent fast cooling is present in the lattice as H_2 molecules occupying the T_d interstices. Hydrogen molecules in silicon are mobile even at room temperature, the activation energy of their diffusion being 0.78 eV [22]. Finding themselves in the course of migration near other crystal lattice defects, H_2 molecules may interact with them. In Cz-Si crystals, interstitial oxygen atoms act as effective sinks for H_2. The O_i–H_2 complex is, however, weakly bound, with its binding energy estimated at 0.28 eV [22]. Heating hydrogenated Cz-Si crystals to 100°C leads to the decomposition of O_i–H_2 complexes and the appearance of mobile H_2 molecules in the lattice. However, on subsequent cooling of the crystals, the molecules are again captured by interstitial oxygen atoms. In the absence of other effective sinks for H_2, except for oxygen atoms, an equilibrium distribution of molecules between the free and bound (by O_i) states is attained rather rapidly at temperatures higher than 295 K. An analytical expression and parameter values characterizing this distribution were obtained in [22]. With knowledge of the equilibrium intensity of the band at 1075.2 cm^{-1}, the concentration of the O_i–H_2 complexes can be evaluated and the content of hydrogen in the form of H_2 molecules in Cz-Si crystals calculated.

Figure 3 shows the concentration of hydrogen molecules and oxygen dimers versus the time of annealing at 300°C for a hydrogenated Cz-Si sample. The concentrations of O_i–H_2 and O_{2i} centers were calculated from the integrated absorption I ($I = \int \alpha \, d\nu$, where α is the absorption coefficient at a frequency ν) for the bands at 1075.2 and 1012.4 cm^{-1}, respectively. The calibration factor for calculating the concentrations was assumed to be equal to that for isolated interstitial oxygen atoms, i.e., 0.94×10^{16} cm^{-1} [32]. It can be seen from Fig. 3 that even in the early stages of thermal treatment the concentration of dimers in Cz-Si:(O, H) grows steeply and then levels off. It should be noted that a similar thermal treatment of control initial crystals caused no noticeable changes in the intensity of the band at 1012.4 cm^{-1}, i.e., in the concentration of oxygen dimers. The highest attainable concentration of dimers in hydrogenated samples greatly exceeded the concentration of O_{2i} centers in the initial material.

Annealing the hydrogenated crystals also led to a higher intensity of the band at 1006.8 cm^{-1} (Fig. 1) and the absorption bands in the wave-number range of 420–550 cm^{-1} (Fig. 2). In the initial material, no noticeable changes in the intensity of these bands were observed. After annealing at $T = 300$°C for 20 h, the intensities of the band at 1006.8 cm^{-1} and the absorption bands related to electron transitions in TD-1 for hydrogenated crystals greatly exceeded the intensities of the corresponding bands in the initial samples. Thus, the obtained data indicate the accelerated formation of dimers and complexes incorporating three or more oxygen atoms in hydrogen-saturated samples.

Analyzing the dependence of the O_{2i} concentration on the duration of annealing at $T = 300$°C, we can eval-

uate the effective diffusivity of oxygen in Si:(O, H) crystals. Previously, it was shown [17] that the kinetics of O_{2i} complex formation is well described in the early stages of oxygen clustering by the following differential equation:

$$\frac{dN_2}{dt} = k_1N_1^2 - k_{-2}N_2 - k_2N_2N_1. \quad (1)$$

Here, N_1 and N_2 are the concentrations of O_i and O_{2i}, respectively; k_1 and k_2 are the rate constants of the interaction of isolated oxygen atoms and oxygen dimers with O_i; and k_{-2} is the rate constant of O_{2i} dissociation. The quasi-equilibrium concentration of dimers is given by

$$N_2^{eq} = k_1N_1^2/k_{-2} + k_2N_1, \quad (2)$$

or, in another form,

$$N_2^{eq} = G_2\tau_2, \quad (3)$$

where G_2 and τ_2 are the generation rate and lifetime of O_{2i} complexes, respectively. It was found that the value of τ_2 is about 115 min at 300°C in the investigated Si:(O, H) crystal. As can be seen from Fig. 3, $N_2^{eq} \approx 5.5 \times 10^{15}$ cm^{-3} for the same crystal. Then, in accordance with Eq. (3), the rate of dimer generation is 8.0×10^{11} cm^{-3} s^{-1}. Since $G_2 = k_1N_1^2 = 4\pi r_1 D_1^{eff} N_1^2$, where r_1 is the interaction radius of two O_i atoms and D_1^{eff} is the effective diffusivity of oxygen, knowing G_2, we can evaluate D_1^{eff}. Assuming that $r_1 = 5$ Å and taking into account that $N_1 = 1.15 \times 10^{18}$ cm^{-3}, we find that $D_1^{eff} = 9.5 \times 10^{-19}$ cm^2 s^{-1}. In accordance with the expression for the normal diffusivity of oxygen ($D_1 = 0.13\exp(-2.53/kT)$) [5]), the D_1 value at 300°C is 7.5×10^{-24} cm^2 s^{-1}. Thus, the analysis we made shows that the effective diffusivity of oxygen in hydrogenated silicon crystals greatly (by more than five orders of magnitude) exceeds the normal value of D_1 at $T = 300$°C.

Since the formation of oxygen dimers constitutes the first stage of all phenomena related to oxygen clustering, an important issue is the nature of processes determining the lifetime of oxygen dimers and, consequently, the value of N_2^{eq} in Si:(O, H) crystals. It is known that O_{2i} dissociation is dominant in the starting crystals at temperatures higher than 500°C [5], which leads to $\tau_2 = 1/k_{-2}$ and a quadratic dependence of N_2^{eq} on the oxygen concentration. At temperatures of ≤400°C, the capture of mobile dimers by O_i is predominant. In this case, $\tau_2 = 1/k_2N_1$ and a linear dependence of the quasi-equilibrium concentration of dimers on the oxygen concentration is observed [17]. The investigations performed demonstrated that the process of dimer capture by O_i is not dominant in hydrogenated crystals in the temperature range of 280–375°C. It was found that the dependence of N_2^{eq} on N_1 is nearly quadratic even at such low temperatures as 300°C. In addition, a substantial increase in N_2^{eq} is observed as the temperature is lowered within the temperature range studied, with an opposite dependence being observed for the starting material (Fig. 4).

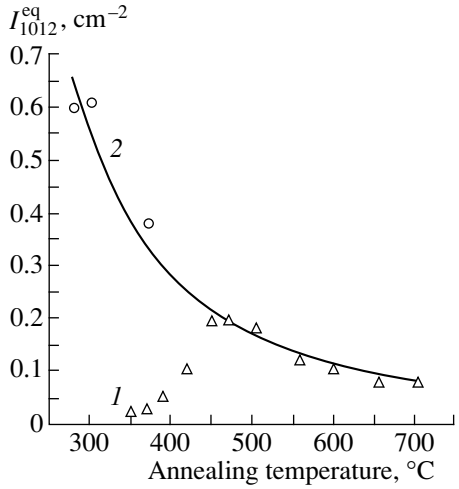

Fig. 4. Quasi-steady integrated absorption due to band at 1012 cm^{-1}, (I_{1012}^{eq}) vs. annealing temperature for (*1*) starting and (*2*) hydrogen-treated silicon samples. The solid line represents the calculation by formula (5) for oxygen dimers with a binding energy of 0.23 eV.

This means that the dissociation of oxygen dimers in hydrogenated crystals is accelerated to a greater extent than the process of their capture; i.e., we have $k_{-2} \gg k_2N_1$ even at 300–400°C. This phenomenon can be explained as follows. According to the principle of detailed balancing [33],

$$k_{-2} = k_1\frac{N_{SO}g_1}{g_2}\exp\left(-\frac{E_{b2}}{kT}\right), \quad (4)$$

where N_{SO} is the number of possible states for an interstitial oxygen in a unit Si crystal volume ($N_{SO} = 10^{23}$ cm^{-3}); g_1 and g_2 are the numbers of possible equivalent sites with an energy minimum for O_i and O_{2i}, respectively, in the unit cell of the Si crystal; and E_{b2} is the binding energy of the O_{2i} complex. Since $k_1 = 4\pi r_1 D_1^{eff}$, $k_{-2} \sim D_1^{eff}$. In other words, the rate of the reverse reaction increases to the same extent, as does that of the forward reaction, in proportion to the increasing effective diffusivity of oxygen.

For the case of $k_{-2} \gg k_2N_1$, taking into account (4), Eq. (2) transforms into

$$N_2^{eq} = k_1N_1^2/k_{-2} = \frac{N_1^2g_2}{N_{SO}g_1}\exp\left(\frac{E_{b2}}{kT}\right). \quad (5)$$

From expression (5) it follows that in the case in question ($k_{-2} \gg k_2 N_1$) the quasi-equilibrium concentration of dimers is governed only by the oxygen concentration, binding energy of dimers, and temperature; i.e., it is independent of the hydrogen content (N_H affects solely the oxygen diffusivity). The solid line in Fig. 4 was calculated by formula (5) for dimers with a binding energy of 0.23 eV.

The dependences shown in Fig. 4 and their interpretation can be used to explain the previously observed phenomenon of a substantially growing influence of hydrogen on processes associated with oxygen clustering at lower thermal-treatment temperatures [8, 32]. In particular, it was found that, while the quenched-in donor generation is accelerated in hydrogenated crystals (compared with the initial silicon) by a factor of 5 at 450°C, this ratio increases to 200 at 350°C [32]. Taking into account that the initial stage of all processes associated with the decomposition of a solid solution of oxygen in Si crystals is the formation of oxygen dimers, this effect can be accounted for by the increasing difference between the quasi-steady concentration of dimers in hydrogenated crystals and in those containing no hydrogen as the temperature is lowered (Fig. 4).

Let us now consider the possible mechanisms of interaction between H and O impurity atoms, which can enhance oxygen diffusion, and the issue of the stability of hydrogen influence on O diffusion. As already noted, it has been established previously that practically the whole amount of hydrogen introduced into high-quality Cz-Si crystals by high-temperature in-diffusion is in the form of H_2 molecules at room temperature [22–24]. The binding energy of the H_2 molecule in the Si lattice has not been determined experimentally. According to some indirect estimates and theoretical calculations, the most probable value is 1.6 eV [33]. Calculations show that, for such a E_b value, the fraction of atomic hydrogen at 300°C is only ~0.01% of the total concentration of hydrogen (for $N_{H\Sigma} = 10^{15}$–10^{16} cm^{-3}) present as isolated atoms and H_2 molecules. This means that, at $T = 300$°C, too, practically the whole amount of mobile hydrogen is in the form of H_2 molecules. However, at the present stage of investigations, it is impossible to state with confidence which form of mobile hydrogen-containing species, atomic or molecular, is responsible for the enhanced oxygen diffusion. The probability that two particles interact is proportional to the product of the concentration of these particles by their diffusivity. Since the diffusivity of individual hydrogen atoms ($D_H = 9.4 \times 10^{-3}\exp(-0.48/kT)$ [33–35]) at $T = 300$°C exceeds that of H_2 ($D_{H2} = 2.6 \times 10^{-4}\exp(-0.78/kT)$ [22]) by a factor of 1.6×10^4, then, in the absence of a barrier for capture, the probability of interaction between individual hydrogen atoms and oxygen is comparable with that of interaction between O_i and H_2. It is also unclear whether or not each event of interaction between hydrogen and a hydrogen-containing center ruptures a Si–O bond and leads to the jump of an O atom into a neighboring interstice. Thus, the issue of the mechanism of hydrogen–oxygen interaction leading to enhanced diffusion of O atoms remains open and invites further research.

As can be seen from Fig. 3, the concentration of hydrogen molecules introduced into crystals by high-temperature in-diffusion decreases when the crystals are annealed at 300°C. Calculations show that the thickness of the subsurface layer which hydrogen leaves as a result of out-diffusion in atomic or molecular form is no thicker than 1 mm after thermal treatment at $T = 300$°C for 10 h. Since the samples studied were no thicker than 6 mm, the observed change in the hydrogen concentration cannot be explained by the mobile hydrogen-containing species leaving for the surface. It may be assumed that hydrogen remains in the crystal bulk in the form of stable hydrogen-containing complexes. Indeed, it has been found that hydrogen is incorporated into shallow-level singly charged donors formed in hydrogenated crystals upon thermal treatment at $T = 350$°C [36]. It was established in this study that the disappearance of hydrogen molecules upon annealing of Si:(O, H) crystals in the temperature range of 280–375°C is accompanied by the emergence of absorption bands at 1956.2, 2131.5, 2191.9, and 2202.8 cm^{-1}. These bands have previously been observed in hydrogenated crystals [37–39]; however, they have not been identified as yet. It is known that absorption bands in this region are characteristic of stretching vibrations related to Si–H bonds in the vicinity of interstitial or vacancy defects in the silicon lattice [40, 41]. Complexes of hydrogen with native defects in the lattice may be rather stable (to 600°C and higher) and act for a long time as a source of mobile hydrogen atoms in the Si lattice. This accounts for the prolonged effect of hydrogen introduced into Cz-Si crystals by high-temperature in-diffusion on processes associated with oxygen clustering at 350–450°C [5].

4. CONCLUSION

Thus, doping of Czochralski-grown crystalline silicon with hydrogen leads to a dramatic increase in the generation rates and quasi-steady concentrations of small oxygen clusters (dimers, trimers, and bistable quenched-in donors) in crystals thermally treated at 280–375°C. The kinetics of accumulation of oxygen dimers was studied in detail in Si:(O, H) crystals. The characteristic formation times of these complexes were determined and the effective oxygen diffusivity was calculated in terms of the theory of diffusion-controlled reactions. In Si crystals containing 10^{15}–10^{16} cm^{-3} of hydrogen, oxygen diffusivity that exceeded 10^5–10^6-fold in crystals with a low content of hydrogen.

Hydrogen enhances to the same extent the direct and reverse reactions related to oxygen clustering. As a result, the quasi-equilibrium concentration of small oxygen clusters is independent of the hydrogen concentration when the latter exceeds some critical value determined solely by the binding energy of the complexes and

by temperature. The obtained results make it possible to explain qualitatively the temperature dependence of the hydrogen-induced enhancement of the loss of interstitial oxygen and generation of quenched-in donors.

The disappearance of mobile hydrogen-containing species (H and H_2) upon thermal treatment of Si crystals in the temperature range of 300–375°C is accompanied by the formation of new optically active centers. The absorption bands associated with these centers are characteristic of stretching vibrations due to Si–H bonds in the vicinity of interstitial or vacancy defects in the silicon lattice.

5. ACKNOWLEDGMENTS

This work was supported in part by the Belarussian Republican Foundation for Basic Research and INTAS (grant Belarus 97-0824).

REFERENCES

1. *Oxygen in Silicon*, Ed. by F. Shimura (Academic, London, 1994); Semicond. Semimet. Series **42** (1994).
2. *Early Stages of Oxygen Precipitation in Silicon*, Ed. by R. Jones (Kluwer, Dordrecht, 1996); NATO ASI Ser., Ser. 3 **17** (1996).
3. A. R. Brown, M. Clayborn, R. Murray, *et al.*, Semicond. Sci. Technol. **3**, 591 (1988).
4. R. C. Newman, J. H. Tucker, A. R. Brown, and S. A. McQuaid, J. Appl. Phys. **70**, 3061 (1991).
5. S. A. McQuaid, M. J. Binns, C. A. Londos, *et al.*, J. Appl. Phys. **77**, 1427 (1995).
6. H. J. Stein and S. Hahn, Appl. Phys. Lett. **56**, 63 (1990).
7. H. J. Stein and S. Hahn, J. Appl. Phys. **75**, 3477 (1994).
8. A. Hara, M. Koizuka, M. Aoki, *et al.*, Jpn. J. Appl. Phys. **33**, 5577 (1994).
9. V. P. Markevich, L. I. Murin, and A. G. Litvinko, Pis'ma Zh. Tekh. Fiz. **19** (19), 39 (1993) [Tech. Phys. Lett. **19**, 617 (1993)].
10. V. P. Markevich and L. I. Murin, Fiz. Tekh. Poluprovodn. (St. Petersburg) **30**, 265 (1996) [Semiconductors **30**, 148 (1996)].
11. S. K. Estreicher, Phys. Rev. B **41**, 9886 (1990).
12. R. Jones, S. Öberg, and A. Umerski, Mater. Sci. Forum **83–87**, 551 (1992).
13. M. Ramamoorthy and S. T. Pantelides, in *Early Stages of Oxygen Precipitation in Silicon*, Ed. by R. Jones (Kluwer, Dordrecht, 1996); NATO ASI Ser., Ser. 3 **17**, 197 (1996).
14. M. Ramamoorthy and S. T. Pantelides, Solid State Commun. **106**, 243 (1998).
15. B. Bech Nielsen, K. Tanderup, M. Budde, *et al.*, Mater. Sci. Forum **258–263**, 391 (1997).
16. L. I. Murin, T. Hallberg, V. P. Markevich, and J. L. Lindström, Phys. Rev. Lett. **80**, 93 (1998).
17. T. Hallberg, J. L. Lindström, L. I. Murin, and V. P. Markevich, Mater. Sci. Forum **258–263**, 361 (1997).
18. S. Öberg, C. P. Ewels, R. Jones, *et al.*, Phys. Rev. Lett. **81**, 2930 (1998).
19. J. L. Lindström and T. Hallberg, J. Appl. Phys. **77**, 2684 (1995).
20. T. Hallberg and J. L. Lindström, J. Appl. Phys. **79**, 7570 (1996).
21. R. E. Pritchard, M. J. Ashwin, R. C. Newman, *et al.*, Phys. Rev. B **56**, 13118 (1997).
22. V. P. Markevich and M. Suezawa, J. Appl. Phys. **83**, 2988 (1998).
23. V. P. Markevich, M. Suezawa, and L. I. Murin, Mater. Sci. Eng. B **58**, 26 (1999).
24. R. E. Pritchard, M. J. Ashwin, J. H. Tucker, and R. C. Newman, Phys. Rev. B **57**, R15048 (1998).
25. A. Baghdadi, W. M. Bullis, M. C. Croarkin, *et al.*, J. Electrochem. Soc. **136**, 2015 (1989).
26. M. Pesola, J. von Boehm, and R. M. Nieminen, Phys. Rev. Lett. **82**, 4022 (1999).
27. L. I. Murin and V. P. Markevich, in *Early Stages of Oxygen Precipitation in Silicon*, Ed. by R. Jones (Kluwer, Dordrecht, 1996); NATO ASI Ser., Ser. 3 **17**, 329 (1996).
28. B. Pajot, in *Oxygen in Silicon*, Ed. by F. Shimura (Academic, London, 1994); Semicond. Semimet. Series **42**, Chap. 6 (1994).
29. P. Wagner and J. Hage, Appl. Phys. A **49**, 123 (1989).
30. V. P. Markevich, M. Suezawa, and K. Sumino, Mater. Sci. Forum **196–201**, 915 (1995).
31. B. Hourahine, R. Jones, S. Öberg, and P. R. Briddon, Mater. Sci. Forum **258–263**, 277 (1997).
32. R. C. Newman, in *Early Stages of Oxygen Precipitation in Silicon*, Ed. by R. Jones (Kluwer, Dordrecht, 1996); NATO ASI Ser., Ser. 3 **17**, 19 (1996).
33. C. Herring and N. M. Johnson, in *Hydrogen in Semiconductors*, Ed. by J. I. Pankove and N. M. Johnson (Academic, San Diego, 1991); Semicond. Semimet. Series **34**, Chap. 10 (1991).
34. A. van Wieringen and N. Warmholtz, Physica (Amsterdam) **22**, 849 (1956).
35. Yu. V. Gorelkinskii and N. N. Nevinnyi, Mater. Sci. Eng. B **36**, 133 (1996).
36. S. A. McQuaid, R. C. Newman, and E. C. Lightowlers, Semicond. Sci. Technol. **9**, 1730 (1994).
37. M. W. Qi, G. R. Bai, T. S. Shi, and L. M. Xie, Mater. Lett. **3**, 467 (1985).
38. B. Pajot, B. Clerjaud, and Z.-J. Xu, Phys. Rev. B **59**, 7500 (1999).
39. N. Fukata and M. Suezawa, J. Appl. Phys. **86**, 1848 (1999).
40. S. J. Pearton, J. W. Corbett, and M. Stavola, *Hydrogen in Crystalline Semiconductors* (Springer-Verlag, Berlin, 1992), Springer Ser. Mater. Sci. **16** (1992).
41. S. Zh. Tokmoldin, B. N. Mukashev, Kh. A. Abdulin, and Yu. V. Gorelkinskii, Physica B (Amsterdam) **273/274**, 204 (1999).

Translated by M. Tagirdzhanov